

Analysis and Optimization of Fuel Cell Based Integrated Powering Systems for Clean Rail Applications

by

Khaled H. M. Al-Hamed

A Thesis Submitted in Partial Fulfillment

of the Requirements for the Degree of

Master of Applied Science in Mechanical Engineering

in

The Faculty of Engineering and Applied Science

University of Ontario Institute of Technology

Oshawa, Ontario, Canada

August 2019

© Khaled H. M. Al-Hamed, 2019

Thesis Examination Information

Submitted by: **Khaled H. M. Al-Hamed**

Master of Applied Science in Mechanical Engineering

Thesis title: Analysis and Optimization of Fuel Cell Based Integrated Powering Systems for Clean Rail Applications

An oral defense of this thesis took place on July 26, 2019 in front of the following examining committee:

Examining Committee:

Chair of Examining Committee	Dr. Martin Agelin-Chaab
Research Supervisor	Dr. Ibrahim Dincer
Examining Committee Member	Dr. Bekir Yilbas
Examining Committee Member	Dr. Dipal Patel
External Examiner	Dr. Shahryar Rahnamayan

The above committee determined that the thesis is acceptable in form and content and that a satisfactory knowledge of the field covered by the thesis was demonstrated by the candidate during an oral examination. A signed copy of the Certificate of Approval is available from the School of Graduate and Postdoctoral Studies.

Abstract

In this thesis, proposals of novel integrated fuel cell powering systems for cleaner railway applications are presented and analyzed thermodynamically. Both energy and exergy analyses are conducted on these systems for such an application to evaluate and compare them thermodynamically, in terms of their power outputs capabilities and energetic and exergetic efficiencies. Next, parametric studies on each of the proposed integrated fuel cell systems are provided to have a deeper understanding of the operation of these systems under various conditions. This understanding can help us in the optimization of exergetic efficiency and packaging feasibility of the systems in a locomotive. A newly introduced method of multi-objective optimization is implemented to optimize the integrated systems in terms of exergetic efficiencies, power split for space reductions, and hydrogen production rate. Lastly, economic and environmental justifications are given through a case study of a duty cycle of a passenger train. Fuel costs and CO₂ emissions of these proposed integrated systems are compared to the current technology of diesel-electric engines used in railways of Canada.

The thermodynamic analysis shows that these systems can reach high energetic and exergetic efficiencies of 80.06% and 77.55%, respectively for methane-based solid oxide fuel cell systems, while ammonia-based systems have the values of energetic and exergetic efficiencies of 61.20%, and 66.30%, respectively. Fuel costs of passenger train operation, using these proposed systems, are significantly reduced compared to diesel-electric engines. The most efficient system is system 3 and has a brake specific fuel consumption of 0.08902 kg kWh⁻¹, whereas a typical diesel-electric engine has a value of 0.2318 kg kWh⁻¹.

Keywords: Clean railway; cost; efficiency; energy; environment; exergy; solid oxide fuel cell; optimization.

Acknowledgements

Professor Dr. Ibrahim Dincer is a great supervisor and an excellent mentor who has been supporting and guiding me through my studies and research. With each passing day, I appreciate more and more his mentorship and direction.

I cannot deny the help of my colleagues in ACE 3030B who assisted me in different aspects of my journey as both an international graduate student and a researcher. Farid Safari is my first friend who showed me how to adapt to this new research environment. Anna Crivellari has been my source of emotional support through my studies and research and I am grateful for her company. Dr. Maan Al-Zareer is the man who I go to whenever I face difficulty in my research and he has always been kind and helpful.

Also, I would like to thank people who kept me motivated throughout my journey as a graduate student, namely Prof. Ahmet Z. Sahin, Prof. Ashfaq H. Bokhari, Dr. Mahmoud E. Khater, Prof. Bekir S. Yilbas, Prof. Tahar Laoui, my brother Abdullah H. M. Al-Hamed, and my dear friend Moiz M. Ali.

It is only just to acknowledge the most important person in my life, my mother. She is the most beloved woman (Sit El Habayeb) who raised me and supported my education since day one. Thank you Nawal A. O. Bawazir.

Statement of Contributions

Part of the work described in Chapter 4 has been published as:

Seyam S, Al-Hamed KHM, Qureshy AMMI, Dincer I, Agelin-Chaab M, Rahnamayan S. Multi-objective Optimization of Hydrogen Production in Hybrid Renewable Energy Systems. 2019 IEEE Congr. Evol. Comput., IEEE Congress on Evolutionary Algorithms; 2019.

Table of Contents

Thesis Examination Information	ii
Abstract	iii
Keywords	iii
Acknowledgements	iv
Statement of Contributions	v
Table of Contents	vi
List of Figures	x
List of Tables	xvii
Nomenclature	xx
Chapter 1: Introduction	1
1.1 Canadian Rail Transportation	1
1.2 Alternative Fuels	1
1.3 Solid Oxide Fuel Cells (SOFCs)	4
1.4 Motivation and Thesis Objectives	5
1.5 Thesis Outline	6
Chapter 2: Literature Review	8
2.1 Alternative Fuels	8
2.2 Fuel Cell Technology in Transportation	11
2.2.1 Solid Oxide Fuel Cell (SOFC) Technology	11
2.2.2 Other Fuel Cell Technologies	13
2.3 Integrated Fuel Cell Systems	14
2.4 Multi-Objective Optimization in Power Systems	16
2.5 Knowledge Gaps	18
Chapter 3: Systems Development	19

3.1 Systems 1a and 1b Description	19
3.1.1 SOFC-GT Cycle with Regeneration	19
3.1.2 Steam Rankine Cycle (SRC)	19
3.1.3 Organic Rankine Cycle (ORC)	20
3.1.4 Small Hot Water Production Cycle.....	20
3.1.5 Reversible Heat Pump Cycle.....	20
3.2 System 2 Description	21
3.2.1 Absorption Chiller with a Heat Exchanger Cycle.....	21
3.3 System 3 Description	22
3.4 System 4 Description	22
3.5 System 5 Description	23
3.6 System 6 Description	23
3.6.1 Ammonia-DSU and PEMFC Cycle	28
3.7 System 7 Description	28
3.7.1 MAHEFC with Regeneration Cycle	33
3.7.2 Ammonia-Organic Rankine Cycle (NH ₃ -ORC) for Fuel Cell Heat Recovery	33
Chapter 4: Thermodynamic Analysis	34
4.1 Thermodynamic Balance Equations	34
4.1.1 Mass Balance Equation.....	34
4.1.2 Energy Balance Equation	34
4.1.3 Entropy Balance Equation	35
4.1.4 Exergy Balance Equation	35
4.1.5 Exergy Destruction Rate and Specific Exergy Values	35
4.1.6 Major Assumptions	36
4.2 Thermodynamic Analysis of the Studied Cycles	37
4.2.1 SOFC-GT Primary Cycle with Regeneration.....	37
4.2.2 Steam Rankine Cycle (SRC)	40
4.2.3 Organic Rankine Cycle (ORC).....	41
4.2.4 Small Hot Water Production Cycle.....	42

4.2.5 Reversible Type Heat Pump Cycle	42
4.2.6 Absorption Chiller with a Heat Exchanger Cycle	45
4.2.7 Partially-Premixed Compression Ignition (PPCI) Engine	48
4.2.8 Heat recovery from SOFC using a preheated ORC cycle	49
4.2.9 Direct Ammonia SOFC-GT Cycle	51
4.2.10 Ammonia-DSU and PEMFC Cycle	52
4.2.11 Direct Ammonia MAHEFC	53
4.3 Overall Performance Parameters	55
4.4 Multi-Objective Optimization with Data Visualization	57
4.5 Fuel Costs and CO ₂ Emissions Analyses: A Case Study	64
Chapter 5: Results and Discussion	66
5.1 System 1a Results	67
5.1.1 Reversible Type Heat Pump Advantages in Railway Applications	67
5.1.2 Reference Case Results	68
5.1.3 Model Validation	71
5.1.4 Parametric Study Results	73
5.2 System 1b Results	84
5.2.1 Reference Case Results	85
5.2.2 Parametric Study Results	88
5.3 System 2 Results	95
5.3.1 Reference Case Results	95
5.3.2 Parametric Study Results	98
5.4 System 3 Results	102
5.4.1 Reference Case Results	102
5.4.2 Parametric Study Results	104
5.5 System 4 Results	112
5.5.1 Reference Case Results	112
5.5.2 Parametric Study Results	115

5.6 System 5 Results	120
5.6.1 Reference Case Results.....	120
5.6.2 Parametric Study Results	123
5.7 System 6 Results	128
5.7.1 Reference Case Results.....	128
5.7.2 Parametric Study Results	132
5.8 System 7 Results	136
5.8.1 Reference Case Results.....	138
5.8.2 Parametric Study Results.....	142
5.9 Systems Optimization Results.....	146
5.10 Comparative Evaluation of the Integrated Systems.....	156
5.10.1 Comparison of Proposed Integrated Systems at their Reference Cases and Optimum Operation Points	156
5.10.2 Fuel Costs and CO ₂ Emissions Comparison: A Case Study	158
Chapter 6: Conclusions and Recommendations.....	163
6.1 Conclusions	163
6.2 Recommendations	164
References.....	166

List of Figures

Figure 1.1: Greenhouse gas emission by economic sector in Canada from 1990 to 2017. Reproduced from [7].	2
Figure 1.2: Breakdown of GHG emissions in the Canadian transportation sector. Reproduced from [7].	3
Figure 2.1: Diesel fuel prices over the weeks of a year, from 2016 to 2019 week 32. Adopted from [37].	10
Figure 3.1: A schematic drawing of the integrated SOFC-GT-SRC-ORC system with a reversible type heat pump (System 1a).	24
Figure 3.2: A schematic drawing of the integrated SOFC-GT-SRC-ORC system with a reversible type heat pump (System 1b).	25
Figure 3.3: A schematic drawing of the integrated SOFC-GT-SRC-ORC system with an absorption chiller (System 2).	26
Figure 3.4: A schematic drawing of the integrated SOFC-PPCI-GT-ORC system with a reversible type heat pump (System 3).	27
Figure 3.5: P-V diagram of the ideal Otto cycle with fuel injection before combustion. This is for the PPCI engine.	28
Figure 3.6: A schematic drawing of the integrated SOFC-GT-SRC-ORC system with heat recovery from SOFC (System 4).	29
Figure 3.7: A schematic drawing of the fully ammonia-based SOFC-GT-ORC system with an absorption chiller (System 5).	30
Figure 3.8: A schematic drawing of the integrated SOFC-GT-SRC-ORC system with ammonia-DSU and PEMFC (System 6).	31
Figure 3.9: A schematic drawing of the integrated MAHEFC-SRC-ORC system with fuel cell heat recovery using ammonia-ORC (System 7).	32
Figure 4.1: Environmental Impact (<i>EI</i>) and Sustainability Index (<i>SI</i>) variation against the overall exergetic efficiency of a system ($\eta_{ex,overall}$) reproduced from [75].	57
Figure 4.2: Flow chart of the multi-objective optimization methods implemented in optimizing the integrated systems.	59

Figure 5.1: Comparison of the energetic and exergetic efficiencies between the subsystems of system 1a.	70
Figure 5.2: Comparison of exergy destruction rates of major components of system 1a.	72
Figure 5.3: Energetic and exergetic efficiencies are plotted against compression ratio across the air compressor. a) For overall integrated system and SOFC-GT subsystem. b) For SRC and NH ₃ -ORC subsystems.....	75
Figure 5.4: Electric power output values of the integrated system and its subsystems are plotted against compression ratio across the air compressor. Arrows indicate the corresponding axis of the parameter.	76
Figure 5.5: Energetic and exergetic efficiencies are plotted against ambient temperature. a) For overall integrated system and SOFC-GT subsystem. b) For SRC and NH ₃ -ORC subsystems.	77
Figure 5.6: Electric power output values of the integrated system and its subsystems are plotted against ambient temperature. Arrows indicate the corresponding axis of the parameter.	78
Figure 5.7: Energetic and exergetic efficiencies are plotted against excess air factor (λ). a) For overall integrated system and SOFC-GT subsystem. b) For SRC and NH ₃ -ORC subsystems.	80
Figure 5.8: Electric power output values of the integrated system and its subsystems are plotted against excess air factor (λ). Arrows indicate the corresponding axis of the parameter.	81
Figure 5.9: Energetic and exergetic efficiencies are plotted against α -parameter. a) For overall integrated system and SOFC-GT subsystem. b) For SRC and NH ₃ -ORC subsystems. $\lambda = 2$ to ensure complete combustion ($\lambda = 1 + \alpha$) and $r_p = 8$ to have reasonable exit turbine temperature.	82
Figure 5.10: Electric power output values of the integrated system and its subsystems are plotted against α -parameter. Arrows indicate the corresponding axis of the parameter. $\lambda = 2$ to ensure complete combustion ($\lambda = 1 + \alpha$) and $r_p = 8$ to have reasonable exit turbine temperature.	83

Figure 5.11: Temperature at Gas Turbine (GT) inlet (state 5) is plotted against α -parameter. $\lambda = 2$ to ensure complete combustion ($\lambda = 1 + \alpha$) and $r_p = 8$ to have reasonable exit turbine temperature.	83
Figure 5.12: Comparison of the energetic and exergetic efficiencies between the subsystems of system 1b.	86
Figure 5.13: Comparison of exergy destruction rates of major components of system 1b.	89
Figure 5.14: Energetic and exergetic efficiencies are plotted against temperature at state 2. a) For overall integrated system and SOFC-GT subsystem. b) For SRC and NH ₃ -ORC subsystems.	91
Figure 5.15: Electric power output values of the integrated system and its subsystems are plotted against temperature at state 2. Arrows indicate the corresponding axis of the parameter.	92
Figure 5.16: Energetic and exergetic efficiencies are plotted against excess air factor (λ). a) For overall integrated system and SOFC-GT subsystem. b) For SRC and NH ₃ -ORC subsystems.	93
Figure 5.17: Electric power output values of the integrated system and its subsystems are plotted against excess air factor (λ). Arrows indicate the corresponding axis of the parameter.	94
Figure 5.18: Temperatures at states 2 and 9 are plotted against excess air factor (λ).	94
Figure 5.19: Comparison of the energetic and exergetic efficiencies between the subsystems of system 2.	98
Figure 5.20: Comparison of exergy destruction rates of major components of system 2.	99
Figure 5.21: Energetic and exergetic efficiencies comparison of systems 1a and 2 are plotted against the cooling load. a) For overall integrated systems. b) For SRC subsystems.	100
Figure 5.22: Total and turbine 3 electric power values comparison of systems 1a and 2 are plotted against the cooling load.	101
Figure 5.23: Temperature at state 34 of system 2 is plotted against absorption chiller cooling load.	102

Figure 5.24: Comparison of the energetic and exergetic efficiencies between the subsystems of system 3.	104
Figure 5.25: Comparison of exergy destruction rates of major components of system 3.	106
Figure 5.26: Energetic and exergetic efficiencies are plotted against engine compression ratio r_v . a) For overall integrated system and SOFC-PPCI-GT subsystem. b) For ORC subsystem.	107
Figure 5.27: Electric power output values of the integrated system and its subsystems are plotted against engine compression ratio r_v . Arrows indicate the corresponding axis of the parameter.	108
Figure 5.28: Energetic and exergetic efficiencies are plotted against air compressor compression ratio. a) For overall integrated system and SOFC-PPCI-GT subsystem. b) For ORC subsystem.	109
Figure 5.29: Electric power output values of the integrated system and its subsystems are plotted against air compressor compression ratio. Arrows indicate the corresponding axis of the parameter.	110
Figure 5.30: Energetic and exergetic efficiencies are plotted against α -parameter. a) For overall integrated system and SOFC-PPCI-GT subsystem. b) For ORC subsystem.	111
Figure 5.31: Electric power output values of the integrated system and its subsystems are plotted against α -parameter. Arrows indicate the corresponding axis of the parameter.	112
Figure 5.32: Comparison of the energetic and exergetic efficiencies between the subsystems of system 4.	113
Figure 5.33: Comparison of exergy destruction rates of major components of system 4.	116
Figure 5.34: Energetic and exergetic efficiencies are plotted against temperature at state 26. a) For overall integrated system. b) For Preheated-ORC subsystem.	117
Figure 5.35: SOFC exergy destruction rate and turbine 3 electric power are plotted against temperature at state 26.	118
Figure 5.36: Energetic and exergetic efficiencies are plotted against Preheated-ORC mass flow rate (state 26). a) For overall integrated system. b) For Preheated-ORC subsystem.	119

Figure 5.37: Turbine 3 electric power is plotted against Preheated-ORC mass flow rate (state 26).	120
Figure 5.38: Comparison of the energetic and exergetic efficiencies between the subsystems of system 5.	122
Figure 5.39: Comparison of exergy destruction rates of major components of system 5.	124
Figure 5.40: Energetic and exergetic efficiencies are plotted against compression ratio across the air compressor. a) For overall integrated system and SOFC-GT subsystem. b) For NH ₃ -ORC subsystem.	126
Figure 5.41: Electric power output values of the integrated system and its subsystems are plotted against compression ratio across the air compressor. Arrows indicate the corresponding axis of the parameter.	127
Figure 5.42: Energetic and exergetic efficiencies are plotted against ORC boiler pressure (state 12), for overall integrated system and NH ₃ -ORC subsystem.	127
Figure 5.43: Turbine 2 electric power and boiler exergy destruction rate are plotted against ORC boiler pressure which is at state 12.	128
Figure 5.44: Comparison of the energetic and exergetic efficiencies between the subsystems of system 6.	130
Figure 5.45: Comparison of exergy destruction rates of major components of system 6.	132
Figure 5.46: Energetic and exergetic efficiencies are plotted against β -parameter. a) For overall integrated system, SOFC-GT and ADSU-PEM subsystems. b) For SRC and NH ₃ -ORC subsystems.	134
Figure 5.47: Electric power output values of the integrated system and its subsystems are plotted against β -parameter. Arrows indicate the corresponding axis of the parameter.	135
Figure 5.48: Energetic and exergetic efficiencies are plotted against ε -parameter. For overall integrated system and ADSU-PEM subsystem.	135
Figure 5.49: PEM fuel cell exergy destruction rate and electric power are plotted against ε -parameter.	136
Figure 5.50: Energetic and exergetic efficiencies are plotted against PEM fuel cell energetic efficiency. For overall integrated system and ADSU-PEM subsystem.	137

Figure 5.51: PEM fuel cell exergy destruction rate and electric power are plotted against PEM fuel cell energetic efficiency.	137
Figure 5.52: Comparison of the energetic and exergetic efficiencies between the subsystems of system 7.	139
Figure 5.53: Comparison of exergy destruction rates of major components of system 7.	141
Figure 5.54: Energetic and exergetic efficiencies are plotted against fuel cell operating temperature. a) For overall integrated system and SRC subsystem. b) For NH ₃ -ORC 1 and 2 subsystems.	143
Figure 5.55: Electric power output values of the integrated system and its subsystems are plotted against fuel cell operating temperature. Arrows indicate the corresponding axis of the parameter.	144
Figure 5.56: Energetic and exergetic efficiencies are plotted against SRC boiler pressure (state 12). a) For overall integrated system and SRC subsystem. b) For NH ₃ -ORC 1 subsystem.	145
Figure 5.57: Electric power output values of the integrated system and its subsystems are plotted against SRC boiler pressure (state 12). Arrows indicate the corresponding axis of the parameter.	146
Figure 5.58: Temperature of the stream leaving turbine 1 (state 13) is plotted against SRC boiler pressure (state 12).	147
Figure 5.59: Normalized values of the optimized possible solutions of MOGA (Pareto front) of system 1a are plotted in parallel coordinates. The mean values for the overall exergetic efficiency, SOFC power, and GT power are 0.63379, 2245.7 kW, and 570.06 kW, respectively. Also, the standard deviation values are 0.069459, 192.40 kW, and 146.35 kW, respectively. The 7 th solution is chosen to be the optimum point of operation which is plotted in bold dot-dash line.	150
Figure 5.60: Normalized values of the optimized possible solutions of MOGA (Pareto front) of system 3 are plotted in parallel coordinates. The mean values for the overall exergetic efficiency, SOFC power, PPCI power, and GT power are 0.79902, 1820.7 kW, 1020.2 kW, and 240.36 kW, respectively. Also, the standard deviation values are 0.076635,	

170.86 kW, 160.22 kW, and 67.524 kW, respectively. The 8th solution is chosen to be the optimum point of operation which is plotted in bold dot-dash line.154

Figure 5.61: Normalized values of the optimized possible solutions of MOGA (Pareto front) of system 6 are plotted in parallel coordinates. The mean values for the overall exergetic efficiency, Hydrogen production, and PEM power are 0.63759, 0.005572 kg s⁻¹, and 710.19 kW, respectively. Also, the standard deviation values are 0.022075, 0.003296 kg s⁻¹, and 187.64 kW, respectively. The 10th solution is chosen to be the optimum point of operation which is plotted in bold dot-dash line.157

Figure 5.62: Overall energetic and exergetic efficiencies are plotted for all the proposed integrated systems at their chosen reference cases.159

Figure 5.63: Overall energetic and exergetic efficiencies are plotted for all the proposed integrated systems at their optimum operation points.159

Figure 5.64: Fuel costs of a diesel-electric engine and all the proposed systems evaluated at their reference cases for the chosen case study.161

Figure 5.65: CO₂ emissions of a diesel-electric engine and all the proposed systems evaluated at their reference cases for the chosen case study.162

List of Tables

Table 2.1: Average price values of natural gas in Canada from 2007 to 2018. Reproduced from [36].	10
Table 4.1a: A list of balance equations for the components of system 1a.	43
Table 4.1b: A continued list of balance equations for the components of system 1a.	44
Table 4.2a: A list of balance equations for the components of the absorption chiller with a heat exchanger cycle.	47
Table 4.2b: A continued list of balance equations for the components of the absorption chiller with a heat exchanger cycle.	47
Table 4.3: Balance equations for the PPCI engine.	49
Table 4.4a: A list of balance equations for the preheated Organic Rankine Cycle (ORC).	50
Table 4.4b: A continued list of balance equations for the preheated Organic Rankine Cycle (ORC).	50
Table 4.5: A list of balance equations for ADSU and PEMFC devices.	54
Table 4.6: Balance equations for MAHEFC.	55
Table 4.7: A list of overall energetic and exergetic efficiency expressions for all the proposed systems. ^a	56
Table 4.8: Energetic and exergetic efficiency definitions for the subsystems.	58
Table 4.9: List of chosen formula building-blocks for multi-objective genetic programming and their complexity level as defined in the Eureka program.	60
Table 4.10: List of parameters and their constraints for the optimization problem of system 1a.	62
Table 4.11: List of parameters and their constraints for the optimization problem of system 3.	63
Table 4.12: List of parameters and their constraints for the optimization problem of system 6.	63
Table 5.1: Common parameters for the thermodynamic analysis at the reference case for all the proposed integrated systems.	66

Table 5.2: Space and weight requirements for a reversible heat pump and an absorption chiller.	68
Table 5.3: Calculated parameters for the thermodynamic analysis of system 1a.	69
Table 5.4: State points and their thermodynamic values of system 1a.	71
Table 5.5: Exergy destruction rates and exergetic efficiencies of major components of system 1a.	72
Table 5.6: Present model comparison of SOFC-GT energetic efficiency with previously published results.	73
Table 5.7: Summary of the effects of chosen parameters on the performance of the integrated system.	84
Table 5.8: Calculated parameters for the thermodynamic analysis of system 1b.	86
Table 5.9: State points and their thermodynamic values of system 1b.	87
Table 5.10: Exergy destruction rates and exergetic efficiencies of major components of system 1b.	88
Table 5.11: Calculated parameters for the thermodynamic analysis of system 2.	96
Table 5.12: State points and their thermodynamic values of system 2.	97
Table 5.13: Exergy destruction rates and exergetic efficiencies of major components of system 2.	98
Table 5.14: Calculated parameters for the thermodynamic analysis of system 3.	103
Table 5.15: State points and their thermodynamic values of system 3.	105
Table 5.16: Exergy destruction rates and exergetic efficiencies of major components of system 3.	105
Table 5.17: Calculated parameters for the thermodynamic analysis of system 4.	113
Table 5.18: State points and their thermodynamic values of system 4.	114
Table 5.19: Exergy destruction rates and exergetic efficiencies of major components of system 4.	116
Table 5.20: Calculated parameters for the thermodynamic analysis of system 5.	121
Table 5.21: State points and their thermodynamic values of system 5.	123
Table 5.22: Exergy destruction rates and exergetic efficiencies of major components of system 5.	124
Table 5.23: Calculated parameters for the thermodynamic analysis of system 6.	129

Table 5.24: State points and their thermodynamic values of system 6.....	131
Table 5.25: Exergy destruction rates and exergetic efficiencies of major components of system 6.	132
Table 5.26: Calculated parameters for the thermodynamic analysis of system 7.	139
Table 5.27: State points and their thermodynamic values of system 7.....	140
Table 5.28: Exergy destruction rates and exergetic efficiencies of major components of system 7.	141
Table 5.29: A list of the chosen objective functions models with their corresponding correlation coefficient and level of complexity resulting from genetic programming (GP) of system 1a.	148
Table 5.30: Overall energetic and exergetic efficiencies of integrated systems and SOFC and GT power outputs at the decided optimum operational point. At this point, these parameters are $r_p = 14.659$, $\lambda = 1.5129$, and $\alpha = 0.061099$	149
Table 5.31: Volumetric power density of several power components.....	149
Table 5.32: Space required by power components and total systems of diesel-electric engine, simple hybrid SOFC-GT system, and system 1a.	151
Table 5.33: A list of the chosen objective functions models with their corresponding correlation coefficient and level of complexity resulting from genetic programming (GP) of system 3.	153
Table 5.34: A list of the chosen objective functions models with their corresponding correlation coefficient and level of complexity resulting from genetic programming (GP) of system 6.	155
Table 5.35: Intercity passenger locomotive duty cycle [90].	160
Table 5.36: Brake specific fuel consumption for a diesel-electric engine and the proposed systems at their reference cases.....	160

Nomenclature

$bsfc$	Brake specific fuel consumption
E	Total energy (kJ)
EI	Environmental impact
$\dot{E}x$	Exergy destruction rate (kW)
ex	Specific exergy (kJ kg ⁻¹)
g	Gravitational acceleration (m s ⁻²)
h	Specific enthalpy (kJ kg ⁻¹)
HHV	High heating value of fuel (kJ kg ⁻¹)
\dot{m}	Mass flow rate (kg s ⁻¹)
N	Normalized value
P	Pressure (kPa)
\dot{Q}	Heat transfer rate (kW)
R^2	Correlation coefficient
r_p	Compression ratio for air compressor
r_v	Engine compression ratio
S	Total entropy (kJ K ⁻¹)
\dot{S}	Entropy rate (kW K ⁻¹)
s	Specific entropy (kJ kg ⁻¹ K ⁻¹)
SI	Sustainability index
T	Temperature (K)
t	Time (s)
U	Utilization factor
V	Flow velocity (m s ⁻¹)
\dot{W}	Power (kW)
X	Actual value of an objective function of a given solution

x_i	Mass ratio of component i
Z	Flow level with respect to a reference level (m)
Greek Letters	
α	Mass flow rate ratio as defined by equations (4.14) or (4.45)
β	Ammonia mass flow rate ratio as defined by equation (4.48)
γ	Specific heat ratio
ε	Mass flow rate ratio of hydrogen stored as defined by equation (4.51)
η	Efficiency
λ	Excess air factor
μ	Mean
σ	Standard deviation
Subscripts	
<i>abs</i>	Absorber
<i>ADSU</i>	Ammonia dissociation and separation unit
<i>ADSU,PEMFC</i>	ADSU and PEMFC subsystem
<i>Air,regen</i>	Air regenerator
<i>Aircomp</i>	Air compressor
<i>avg</i>	Average
<i>boiler</i>	Boiler
<i>Boiler2</i>	Boiler 2
<i>CH4</i>	Methane
<i>CO2</i>	Carbon dioxide
<i>combustor</i>	Combustor
<i>comp</i>	Compression
<i>comp2</i>	Compressor 2
<i>cond1</i>	Condenser 1
<i>cond2</i>	Condenser 2
<i>CV</i>	Control volume

<i>dest</i>	Destruction
<i>elect</i>	Electric power output
<i>elect,total</i>	Total electric power output by the integrated system
<i>en</i>	Energetic
<i>engine</i>	PPCI engine
<i>evap</i>	Evaporator
<i>ex</i>	Exergetic
<i>exp</i>	Expansion
<i>fuel</i>	Fuel
<i>Fuel,regen</i>	Fuel regenerator
<i>Gas,turb</i>	Gas turbine (GT)
<i>gen</i>	Generation
<i>generator</i>	Generator
<i>H2</i>	Hydrogen
<i>H2O</i>	Water
<i>Heater</i>	Heater
<i>HX1</i>	HX 1, heat exchanger 1 of the heat pump cycle connected to the indoors
<i>HX2</i>	HX 2, heat exchanger 2 of the heat pump cycle connected to the outdoors
<i>HX3</i>	HX 3, heat exchanger 3
<i>i</i>	Component i of a gas mixture
<i>in</i>	Inlet
<i>is</i>	Isentropic
<i>j</i>	Thermodynamic state at j
<i>k</i>	Summation variable
<i>loss</i>	Heat transfer rate losses
<i>MAHEFC</i>	Molten alkaline hydroxide electrolyte fuel cell

<i>mix</i>	Mixing chamber
<i>N₂</i>	Nitrogen
<i>net</i>	Net engine power
<i>NH₃</i>	Ammonia
<i>o</i>	Ambient state
<i>O₂</i>	Oxygen
<i>ORC</i>	Organic Rankine cycle
<i>out</i>	Outlet
<i>overall</i>	Overall integrated system
<i>P,ORC</i>	Preheated organic Rankine cycle
<i>PEMFC</i>	Proton exchange membrane fuel cell
<i>Preheater</i>	Preheater
<i>Regenerator</i>	Regenerator
<i>SOFC</i>	Solid oxide fuel cell
<i>SOFC,GT</i>	Solid oxide fuel cell (SOFC) and gas turbine (GT) subsystem
<i>SOFC,PPCI,GT</i>	Solid oxide fuel cell (SOFC), PPCI engine, and gas turbine (GT) subsystem
<i>SRC</i>	Steam Rankine cycle
<i>System1a</i>	Integrated system 1a
<i>System2</i>	Integrated system 2
<i>turb2</i>	Turbine 2
<i>turb3</i>	Turbine 3
Superscripts	
<i>ch</i>	Chemical
<i>ke</i>	Kinetic energy
<i>pe</i>	Potential energy
<i>ph</i>	Physical

Acronyms

ADSU	Ammonia Dissociation and Separation Unit
Br	Bromide
CERL	Clean Energy Research Laboratory
CH ₄	Methane
CO ₂	Carbon dioxide
CV	Control volume
DRM	Dry reforming of methane
EES	Engineering Equation Solver software
eq	Equivalent
GA	Genetic algorithm
GHG	Greenhouse gas
GP	Genetic Programming
GT	Gas Turbine
GWP	Global Warming Potential
H ₂	Hydrogen
H ₂ O	Water
HX	Heat exchanger
IEA	International Energy Agency
IT-SOFC	Intermediate-Temperature Solid Oxide Fuel Cell
LCA	Life Cycle Assessment
Li	Lithium
MAHEFC	Molten Alkaline Hydroxide Electrolyte Fuel Cell
MOGA	Multi-Objective Genetic Algorithm
Mt	Megatonnes
N ₂	Nitrogen
NH ₃	Ammonia

NH ₃ -ORC	Ammonia-Organic Rankine Cycle
NSGA-II	Non-dominated Sorting Genetic Algorithm II
O ₂	Oxygen
ORC	Organic Rankine Cycle
P2G	Power-to-Gas
PEMFC	Proton Exchange Membrane Fuel Cell
PPCI	Partially-premixed compression ignition
PV	Photovoltaic
SOFC	Solid Oxide Fuel Cell
SRC	Steam Rankine Cycle
SUCP	Sum of unit costs of products
ULSD	Ultra-Low Sulfur Diesel

Chapter 1: Introduction

The current practices in powering locomotives on Canadian railways are damaging to the environment and not sustainable in the long term future. This thesis explores alternative powering options for cleaner and more environmentally friendly rail transportation.

1.1 Canadian Rail Transportation

The greenhouse gas (GHG) emissions in Canada has peaked at a value of 744 Megatonnes of CO₂ equivalent in 2007. Two years later, they dropped dramatically which is a good sign in terms of environmental impact, but this decrease has been reversed since then as seen in Figure 1.1. The transportation sector is the second largest contributor to these GHG emissions with a value of 174 Mt CO₂ eq (24% of total emissions). In order to reach the GHG emissions goals of 2030 of annual 513 Mt CO₂ eq [1], serious changes in the powering options for the transportation sector have to be made. The effect of making these changes in the transportation sector will be significant. Figure 1.2 shows the breakdown of the emissions in the transportation sector. It is clearly seen that the major increase in GHG emissions from 1990 to 2017 with emissions values of 122 to 174 Mt CO₂ eq occurred due to freight trucks and passenger light trucks. If freight and passengers can be transported using clean railways instead of trucks, major reductions in GHG emissions will happen, up to 110.4 Mt CO₂ eq. This can be possible by imposing governmental regulations on the transportation sector and implementing clean powering systems in railways. It is the purpose of this thesis to address the second issue by exploring and investigating possible powering systems that are economically feasible for clean rail operation.

1.2 Alternative Fuels

The choice of transportation fuel is very critical in reducing GHG emissions. Current railway companies operate compression diesel-electric engines that utilize Ultra-Low Sulfur Diesel (ULSD) as an injection fuel [2]. If these companies keep using diesel-electric engines, the elimination or even major reductions in GHG emissions will not be achievable. Therefore, alternative fuels, such as methane, ammonia, and hydrogen are possible candidates. Methane has a single carbon atom per molecule, while typical diesel fuel has 12. Upon combustion, methane produces 12 times less CO₂ emissions than diesel. Also,

methane has a higher heating value of 52225 kJ kg^{-1} and diesel has it at a value of 46536 kJ kg^{-1} [3]. This means that this alternative fuel has more potential to produce power which reduces the amount of fuel consumed per energy produced by the powering system. Furthermore, methane can be produced from renewable energy sources, like wind and solar along with carbon capturing [4–6]. This results in net-zero emissions when using methane as a transportation fuel. For example, Stempien et al. [5] proposed a methane production plant with carbon capturing using a solid oxide electrolyzer with renewable electricity as power input. Such a technique is commonly referred to as Renewable Gas-to-Power technology [4].

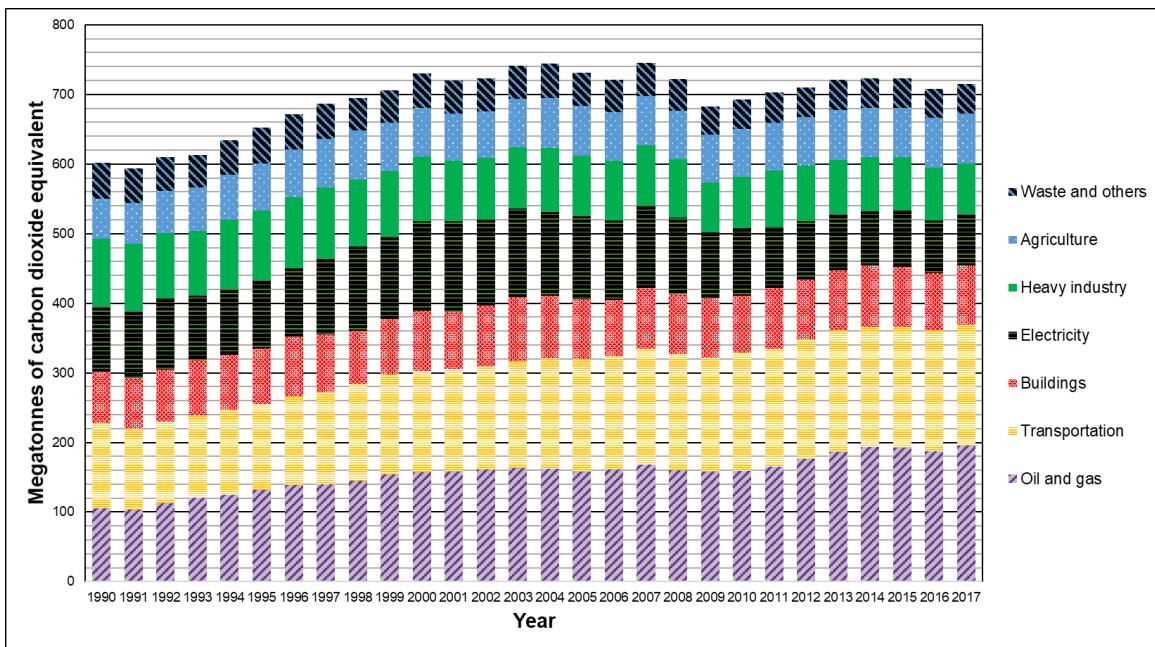


Figure 1.1: Greenhouse gas emission by economic sector in Canada from 1990 to 2017. Reproduced from [7].

Another possible alternative fuel for transportation purposes is ammonia. Ammonia is a molecule that stores hydrogen in a chemical form, NH_3 . This stored energy can be released using several ways, like immediate combustion, direct injection to an appropriate fuel cell, or hydrogen recovery using an ammonia dissociation and separation unit. The recovered hydrogen then can be as input fuel to a fuel cell. Ammonia can also be blended with conventional fuels, like diesel to reduce the emissions by 8 tonnes CO_2 eq and to provide a cheaper fuel option for railways as investigated by Hogerwaard [8]. When compared to diesel fuel, ammonia is cheaper and more environmentally- friendly as it only costs \$0.900

CAD kg⁻¹ [9], while diesel costs \$1.153 CAD kg⁻¹ [10]. Other advantages of using ammonia can be listed as follows which are derived from these sources [11–13]:

- Ammonia is not flammable in air unlike hydrogen, methane and conventional fuels, such as gasoline.
- Toxicity of ammonia can be significantly reduced if it is stored in metal amines. This level of toxicity drops below that of gasoline.
- Storage and delivery to end-user infrastructure is well established which makes it a viable marketable transportation fuel in a short period of time.
- In case of leakage, it can be noticed immediately by smelling it, unlike hydrogen.
- It can be produced from renewable energy sources and it only uses abundant substances, like nitrogen from air and water.
- Ammonia has high volumetric energy density and cheapest in terms of driving range.
- It is not a greenhouse gas and does not cause harmful emissions when oxidized.
- Energy can be extracted from it using multiple methods, namely combustion, blending with conventional fuels, direct injection in fuel cells, and dissociation to hydrogen.

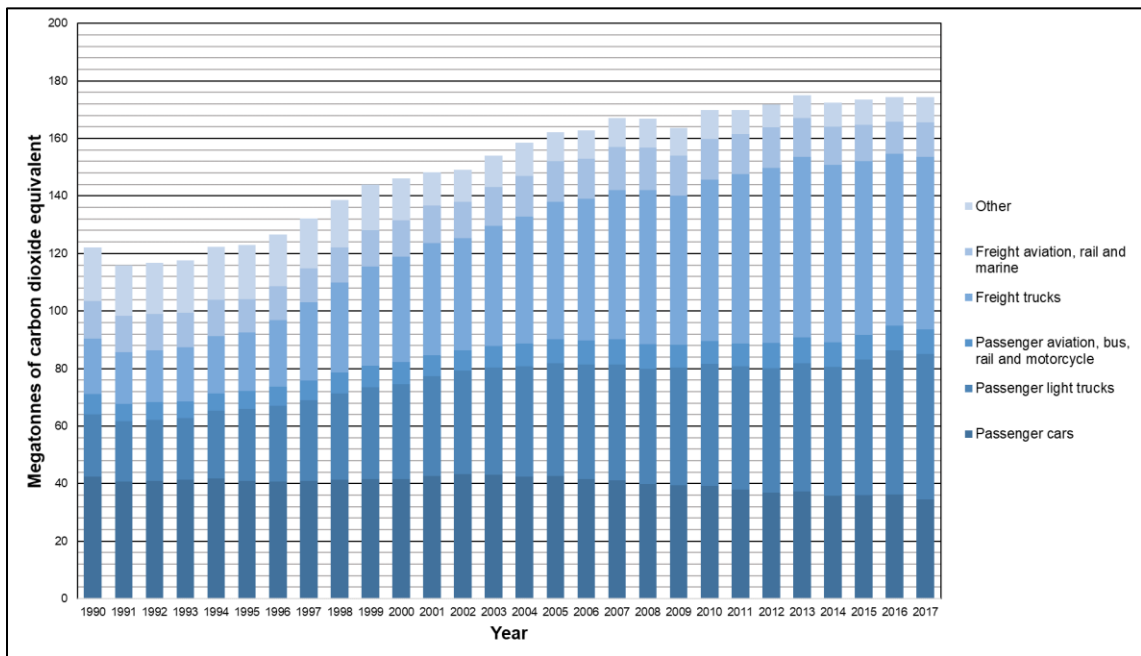


Figure 1.2: Breakdown of GHG emissions in the Canadian transportation sector. Reproduced from [7].

Hydrogen is the fuel of the future according to the International Energy Agency (IEA) [14]. However, current storage and delivery technologies are not developed enough to make it commercially available. Safer and more reliable storage techniques need to be developed [15]. Hydrogen is being used as a transportation fuel for passenger cars in many countries in the world. This fuel has reached the market too soon because the storage technology for hydrogen is not as developed as it should be. For example, a recent unfortunate incident happened in Norway [12]. A hydrogen fueling station operated by Nel Hydrogen has exploded and the fire was contained within three hours from the first sight of the explosion. As a reaction to this incident, Toyota and Hyundai, which are fuel cell car manufacturers, paused selling their fuel cell cars in Norway as several hydrogen fueling stations were shut down temporarily. This has dramatic effects on the economy of hydrogen and related transportation technologies as well as the image of hydrogen as a future alternative fuel. So, for now, using more reliable and safer alternative fuels that can be handled appropriately for transportation purposes is a good idea. Such fuels are methane and ammonia. These alternative fuels will act as transition fuels from conventional high carbon-content fuels until hydrogen becomes a viable safe option. In this thesis, it will be shown that using these transition fuels is an efficient and economical way for operating railways. Also, hydrogen with its extremely high heating value of 14218 kJ kg^{-1} and zero CO_2 emissions will be noticed as a better option in the future [3].

1.3 Solid Oxide Fuel Cells (SOFCs)

Fuel cell technology has been adopted by the industry and it is used in on-road vehicles already. The type of fuel cell used in these transportation means is Proton Exchange Membrane Fuel Cells (PEMFCs) and the power loads of these powering systems are typically around 110 kW [16,17]. Railway transportation power demands are much higher than this range and require a different kind of fuel cell technology, namely solid oxide fuel cells (SOFCs). The power demands are in the range of 3 MW (4000 hp) and this type of fuel cell has been demonstrated to be suitable for delivering such level of power demands. Normally, SOFC is integrated with an afterburner and a gas turbine to recover some of the waste heat for extra power production and efficiency enhancement. Also, this hybrid system is typically used for stationary and centralized power production and never been

implemented for transportation purposes. In 2012, Martinez et al. [18,19] studied the possibility of using SOFC-GT hybrid systems for railway applications by creating dynamic modelling of the hybrid system. Their results show that it is possible to implement this technology in regards to power demands and space requirements. This can have positive impacts on rail transportation as SOFC is fuel-flexible and can be operated using the alternative fuels mentioned above [20–22]. Direct injections of methane and ammonia into SOFC have been developed [21,23]. The necessity of reforming the fuel can be discarded. This feature is important in lowering the packaging requirements of an integrated SOFC system in a locomotive. This makes it more economic and feasible to replace current diesel-electric engines with these systems. Another kind of SOFC that has been developed in the last decade is reduced-temperature SOFC [24]. Conventional SOFCs operate at a temperature range of 800°C to 1000°C, but these reduced-temperature SOFCs operate at temperatures as low as 500°C without sacrificing fuel flexibility and power density [25].

Another option for high power production is molten alkaline fuel cells. This intermediate-temperature fuel cell accepts ammonia directly as a fuel. Its advantage over SOFC is the lower operating temperature level that ranges from 200°C to 450°C (or 473 to 723 K). The main problem with a molten alkaline fuel cell is its energetic conversion efficiency of (30% - 40%) is lower than SOFC [26]. To get more information on the effects of operating temperature and fuel cell efficiency, an integrated system will be proposed and studied thermodynamically in this thesis.

1.4 Motivation and Thesis Objectives

The drive for conducting the research in this thesis arises from the need to develop integrated fuel cell-based powering systems suitable for clean railway applications. These systems have to avoid using conventional high carbon-content fuels and use alternative fuels instead. Moreover, these systems must be optimized for highest efficiency and feasibility in terms of packaging, to replace the diesel-electric engine in a Canadian locomotive. Fuel costs and CO₂ emissions of these integrated systems have to be competitive to the current diesel engine technology in order to attract the rail industry.

The specific objectives of the thesis study are listed as follows:

- To propose conceptual designs of eight integrated fuel cell-based powering systems for clean railway applications, specifically solid oxide and molten alkaline fuel cells. The three main advantages of these integrated systems are high energetic and exergetic efficiencies, multigeneration to meet the power, space heating and cooling, hot water demands of a passenger locomotive, and compactness to facilitate solid oxide fuel cell technology for mobile applications.
- To develop thermodynamic models to simulate the integrated systems and evaluate them energetically and exergetically.
- To perform parametric studies of the integrated systems to understand their thermodynamic behaviors under varying operating conditions and state properties. The energetic and exergetic efficiencies of the overall systems and their subsystems are investigated. Plus, the power outputs of the power producing devices, like fuel cells and turbines, are examined.
- To optimize the integrated systems in terms of overall exergetic efficiency, space requirements, and hydrogen production using multi-objective optimization methods. High efficient and compact powering systems are desired for clean rail applications.
- To compare the overall efficiencies of the eight proposed systems at a selected point of passenger locomotive operation with determined power, cooling, and hot water demands. Also, these integrated systems are compared at their optimum operating points.
- To evaluate the integrated systems with a typical diesel-electric engine in regards to fuel costs and CO₂ emissions for a passenger locomotive duty cycle. This comparison is required to present clear economic and environmental justifications for implementing these integrated systems.

1.5 Thesis Outline

The structure of the thesis and how it addresses the objectives are explained here. In chapter 1, an introduction of the thesis is provided to show the environmental problems concerning rail transportation and the possible technologies and fuels that can help in solving these

problems. The objectives of this thesis are listed for clarity. In chapter 2, Fuel production from renewables, their environmental impact, and fuel economy are also mentioned. Then, a literature review of the recent fuel cell technologies and their application to transportation is given. The importance of integration and multigeneration in power systems is explained with some examples from the literature. Next, multi-objective optimization techniques and their application to energy systems are reviewed. At the end of this chapter, knowledge gaps are identified and how this work will fulfill them. The third chapter describes the eight proposed systems and their operation to deliver the desired outputs. Each subsystem is explained in separate subsections. Schematic drawings are provided. The next chapter addresses one of the objectives which is developing thermodynamic models to simulate the steady-state operation of the proposed systems. These models are based on 1st and 2nd law analyses. After that, the results and discussions chapter is given. In this chapter, each integrated system has two parts of discussion, namely the reference case to fit the operation of a passenger locomotive, and parametric studies. After understanding the thermodynamic behaviors of these integrated systems, it is time to apply multi-objective optimization methods with data visualization. System 1a is firstly optimized and its optimized parameters are shared with other similar systems, which are systems 1b, 2, 4, and 5. Then, systems 3 and 6 are optimized as they have very different configurations and parameters. System 7 is only optimized using single-objective genetic algorithm optimization method for its exergetic efficiency. The last section of the results and discussions chapter deals with comparing the energetic and exergetic efficiencies of the proposed systems as well as presenting a case study of an intercity passenger train duty cycle. This case study involves the comparison of these newly proposed fuel cell-based systems with a typical diesel-electric engine to show some justification for adopting such systems. We compare fuel costs and CO₂ emissions for a single duty cycle. The final chapter summarizes the main outcomes and recommends future research directions on the topic of clean railways.

Chapter 2: Literature Review

This chapter reviews recent and the most relevant research that has been conducted on clean rail transportation and fuel cell powering integrated systems. Also, it discusses the application of some optimization methods in energy systems. This review ends with a discussion of the knowledge gaps found and how they will be addressed in this thesis.

2.1 Alternative Fuels

The current production practices of alternative fuels are not friendly to the environment, as they release GHG emissions in the process. A number of proposed clean systems that utilize excess renewable power have been outlined in the literature. For instance, Safari and Dincer [27] investigated the production of hydrogen and methane in an integrated wind power system. They proposed a renewable Power-to-Gas (P2G) integrated system for concurrent methane and hydrogen production with carbon capturing from the residential sector. They achieved overall energetic and exergetic efficiencies of 44% and 45%, respectively. The system can produce methane at a rate of 1.68 kg h^{-1} . Another example of such a renewable production plant for alternative fuels is given by Michalsky et al. [28]. Ammonia production is investigated as a mean of hydrogen storage and as a transportation fuel using solar energy as a renewable power input to the ammonia synthesis cycle. Their thermodynamic analysis shows that the system can have an energetic efficiency range between 23% and 30%. At optimum operation of the plant, ammonia is produced at a rate of 900 tonnes per day. An experimental study conducted by Veselovskaya et al. [29] demonstrated the use of nickel catalyst NKM-2V in a Sabatier reactor for methane production and carbon dioxide capturing from ambient air. Their experimental results show excellent conversion performance higher than 99% at a temperature of 425°C . The input power to this reactor can be a renewable source of energy, like wind and PV solar. A more comprehensive review of the topic of methane production and other alternative fuels from renewable energy sources is provided in this paper by Bailera et al. [30].

Life Cycle Assessments (LCAs) of alternative fuels are good ways to measure the environmental impact of the production of such kind of fuels [31–33]. Parra et al. [31] performed an integrated assessment of the power-to-gas technology, more specifically the

use of renewable and non-renewable energy sources for methane production. Their findings present that the source of CO₂, whether from ambient air or biogas, can have dramatic effects on the economic viability of such technology. It is only viable when biogas is used as input for the methanation process. Another important factor is the electrolysis efficiency in the PEM electrolyzer. This hydrogen production step is causing large inefficiencies and makes the whole process not economically feasible. Increasing this efficiency is of main research concern. Also, Sternberg and Bardow [32] compared two kinds of alternative fuels, that are syngas and synthetic natural gas. They found that when renewable energy supply is limited, it is more environmental to use the dry reforming of methane (DRM) process for syngas production. In regards to ammonia production, Bicer et al. [34] have conducted a comparative LCA for the different methods of ammonia production in 2016. They studied four kinds of methods, namely nuclear, biomass, hydropower, and municipal waste based methods. The environmental impact has been compared in terms of CO₂ eq emissions per 1 kg of ammonia produced. They found that nuclear, biomass, hydropower, and municipal waste based methods have values of 0.84 kg CO₂ eq, 0.85 kg CO₂ eq, 0.38 kg CO₂ eq, and 0.34 kg CO₂ eq. This means that using the municipal waste-based method of ammonia production is the least harmful. Another study by the same lab [35], called Clean Energy Research Laboratory (CERL), has considered the ammonia consumption as a transportation fuel. The results of the assessment show that using ammonia for transportation purposes causes less CO₂ eq emissions and only produces 100 g of CO₂ eq per 1 km of vehicle driving, while gasoline and diesel have 270 g and 230 g of CO₂ eq, respectively. A study of LCA for the production of 99% purity ammonia in Algeria has been executed by Makhoul et al. [36]. From their paper, it is concluded that the production of ammonia has a Global Warming Potential (GWP) of 1.44 tonnes CO₂ eq per tonnes of produced ammonia and this is less than the world average. From above, we learn that the production of methane, syngas, or ammonia can reduce GHG emissions in both fuel production and transportation sectors, which are the largest in terms of GHG emissions as discussed in the introduction earlier.

One of the most important factors in the utilization of alternative fuels is their economy. Studying this factor helps in understanding how the market and railway industry will accept the adaptation of alternative fuels, such as methane and ammonia. In Canada, Natural

Resources Canada has reported the prices of natural gas from 2007 to the first four months of 2018 [36]. In Table 2.1, we see that the average price per kWh is dropping in the last three years from 1.43 cents down to 0.641 cents. On the other hand, the prices of ammonia are somewhat increasing from 2007 at a value of \$0.870 CAD to 2016 at a value of \$0.900 CAD per 1 kg of ammonia in Canada [9]. This increase is not dramatic and it is still significantly lower than the reported Canadian price of diesel in 2016 of \$1.153 CAD kg⁻¹ [10]. The price of ammonia actually has decreased by more than \$0.200 CAD since 2012. Therefore, the projections of fuel prices for methane and ammonia seem to be going downward, which is encouraging for replacing diesel with these alternative fuels in rail transportation. What is more, diesel fuel prices are increasing considerably as shown in Figure 2.1. In 2016, they were averaged at around 9.12 cents per kWh, then increased to almost 11.4 cents per kWh by the middle of 2019.

Table 2.1: Average price values of natural gas in Canada from 2007 to 2018. Reproduced from [36].

Time Range in Years	Average Natural Gas Price in Cents kWh ⁻¹
2007 – 2016	1.43
2015	0.921
2016	0.744
2017	0.751
2018 (first four months)	0.641

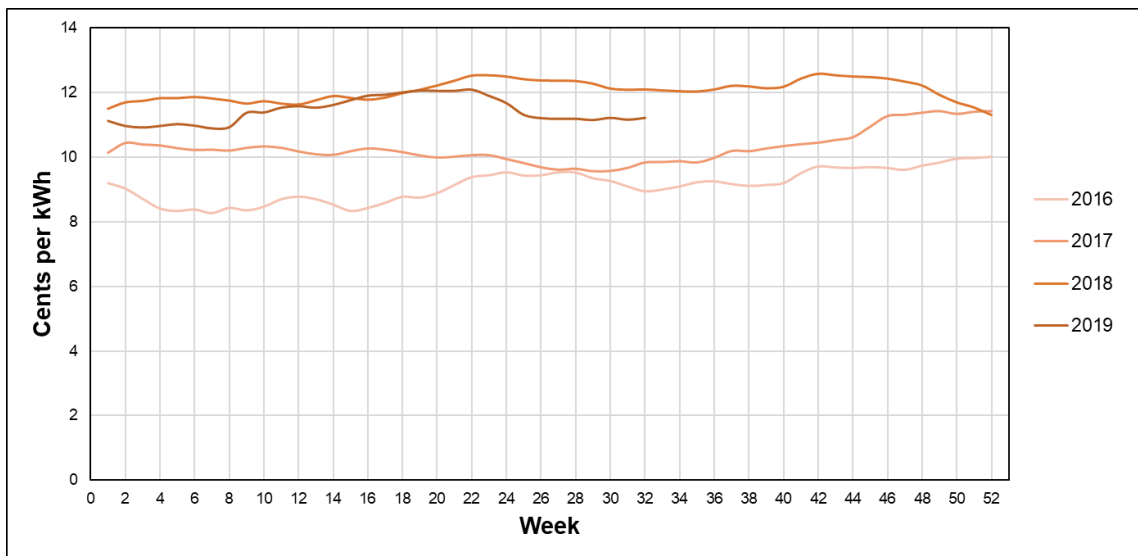


Figure 2.1: Diesel fuel prices over the weeks of a year, from 2016 to 2019 week 32. Adopted from [37].

2.2 Fuel Cell Technology in Transportation

The application of different kinds of fuel cell in the transportation sector of economy is discussed next. Three kinds of fuel cell will be mentioned, namely Solid Oxide, Proton Exchange Membrane, and Molten Alkaline fuel cells.

2.2.1 Solid Oxide Fuel Cell (SOFC) Technology

There are different types of fuel cell technology that serve a wide range of applications that range from military all the way to civil transportation and including space powering and backup power management. The Solid Oxide Fuel Cell (SOFC) is typically used for stationary power generation in magnitudes of Megawatt (MW). The structure of this fuel cell contains porous cathode and anode, they are separated by a solid electrolyte that allows oxygen ions to pass through. This feature of the electrolyte makes SOFC accept any kind of fuel, such as hydrogen, ammonia, methane, and other hydrocarbon fuels. Unlike PEM fuel cells, SOFCs have great fuel flexibility. The main disadvantage of SOFCs is their operating temperature range that is between 800°C to 1000°C. Luckily, efforts have been put to reduce the operating temperature of this fuel cell. Wachsman and Lee [24] have reviewed the developments in reducing the operating temperature of SOFC by developing innovative solutions and synthesizing high-conductive electrolyte materials. The reduction of operating temperature has reached as low as 350°C. Also, researchers have achieved stable operation of an SOFC in single and dual cell setups at a temperature range of 500°C - 600°C, without sacrificing energetic efficiency and power density [25]. For the dual-cell setup, they were able to achieve a power density of 246.5 mW cm⁻². To add, the fuel they tested is propane with direct injection to the fuel cell and no hydrogen external reforming was necessary. Most studies on SOFC-based power systems include methane or hydrocarbon reforming for hydrogen production. This hydrogen is then injected to the SOFC stack. Using reforming, most commonly steam reforming, reduces the overall efficiency of the system. Therefore, direct-injection SOFCs have been developed with various electrolytes to eliminate the need for reforming [38]. For example, using methane as a fuel, Bogolowski et al. [21] have synthesized a coking-resistant anode for internal reforming of CH₄. They studied this new Nickel-based anode over a temperature range of 600°C - 1000°C, and found that no carbon residuals were detected. Ammonia is another

possible fuel that can be directly injected to SOFCs. An experimental study by Ma et al. [23] tested an intermediate-temperature SOFC (IT-SOFC) with direct injection of ammonia. They compared the power density of the IT-SOFC under direct injection of ammonia and under direct injection of hydrogen. Their findings show that using ammonia does not affect the performance of the IT-SOFC significantly, since the power density with hydrogen is 191.8 mW cm^{-2} , and with ammonia is 168.1 mW cm^{-2} . The IT-SOFC was operated at a temperature of 600°C for both cases. An additional advantage of using direct-injection SOFCs is reducing space requirements for installing the power system because fuel processing devices are no longer needed. According to Martinez et al [19], the removal of fuel processing devices can save up space up to 7.74 m^3 .

One important application of this kind of fuel cell is railway passenger trains. Current passenger trains used in Canada are operated using diesel-electric engines [2]. This fuel is a heavy type of fuel and it produces a significant amount of emissions. Cleaner fuels need to be used if the transportation sector in Canada wants to meet its emissions targets by 2030 which is 513 megatonnes of CO_2 emissions in a year [1]. The application of SOFC in trains has been investigated by Schroeder and Majumdar [39] in which they studied the feasibility of using SOFC technology fueled by biodiesel in terms of efficiencies, life cycle costs, and equipment sizes. Although SOFC is found to have higher efficiency than a typical diesel internal combustion engine in utilizing fuel, SOFC is still not economically feasible unless the cost of fuel increases annually by at least 9% or higher. Another factor that could make SOFC more economically feasible for the railway industry is imposing a carbon tax on CO_2 emissions. More recently, a feasibility study of the utilization of a hybrid SOFC-GT system on a train was conducted by Martinez et al. [18,19]. They concluded that the required space for the installation of such a system is similar to currently used diesel internal combustion engines. Also, they simulated the use of this hybrid SOFC-GT system on a train that takes a route in Southern California as a case study. Significant savings in terms of fuel use and CO_2 emissions were realized. A complete review is presented by Damo et al. [40] that evaluates the environmental impact of using hybrid SOFC systems. They also show that the use of clean energy power movers, specifically hybrid SOFC technology will be commercialized within a few years as several companies have already invested in building prototypes of hybrid SOFC-GT system.

One research gap that can be identified here is the configurations of SOFC-based powering systems that are feasible for a locomotive operation. So far, only simple Solid Oxide Fuel Cell with Gas Turbine hybrid systems have been considered. The recovery of waste heat leaving the gas turbine is essential for producing more power and getting other desirable outputs, like space heating and cooling, and hot water for passenger locomotives.

2.2.2 Other Fuel Cell Technologies

Proton Exchange Membrane Fuel Cells (PEMFCs) are the common choice for vehicle transportation. Two major car manufacturers have already commercialized the use of PEM fuel cell cars, namely Toyota Mirai [16], and Hyundai Nexo [41]. The fuel for these cars is compressed hydrogen. As mentioned in the previous chapter, using such a flammable fuel for transportation purposes is dangerous and not viable. Governmental policies and the media have pushed hydrogen to the market faster than it should be without proper storage hydrogen technologies. From the technical specs of the commercial fuel cell vehicles, it is seen that the mile ranges are limited to 312 miles and 380 miles, respectively. Gasoline vehicles have more driving range that can reach 703 miles [42]. As a conclusion, methane and ammonia are suitable transportation fuels. In addition, their infrastructure is already established for distribution and storage [43,44]. As a result, the time-to-market for these alternative fuels is significantly reduced compared to hydrogen.

For railway applications, Germany has led the world in announcing the first Hydrogen fuel cell powered train [45]. They have achieved a range on full tanks of hydrogen of 1000 km, which is similar to the previous operating train that used diesel. In Canada, Metrolinx [46] has conducted a comprehensive feasibility study on the implementation of hydrogen-powered trains (Hydrail) in 2018. Their objective is to electrify some parts of the GO Transit network by 2025. The report has identified two main challenges. Firstly, fleet implementation which is the delay caused by designing new rail vehicles that will incorporate fuel cells as powering options. Secondly, electricity or hydrogen pricing that is a tremendous amount of electricity is needed to produce the hydrogen fuel using electrolysis for the operation of these Hydrails. There is variability in electricity prices and therefore it may not be always economically viable to operate such trains. Notice that these

two problems do not exist if either methane or ammonia are used as a transportation fuel for clean railways.

It is interesting to mention the third type of fuel cell that is potentially practical to power a clean locomotive using ammonia fuel. Molten Alkaline Hydroxide Electrolyte Fuel Cell (MAHEFC) has been tested experimentally to oxidize ammonia with ambient air at intermediate temperature level, 200°C to 450°C [47,48]. In 2015, Wang and Gyenge [49] have even reached a lower operating temperature of 185°C for direct injection of ammonia in a molten alkaline fuel cell. Their fuel cell has attained a power density of 28 mW cm⁻² at a voltage potential of 0.54 V. This kind of fuel cell has not been considered for rail transportation yet. In this thesis, we will propose a power system based on MAHEFC and evaluate it thermodynamically and assess its fuel costs for a duty cycle operation of a passenger train.

2.3 Integrated Fuel Cell Systems

The integration of systems increases the overall efficiency by recovering waste heat for power production and generating multiple desired outputs, such as space heating and cooling, domestic hot water, and desalination. Fuel cells have a chemical to electrical energy conversion efficiency between 45% and 65% [24]. However, this can be increased by using the high-temperature exhaust gases to produce more electric power and produce more than one type of useful output, like space heating, space cooling and hot water for the passengers of a locomotive. This is achieved usually by using integrated systems that utilize the multi-generation concept [50]. One example is given by Siddiqui and Dincer [51] where they added a Steam Rankine Cycle (SRC) and an ammonia absorption chiller to the exhaust of the integrated SOFC-GT cycle for increasing the number of outputs and utilization of the waste heat from this primary cycle. They achieved an overall energetic efficiency increase of 19.3% due to multi-generation. Another example is the investigation of Sadeghi et al [52] in which they used the waste heat from an SOFC-GT cycle to produce two more useful outputs which are cooling and heating by implementing an absorption chiller and a heat exchanger. They did an exergoeconomic analysis using genetic algorithm optimization method to optimize the system and they achieved an optimum value of 48.24% for the exergetic efficiency of the overall system. Furthermore, such SOFC-GT

hybrid system can be integrated with desalination units to produce fresh water as an additional product which increases the overall efficiency of the system as presented in [53,54]. A different approach of multigeneration is investigated by Jing et al. [55] in which the authors combined heating, cooling, and hot water generator cycles with an SOFC to meet multiple demands of public buildings in China. This increased the overall energy efficiency of the system with a reduction in CO₂ emissions compared to typical systems. Also, a comprehensive review of the topic of combined and multi-generation using SOFC-GT integrated systems was written by Buonomano et al. [56].

Although the SOFC-GT-ORC integrated system has been investigated by a number of researchers like in [51,57–61], adding an ammonia Organic Rankine Cycle (NH₃-ORC) and using a reversible heat pump to provide space heating or cooling for a passenger train will increase the overall energetic efficiency significantly as will be shown in this study. Furthermore, the use of steam Rankine cycle (SRC) can be applied in this case because of the direct injection of fuel to the solid oxide fuel cell and to the redirection of some fresh charge of the methane or ammonia fuel to the combustor which produces high-temperature exhaust gases entering the gas turbine. This increases the power production of the gas turbine tremendously and makes it possible to run a steam Rankine cycle using the exhaust gases leaving the gas turbine. These new integrated systems feature multi-generation using waste heat recovery and compactness by the reversible heat pump. This makes them more suitable and cleaner candidates for replacing diesel-electric engines for railway applications. Such systems have not been investigated yet. For this reason, the main objective of this work is to thermodynamically assess the performance of these proposed integrated systems. A reversible heat pump is used to provide either space heating or cooling to the passenger coaches without consuming much space and weight on the train and it is easily switched between the two modes of operation by a reversible valve [62]. Using heat pumps for meeting space heating demands has shown significant savings in energy and costs which was presented in a case study by Lazzarin and Noro [63]. A detailed discussion and comparison will be presented in this thesis to show the advantages of choosing a reversible heat pump over other options for space heating and cooling. Hot water is needed in relatively small quantities in such passenger trains.

2.4 Multi-Objective Optimization in Power Systems

Evolutionary algorithms have been developed for the aim of establishing explorative and exploitive algorithms that can identify the optimum points of a given data set, called a landscape. These data (landscape) can be represented as mathematical functions referred to as objective functions that need to be optimized (i.e. maximization or minimization). The solution of the optimization problem is to find values of the input variables to the objective functions such as these functions are optimized simultaneously. When there are more than one objective function to be optimized, the problem is characterized as a multi-objective optimization problem. One method of optimization is called Multi-Objective Genetic Algorithm (MOGA) which has been used extensively in the literature to design and optimize power systems in terms of efficiency and fuel costs [64–67]. For example, Sharifzadeh et al. [68] have implemented MOGA with Aspen simulator to optimize a triple combined-power cycle that uses SOFC-GT hybrid system with a steam Rankine cycle with three pressure levels. The objective functions for this optimization problem are safe operating window of the power system and profitability. These are found to have a strong trade-off and several possible solutions have been calculated using the MOGA. The possible solutions are referred to as the Pareto front. Another study by Gholamian et al. [69] shows the application of MOGA to optimize the exergetic efficiency of the SOFC-GT biomass based-power system with hydrogen production and the cost of products produced. The authors have identified the best solution from the Pareto front and the corresponding objective function values are 33.22% for the exergetic efficiency, and 19.01 \$ GJ⁻¹ for the total product cost. Exergoeconomic analysis of SOFC power systems has been conducted with the assistance of MOGA. Khani et al. [70] have developed, modelled and then optimized the SOFC-GT system with an absorption chiller. Two output quantities are desired to be optimized, namely the maximization of the overall exergetic efficiency of the system, and the minimization of sum of unit costs of products (SUCP). For a hydrogen unit cost of 6 \$ GJ⁻¹, the overall exergy efficiency is 60.44%, while the SUCP is 88.19 \$ GJ⁻¹.

Genetic Programming (GP) is another useful evolutionary algorithm that takes in large data sets and uses genetic operations on mathematical operations, like addition and

multiplication, to compute mathematical expressions of the wanted objective functions. These expressions can help engineers to see the effects of input operating parameters, such as operating temperature or pressure on the energetic efficiency of the power system in an explicit clear form. Furthermore, these expressions show the interaction between the input operating parameters. The application of this method of optimization has been employed in several powering systems. For instance, Salehi and Gholaminezhad [71] have used GP to predict a mathematical model for a reversible Solid Oxide Fuel Cell by training input and output experimental data sets. Their model helped in finding the optimum operating temperature of the fuel cell which was found to be at 762°C.

One common issue that rises in multi-objective optimization problems is the representation of the optimized solutions for three dimensional or more problems. Parallel coordinates technique comes to the rescue by representing the Pareto front in a two-dimensional plot where the horizontal axis contains the objective functions and the vertical axis has the normalized values of the optimized objective functions. Each solution can be noticed through a distinct color. One example of the use of this kind of data visualization is done by Woolf et al. [72]. They applied this method to represent 4500 optimum solutions for ten objective functions. From the plot, patterns have emerged. To illustrate, from their parallel coordinate plot, increasing the crop price, increases, in general, the relative net present value of the application of bioenergy with carbon capture and storage technology.

Recently, Seyam et al. [73] have combined the above optimization methods with data visualization technique to optimize the outputs of a hybrid renewable energy system that features hydrogen production. The training data for genetic programming (GP) comes from the thermodynamic modelling of the integrated system. They reported the optimum operation of the hybrid system at an exergetic efficiency of 65% and the hydrogen production rate reached a value of 0.2 kg s⁻¹. This newly developed sequence of optimization methods with parallel coordinates for data visualization is implemented in this thesis.

2.5 Knowledge Gaps

From looking at the previous literature review, we identify some research gaps that are listed below with how this thesis tries to fulfill them:

- One research gap that can be identified here is the configurations of SOFC-based powering systems that are feasible for a locomotive operation. So far, only simple Solid Oxide Fuel Cell with Gas Turbine hybrid systems have been considered. The recovery of waste heat leaving the gas turbine is essential for producing more power and getting other desirable outputs, like space heating and cooling, and hot water for passenger locomotives. Here, we propose eight suitable fuel cell-based powering options for locomotives that use alternative fuels, such as methane and ammonia.
- Furthermore, the application of intermediate-temperature Solid Oxide Fuel Cell (IT-SOFC) integrated systems with direct injection has not been studied extensively enough. Another feature of SOFC-GT hybrid systems is the redirection of fuel to the combustor which increases the inlet turbine temperature. These features are thermodynamically modelled and their effects on power production and energetic and exergetic efficiencies are evaluated.
- Most optimization problems in the literature for SOFC-GT power systems are concerned mainly with the efficiency and economy related to these systems. However, for rail transportation purposes, it is important to look at the packaging feasibility of the integrated powering system which has not been considered yet. In this thesis, we focus on the multi-objective optimization of the overall exergetic efficiency of the proposed integrated systems and their packaging feasibility (space requirements) by optimizing the power split between the power devices, like SOFC, and gas turbine (GT).

Chapter 3: Systems Development

This chapter describes the proposed integrated systems and the operation of their different cycles. The first system will be explained completely, and other systems are described by comparison to the first system.

3.1 Systems 1a and 1b Description

At the beginning, we describe system 1a by discussing the operation of the subsystems that consists of the integrated system shown in Figure 3.1.

3.1.1 SOFC-GT Cycle with Regeneration

This regenerative integrated cycle consists of an air compressor, two regenerative heat exchangers, one for incoming air and another for the incoming fuel, Solid Oxide Fuel Cell (SOFC), a combustor and a Gas Turbine (GT) that is attached to an electric generator and the air compressor. The cycle starts by air entering the air compressor to increase its pressure by a certain compression ratio. This air is then preheated inside the air regenerator to recover some of the waste heat coming from the exhaust gases exiting the gas turbine before it enters the cathode side of the SOFC. Fuel coming in from a pressurized vessel goes through the fuel regenerator to gain some recovered thermal energy before splitting into two streams, most of it enters the anode side of the SOFC and the rest goes directly to the combustor. The SOFC does not consume the whole stream of methane. It only consumes it with a predetermined utilization factor of around 0.85. A mixture of exhaust gases+methane+air goes to the combustor, it mixes with some preheated methane fuel and burns completely and adiabatically to produce a gas mixture of carbon dioxide, water vapor, nitrogen, and excess oxygen. Next, most of the exhaust gases proceed to the gas turbine for power production to the electric generator and the attached air compressor and some go to the fuel regenerator for heat recovery. Then, the exhaust gases leave this cycle and continue to the other cycles.

3.1.2 Steam Rankine Cycle (SRC)

This Steam Rankine Cycle (SRC) starts by pumping the compressed liquid water to the boiler at high pressure. The liquid vaporizes completely at constant pressure in the boiler.

The heat source for this boiler is the exhaust gases leaving the air regenerator from the SOFC-GT cycle. After that, the fluid goes through Turbine 2 where it produces power and its pressure is dropped. To complete the cycle, the working fluid goes through HX 3 where it condenses at constant pressure and delivers its waste heat to the Organic Rankine Cycle (ORC).

3.1.3 Organic Rankine Cycle (ORC)

This Rankine Cycle uses an organic working fluid that undergoes phase change in the turbine. The working fluid chosen could be ammonia or Isobutane. This working fluid is first pumped at high pressure to HX 3 where it changes its phase from liquid to vapor, completely. This process happens at an intermediate temperature. This intermediate-temperature high-pressure vapor enters Turbine 3 and it causes the device to produce some extra electric power for the locomotive. The fluid leaves Turbine 3 as a saturated mixture and returns back to a liquid form as it passes through Condenser 1.

3.1.4 Small Hot Water Production Cycle

This simple cycle uses the exhaust gases coming from the SOFC-GT and the SRC to heat up the water and store it in a tank. Water is fed by a pump to the heater which is stored in a hot water tank for later use. Two exhaust gases are mixed in the mixing chamber before entering the heater to provide thermal energy for the water, and then it is released to the environment.

3.1.5 Reversible Heat Pump Cycle

A reversible heat pump can provide heating or cooling without changing the setup of the system. The provided service is controlled by a reversible valve which directs the flow of the compressed working fluid to provide either heating or cooling to the encapsulated area of the passenger train as needed. Firstly, the heating mode is described. Choosing refrigerant R134a as a working fluid, it gets into Compressor 2 that is powered by the Steam Rankine Cycle discussed earlier and it exits with higher pressure and higher temperature than the indoor area. As the working fluid goes through HX 1, which it acts as a condenser in the heating mode, it releases heat to the indoor area by a mean of using a fan. After that, the valve reduces the pressure of the working fluid and cools it down to a

point where its temperature is lower than the outside environment. To complete the cycle, in HX 2, the working fluid absorbs heat from the surroundings to evaporate it. In the cooling mode, the direction of the flow is reversed. The fluid leaves Compressor 2 and goes directly to HX 2 to release heat to the surroundings, this heat exchanger acts as a condenser in this cooling mode as opposed to the previous case. Similarly, the valve reduces the pressure and temperature of the fluid so that it can absorb heat from the indoor area as it passes through HX 1 in order to produce the required cooling effect.

Secondly, system 1b is presented in Figure 3.2. This system defers from the above system in the regeneration of SOFC-GT primary cycle. The stream leaving the gas turbine goes through the regenerators in series. It goes through the air regenerator then the fuel regenerator. The high-temperature exhaust gases leaving the SOFC-GT cycle enters the Steam Rankine Cycle (SRC) to boil the water. Since there is a single stream exiting the SOFC-GT subsystem, there is no need for the mixing chamber for the hot water production cycle.

3.2 System 2 Description

This integrated system is shown in Figure 3.3 which replaces the reversible heat pump with an absorption chiller. This chiller uses exhaust gases which contains thermal energy to produce the cooling effect. This makes this cycle exergetically more efficient than a reversible heat pump because lower grade source of energy is used to produce the cooling effect, unlike the heat pump which consumes mechanical power to produce either heating or cooling effects. The heating effect is generated by utilizing a regular heat exchanger after the hot water production cycle, namely HX1.

3.2.1 Absorption Chiller with a Heat Exchanger Cycle

The operation of the absorption chiller is described. When the system is in the cooling mode, Pump 3 is turned on and it pumps a mixture of refrigerant and absorbent to the regenerator for preheating before it enters the generator. This mixture could be a mixture of water-Li/Br or ammonia-water. In the generator, the mixture is separated into refrigerant vapor and liquid absorbent by means of heating supplied by a hot stream of exhaust gases leaving the fuel regenerator. The liquid absorbent flows back to the absorber after it passes through the regenerator and the expansion valve. The refrigerant vapor proceeds to

Condenser 2 and Expansion valve 2 to reduce its pressure and temperature. This low-temperature liquid enters the evaporator to absorb heat from the indoor area of the train which causes the desired cooling effect. Next, for the heating mode, this absorption chiller cycle is turned off and a fan is turned on instead to blow cold air across the pipes of HX1. The heat is supplied from the exhaust gases leaving the heater from the hot water production cycle.

3.3 System 3 Description

In Figure 3.4, the system replaces the combustor in previous systems with a Partially-Premixed Compression Ignition (PPCI) engine. This is to reduce the exergy destruction rate at that step as will be shown in the results. This engine produces power by using the premixed fuel+air+exhaust gases mixture with a fresh charge of fuel added at the beginning of the combustion stage. The engine follows the Otto cycle with fuel injection added before combustion (heat addition). The engine receives the partially consumed fuel leaving the SOFC and it is premixed with air and exhaust gases. Then, the piston compresses the mixture to a certain small volume. At this instant, the main fuel fresh charge redirected to the engine is added to initiate the combustion process. This combustion produces high-temperature and high-pressure exhaust gases that expand the piston for power production. This is illustrated in Figure 3.5. The stream exiting the engine is at high pressure and temperature which is split into two streams, one gets expanded in the gas turbine and the other goes through the fuel regenerator to preheat the fuel coming from the storage tanks. The fuel and air regenerators are arranged in parallel because the temperature of the exhaust gases leaving the gas turbine is not enough to provide for both regenerators. A Steam Rankine Cycle (SRC) cannot be used in this system as the stream leaving the air regenerator has a low temperature which cannot boil water. For this reason, an Organic Rankine Cycle (ORC) is placed to recover some of the waste heat.

3.4 System 4 Description

The system is shown in Figure 3.6. This system is similar to system 1b mentioned earlier, but it uses the heat loss from the Solid Oxide Fuel Cell (SOFC) to produce power using an Organic Rankine Cycle (ORC). Pump 3 circulates water to absorb heat from the SOFC and drops some of this thermal energy at Boiler 2 to evaporate the organic working fluid of the

ORC. This ORC starts by pumping an organic fluid to the preheater where it gains some heat from the exit stream of Turbine 2 of the SRC. The fluid is partially evaporated, and it is in the saturated mixture phase. Next, it goes through Boiler 2 to evaporate completely. After that, the evaporated fluid is expanded in Turbine 3 for power production. The exiting stream passes through Condenser 2 to condense the organic working fluid which completes the cycle.

3.5 System 5 Description

This is a simple system in which the main working fluid is ammonia in all of the subsystems. This is illustrated in Figure 3.7. Starting with this system and later systems, the fuel for the fuel cell is ammonia instead of methane. The exhaust gases stream leaving the fuel regenerator is split into two streams. One goes to thermally feed the generator of the absorption chiller to provide space cooling. The other stream goes through the Boiler of the NH₃-ORC for power production. The use of a steam Rankine cycle is abandoned for reducing system complexity and space requirements. To provide high power production that can compensate for the cascaded Rankine cycles, the ammonia organic Rankine cycle will operate at high pressures and supercritical conditions as well. Pump 1 increases the liquid ammonia to high pressure with consuming a marginal amount of power that comes from Turbine 2. This liquid ammonia goes through the Boiler and evaporates completely to reach superheated conditions by absorbing heat from the exhaust gases leaving the SOFC-GT cycle. The superheated working fluid expands at Turbine 2 for power production. To complete the cycle, the saturated mixture ammonia is cooled by passing through Condenser 1. Space heating can be provided by turning the fan on, next to HX1. This heat exchanger utilizes the excess thermal energy at a human comfort temperature level of the exhaust gases exiting the small hot water production cycle.

3.6 System 6 Description

In Figure 3.8, system 6 is presented. This system integrates an Ammonia Dissociation and Separation Unit (ADSU) for onboard hydrogen production. The hydrogen produced is either stored in a compressed tank or supplied to a Proton Exchange Membrane Fuel Cell (PEMFC) for power production. The need to produce hydrogen stems from operating a PEMFC that has a much higher volume power density than the gas turbine. This reduces the overall system space requirements.

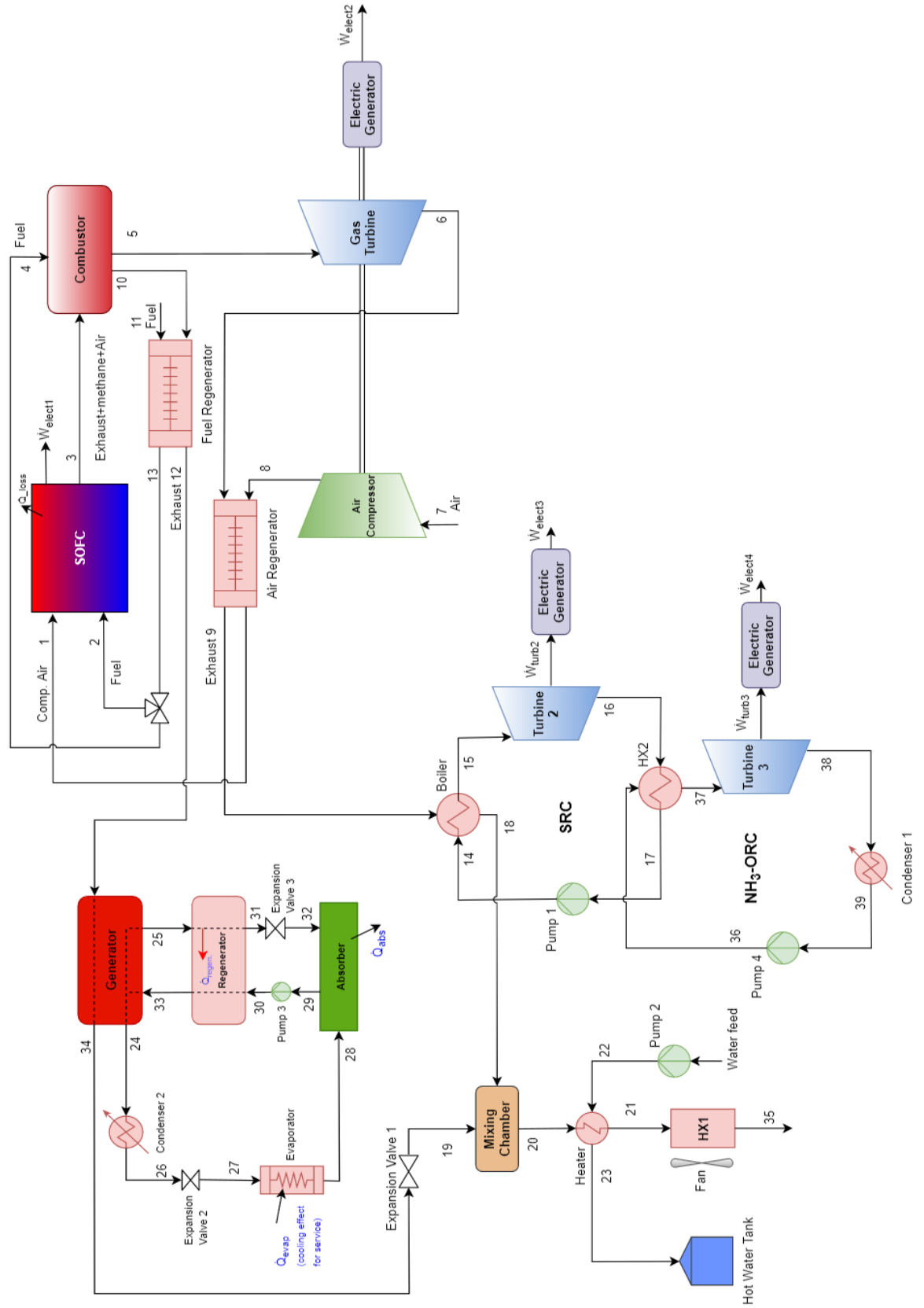


Figure 3.3: A schematic drawing of the integrated SOFC-GT-SRC-ORC system with an absorption chiller (System 2).

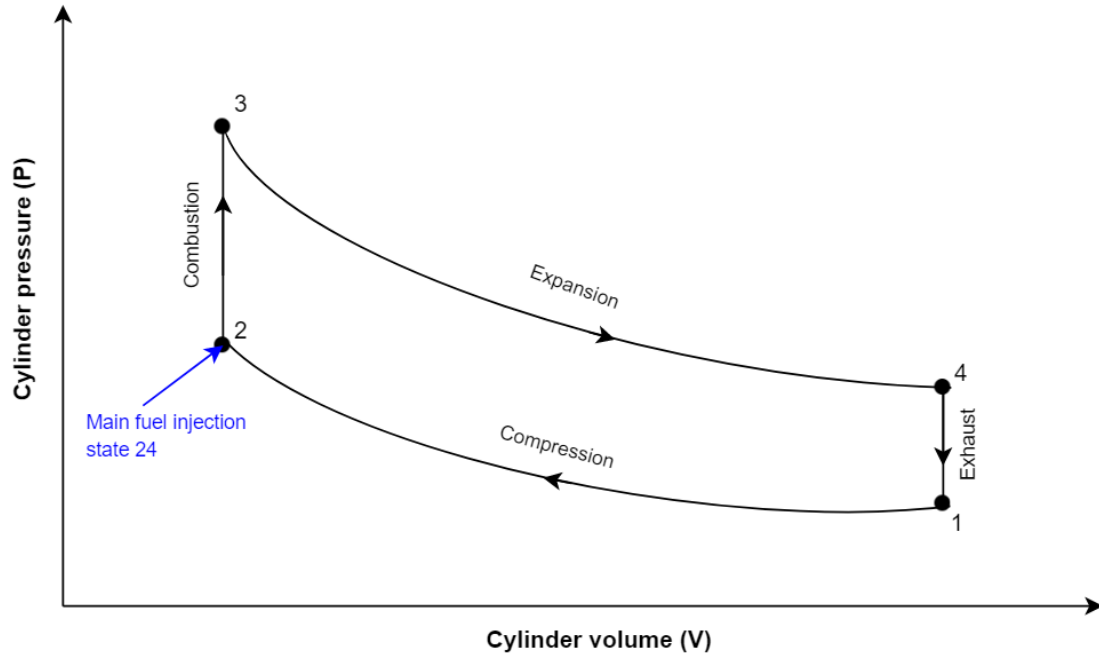


Figure 3.5: P-V diagram of the ideal Otto cycle with fuel injection before combustion. This is for the PPCI engine.

3.6.1 Ammonia-DSU and PEMFC Cycle

The cycle starts by supplying the ADSU with compressed ammonia from the storage tank. This ammonia first evaporates then disassociates into hydrogen and nitrogen by absorbing the heat coming from the exhaust gases leaving the SOFC-GT cycle. A hydrogen purification unit separates the hydrogen from the gas mixture by using metal compounds that adsorb hydrogen molecules at their surface. The produced hydrogen gets split into two streams. One is stored in a compressed hydrogen tank for a quick startup of the powering system and the other stream enters the PEM fuel cell with a fresh stream of air for electric power production. The nitrogen produced that is at high pressure gets expanded in turbine 4 to produce a small amount of power. The exhaust gases exit the ADSU continue to supply the SRC and then the hot water production cycle.

3.7 System 7 Description

The last system studied in this thesis is schematically displayed in Figure 3.9. Here, we implement a different type of fuel cell called Molten Alkaline Hydroxide Electrolyte Fuel Cell (MAHEFC) in place of SOFC. This fuel cell can operate with direct injection of ammonia fuel at intermediate temperatures that range from 250°C to 450°C [47,48].

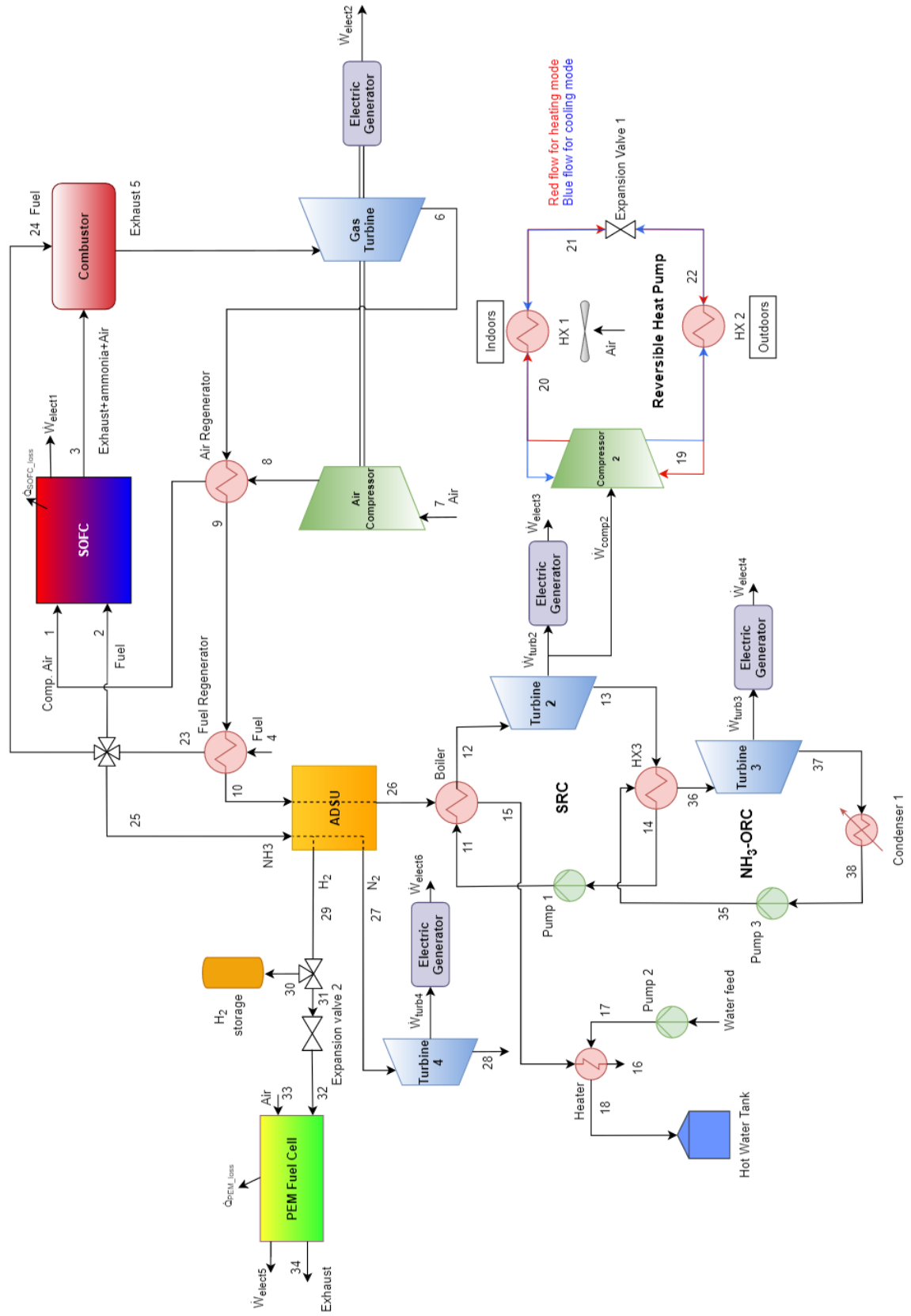


Figure 3.8: A schematic drawing of the integrated SOFC-GT-SRC-ORC system with ammonia-DSU and PEMFC (System 6).

3.7.1 MAHEFC with Regeneration Cycle

The cycle starts by compressing air slightly and sending it to the air regenerator where the air stream gets preheated to the necessary fuel cell temperature. It gets heated by the exhaust gases leaving the Steam Rankine Cycle (SRC). Ammonia fuel is supplied to the fuel regenerator for preheating before going to the fuel cell. Both air and ammonia fuel enter the fuel cell and react chemically to produce electric power. The ammonia fuel is partially consumed by the fuel cell by a factor defined earlier for SOFC called the utilization factor. A mixture stream of exhaust gases+air+ammonia leaves the fuel cell. In the combustor, the remaining fuel gets completely burned. The high-temperature exhaust gases pass through the boiler to supply heat to the SRC. No gas turbine is used as the exhaust gases temperature is not high enough to operate a Bryton cycle as for the previous systems.

3.7.2 Ammonia-Organic Rankine Cycle (NH₃-ORC) for Fuel Cell Heat Recovery

A second ammonia-ORC operates by absorbing heat losses from the fuel cell. The cycle starts by pumping liquid ammonia through the MAHE fuel cell to evaporate it by receiving heat from the fuel cell. The high-pressure intermediate temperature stream of vapor ammonia expands in turbine 3 for power production. In order to complete the cycle, the saturated mixture ammonia stream goes through condenser 2 and losses heat to the surroundings. The ammonia leaves the condenser as a liquid state and gets pumped again.

Chapter 4: Thermodynamic Analysis

The thermodynamic modelling of the previously presented systems and their subsystems is explained in this chapter. The first subsection discusses the main balance equations applied to the components of each proposed system. Next, the thermodynamic analysis is described for every cycle used in all of the seven systems mentioned earlier. Finally, the fuel cost analysis applied to every system for the case study is given.

4.1 Thermodynamic Balance Equations

In this subsection, the general forms of the balance equations used in the modelling of systems are described. These are the mass balance equation, energy balance equation, entropy balance equation, and definition of exergy destruction rate. Plus, the general assumptions used in this analysis are listed.

4.1.1 Mass Balance Equation

The law of mass conservation can be written in the rate form as

$$\sum_{in} \dot{m}_{in} - \sum_{out} \dot{m}_{out} = \frac{dm_{CV}}{dt} = 0 \quad (4.1)$$

This form is very suitable for steady-state devices. This relation says that the total mass flow rates entering a control volume (CV) and subtracting the total mass flow rates leaving this control volume equals to the rate of change in total mass within the control volume. Any device that is modelled thermodynamically can be treated as a control volume. At steady-state conditions, the rate of change of mass in a control volume (device) is zero.

4.1.2 Energy Balance Equation

The law of energy conservation, also known as the first law of thermodynamics, can be written in the rate form as

$$\dot{Q} - \dot{W} + \sum_{in} \dot{m}_{in} \left(h_{in} + \frac{v_{in}^2}{2} + gZ_{in} \right) - \sum_{out} \dot{m}_{out} \left(h_{out} + \frac{v_{out}^2}{2} + gZ_{out} \right) = \frac{dE_{CV}}{dt} = 0 \quad (4.2)$$

This form is very suitable for steady-state devices. This relation says that the total energy rates entering a control volume (CV) and subtracting the total energy rates leaving this control volume equal to the rate of change in total energy within the control volume. Any

device that is modelled thermodynamically can be treated as a control volume. At steady-state conditions, the rate of change of energy in a control volume (device) is zero. The specific kinetic and potential energy values that are associated with the entering and leaving mass flow rates are assumed to be negligible and ignored in the thermodynamic analysis.

4.1.3 Entropy Balance Equation

The rate of change of entropy within a control volume is expressed as

$$\sum_k \frac{\dot{Q}_k}{T_k} + \sum_{in} \dot{m}_{in}(s_{in}) - \sum_{out} \dot{m}_{out}(s_{out}) + \dot{S}_{gen} = \frac{dS_{CV}}{dt} = 0 \quad (4.3)$$

The second law of thermodynamics states that in any natural process, the entropy generation rate must be a positive value. At steady-state conditions, the rate of change of entropy in a control volume (device) is zero.

4.1.4 Exergy Balance Equation

The rate of change of exergy within a control volume is expressed as

$$\sum_k (1 - \frac{T_o}{T_k}) \dot{Q}_k - \dot{W} + \sum_{in} \dot{m}_{in}(ex_{in}) - \sum_{out} \dot{m}_{out}(ex_{out}) - \dot{Ex}_{dest} = \frac{dEx_{CV}}{dt} = 0 \quad (4.4)$$

This is an alternative expression for the second law of thermodynamics. At steady-state conditions, the rate of change of exergy in a control volume (device) is zero.

4.1.5 Exergy Destruction Rate and Specific Exergy Values

The exergy destruction rate for each control volume or device can be calculated by knowing the entropy generation rate from the entropy balance equation. They are related as

$$\dot{Ex}_{dest} = T_o \dot{S}_{gen} \quad (4.5)$$

where T_o is the ambient temperature. For finding the specific exergy values at each state j in a system, we define the total specific exergy as

$$ex_j = ex_j^{ph} + ex_j^{ch} + ex_j^{ke} + ex_j^{pe} \quad (4.6)$$

where the first term on the right is the physical exergy that can be expressed as

$$ex_j^{ph} = (h_j - h_o) - T_o(s_j - s_o)$$

and the second term is the chemical exergy of a fuel. This value is constant and has a standard value if the fuel stream is not mixed. The value of each fuel can be found from references like in [26,74]. The last two terms are the specific kinetic and potential exergy values, respectively. In this analysis, we are assuming them to be negligible as they are equal to the specific kinetic and potential energy values mentioned in the energy balance equation stated earlier.

4.1.6 Major Assumptions

Now, we list the common thermodynamic assumptions used in all of the studied systems. In later sections, more specific assumptions are made for each component of the proposed systems:

- Steady-state steady and uniform-flow processes for every component of the proposed systems.
- The changes in kinetic and potential energy and exergy across the devices are so small that they can be neglected.
- Pressure losses in the tubes connecting the different components or across heat exchangers are neglected.
- All heat exchangers, that have the four states studied, are assumed to be adiabatic. Evaporators, condensers and heat exchangers for space heating and cooling are not adiabatic since they lose or gain heat to and from the surroundings.
- All compressors are assumed adiabatic and have an isentropic efficiency of 80%.
- All turbines are assumed adiabatic and have an isentropic efficiency of 90%.
- In combustors, PPCI engine, ADSU, and PEMFC, the chemical reactions are assumed to be complete, that is no fuel leaves with the exhaust gases.
- Air and exhaust gases are assumed to follow ideal gas behavior.
- The standard ambient temperature and pressure are 298 K and 100 kPa, respectively.

4.2 Thermodynamic Analysis of the Studied Cycles

In this section, a more detailed analysis of each component within every chosen cycle (subsystem) is provided. It is noted that the states numbers used in expressing the balance equations and other formulas are for system 1a or the earliest system that presents the cycle.

4.2.1 SOFC-GT Primary Cycle with Regeneration

We start by the primary cycle of SOFC-GT hybrid system with fuel and air regeneration. Every component of this cycle is discussed by mentioning relevant mathematical expressions and the assumptions that are made for the thermal process in the component.

- Air Compressor:

This device is assumed to be adiabatic and it has an isentropic efficiency of

$$\eta_{is,Aircomp} = \frac{h_{8,is} - h_7}{h_8 - h_7} \quad (4.7)$$

Assuming air to be an ideal gas that is its enthalpy is only a function of temperature, we can estimate the isentropic enthalpy from the following relation for isentropic processes

$$\frac{T_{8,is}}{T_7} = \left(\frac{P_8}{P_7}\right)^{\frac{\gamma-1}{\gamma}} \quad (4.8)$$

where γ is the specific heat ratio for air. It is assumed to be constant with a value of 1.4. Also, the compression ratio for the Air Compressor is

$$r_p = \frac{P_8}{P_7}$$

The exergetic efficiency is defined as

$$\eta_{ex,Aircomp} = \frac{\dot{m}_8 ex_8 - \dot{m}_7 ex_7}{\dot{W}_{Aircomp}} \quad (4.9)$$

- Air and Fuel Regenerators:

These are assumed to be adiabatic heat exchangers. The specific enthalpy and entropy of exhaust gases are calculated using a weighted average formula that applies to ideal gas mixtures. The expressions are shown below.

For specific enthalpy,

$$h_9 = x_{CO_2}h_{CO_2,9} + x_{H_2O}h_{H_2O,9} + x_{N_2}h_{N_2,9} + x_{O_2}h_{O_2,9} \quad (4.10)$$

and for specific entropy,

$$s_9 = x_{CO_2}s_{CO_2,9} + x_{H_2O}s_{H_2O,9} + x_{N_2}s_{N_2,9} + x_{O_2}s_{O_2,9} \quad (4.11)$$

where x_i represents the mass ratio of the gas component i over the total mass of the gas mixture and $h_{i,j}$ and $s_{i,j}$ are the specific enthalpy and entropy, respectively, of component i of the gas mixture at state j . Note that these two expressions are used whenever there is a need to calculate the specific enthalpy and entropy of a gas mixture at any given state in the proposed integrated system.

- Solid Oxide Fuel Cell (SOFC):

One possible assumption for this kind of fuel cell is the complete electro-oxidation of methane which makes the overall chemical equation inside SOFC to be



where U is the utilization factor and λ is the excess air factor.

This fuel cell has heat losses and they can be calculated from the energetic efficiency of SOFC which is

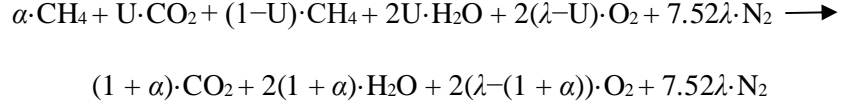
$$\eta_{en,SOFC} = \frac{\dot{W}_{elect,1}}{\dot{m}_1 h_1 + \dot{m}_2 h_2 - \dot{m}_3 h_3} \quad (4.12)$$

and its exergetic efficiency is

$$\eta_{ex,SOFC} = \frac{\dot{W}_{elect,1}}{\dot{m}_1 ex_1 + \dot{m}_2 ex_2 - \dot{m}_3 ex_3} \quad (4.13)$$

- Combustor:

This device burns the remaining methane in the exhaust of SOFC with some preheated methane fuel to produce high-temperature value for the Gas Turbine (GT). We are assuming adiabatic complete combustion of the reactants. The chemical balance equation of this reaction is



where α is the ratio defined as

$$\alpha = \frac{\dot{m}_4}{\dot{m}_2} \quad (4.14)$$

So, the overall chemical balance equation for both SOFC and combustor is



Here, α appears in the final chemical equation since these equations are considered for 1 kmol of methane entering the SOFC. In addition, we split the exiting stream into two, called states 5 and 10, and they both have the same values of specific enthalpy and specific entropy. 90% of the exiting stream goes to the Gas Turbine (GT).

The exergetic efficiency of this device is

$$\eta_{ex,combust} = \frac{\dot{m}_5 ex_5 + \dot{m}_{10} ex_{10}}{\dot{m}_3 ex_3 + \dot{m}_4 ex_4} \quad (4.15)$$

- Gas Turbine (GT):

This turbine is assumed to be adiabatic and it has an isentropic efficiency of

$$\eta_{is,Gas,turb} = \frac{h_5 - h_6}{h_5 - h_{6,is}} \quad (4.16)$$

Assuming ideal gas behavior for the fluid going through the turbine, we get the enthalpy to be a function of temperature only. The isentropic enthalpy can be found from knowing the isentropic temperature which is found from the relation presented here.

$$\frac{T_{6,is}}{T_5} = \left(\frac{P_6}{P_5} \right)^{\frac{\gamma-1}{\gamma}} \quad (4.17)$$

where γ is taken for air at a value of 1.4. Since some of the turbine power is used up by the Air compressor, it is useful to define the amount of power that reaches the Electric Generator attached to the Gas Turbine (GT).

$$\dot{W}_{elect,2} = \dot{W}_{Gas,turb} - \dot{W}_{Aircomp} \quad (4.18)$$

The exergetic efficiency can be expressed as

$$\eta_{ex,Gas,turb} = \frac{\dot{W}_{Gas,turb}}{\dot{m}_5 ex_5 - \dot{m}_6 ex_6} \quad (4.19)$$

4.2.2 Steam Rankine Cycle (SRC)

Secondly, this cycle is the first part of the waste heat recovery system for the primary SOFC-GT cycle. Here, we introduce the mathematical relations and assumptions made for every component of the Steam Rankine Cycle.

- Boiler:

Assuming an adiabatic heat exchanger and its exergetic efficiency is defined as

$$\eta_{ex,boiler} = \frac{\dot{m}_{15} ex_{15} - \dot{m}_{14} ex_{14}}{\dot{m}_9 ex_9 - \dot{m}_{18} ex_{18}} \quad (4.20)$$

- Turbine 2:

This turbine is assumed to be adiabatic and connected to both an electric generator and Compressor 2. The isentropic efficiency of this turbine is

$$\eta_{is,turb2} = \frac{h_{15} - h_{16}}{h_{15} - h_{16,is}} \quad (4.21)$$

Since some of the power coming out of Turbine 2 is consumed by Compressor 2, it is helpful to know the net power that reaches the electric generator. This can be computed by this relation

$$\dot{W}_{elect,3} = \dot{W}_{turb2} - \dot{W}_{comp2} \quad (4.22)$$

The exergetic efficiency can be expressed as

$$\eta_{ex,turb2} = \frac{\dot{W}_{turb2}}{\dot{m}_{15} ex_{15} - \dot{m}_{16} ex_{16}} \quad (4.23)$$

- Heat Exchanger 3 (HX 3):

This heat exchanger is adiabatic in which heat transfers from the condensing fluid of the SRC to vaporize the working fluid in the NH₃-ORC.

- Pump 1:

The process through this pump is assumed to be isenthalpic which means the power input to this pump is negligible and the following relation is satisfied $h_{17} = h_{14}$, accordingly.

4.2.3 Organic Rankine Cycle (ORC)

Thirdly, this cycle is recovering the waste heat from the Steam Rankine Cycle at an intermediate temperature to produce more power. Here, we introduce the mathematical relations and assumptions made for every component of the Organic Rankine Cycle with ammonia or Isobutane as a working fluid.

- Turbine 3:

This turbine is assumed to be adiabatic and has an isentropic efficiency of

$$\eta_{turb3} = \frac{h_{29} - h_{30}}{h_{29} - h_{30,is}} \quad (4.24)$$

The electric power produced by this turbine is equal to the mechanical power generated because we are assuming no losses in any of the electric generators.

$$\dot{W}_{elect,4} = \dot{W}_{turb3} \quad (4.25)$$

The exergetic efficiency can be expressed as

$$\eta_{ex,turb3} = \frac{\dot{W}_{turb3}}{\dot{m}_{29}ex_{29} - \dot{m}_{30}ex_{30}} \quad (4.26)$$

- Condenser 1:

This heat exchanger is not adiabatic since some heat transfer takes place between the working fluid and the surroundings.

- Pump 3:

The process through this pump is assumed to be isenthalpic which means the power input to this pump is negligible and the following relation is satisfied by $h_{31} = h_{28}$.

4.2.4 Small Hot Water Production Cycle

Similar to the above cycles, we describe the thermal processes of the components of this cycle, namely Mixing Chamber and Heater. The mathematical expressions and assumptions are outlined below for each component.

- Mixing Chamber:

Before coming to the Mixing Chamber, Expansion Valve 1 reduces the pressure of the exhaust gases leaving the Fuel Regenerator in an isenthalpic process according to $h_{12} = h_{19}$.

The assumption made on this Mixing Chamber is that it is adiabatic.

- Heater:

This heat exchanger is assumed to be adiabatic and its exergetic efficiency is

$$\eta_{ex,Heater} = \frac{\dot{m}_{23}ex_{23} - \dot{m}_{22}ex_{22}}{\dot{m}_{20}ex_{20} - \dot{m}_{21}ex_{21}} \quad (4.27)$$

4.2.5 Reversible Type Heat Pump Cycle

Also, the components of this reversible heat pump cycle are described thermodynamically by mentioning the assumptions and mathematical definitions of each component in the cycle.

- Compressor 2:

This compressor is assumed to be adiabatic and it has an isentropic efficiency expressed as

$$\eta_{comp2} = \frac{h_{25,is} - h_{24}}{h_{25} - h_{24}} \quad (4.28)$$

and its exergetic efficiency is

$$\eta_{ex,comp2} = \frac{\dot{m}_{25}ex_{25} - \dot{m}_{24}ex_{24}}{\dot{W}_{comp2}} \quad (4.29)$$

- Heat Exchanger 1 (HX 1):

This heat exchanger interacts with the indoor area which is not to be assumed adiabatic. The balance equations, written in Table 4.1, are when the heat pump cycle is in the heating mode. The same balance equations are applicable except for the heat transfer rate value which becomes negative. For this device, the exergetic efficiency is defined as

$$\eta_{ex,HX1} = \frac{\dot{Q}_{HX1} \left(1 - \frac{T_o}{T_{avg,HX1}}\right)}{\dot{m}_{25}ex_{25} - \dot{m}_{26}ex_{26}} \quad (4.30)$$

- Expansion Valve 2:

An isenthalpic process occurs in the valve and it is assumed to follow: $h_{26} = h_{27}$.

Table 4.1a: A list of balance equations for the components of system 1a.

Component	Mass Balance	Energy Balance
Air Compressor	$\dot{m}_7 = \dot{m}_8$	$\dot{m}_7 h_7 + \dot{W}_{Aircomp} = \dot{m}_8 h_8$
Air Regenerator	$\dot{m}_1 = \dot{m}_8$, $\dot{m}_6 = \dot{m}_9$	$\dot{m}_6 h_6 + \dot{m}_8 h_8 = \dot{m}_1 h_1 + \dot{m}_9 h_9$
Fuel Regenerator	$\dot{m}_{13} = \dot{m}_{11}$, $\dot{m}_{12} = \dot{m}_{10}$	$\dot{m}_{10} h_{10} + \dot{m}_{11} h_{11} = \dot{m}_{12} h_{12} + \dot{m}_{13} h_{13}$
Solid Oxide Fuel Cell (SOFC)	$\dot{m}_1 + \dot{m}_2 = \dot{m}_3$	$\dot{m}_1 h_1 + \dot{m}_2 h_2 = \dot{m}_3 h_3 + \dot{W}_{elect,1} + \dot{Q}_{SOFC,loss}$
Combustor	$\dot{m}_3 + \dot{m}_4 = \dot{m}_5 + \dot{m}_{10}$	$\dot{m}_3 h_3 + \dot{m}_4 h_4 = \dot{m}_5 h_5 + \dot{m}_{10} h_{10}$
Gas Turbine (GT)	$\dot{m}_5 = \dot{m}_6$	$\dot{m}_5 h_5 = \dot{m}_6 h_6 + \dot{W}_{Gas,turb}$
Boiler	$\dot{m}_{14} = \dot{m}_{15}$, $\dot{m}_9 = \dot{m}_{18}$	$\dot{m}_9 h_9 + \dot{m}_{14} h_{14} = \dot{m}_{15} h_{15} + \dot{m}_{18} h_{18}$
Turbine 2	$\dot{m}_{15} = \dot{m}_{16}$	$\dot{m}_{15} h_{15} = \dot{m}_{16} h_{16} + \dot{W}_{turb2}$
Heat Exchanger 3 (HX 3)	$\dot{m}_{16} = \dot{m}_{17}$, $\dot{m}_{28} = \dot{m}_{29}$	$\dot{m}_{16} h_{16} + \dot{m}_{28} h_{28} = \dot{m}_{17} h_{17} + \dot{m}_{29} h_{29}$
Turbine 3	$\dot{m}_{29} = \dot{m}_{30}$	$\dot{m}_{29} h_{29} = \dot{m}_{30} h_{30} + \dot{W}_{turb3}$
Condenser 1	$\dot{m}_{30} = \dot{m}_{31}$	$\dot{m}_{30} h_{30} = \dot{m}_{31} h_{31} + \dot{Q}_{cond1}$
Mixing Chamber	$\dot{m}_{18} + \dot{m}_{19} = \dot{m}_{20}$	$\dot{m}_{18} h_{18} + \dot{m}_{19} h_{19} = \dot{m}_{20} h_{20}$
Heater	$\dot{m}_{20} = \dot{m}_{21}$, $\dot{m}_{22} = \dot{m}_{23}$	$\dot{m}_{20} h_{20} + \dot{m}_{22} h_{22} = \dot{m}_{21} h_{21} + \dot{m}_{23} h_{23}$
Compressor 2	$\dot{m}_{24} = \dot{m}_{25}$	$\dot{m}_{24} h_{24} + \dot{W}_{comp2} = \dot{m}_{25} h_{25}$
Heat Exchanger 1 (HX 1)	$\dot{m}_{25} = \dot{m}_{26}$	$\dot{m}_{25} h_{25} = \dot{m}_{26} h_{26} + \dot{Q}_{HX1}$
Heat Exchanger 2 (HX 2)	$\dot{m}_{27} = \dot{m}_{24}$	$\dot{m}_{27} h_{27} + \dot{Q}_{HX2} = \dot{m}_{24} h_{24}$

Table 4.1b: A continued list of balance equations for the components of system 1a.

Component	Entropy Balance	Exergy Balance
Air Compressor	$\dot{m}_7 s_7 + \dot{S}_{gen,Aircomp}$ $= \dot{m}_8 s_8$	$\dot{m}_7 ex_7 + \dot{W}_{Aircomp} = \dot{m}_8 ex_8 + \dot{E}x_{dest,Aircomp}$
Air Regenerator	$\dot{m}_6 s_6 + \dot{m}_8 s_8$ $+ \dot{S}_{gen,Air,regen}$ $= \dot{m}_1 s_1 + \dot{m}_9 s_9$	$\dot{m}_6 ex_6 + \dot{m}_8 ex_8$ $= \dot{m}_1 ex_1 + \dot{m}_9 ex_9$ $+ \dot{E}x_{dest,Air,regen}$
Fuel Regenerator	$\dot{m}_{10} s_{10} + \dot{m}_{11} s_{11}$ $+ \dot{S}_{gen,Fuel,regen}$ $= \dot{m}_{12} s_{12} + \dot{m}_{13} s_{13}$	$\dot{m}_{10} ex_{10} + \dot{m}_{11} ex_{11}$ $= \dot{m}_{12} ex_{12} + \dot{m}_{13} ex_{13}$ $+ \dot{E}x_{dest,Fuel,regen}$
Solid Oxide Fuel Cell (SOFC)	$\dot{m}_1 s_1 + \dot{m}_2 s_2 + \dot{S}_{gen,SOFC}$ $= \dot{m}_3 s_3$ $+ \frac{\dot{Q}_{SOFC,loss}}{T_{avg,SOFC}}$	$\dot{m}_1 ex_1 + \dot{m}_2 ex_2 = \dot{m}_3 ex_3 + \dot{W}_{elect,1}$ $+ (1 - \frac{T_o}{T_{avg,SOFC}}) \dot{Q}_{SOFC,loss}$ $+ \dot{E}x_{dest,SOFC}$
Combustor	$\dot{m}_3 s_3 + \dot{m}_4 s_4 + \dot{S}_{gen,combust}$ $= \dot{m}_5 s_5$ $+ \dot{m}_{10} s_{10}$	$\dot{m}_3 ex_3 + \dot{m}_4 ex_4$ $= \dot{m}_5 ex_5 + \dot{m}_{10} ex_{10}$ $+ \dot{E}x_{dest,combust}$
Gas Turbine (GT)	$\dot{m}_5 s_5 + \dot{S}_{gen,Gas,turb}$ $= \dot{m}_6 s_6$	$\dot{m}_5 ex_5 = \dot{m}_6 ex_6 + \dot{W}_{Gas,turb} + \dot{E}x_{dest,Gas,turb}$
Boiler	$\dot{m}_9 s_9 + \dot{m}_{14} s_{14} + \dot{S}_{gen,boiler}$ $= \dot{m}_{15} s_{15}$ $+ \dot{m}_{18} s_{18}$	$\dot{m}_9 ex_9 + \dot{m}_{14} ex_{14}$ $= \dot{m}_{15} ex_{15} + \dot{m}_{18} ex_{18}$ $+ \dot{E}x_{dest,boiler}$
Turbine 2	$\dot{m}_{15} s_{15} + \dot{S}_{gen,turb2}$ $= \dot{m}_{16} s_{16}$	$\dot{m}_{15} ex_{15} = \dot{m}_{16} ex_{16} + \dot{W}_{turb2} + \dot{E}x_{dest,turb2}$
Heat Exchanger 3 (HX 3)	$\dot{m}_{16} s_{16} + \dot{m}_{28} s_{28}$ $+ \dot{S}_{gen,HX3}$ $= \dot{m}_{17} s_{17}$ $+ \dot{m}_{29} s_{29}$	$\dot{m}_{16} ex_{16} + \dot{m}_{28} ex_{28}$ $= \dot{m}_{17} ex_{17} + \dot{m}_{29} ex_{29}$ $+ \dot{E}x_{dest,HX3}$
Turbine 3	$\dot{m}_{29} s_{29} + \dot{S}_{gen,turb3}$ $= \dot{m}_{30} s_{30}$	$\dot{m}_{29} ex_{29} = \dot{m}_{30} ex_{30} + \dot{W}_{turb3} + \dot{E}x_{dest,turb3}$
Condenser 1	$\dot{m}_{30} s_{30} + \dot{S}_{gen,cond1}$ $= \dot{m}_{31} s_{31}$ $+ \frac{\dot{Q}_{cond1}}{T_{avg,cond1}}$	$\dot{m}_{30} ex_{30} = \dot{m}_{31} ex_{31} + (1 - \frac{T_o}{T_{avg,cond1}}) \dot{Q}_{cond1}$ $+ \dot{E}x_{dest,cond1}$
Mixing Chamber	$\dot{m}_{18} s_{18} + \dot{m}_{19} s_{19} + \dot{S}_{gen,mix}$ $= \dot{m}_{20} s_{20}$	$\dot{m}_{18} ex_{18} + \dot{m}_{19} ex_{19} = \dot{m}_{20} ex_{20} + \dot{E}x_{dest,mix}$
Heater	$\dot{m}_{20} s_{20} + \dot{m}_{22} s_{22}$ $+ \dot{S}_{gen,Heater}$ $= \dot{m}_{21} s_{21} + \dot{m}_{23} s_{23}$	$\dot{m}_{20} ex_{20} + \dot{m}_{22} ex_{22}$ $= \dot{m}_{21} ex_{21} + \dot{m}_{23} ex_{23}$ $+ \dot{E}x_{dest,Heater}$
Compressor 2	$\dot{m}_{24} s_{24} + \dot{S}_{gen,comp2}$ $= \dot{m}_{25} s_{25}$	$\dot{m}_{24} ex_{24} + \dot{W}_{comp2} = \dot{m}_{25} ex_{25} + \dot{E}x_{dest,comp2}$
Heat Exchanger 1 (HX 1)	$\dot{m}_{25} s_{25} + \dot{S}_{gen,HX1}$ $= \dot{m}_{26} s_{26}$ $+ \frac{\dot{Q}_{HX1}}{T_{avg,HX1}}$	$\dot{m}_{25} ex_{25} = \dot{m}_{26} ex_{26} + (1 - \frac{T_o}{T_{avg,HX1}}) \dot{Q}_{HX1}$ $+ \dot{E}x_{dest,HX1}$
Heat Exchanger 2 (HX 2)	$\dot{m}_{27} s_{27} + \frac{\dot{Q}_{HX2}}{T_{avg,HX2}}$ $+ \dot{S}_{gen,HX2}$ $= \dot{m}_{24} s_{24}$	$\dot{m}_{27} ex_{27} + (1 - \frac{T_o}{T_{avg,HX2}}) \dot{Q}_{HX2}$ $= \dot{m}_{24} ex_{24} + \dot{E}x_{dest,HX2}$

- Heat Exchanger 2 (HX 2):

This heat exchanger interacts with the surroundings which it is not to be assumed adiabatic. The equations mentioned here are when the heat pump cycle is in the heating mode. The same balance equations are applicable except for the heat transfer rate value which becomes negative.

4.2.6 Absorption Chiller with a Heat Exchanger Cycle

Now, we describe the thermal processes mathematically and their assumptions for this cooling and heating subsystem in system 2. Subsystem and cycle terms are used interchangeably.

In the case of heating mode, we only have HX 1 from system 2 as shown in Figure 3.3.

- Heat Exchanger 1 (HX 1):

This heat exchanger is releasing heat to the environment, so the thermal process is not adiabatic. Its exergetic efficiency can be described as

$$\eta_{ex,HX1} = \frac{\dot{Q}_{HX1} \left(1 - \frac{T_o}{T_{avg,HX1}}\right)}{\dot{m}_{21}ex_{21} - \dot{m}_{35}ex_{35}} \quad (4.31)$$

In this mode, the Generator does not absorb any heat from the exhaust gases leaving the SOFC-GT cycle, this means that states 12 and 34 are the same in system 2.

For the cooling mode, we have the following.

- Generator:

In this device, the heat transfer is within the device so the process is adiabatic. The exiting separated streams of refrigerant vapor and liquid absorbent leave the generator at the same temperature. The separation follows the ammonia mass balance which is

$$x_{30}\dot{m}_{30} = x_{21}\dot{m}_{21} + x_{22}\dot{m}_{22} \quad (4.32)$$

The exergetic efficiency is

$$\eta_{ex,generator} = \frac{\dot{m}_{24}ex_{24} + \dot{m}_{25}ex_{25} - \dot{m}_{33}ex_{33}}{\dot{m}_{12}ex_{12} - \dot{m}_{34}ex_{34}} \quad (4.33)$$

- Condenser:

The refrigerant vapor condenses by releasing heat to the environment to become in a compressed liquid form. The balance equations for this component are mentioned in Table 4.2.

- Expansion Valves 2 and 3:

Isenthalpic processes occur in the valves and they are assumed to follow these relations, $h_{26} = h_{27}$ and $h_{31} = h_{32}$, respectively.

- Evaporator:

The cooling effect happens in this device by absorbing heat from the indoor area of the train. The exergetic efficiency of this device is

$$\eta_{ex,evap} = \frac{\dot{Q}_{evap} \left(\frac{T_o}{T_{avg,evap}} - 1 \right)}{\dot{m}_{28}ex_{28} - \dot{m}_{27}ex_{27}} \quad (4.34)$$

- Absorber:

This component does the opposite of what the generator does. It mixes the refrigerant vapor with the liquid absorbent and in the process releases heat to the environment to become a liquid mixture. Its exergetic efficiency can be calculated by

$$\eta_{ex,abs} = \frac{\dot{m}_{29}ex_{29}}{\dot{m}_{28}ex_{28} + \dot{m}_{32}ex_{32}} \quad (4.35)$$

- Pump 3:

An isenthalpic process occurs in the pump and it is assumed to follow: $h_{29} = h_{30}$

- Regenerator:

This component is basically an adiabatic heat exchanger that restores some of the heat to the mixture before it goes to the generator. The balance equations of this absorption chiller cycle are expressed mathematically in Table 4.2.

Table 4.2a: A list of balance equations for the components of the absorption chiller with a heat exchanger cycle.

Component	Mass Balance	Energy Balance
Generator	$\dot{m}_{12} = \dot{m}_{34}$, $\dot{m}_{33} = \dot{m}_{24} + \dot{m}_{25}$	$\dot{m}_{12} h_{12} + \dot{m}_{33} h_{33} = \dot{m}_{24} h_{24} + \dot{m}_{25} h_{25} + \dot{m}_{34} h_{34}$
Condenser 2	$\dot{m}_{24} = \dot{m}_{26}$	$\dot{m}_{24} h_{24} = \dot{m}_{26} h_{26} + \dot{Q}_{cond2}$
Evaporator	$\dot{m}_{27} = \dot{m}_{28}$	$\dot{m}_{27} h_{27} + \dot{Q}_{evap} = \dot{m}_{28} h_{28}$
Absorber	$\dot{m}_{28} + \dot{m}_{32} = \dot{m}_{29}$	$\dot{m}_{28} h_{28} + \dot{m}_{32} h_{32} = \dot{m}_{29} h_{29} + \dot{Q}_{abs}$
Regenerator	$\dot{m}_{25} = \dot{m}_{31}$, $\dot{m}_{30} = \dot{m}_{33}$	$\dot{m}_{25} h_{25} + \dot{m}_{30} h_{30} = \dot{m}_{31} h_{31} + \dot{m}_{33} h_{33}$
Heat Exchanger 1 (HX 1)	$\dot{m}_{21} = \dot{m}_{35}$	$\dot{m}_{21} h_{21} = \dot{m}_{35} h_{35} + \dot{Q}_{HX1}$

Table 4.2b: A continued list of balance equations for the components of the absorption chiller with a heat exchanger cycle.

Component	Entropy Balance	Exergy Balance
Generator	$\dot{m}_{12} s_{12} + \dot{m}_{33} s_{33}$ $+ \dot{S}_{gen,generator}$ $= \dot{m}_{24} s_{24} + \dot{m}_{25} s_{25}$ $+ \dot{m}_{34} s_{34}$	$\dot{m}_{12} ex_{12} + \dot{m}_{33} ex_{33}$ $= \dot{m}_{24} ex_{24} + \dot{m}_{25} ex_{25}$ $+ \dot{m}_{34} ex_{34} + \dot{E}x_{dest,generator}$
Condenser 2	$\dot{m}_{24} s_{24} + \dot{S}_{gen,cond2}$ $= \dot{m}_{26} s_{26} + \frac{\dot{Q}_{cond2}}{T_{avg,cond2}}$	$\dot{m}_{24} ex_{24} = \dot{m}_{26} ex_{26} + \left(1 - \frac{T_o}{T_{avg,cond2}}\right) \dot{Q}_{cond2}$ $+ \dot{E}x_{dest,cond2}$
Evaporator	$\dot{m}_{27} s_{27} + \frac{\dot{Q}_{evap}}{T_{avg,evap}}$ $+ \dot{S}_{gen,evap} = \dot{m}_{28} s_{28}$	$\dot{m}_{27} ex_{27} + \left(1 - \frac{T_o}{T_{avg,evap}}\right) \dot{Q}_{evap}$ $= \dot{m}_{28} ex_{28} + \dot{E}x_{dest,evap}$
Absorber	$\dot{m}_{28} h_{28} + \dot{m}_{32} h_{32}$ $+ \dot{S}_{gen,abs}$ $= \dot{m}_{29} h_{29}$ $+ \frac{\dot{Q}_{abs}}{T_{avg,abs}}$	$\dot{m}_{28} ex_{28} + \dot{m}_{32} ex_{32}$ $= \dot{m}_{29} ex_{29} + \left(1 - \frac{T_o}{T_{avg,abs}}\right) \dot{Q}_{abs} + \dot{E}x_{dest,abs}$
Regenerator	$\dot{m}_{25} s_{25} + \dot{m}_{30} s_{30}$ $+ \dot{S}_{gen,Regenerator}$ $= \dot{m}_{31} s_{31} + \dot{m}_{33} s_{33}$	$\dot{m}_{25} ex_{25} + \dot{m}_{30} ex_{30}$ $= \dot{m}_{31} ex_{31} + \dot{m}_{33} ex_{33}$ $+ \dot{E}x_{dest,Regenerator}$
Heat Exchanger 1 (HX 1)	$\dot{m}_{21} s_{21} + \dot{S}_{gen,HX1}$ $= \dot{m}_{35} s_{35}$ $+ \frac{\dot{Q}_{HX1}}{T_{avg,HX1}}$	$\dot{m}_{21} ex_{21} = \dot{m}_{35} ex_{35} + \left(1 - \frac{T_o}{T_{avg,HX1}}\right) \dot{Q}_{HX1}$ $+ \dot{E}x_{dest,HX1}$

4.2.7 Partially-Premixed Compression Ignition (PPCI) Engine

This component replaces the combustor and produces electric power by completing the combustion of the remaining fuel and uses an additional fuel charge as the main injection. Air Standard assumptions are applied in this engine.

This device is modelled as an ideal Otto cycle as follows. Referring to Figure 3.4, the compression process is assumed to be isentropic and it is expressed as

$$\frac{P_{2,engine}}{P_{1,engine}} = (r_v)^\gamma \quad (4.36)$$

$$\frac{T_{2,engine}}{T_{1,engine}} = (r_v)^{\gamma-1} \quad (4.37)$$

where r_v is the engine compression ratio defined as

$$r_v = \frac{V_{1,engine}}{V_{2,engine}}$$

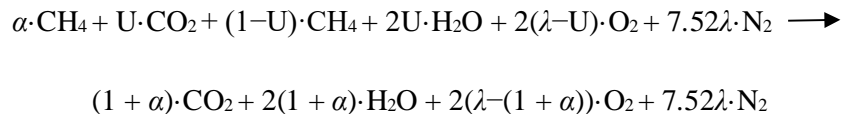
The compression power consumed is expressed as

$$\dot{W}_{comp,engine} = \dot{m}_{1,engine}(h_{2,engine} - h_{1,engine})$$

The main injection process and the combustion process are assumed to happen at constant volume conditions. Thus, the ideal gas law becomes

$$\frac{T_{3,engine}}{T_{2,engine}} = \frac{P_{3,engine}}{P_{2,engine}} \quad (4.38)$$

The chemical reaction of the combustion stage is



where α was defined earlier in the combustor subsection.

Then, the isentropic expansion of the piston follows these relations

$$\frac{P_{4,engine}}{P_{3,engine}} = \left(\frac{1}{r_v}\right)^\gamma \quad (4.39)$$

$$\frac{T_{4,engine}}{T_{3,engine}} = \left(\frac{1}{r_v}\right)^{\gamma-1} \quad (4.40)$$

The expansion power is

$$\dot{W}_{exp,engine} = \dot{m}_{4,engine}(h_{4,engine} - h_{3,engine})$$

Therefore, the net power output of the engine is

$$\dot{W}_{elect,2} = \dot{W}_{net,engine} = \dot{W}_{exp,engine} - \dot{W}_{comp,engine}$$

The balance equations of this engine are expressed in Table 4.3.

Table 4.3: Balance equations for the PPCI engine.

Component	Mass Balance	Energy Balance	Entropy Balance	Exergy Balance
PPCI engine	$\dot{m}_3 + \dot{m}_{24} = \dot{m}_5$	$\dot{m}_3 h_3 + \dot{m}_{24} h_{24} = \dot{m}_5 h_5 + \dot{W}_{net,engine}$	$\dot{m}_{12} s_{12} + \dot{m}_{24} s_{24} + \dot{S}_{gen,engine} = \dot{m}_5 s_5$	$\dot{m}_3 ex_3 + \dot{m}_{24} ex_{24} = \dot{m}_5 ex_5 + \dot{W}_{net,engine} + \dot{E}x_{dest,engine}$

Lastly, the energetic and exergetic efficiencies of the PPCI engine can be defined respectively as

$$\eta_{en,engine} = 1 - \frac{1}{r_v^{\gamma-1}} \quad (4.41)$$

$$\eta_{ex,engine} = \frac{\dot{W}_{net,engine}}{\dot{m}_3 ex_3 + \dot{m}_{24} ex_{24} - \dot{m}_5 ex_5} \quad (4.42)$$

4.2.8 Heat recovery from SOFC using a preheated ORC cycle

Heat losses are recovered from the Solid Oxide Fuel Cell (SOFC) and are supplied to a preheated Organic Rankine Cycle (ORC) as shown in Figure 3.6. The balance equations involving SOFC will change slightly as there is a water cooling cycle that takes the heat

losses at high temperature and delivers them to the preheated ORC. These balance equations and the exergy destruction rate definitions are listed in Table 4.4. Definitions of isentropic turbine efficiency and SOFC efficiency have been mentioned before. Also, exergetic efficiency expressions of the added heat exchanger are the same as the expressions stated earlier for previous systems.

Table 4.4a: A list of balance equations for the preheated Organic Rankine Cycle (ORC).

Component	Mass Balance	Energy Balance
Solid Oxide Fuel Cell (SOFC)	$\dot{m}_1 + \dot{m}_2 = \dot{m}_3,$ $\dot{m}_{25} = \dot{m}_{26}$	$\dot{m}_1 h_1 + \dot{m}_2 h_2 + \dot{m}_{25} h_{25}$ $= \dot{m}_3 h_3 + \dot{m}_{26} h_{26}$ $+ \dot{W}_{elect,1}$
Preheater	$\dot{m}_{13} = \dot{m}_{14},$ $\dot{m}_{28} = \dot{m}_{29}$	$\dot{m}_{13} h_{13} + \dot{m}_{28} h_{28} = \dot{m}_{14} h_{14} + \dot{m}_{29} h_{29}$
Boiler 2	$\dot{m}_{26} = \dot{m}_{27},$ $\dot{m}_{29} = \dot{m}_{30}$	$\dot{m}_{26} h_{26} + \dot{m}_{29} h_{29} = \dot{m}_{27} h_{27} + \dot{m}_{30} h_{30}$
Turbine 3	$\dot{m}_{30} = \dot{m}_{31}$	$\dot{m}_{30} h_{30} = \dot{m}_{31} h_{31} + \dot{W}_{turb3}$
Condenser 1	$\dot{m}_{31} = \dot{m}_{32}$	$\dot{m}_{31} h_{31} = \dot{m}_{32} h_{32} + \dot{Q}_{cond1}$

Table 4.4b: A continued list of balance equations for the preheated Organic Rankine Cycle (ORC).

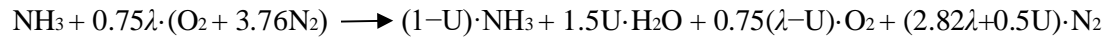
Component	Entropy Balance	Exergy Balance
Solid Oxide Fuel Cell (SOFC)	$\dot{m}_1 s_1 + \dot{m}_2 s_2 + \dot{m}_{25} s_{25}$ $+ \dot{S}_{gen,SOFC}$ $= \dot{m}_3 s_3 + \dot{m}_{26} s_{26}$	$\dot{m}_1 ex_1 + \dot{m}_2 ex_2 + \dot{m}_{25} ex_{25}$ $= \dot{m}_3 ex_3 + \dot{m}_{26} ex_{26}$ $+ \dot{W}_{elect,1} + \dot{E}x_{dest,SOFC}$
Preheater	$\dot{m}_{13} s_{13} + \dot{m}_{28} s_{28}$ $+ \dot{S}_{gen,Preheater}$ $= \dot{m}_{14} s_{14} + \dot{m}_{29} s_{29}$	$\dot{m}_{13} ex_{13} + \dot{m}_{28} ex_{28}$ $= \dot{m}_{14} ex_{14} + \dot{m}_{29} ex_{29}$ $+ \dot{E}x_{dest,Preheater}$
Boiler 2	$\dot{m}_{26} s_{26} + \dot{m}_{29} s_{29}$ $+ \dot{S}_{gen,Boiler2}$ $= \dot{m}_{27} s_{27} + \dot{m}_{30} s_{30}$	$\dot{m}_{26} ex_{26} + \dot{m}_{29} ex_{29}$ $= \dot{m}_{27} ex_{27} + \dot{m}_{30} ex_{30}$ $+ \dot{E}x_{dest,Boiler2}$
Turbine 3	$\dot{m}_{30} s_{30} + \dot{S}_{gen,turb3}$ $= \dot{m}_{31} s_{31}$	$\dot{m}_{30} ex_{30} = \dot{m}_{31} ex_{31} + \dot{W}_{turb3}$ $+ \dot{E}x_{dest,turb3}$
Condenser 1	$\dot{m}_{31} s_{31} + \dot{S}_{gen,cond1}$ $= \dot{m}_{32} s_{32} + \frac{\dot{Q}_{cond1}}{T_{avg,cond1}}$	$\dot{m}_{31} ex_{31} = \dot{m}_{32} ex_{32} + \left(1 - \frac{T_o}{T_{avg,cond1}}\right) \dot{Q}_{cond1}$ $+ \dot{E}x_{dest,cond1}$

4.2.9 Direct Ammonia SOFC-GT Cycle

Now, we need to introduce the direct ammonia injection Solid Oxide Fuel Cell reactions and processes. Two devices have different chemical modelling than what has been discussed earlier, namely the SOFC and the combustor.

- Ammonia-Solid Oxide Fuel Cell (SOFC):

The complete electro-oxidation of ammonia is assumed which makes the overall chemical equation inside SOFC to be



where U is the utilization factor and λ is the excess air factor.

This fuel cell has heat losses and they can be calculated from the energetic efficiency of SOFC which is

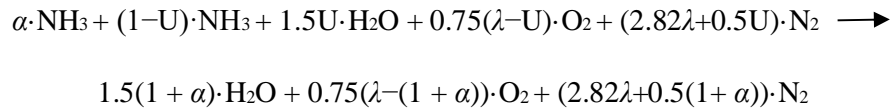
$$\eta_{en,SOFC} = \frac{\dot{W}_{elect,1}}{\dot{m}_1 h_1 + \dot{m}_2 h_2 - \dot{m}_3 h_3} \quad (4.43)$$

and its exergetic efficiency is

$$\eta_{ex,SOFC} = \frac{\dot{W}_{elect,1}}{\dot{m}_1 ex_1 + \dot{m}_2 ex_2 - \dot{m}_3 ex_3} \quad (4.44)$$

- Combustor:

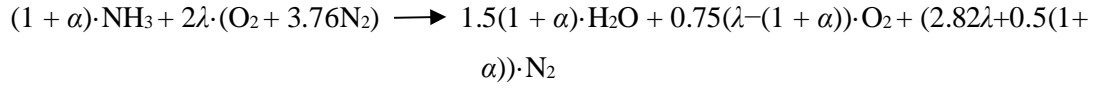
The remaining ammonia is combusted in this device. As before, some fresh charge injection is implemented to increase the inlet turbine temperature. We are assuming adiabatic complete combustion of the reactants. The chemical balance equation of this reaction is



where α is the ratio defined as

$$\alpha = \frac{\dot{m}_{24}}{\dot{m}_2} \quad (4.45)$$

So, the overall chemical balance equation for both SOFC and combustor is



Here, α appears in the final chemical equation since these equations are considered for 1 kmol of ammonia directly injected to the SOFC. The exergetic efficiency of this device is

$$\eta_{ex,combustor} = \frac{\dot{m}_5 ex_5}{\dot{m}_3 ex_3 + \dot{m}_{24} ex_{24}} \quad (4.46)$$

4.2.10 Ammonia-DSU and PEMFC Cycle

The Ammonia Dissociation and Separation Unit (ADSU) and the Proton Exchange Membrane Fuel Cell (PEMFC) are introduced in this cycle. Other components have been discussed previously.

- Ammonia Dissociation and Separation Unit (ADSU):

This unit is assumed to absorb heat from the exhaust gases and uses it to dissociate the hydrogen from the nitrogen of the ammonia fuel stream. No heat losses are assumed, and the unit separates hydrogen and nitrogen streams completely. Other assumptions are no pressure losses and the hydrogen and nitrogen streams leave at the same temperature. The exergetic efficiency of this unit is

$$\eta_{ex,ADSU} = \frac{\dot{m}_{27} ex_{27} + \dot{m}_{29} ex_{29}}{\dot{m}_{10} ex_{10} - \dot{m}_{26} ex_{26} + \dot{m}_{25} ex_{25}} \quad (4.47)$$

The chemical reaction that undergoes within this unit which describes the dissociation process is



One parameter needs to be defined here which is the ratio of ammonia fuel going to the ADSU.

$$\beta = \frac{\dot{m}_{25}}{\dot{m}_2} \quad (4.48)$$

- Proton Exchange Membrane Fuel Cell (PEMFC):

This fuel cell takes in pure hydrogen and fresh air stream to deliver electric power at low temperature. The complete electro-oxidation of hydrogen is assumed which makes the overall chemical equation inside PEMFC to be



where λ_{PEMFC} is the excess air factor for the PEM fuel cell.

This fuel cell has heat losses and they can be calculated from the energetic efficiency of PEMFC which is

$$\eta_{en,PEMFC} = \frac{\dot{W}_{elect,5}}{\dot{m}_{32} h_{32} + \dot{m}_{33} h_{33} - \dot{m}_{34} h_{34}} \quad (4.49)$$

and its exergetic efficiency is

$$\eta_{ex,PEMFC} = \frac{\dot{W}_{elect,5}}{\dot{m}_{32} ex_{32} + \dot{m}_{33} ex_{33} - \dot{m}_{34} ex_{34}} \quad (4.50)$$

The ratio of hydrogen fuel being stored in the tank is defined as

$$\varepsilon = \frac{\dot{m}_{30}}{\dot{m}_{29}} \quad (4.51)$$

Balance equations of these two devices are expressed mathematically in Table 4.5.

4.2.11 Direct Ammonia MAHEFC

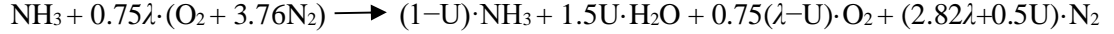
In the last proposed system, two changes are made. Firstly, a new kind of fuel cell replaced the SOFC which is Molten Alkaline Hydroxide Electrolyte Fuel Cell (MAHEFC). This fuel cell operates at intermediate temperatures, unlike SOFC. For this reason, the gas turbine is not present and replaced by a Steam Rankine Cycle (SRC). In this subsection, the modelling of this new kind of fuel cell will be discussed here, which is similar to SOFC but at lower operating temperature. All the other cycles have already been mentioned earlier.

Table 4.5: A list of balance equations for ADSU and PEMFC devices.

Component	Mass Balance	Energy Balance	Entropy Balance	Exergy Balance
Ammonia Dissociation and Separation Unit (ADSU)	\dot{m}_{10} = \dot{m}_{26} , \dot{m}_{25} = \dot{m}_{27} + \dot{m}_{29}	$\dot{m}_{10} h_{10}$ + $\dot{m}_{25} h_{25}$ = $\dot{m}_{26} h_{26}$ + $\dot{m}_{27} h_{27}$ + $\dot{m}_{29} h_{29}$	$\dot{m}_{10} s_{10} + \dot{m}_{25} s_{25}$ + $\dot{S}_{gen,ADSU}$ = $\dot{m}_{26} s_{26}$ + $\dot{m}_{27} s_{27}$ + $\dot{m}_{29} s_{29}$	$\dot{m}_{10} ex_{10} + \dot{m}_{25} ex_{25}$ = $\dot{m}_{26} ex_{26}$ + $\dot{m}_{27} ex_{27}$ + $\dot{m}_{29} ex_{29}$ + $\dot{E}x_{dest,ADSU}$
Proton Exchange Membrane Fuel Cell (PEMFC)	$\dot{m}_{32} + \dot{m}_{33}$ = \dot{m}_{34}	$\dot{m}_{32} h_{32}$ + $\dot{m}_{33} h_{33}$ = $\dot{m}_{34} h_{34}$ + $\dot{W}_{elect,5}$ + $\dot{Q}_{PEMFC,loss}$	$\dot{m}_{32} s_{32} + \dot{m}_{33} s_{33}$ + $\dot{S}_{gen,PEMFC}$ = $\dot{m}_{34} s_{34}$ + $\frac{\dot{Q}_{PEMFC,loss}}{T_{avg,PEMFC}}$	$\dot{m}_{32} ex_{32} + \dot{m}_{33} ex_{33}$ = $\dot{m}_{34} ex_{34} + \dot{W}_{elect,5}$ + $\left(1 - \frac{T_o}{T_{avg,PEMFC}}\right) \dot{Q}_{PEMFC,loss}$ + $\dot{E}x_{dest,PEMFC}$

- Ammonia-Molten Alkaline Hydroxide Electrolyte Fuel Cell (MAHEFC):

The complete electro-oxidation of ammonia is assumed which makes the overall chemical equation inside MAHEFC to be



where U is the utilization factor and λ is the excess air factor.

This fuel cell has heat losses and they can be calculated from the energetic efficiency of MAHEFC which is

$$\eta_{en,MAHEFC} = \frac{\dot{W}_{elect,1}}{\dot{m}_2 HHV_{NH3}} \quad (4.52)$$

where HHV_{NH3} is the high heating value of ammonia which is 22477 kJ kg⁻¹ taken from [26], and its exergetic efficiency is

$$\eta_{ex,MAHEFC} = \frac{\dot{W}_{elect,1} + \dot{m}_{29} ex_{29} - \dot{m}_{28} ex_{28}}{\dot{m}_1 ex_1 + \dot{m}_2 ex_2 - \dot{m}_3 ex_3} \quad (4.53)$$

Since the heat losses are absorbed by a secondary Organic Rankine Cycle, the balance equations in Table 4.6 do not show the rate of heat loss in the fuel cell.

Table 4.6: Balance equations for MAHEFC.

Component	Mass Balance	Energy Balance	Entropy Balance	Exergy Balance
Molten Alkaline Hydroxide Electrolyte Fuel Cell (MAHEFC)	$\dot{m}_1 + \dot{m}_2 = \dot{m}_3,$ $\dot{m}_{28} = \dot{m}_{29}$	$\dot{m}_1 h_1 + \dot{m}_2 h_2 + \dot{m}_{28} h_{28} = \dot{m}_3 h_3 + \dot{W}_{elect,1} + \dot{m}_{29} h_{29}$	$\dot{m}_1 s_1 + \dot{m}_2 s_2 + \dot{m}_{28} s_{28} + \dot{S}_{gen,MAHEFC} = \dot{m}_3 s_3 + \dot{m}_{29} s_{29}$	$\dot{m}_1 ex_1 + \dot{m}_2 ex_2 + \dot{m}_{28} ex_{28} = \dot{m}_3 ex_3 + \dot{m}_{29} ex_{29} + \dot{W}_{elect,1} + \dot{E}x_{dest,MAHEFC}$

4.3 Overall Performance Parameters

Here, we define some important parameters that can help in understanding the performance of the entire proposed systems and their subsystems. Firstly, the total electric power produced is defined as

$$\dot{W}_{elect,total} = \sum_i \dot{W}_{elect,i} \quad (4.54)$$

where i runs from 1 to the total number of output power sources in a system. Next, we define the overall energetic and exergetic efficiencies of the proposed systems in the cooling mode. These definitions are listed in Table 4.7.

We can use the overall exergetic efficiency of a system to evaluate the Environmental Impact (EI) of the system and its Sustainability Index (SI) [75]. The former can be defined as

$$EI = \frac{1}{\eta_{ex,overall}} - 1 \quad (4.55)$$

and the Sustainability Index (SI) as

$$SI = \frac{1}{1 - \eta_{ex,overall}} - 1 \quad (4.56)$$

These two definitions show that if the EI is less than unity, then the system is sustainable ($SI > 1$) and considered to be clean and vice versa. Graphically, they can be represented as shown in Figure 4.1.

Table 4.7: A list of overall energetic and exergetic efficiency expressions for all the proposed systems. ^a

System	Overall Energetic Efficiency	Overall Exergetic Efficiency
1a	$\eta_{en,overall}$ $= \frac{\dot{W}_{elect,total} + \dot{Q}_{HX1} + \dot{m}_{23}(h_{23} - h_{22})}{\dot{m}_{11}HHV_{CH4}}$	$\eta_{ex,overall}$ $= \frac{\dot{W}_{elect,total} + \dot{Q}_{HX1}\left(\frac{T_o}{T_{avg,HX1}} - 1\right) + \dot{m}_{23}(ex_{23} - ex_{22})}{\dot{m}_{11}ex_{11}}$
1b	$\eta_{en,overall}$ $= \frac{\dot{W}_{elect,total} + \dot{Q}_{HX1} + \dot{m}_{18}(h_{18} - h_{17})}{\dot{m}_4HHV_{CH4}}$	$\eta_{ex,overall}$ $= \frac{\dot{W}_{elect,total} + \dot{Q}_{HX1}\left(\frac{T_o}{T_{avg,HX1}} - 1\right) + \dot{m}_{18}(ex_{18} - ex_{17})}{\dot{m}_4ex_4}$
2	$\eta_{en,overall}$ $= \frac{\dot{W}_{elect,total} + \dot{Q}_{evap} + \dot{m}_{23}(h_{23} - h_{22})}{\dot{m}_{11}HHV_{CH4}}$	$\eta_{ex,overall}$ $= \frac{\dot{W}_{elect,total} + \dot{Q}_{evap}\left(\frac{T_o}{T_{avg,evap}} - 1\right) + \dot{m}_{23}(ex_{23} - ex_{22})}{\dot{m}_{11}ex_{11}}$
3	$\eta_{en,overall}$ $= \frac{\dot{W}_{elect,total} + \dot{Q}_{HX1} + \dot{m}_{18}(h_{18} - h_{17})}{\dot{m}_4HHV_{CH4}}$	$\eta_{ex,overall}$ $= \frac{\dot{W}_{elect,total} + \dot{Q}_{HX1}\left(\frac{T_o}{T_{avg,HX1}} - 1\right) + \dot{m}_{18}(ex_{18} - ex_{17})}{\dot{m}_4ex_4}$
4	$\eta_{en,overall}$ $= \frac{\dot{W}_{elect,total} + \dot{Q}_{HX1} + \dot{m}_{18}(h_{18} - h_{17})}{\dot{m}_4HHV_{CH4}}$	$\eta_{ex,overall}$ $= \frac{\dot{W}_{elect,total} + \dot{Q}_{HX1}\left(\frac{T_o}{T_{avg,HX1}} - 1\right) + \dot{m}_{18}(ex_{18} - ex_{17})}{\dot{m}_4ex_4}$
5	$\eta_{en,overall}$ $= \frac{\dot{W}_{elect,total} + \dot{Q}_{evap} + \dot{m}_{18}(h_{18} - h_{17})}{\dot{m}_4HHV_{NH3}}$	$\eta_{ex,overall}$ $= \frac{\dot{W}_{elect,total} + \dot{Q}_{evap}\left(\frac{T_o}{T_{avg,evap}} - 1\right) + \dot{m}_{18}(ex_{18} - ex_{17})}{\dot{m}_4ex_4}$
6	$\eta_{en,overall}$ $= \frac{\dot{W}_{elect,total} + \dot{Q}_{HX1} + \dot{m}_{18}(h_{18} - h_{17}) + \dot{m}_{30}HHV_{H2}}{\dot{m}_4HHV_{NH3}}$	$\eta_{ex,overall}$ $= \frac{\dot{W}_{elect,total} + \dot{Q}_{HX1}\left(\frac{T_o}{T_{avg,HX1}} - 1\right) + \dot{m}_{18}(ex_{18} - ex_{17}) + \dot{m}_{30}ex_{30}}{\dot{m}_4ex_4}$
7	$\eta_{en,overall}$ $= \frac{\dot{W}_{elect,total} + \dot{Q}_{HX1} + \dot{m}_{18}(h_{18} - h_{17})}{\dot{m}_4HHV_{NH3}}$	$\eta_{ex,overall}$ $= \frac{\dot{W}_{elect,total} + \dot{Q}_{HX1}\left(\frac{T_o}{T_{avg,HX1}} - 1\right) + \dot{m}_{18}(ex_{18} - ex_{17})}{\dot{m}_4ex_4}$

a. HHV_{CH4} is the high heating value of methane which is 52225 kJ kg⁻¹ and HHV_{H2} is the high heating value of hydrogen which is 141800 kJ kg⁻¹ both taken from [3].

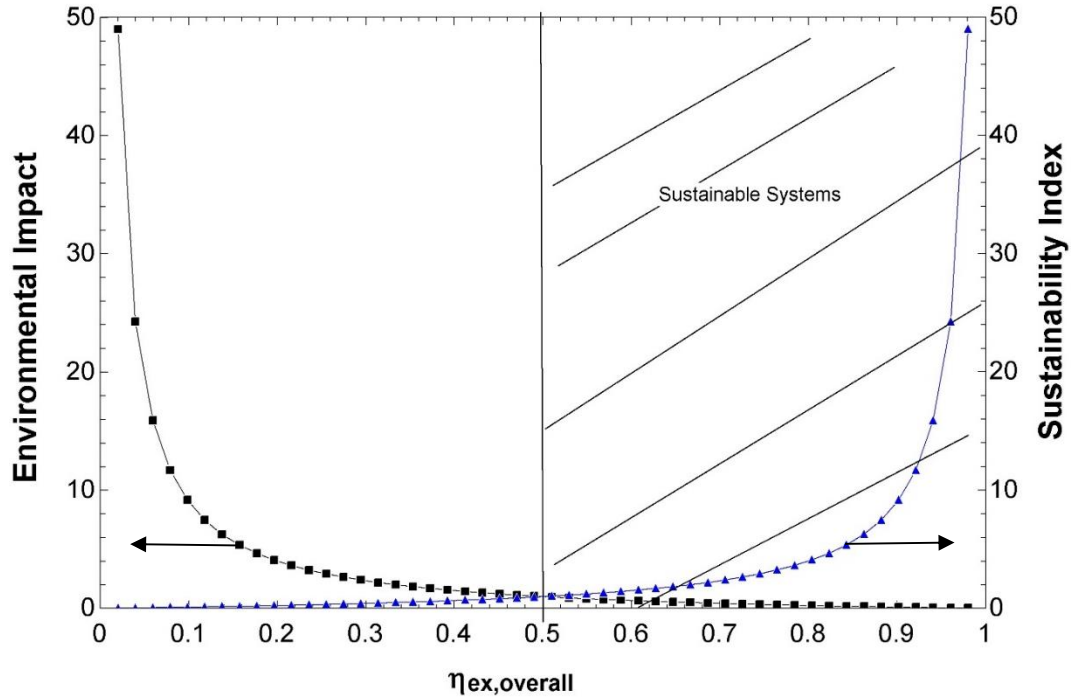


Figure 4.1: Environmental Impact (EI) and Sustainability Index (SI) variation against the overall exergetic efficiency of a system ($\eta_{ex,overall}$) reproduced from [75].

In Table 4.8, we define the energetic and exergetic efficiencies of the subsystems, like SOFC-GT prime cycle, SRC, and NH_3 -ORC. Note that the terms cycle and subsystem are used interchangeably. Note that state point numbers are from the earliest system defined that includes the subsystem.

4.4 Multi-Objective Optimization with Data Visualization

This section explains the newly established sequence of multi-objective optimization methods with data visualization by Seyam et al. [73]. In Figure 4.2, this sequence is displayed in the form of a flow chart that makes it easy to understand. The optimization procedure starts with modelling each integrated system thermodynamically by applying the balance equations mentioned above and then identify some input variables (parameters) as well as objective functions (desired outputs to be optimized). For these inputs and outputs, a large data set is generated using parametric tables in Engineering Equation Solver (EES) software.

Table 4.8: Energetic and exergetic efficiency definitions for the subsystems.

Subsystem	Energetic Efficiency	Exergetic Efficiency
SOFC-GT	$\eta_{en,SOFC,GT} = \frac{\dot{W}_{elect,1} + \dot{W}_{elect,2}}{\dot{m}_{11}HHV_{CH_4}}$	$\eta_{ex,SOFC,GT} = \frac{\dot{W}_{elect,1} + \dot{W}_{elect,2}}{\dot{m}_{11}ex_{11}}$
SRC	$\eta_{en,SRC} = \frac{\dot{W}_{elect,3}}{\dot{m}_9(h_9 - h_{18})}$	$\eta_{ex,SRC} = \frac{\dot{W}_{elect,3}}{\dot{m}_9(ex_9 - ex_{18})}$
NH ₃ -ORC	$\eta_{en,ORC} = \frac{\dot{W}_{elect,4}}{\dot{m}_{16}(h_{16} - h_{17})}$	$\eta_{ex,ORC} = \frac{\dot{W}_{elect,4}}{\dot{m}_{16}(ex_{16} - ex_{17})}$
PPCI engine	$\eta_{en,engine} = 1 - \frac{1}{r_v^{\gamma-1}}$	$\eta_{ex,engine} = \frac{\dot{W}_{net,engine}}{\dot{m}_3ex_3 + \dot{m}_{24}ex_{24} - \dot{m}_5ex_5}$
SOFC-PPCI-GT	$\eta_{en,SOFC,PPCI,GT} = \frac{\dot{W}_{elect,1} + \dot{W}_{elect,2} + \dot{W}_{elect,3}}{\dot{m}_4HHV_{CH_4}}$	$\eta_{ex,SOFC,PPCI,GT} = \frac{\dot{W}_{elect,1} + \dot{W}_{elect,2} + \dot{W}_{elect,3}}{\dot{m}_4ex_4}$
Preheated-ORC	$\eta_{en,P,ORC} = \frac{\dot{W}_{elect,4}}{\dot{m}_{13}(h_{13} - h_{14}) + \dot{m}_{26}(h_{26} - h_{27})}$	$\eta_{ex,P,ORC} = \frac{\dot{W}_{elect,4}}{\dot{m}_{13}(ex_{13} - ex_{14}) + \dot{m}_{26}(ex_{26} - ex_{27})}$
Ammonia-SOFC-GT	$\eta_{en,SOFC,GT} = \frac{\dot{W}_{elect,1} + \dot{W}_{elect,2}}{\dot{m}_4HHV_{NH_3}}$	$\eta_{ex,SOFC,GT} = \frac{\dot{W}_{elect,1} + \dot{W}_{elect,2}}{\dot{m}_4ex_4}$
ADSU-PEMFC	$\eta_{en,ADSU,PEMFC} = \frac{\dot{W}_{elect,5} + \dot{W}_{elect,6} + \dot{m}_{30}HHV_{H_2}}{\dot{m}_{10}(h_{10} - h_{26}) + \dot{m}_{25}HHV_{NH_3}}$	$\eta_{ex,ADSU,PEMFC} = \frac{\dot{W}_{elect,5} + \dot{W}_{elect,6} + \dot{m}_{30}ex_{30}}{\dot{m}_{10}(ex_{10} - ex_{26}) + \dot{m}_{25}ex_{25}}$
MAHEFC	$\eta_{en,MAHEFC} = \frac{\dot{W}_{elect,1}}{\dot{m}_2 HHV_{NH_3}}$	$\eta_{ex,MAHEFC} = \frac{\dot{W}_{elect,1} + \dot{m}_{29}ex_{29} - \dot{m}_{28}ex_{28}}{\dot{m}_1ex_1 + \dot{m}_2ex_2 - \dot{m}_3ex_3}$

In order to see explicit mathematical relations between the chosen parameters and the desired outputs, the data set is entered as inputs to Eureka program where this piece of software runs the multi-objective genetic programming optimization method to produce explicit mathematical expressions that describe the objective functions. This optimization method strives to produce models that are optimum in terms of maximum accuracy and minimum complexity level. Usually, as accuracy increases, complexity increases with it. Here, we determine the accuracy of a model by measuring the correlation coefficient (R^2) of the model against the generated data set. For the complexity level, it depends on the number and level of complexity of chosen formula building-blocks existing in the model.

Each block (mathematical operation) has designated complexity level which is defined in the Eureka program. The chosen formula building-blocks are listed in Table 4.9. Genetic programming optimization is a type of evolutionary algorithm that starts with a population of possible models. Then, it applies crossover and mutation operators to produce a second generation of these models. The crossover operator takes two models and randomly switches the order of mathematical operations at a certain point to produce new two off-springs (models) for the second generation. The mutation operator causes changes within each off-spring with a predetermined probability by changing a mathematical operation within the model (off-spring). After that, these new models are evaluated in terms of their accuracy and complexity level to determine their fitness. The highest fitness models are presented as part of the Pareto front of the accuracy versus complexity plot, which are the models that are not dominated by any other model within the current population. These non-dominated models are copied through the generations as long as no new model dominates their fitness value. This process is repeated until a predetermined stopping criterion is satisfied. Lastly, the decision of choosing a single model to represent an objective function of the integrated system is made by the user. This decision comes with the consideration of the accuracy of the model and its level of complexity. In this optimization study, the stopping criterion for models search is chosen to be one of the confidence parameters of the GP search which is named Percent converged. When its value reaches 50%, the search is stopped. In addition, for the training process, half of the data set is used for training while the other half is used for fitness evaluations. All the data sets generated from EES have 641 points.

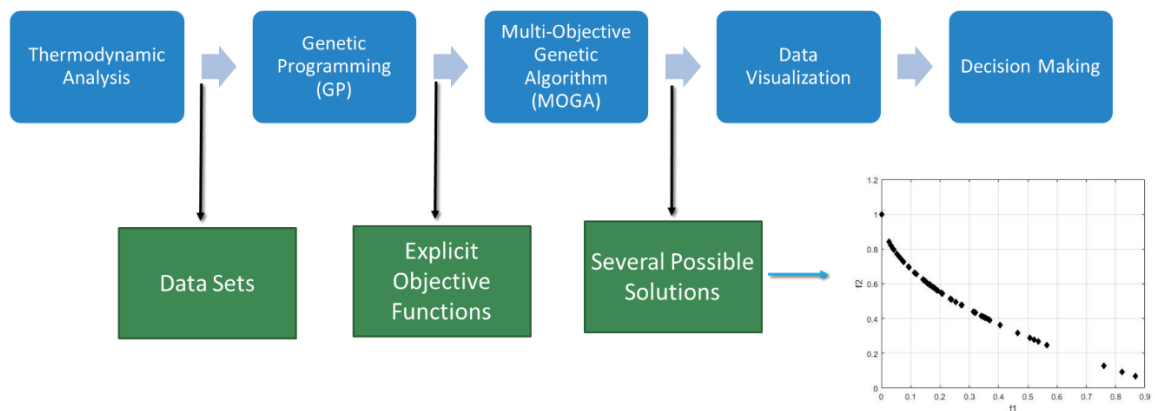


Figure 4.2: Flow chart of the multi-objective optimization methods implemented in optimizing the integrated systems.

Table 4.9: List of chosen formula building-blocks for multi-objective genetic programming and their complexity level as defined in the Eureka program.

Mathematical Operation	Complexity Level
Constant	1
Input Variable	1
Addition	1
Subtraction	1
Multiplication	1
Division	2
Exponential	4
Power	5

After selecting mathematical models to describe the desired objective functions, these functions with the selected parameters are given as inputs to the Multi-Objective Genetic Algorithm (MOGA). This algorithm is also a type of an evolutionary algorithm which includes the reproduction of new off-spring solutions by the crossover and mutation operators. Then, these solutions are evaluated for their fitness and ranked accordingly. The algorithm implemented in this study is the Non-dominated Sorting Genetic Algorithm II (NSGA-II) which was introduced by Deb et al. in 2002 [76]. The fitness of solutions in the population is determined in two steps. Firstly, the non-dominated solutions in terms of either maximizing or minimizing the objective functions are classified and assigned a value of Rank 1, then these are separated from the population. Next, the non-dominated solutions of the remaining population are given Rank 2 and this is repeated until all the solutions are assigned a rank number. Secondly, within each rank, the solutions are sorted according to a parameter called the crowding distance. This distance is calculated by measuring the difference in objective function values between a given solution and its closest neighbors. The higher the crowding distance of a given solution, the better its fitness as this encourages diversity in solutions and makes the Pareto front wider. Similarly, this search process continues until a stopping criterion is reached. MATLAB has been used to implement this evolutionary algorithm. The specifications of the algorithm are given in MATLAB documentations. The crossover operator is chosen to be “intermediate” with Ratio = 1. The mutation operator is adaptive feasible, which means it changes as the algorithm and

solutions evolve. The population size is 50 and the stopping criteria are either number of generations reaches 100 times of the number of variables (i.e. 3 variables means 300 generations maximum), or the average spread change in the Pareto front is less than the function tolerance which is predetermined by MATLAB software at a value of 1×10^{-6} .

The resulted Pareto front from MOGA is a list of non-dominated solutions that are hard to compare and see the relations between the maximization and minimization of the desired objective functions. To resolve this issue, parallel coordinates is used which is a data visualization technique. It generates a plot that has two axes. The horizontal axis is a discrete axis that shows the objective functions. The vertical axis is continues and presents the normalized values of the objective functions. The normalized values are evaluated as follows

$$N = \frac{X - \mu}{\sigma} \quad (4.57)$$

where X is the actual value of the objective function of a given solution, μ is the mean of the objective function over all the Pareto front solutions, and σ is its standard deviation. The different solutions are colored differently and given an order from 1st, 2nd...etc. The final step of any optimization problem is to make a decision to choose a specific optimum solution for the operation of the integrated system.

Now, for the eight proposed integrated systems, four optimization problems are undertaken with different parameters, constraints, and objective functions. To start with, system 1a parameters with their constraint are shown in Table 4.10. The objective functions selected for the first optimization problem are the overall exergetic efficiency, SOFC power output, and GT power output. It is desired to maximize the efficiency which is natural and to maximize the SOFC power output. However, the GT power output needs to be minimized. The choice of these objective functions comes from the feasibility study of employing hybrid SOFC-GT power systems in railway applications conducted by Martinez et al. [19]. One of the main issues mentioned in this study is the power split between SOFC and GT. This heavily affects the packaging feasibility of this hybrid system. Since almost 89% of the power produced is coming from the SOFC and GT, the bottoming Steam and Organic Rankine cycles are ignored in terms of sizing. Another reason is that the volumetric power

density of such Rankine cycles is around 0.2018 W cm^{-3} [77]. The maximization of SOFC power makes the space requirements of the integrated system less since it has a high volumetric power density of 1.00 W cm^{-3} as reported in [19]. Also, they conducted a survey of possible gas turbines and found that the volumetric power density of such devices is extremely low in the range of $0.048 - 0.050 \text{ W cm}^{-3}$. Current diesel compression engines also have a low volumetric power density of 0.063 W cm^{-3} . Using SOFC-GT with proper power split could reduce the space requirements compared to the current technology of compression engines. Another advantage of using the redirecting of the mass flow rate of fuel to the combustor (α -parameter) is increasing the turbine inlet temperature as will be shown later. According to Martinez et al. [19], when choosing gas turbines, they need to be with higher power ratings than the actual operating power load in the hybrid SOFC-GT system. This is because the inlet temperature of the gas turbine will be lower than the design point. However, this issue can be resolved by injecting a proper amount of fuel directly to the combustor to maintain the design temperature level of the gas turbine. Going for higher rating gas turbines requires more space allocation, but if a gas turbine is selected with a power rating that meets the actual power load as estimated for the integrated system, then less space is required and the system becomes more feasible.

Table 4.10: List of parameters and their constraints for the optimization problem of system 1a.

Parameter (Variable)	Constraint
Compression ratio of air (r_p)	$4 < r_p < 15$
Excess air factor (λ)	$1.3 < \lambda < 2.8$
α -parameter	$0 < \alpha < 0.3$
Total power production rate	3100 kW

For the optimization of system 3, the parameters and their constraints are listed in Table 4.11. The selected objective functions are the overall exergetic efficiency, SOFC power output, PPCI engine power output, and GT power output. The optimization problem is to maximize both the efficiency and the SOFC power output while minimizing the PPCI engine and GT power outputs. These are for the same reasons mentioned for the optimization problem of system 1a. We are trying to make the power split between these power producing devices appropriate for feasible packaging.

Table 4.11: List of parameters and their constraints for the optimization problem of system 3.

Parameter (Variable)	Constraint
Compression ratio of air (r_p)	$1.2 < r_p < 11$
Engine compression ratio (r_v)	$12 < r_v < 20$
α -parameter	$0.1 < \alpha < 0.35$

System 6 is initially optimized for its packaging by adopting the optimum operation parameters values from the optimization of system 1a as both systems have similar SOFC-GT subsystem designs. In this system, the PEM fuel cell power output is wanted to be maximized as it supports feasible packaging because such type of fuel cell has the high volumetric power density of 3.1 W cm^{-3} [16]. Other objective functions are the overall exergetic efficiency and the rate of hydrogen production and storage in the tank. The optimization variables and their corresponding constraints are listed in Table 4.12.

Table 4.12: List of parameters and their constraints for the optimization problem of system 6.

Parameter (Variable)	Constraint
β -parameter	$0 < \beta < 0.5$
ε -parameter	$0 < \varepsilon < 0.5$
PEMFC energetic efficiency ($\eta_{en,PEMFC}$)	$0.4 < \eta_{en,PEMFC} < 0.6$

Finally, for system 7, there is only one objective function to be maximized which is the overall exergetic efficiency. This is because there are no power devices with low volumetric power density, such as gas turbines and compression engines. The method of optimization implemented here is single-objective Genetic Algorithm (GA). This algorithm uses the same operators of the MOGA, but the fitness evaluation involves neither ranking nor crowding distance. The solutions are sorted according to their fitness value which is evaluated by the objective function. If this function is wanted to be maximized, then the best fit solution has the highest value of objective function output. Also, no need for data visualization and decision making steps here as there is only a single global optimum solution. EES has been used for the implementation of this algorithm with the following specifications. Population size is 50, the mutation rate is 0.10, and the stopping criterion is maximum number of generations is 110. Two optimization variables are selected, namely the fuel cell operating temperature which is linearly constrained between

523 K and 723 K. The second variable is the SRC boiler pressure (pressure at state 12) that is also linearly constrained between 2000 and 4500 kPa.

4.5 Fuel Costs and CO₂ Emissions Analyses: A Case Study

The last section in this chapter is concerned with the case study chosen to compare fuel costs and CO₂ emissions between a typical diesel-electric engine and the proposed integrated systems at their reference cases. The case study is chosen for the duty cycle of an intercity passenger train. The data and values used for this case study will be mentioned later in the case study part of the results and discussions chapter. Here, we mention how these data are used to calculate the fuel costs and CO₂ emissions for each system. Starting with calculating the brake specific fuel consumption for every integrated system, it is by this expression

$$bsfc = \frac{\dot{m}_{fuel}}{\dot{W}_{elect,total}} \quad (4.58)$$

Next, the energy consumed by the passenger train in a duty cycle is calculated by multiplying the power at a selected notch by the time in hours at the corresponding notch, then summing all the values to get the amount of energy consumed per duty cycle. By knowing this energy consumption and the market fuel costs of diesel, methane, and ammonia, the fuel cost for each system is found by

$$\begin{aligned} \text{Fuel Cost} \left(\frac{\$CAD}{\text{Duty cycle}} \right) &= \text{Fuel Cost} \left(\frac{\$CAD}{kg} \right) \times \text{Energy Consumed} \left(\frac{kWh}{\text{Duty cycle}} \right) \\ &\times bsfc \left(\frac{kg}{kWh} \right) \end{aligned} \quad (4.59)$$

Next, carbon dioxide emissions for each system are estimated by calculating the mass ratio of the CO₂ component of the total mass of the exhaust gases mixture (x_{CO_2}), and the mass ratio of the fuel component of the total mass of input streams, namely air and fuel (x_{fuel}). Therefore, the CO₂ emissions are found as

$$\begin{aligned} CO_2 \text{ emissions} \left(\frac{kg}{\text{Duty cycle}} \right) &= \frac{x_{CO_2}}{x_{fuel}} \times \text{Energy Consumed} \left(\frac{kWh}{\text{Duty cycle}} \right) \times bsfc \left(\frac{kg}{kWh} \right) \end{aligned} \quad (4.60)$$

For the diesel-electric engine and methane-based systems, the values of CO₂ mass ratio are 0.2028 (at stoichiometric conditions for C₁₂H₂₃ diesel fuel) and 0.1284 (at reference cases for methane fuel), respectively. Also, the fuel mass ratios are 0.06414 for diesel and 0.04701 for methane. Ammonia-based systems have zero CO₂ emissions since the fuel used has no carbon in it.

Chapter 5: Results and Discussion

This chapter presents the results of the thermodynamic modelling of the eight proposed systems. This modelling has been executed by using the Engineering Equation Solver (EES) software developed by F-Chart Software [78]. For every proposed integrated system, a reference case is presented, then parametric studies are given and discussed to understand the behavior of the proposed system under varying conditions, like the ambient temperature, the compression ratio of the compressor and other related parameters. Next, the multi-objective optimization of these systems with appropriate visualization is given. After that, a comparative study of all the systems is provided. There are two main parts to this study. Firstly, we will compare the energetic and exergetic efficiencies of all the systems at their selected reference cases and their optimum operating points. Secondly, a case study of the steady-state operation of each system is presented at its reference case. This case study compares fuel costs and CO₂ emissions for the duty cycle of an intercity passenger locomotive in Canada. Before going the results of each system, Table 5.1 lists the common parameters chosen for the thermodynamic analysis of all the proposed systems at their reference cases. The operation mode of the system will be under a cooling load of 105 kW for a 12-coach locomotive.

Table 5.1: Common parameters for the thermodynamic analysis at the reference case for all the proposed integrated systems.

Parameter	Value
Ambient temperature	303 K
Ambient pressure	1 atm
α	0.1765
Utilization factor (U)	0.85
Excess air factor (λ)	1.4
SOFC efficiency	0.65
Desired indoors temperature	293 K
Air compression ratio	4
Total power required by the train at maximum load [2]	3100 kW
Cooling load	105 kW
Hot water production rate	0.00625 kg s ⁻¹

5.1 System 1a Results

Starting with system 1a, named SOFC-GT-SRC-ORC system with a reversible heat pump and with a parallel arrangement of the fuel and air regenerators, the advantages of using a reversible heat pump for satisfying the space heating and cooling demands of a locomotive are discussed. Next, the thermodynamic results are presented at a selected reference case for operating a passenger train at maximum load. Model validation is presented to show the precision and accuracy of the thermodynamic analysis performed on this system. Fourthly, parametric studies are given for a deeper understanding of this system when certain parameters of the system are changed.

5.1.1 Reversible Type Heat Pump Advantages in Railway Applications

Space heating and cooling for a locomotive is an important energy issue that is concerned with the comfort of its passengers. There are several options for the delivery of space heating and cooling to the inside of a locomotive, such as a furnace with air conditioning, absorption chiller with a heat exchanger, and a reversible heat pump. In this study, we choose the latter because it provides cost savings over the furnace option and requires less space and weight than an absorption chiller. Martinez et al. [18,19] have presented a feasibility study for using a SOFC-GT hybrid system for a locomotive. Now, we justify our selection of the reversible heat pump over other possible options for multigeneration in a locomotive.

Comparing the furnace with air conditioning option with a reversible heat pump [79], the annual energy costs to operate a furnace with air conditioning in Toronto ranges between \$1,082 CAD and \$1,854 CAD. On the other hand, an air-source reversible heat pump with electrical resistance as backup costs annually between \$529 CAD and \$873 CAD. This clearly shows significant financial savings when choosing a reversible heat pump for space heating and cooling in a locomotive. Next, using an absorption chiller with a heat exchanger is a viable option in terms of using waste heat to produce either cooling or heating effects. In railway applications, reducing space and weight requirements of the different devices on board is an important design concern. Table 5.2 presents a clear indication that using a reversible heat pump requires almost 4 times less space and has much less operating weight than an absorption chiller. It is noted that the weight and space

for the heat exchanger to provide space heating is not included in the table. This means that additional space and weight for the absorption chiller with a heat exchanger option is needed, unlike the reversible heat pump which operates in two modes without any additional equipment. Furthermore, the reduction of weight from 2993.7 kg, for an absorption chiller, to 1354.5 kg, for a reversible heat pump, causes fuel savings since the overall weight of a locomotive is less.

Table 5.2: Space and weight requirements for a reversible heat pump and an absorption chiller.

Space Cooling Option	Cooling Capacity (kW)	Indoor Unit Space (m ³)	Operating Weight (kg)
Reversible HP (Cooling mode) [80]	105	1.574	1354.5
Absorption Chiller (LT 3) [81]	105	6.673	2993.7

5.1.2 Reference Case Results

From Table 5.3, it is seen that the total power generated, 3113 kW, is enough to operate a passenger train at maximum power according to [2]. Most of the power produced, 2194 kW, is by the Solid Oxide Fuel Cell (SOFC) which is reasonable because 85% of the fuel is consumed by this device. It is followed by the Gas Turbine (GT), Turbine 2, and Turbine 3, producing power at 593.8 kW, 237.3 kW, and 87.76 kW, respectively. In addition, the energetic and exergetic efficiency values of the subsystems are calculated. SOFC-GT primary cycle has a reasonable value for the energetic efficiency that is 59.32% and it is lower than the SOFC conversion efficiency of 65% due to the regenerators. SOFC-GT exergetic efficiency of 59.35% is very close to its energetic value. SRC and ORC subsystems have energetic efficiencies of 21.44% and 10.52%, respectively. Their corresponding exergetic efficiency values are higher than the energetic at 46.38% and 63.56%, respectively. From Figure 5.1, we notice that the ORC exergetic efficiency is higher than SRC because the Organic Rankine cycle is using an intermediate to low heat source, unlike the SRC. Looking at the overall energetic efficiency of the system (68.50%), it is higher than the SOFC efficiency (65%) because the integrated system is producing multiple outputs at the same time. For the overall exergetic efficiency of 66.35%, it is higher than 50% which is the minimum value for considering this system to be a sustainable one according to Figure 4.1. This is also shown in the values of *EI* and *SI*, 0.5072 and

1.971, respectively. Some interesting observation of using a reversible heat pump for a cooling duty is that the overall exergetic efficiency is only lower by 2% than the overall energetic efficiency. This is due to the fact that the coefficient of performance of regular heat pumps is always higher than unity, unlike absorption chillers. So, only a small amount of power is needed to satisfy the cooling load of 105 kW.

Table 5.3: Calculated parameters for the thermodynamic analysis of system 1a.

Parameter	Value
SOFC electric power	2194 kW
Gas Turbine (GT) electric power	593.8 kW
Turbine 2 electric power	237.3 kW
Turbine 3 electric power	87.76 kW
Total electric power of the integrated system	3113 kW
Total power required by the train at maximum load	3100 kW
HX 1 heat transfer rate (cooling mode)	105 kW
SOFC-GT energetic efficiency	59.32%
SOFC-GT exergetic efficiency	59.35%
SRC energetic efficiency	21.44%
SRC exergetic efficiency	46.38%
ORC energetic efficiency	10.52%
ORC exergetic efficiency	63.56%
Overall energetic efficiency	68.50%
Overall exergetic efficiency	66.35%
Environmental Impact (<i>EI</i>)	0.5072
Sustainability Index (<i>SI</i>)	1.971

Table 5.4 presents the thermodynamic properties of the state points of the integrated system. It interesting to look at the stream temperature leaving the Combustor, namely state 5. The temperature is 1436 K which is higher than usual SOFC-GT systems due to the redirecting of fuel to the Combustor. The α -parameter characterizes this redirecting behavior. At this reference case, it has a value of 0.1765. It is expected that as this value increases, the state 5 temperature increases. However, if α is zero (all fuel stream goes through the SOFC), then the Gas Turbine (GT) receives a lower temperature stream which

reduces the amount of power production at this device. A study on this parameter is given in the next subsection.

From Table 5.5, the turbines and the compressors seem to have exergetic efficiency values higher than 80% mainly because they are assumed to be adiabatic. On the other hand, SOFC has lower exergetic efficiency of 72.85% as there are heat losses in this device. When comparing the exergy destruction rates of the major components of the system in order to identify the locations of possible improvement as they are shown in Figure 5.2, it is clear that both the SOFC and Combustor devices are the highest at 1286 kW, 380.2 kW, respectively. They are followed by the Boiler at 75.63 kW and air compressor at 53.35 kW. One possibility of reducing the exergy destruction rate at the fuel cell is by utilizing the high-temperature heat losses to run a power cycle, like an Organic Rankine Cycle. Another option is to store it in a thermal energy storage device for later use as a source for space heating.

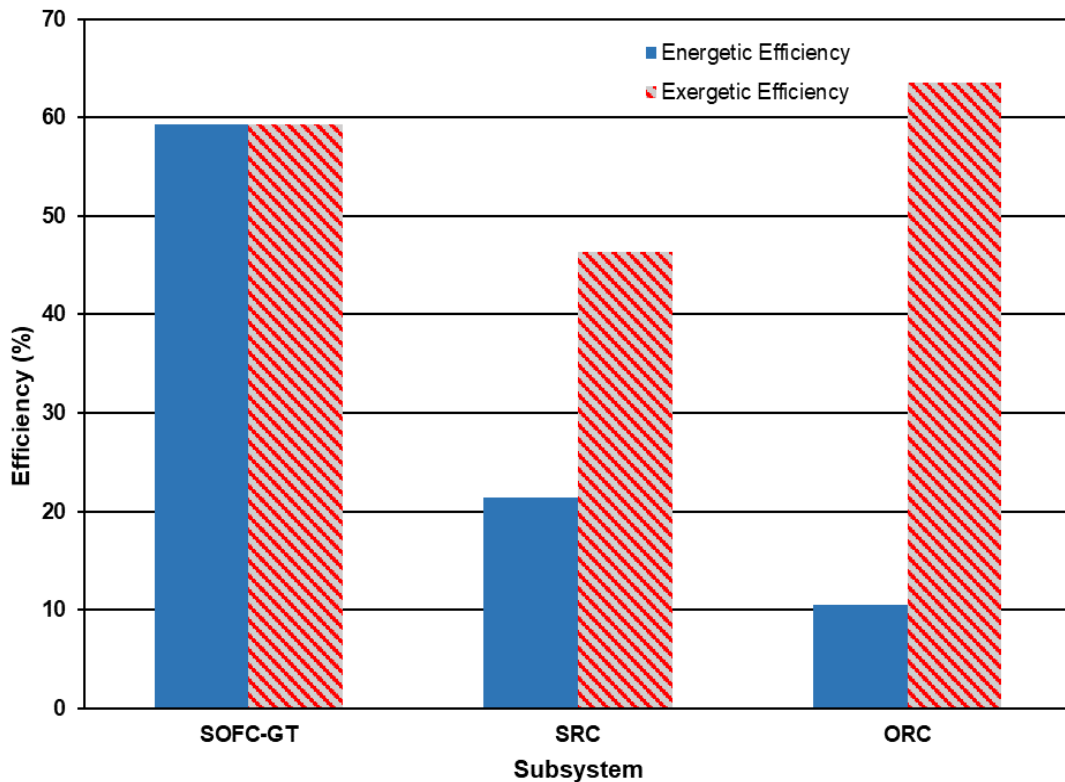


Figure 5.1: Comparison of the energetic and exergetic efficiencies between the subsystems of system 1a.

Table 5.4: State points and their thermodynamic values of system 1a.

State #	Fluid	Temperature (K)	Pressure (kPa)	Specific Enthalpy (kJ kg ⁻¹)	Specific Entropy (kJ kg ⁻¹ K ⁻¹)	Specific Exergy (kJ kg ⁻¹)	Mass Flow Rate (kg s ⁻¹)
1	Air	765.8	400	486.4	6.276	311.8	2.162
2	Methane	900	400	-2685	14.3	53133	0.0765
3	Exhaust+methane+air	950	400	-1130	7.841	481.1	2.239
4	Methane	900	400	-2685	14.3	53133	0.0135
5	Exhaust gases	1436	400	-1139	8.437	968.9	2.027
6	Exhaust gases	1071	100	-1631	8.457	471.2	2.027
7	Air	303	100	5.024	5.716	0	2.162
8	Air	486.6	400	191.1	5.797	161.4	2.162
9	Exhaust gases	824.2	100	-1946	8.123	257.4	2.027
10	Exhaust gases	1436	400	-1139	8.437	968.9	0.2252
11	Methane	303	400	-4639	10.93	52198	0.09
12	Exhaust gases	844.9	400	-1920	7.74	399.4	0.2252
13	Methane	900	400	-2685	14.3	53133	0.09
14	Water	363.3	3500	380.3	1.192	25.61	0.4
15	Water	641.2	3500	3148	6.728	1116	0.4
16	Water	363.1	70	2463	6.938	367.3	0.4
17	Water	363.1	70	376.8	1.192	22.06	0.4
18	Exhaust gases	358	100	-2492	7.154	4.931	2.027
19	Exhaust gases	844.9	100	-1920	8.154	273.8	0.2252
20	Exhaust gases	409.4	100	-2435	7.303	16.9	2.252
21	Exhaust gases	408.9	100	-2435	7.302	16.74	2.252
22	Water	303	120	125.2	0.4347	0.02009	0.00625
23	Water	353	120	334.4	1.074	15.6	0.00625
24	R134a	268	242.1	247.4	0.9344	23.07	0.8251
25	R134a	334.5	1249	290.1	0.9603	57.97	0.8251
26	R134a	321	1249	120.2	0.4317	48.13	0.8251
27	R134a	268	242.1	120.2	0.4596	39.68	0.8251
28	Ammonia	306.8	4000	360.2	1.533	351.4	0.7456
29	Ammonia	352.2	4000	1479	4.761	492.5	0.7456
30	Ammonia	306	1271	1357	4.806	356.7	0.7456
31	Ammonia	306	1271	355.6	1.533	346.8	0.7456

5.1.3 Model Validation

For model validation, we choose the energetic efficiency of the SOFC-GT subsystem at this reference case. Table 5.6 presents a comparison between the present model value of 59.32% and previously published values at operating conditions close to this reference case in terms of compression ratio, isentropic efficiencies, and energetic SOFC efficiency. There is a good agreement between the present model result and previously published

modelling studies. However, this agreement only shows the precision of the present model. To measure the accuracy of the present model, we compare it to an experimental result of a demonstration power plant built in California [82]. The demonstration was operated on a pressure of 3 atm which is close to our reference case of 4 atm. The calculated difference between this experimental result and our present model is 12.2% which is acceptable for validating the accuracy of this model. Therefore, both the precision and accuracy of the present model have been validated using earlier models and experimental results. Another point that supports the validation of the proposed models is that the conservation laws of mass and energy and the second law of thermodynamics are all satisfied for every component of the proposed integrated systems.

Table 5.5: Exergy destruction rates and exergetic efficiencies of major components of system 1a.

Component	Exergy Destruction Rate (kW)	Exergetic Efficiency
Air Compressor	53.35	86.74%
SOFC	1286	72.85%
Combustor	380.2	78.81%
Gas Turbine (GT)	12.49	98.76%
Boiler	75.63	85.22%
Turbine 2	25.41	91.51%
HX 3	32.89	76.19%
Turbine 3	10.03	90.09%
Heater	0.2417	28.72%
Compressor 2	6.461	81.67%
HX 1	0.2536	96.88%

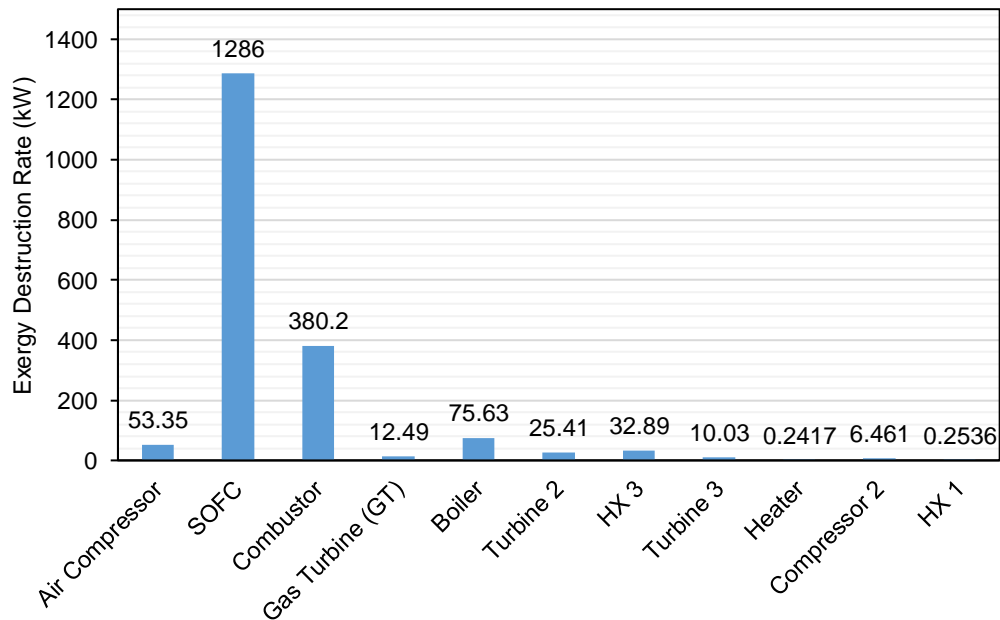


Figure 5.2: Comparison of exergy destruction rates of major components of system 1a.

Table 5.6: Present model comparison of SOFC-GT energetic efficiency with previously published results.

Source of Study	Type of Study	Reported SOFC-GT Energetic Efficiency	Difference with Present Model
Present model	Modelling	59.32%	0%
Meratizaman et al. [53]	Modelling	64%	7.89%
Shirazi et al. [83]	Modelling	61.3%	3.34%
Chan et al. [84]	Modelling	58.5%	-1.38%
Saisirirat [85]	Modelling	58%	-2.23%
Hosseini et al. [86]	Modelling	50%	-15.7%
Leeper [82]	Experimental	52.1%	-12.2%

5.1.4 Parametric Study Results

Additionally, parametric studies of the proposed system are conducted to see how changing several variables can affect the overall energetic and exergetic efficiencies as well as the efficiencies of the subsystems, namely SOFC-GT, SRC, and NH₃-ORC. Electric power output values from the fuel cell, GT, Turbine 2, and Turbine 3 are also studied under the variation of some variables. The variables chosen for this study are the compression ratio of air, the ambient temperature, the excess air factor (λ), and the α -parameter defined earlier. Such a study helps designers and engineers understand the proposed system better during operation.

In Figure 5.3, varying the compression ratio in the air compressor shows nonlinear behaviors for both types of efficiency for the overall system and subsystems except the NH₃-ORC which is not affected by the compression ratio. This makes sense as it is not directly related to the Bryton cycle. Increasing the compression ratio enhances the efficiencies of the overall system and SOFC-GT subsystem. The system is optimized at a compression ratio of 9.0 where the energetic and exergetic efficiencies of the integrated system are 69.68% and 67.37%, respectively, and for the SOFC-GT subsystem, they are 61.35% and 61.23%, respectively. On the other hand, the SRC subsystem is affected negatively as it receives lower temperatures from the exit of the SOFC-GT subsystem. This is because the pressure drop across the gas turbine is high which means the exit turbine temperature is low at constant isentropic efficiency. At a compression ratio of 9.0, the SRC subsystem reaches minimum values of its energetic and exergetic efficiencies of 20.18%

and 45.14%, respectively. The NH₃-ORC energetic and exergetic efficiencies remain constant at 10.52% and 63.56%, respectively.

In Figure 5.4, the electric power outputs of the integrated system and its subsystems are presented separately to provide more details. We see that the power output of the SOFC is not affected by the variation of compression ratio and stays at 2194 kW, while the gas turbine net power output reaches a maximum of 689.4 kW at a compression ratio of 9.0. This means that the integrated system performance is mostly determined by the performance of the Bryton cycle, not any other subsystem. The SRC power output reaches a minimum of 204.1 kW at this compression ratio. NH₃-ORC has a constant power output of 81.22 kW and only has small changes over the span of compression ratio values. Overall, the power output behaviors agree and confirm the above discussion on the energetic and exergetic efficiencies.

In Figure 5.5, the ambient temperature is varied to see its effects on the energetic and exergetic efficiencies of the integrated system and its subsystems. As the ambient temperature increases, the energetic and exergetic efficiencies of the overall integrated system, SOFC-GT subsystem, and NH₃-ORC subsystem slightly decrease. At a temperature of 313 K, they reach their lowest values. For the integrated system, these values are 68.15% and 66.08%, respectively. For the SOFC-GT subsystem, they are 59.03% and 59.05%, respectively. For the NH₃-ORC, they are 8.323% and 60.34%, respectively. However, the SRC energetic and exergetic efficiencies increase as the ambient temperature increases. They are maximized at a temperature of 313 K where they reach values of 22.03% and 48.95%, respectively.

In Figure 5.6, the power outputs of the overall system, Bryton cycle, and NH₃-ORC subsystem are decreasing as the ambient temperature increases. This agrees well with the evaluated efficiencies mentioned earlier. The power outputs at their lowest point, when the ambient temperature is 313 K, are 3097 kW, 580.2 kW, and 71.2 kW, respectively. The SOFC electric power remains unaffected at a value of 2194 kW. The SRC subsystem produces its maximum power output of 251.6 kW at 313 K.

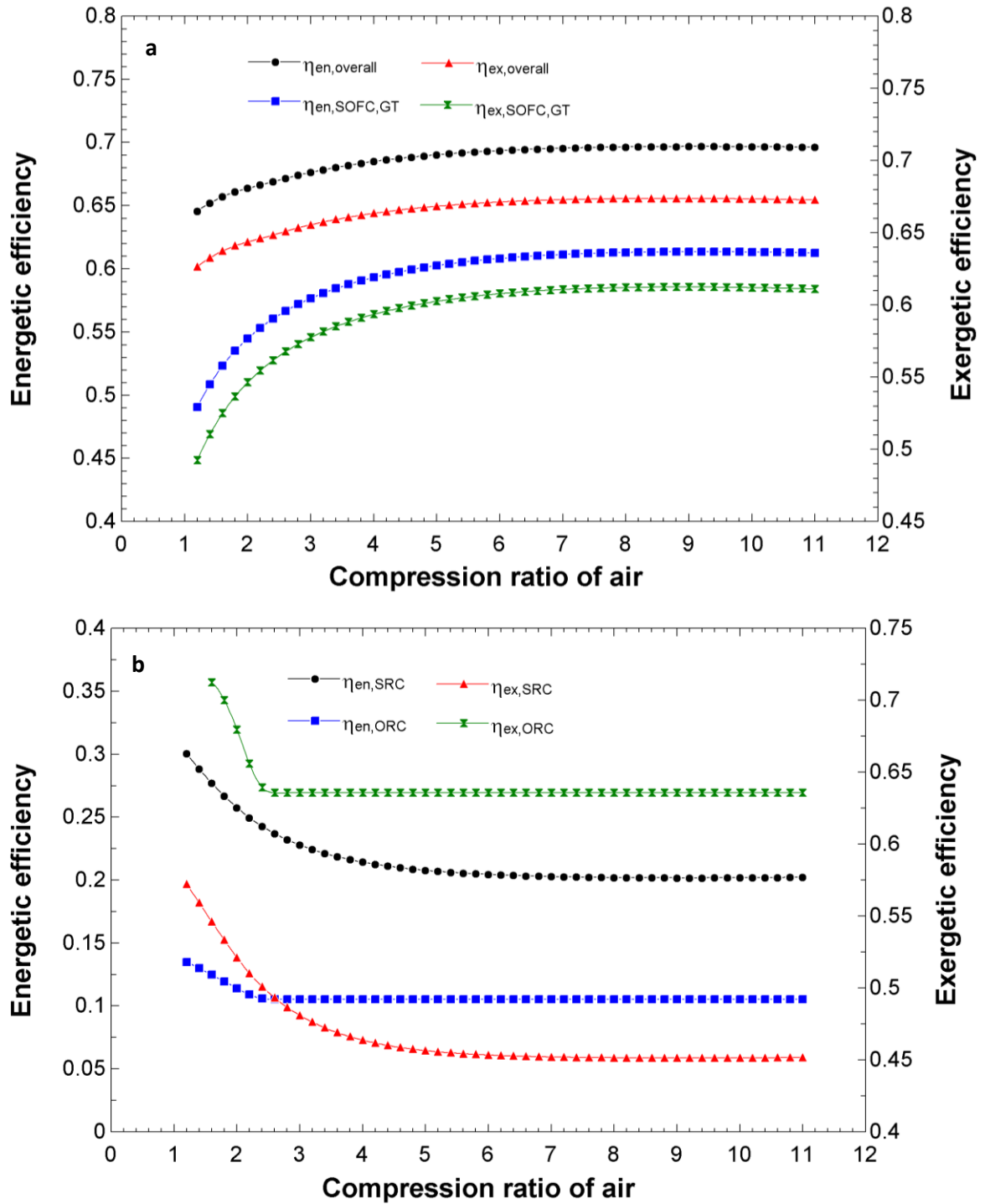


Figure 5.3: Energetic and exergetic efficiencies are plotted against compression ratio across the air compressor. a) For overall integrated system and SOFC-GT subsystem. b) For SRC and NH₃-ORC subsystems.

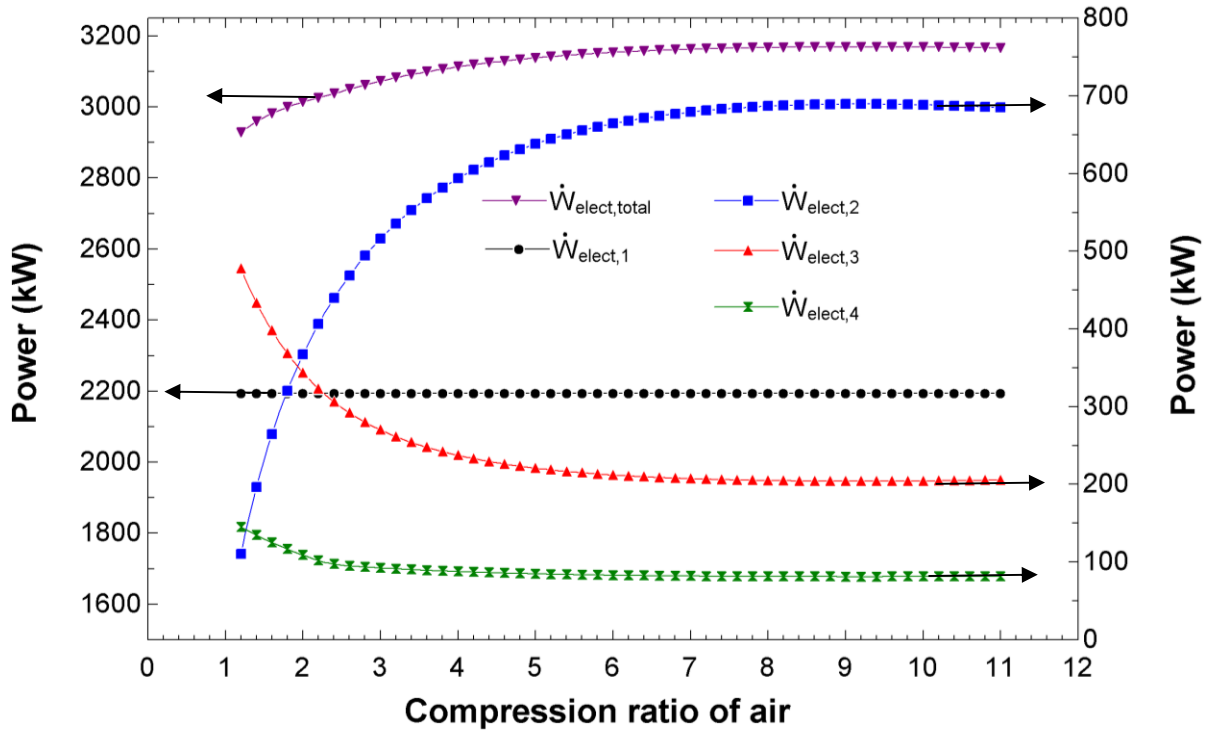


Figure 5.4: Electric power output values of the integrated system and its subsystems are plotted against compression ratio across the air compressor. Arrows indicate the corresponding axis of the parameter.

In Figure 5.7, another variable is changed to observe its effects on the integrated system and its subsystems, namely SOFC-GT, SRC, and NH₃-ORC. This variable is the excess air factor entering the SOFC-GT subsystem. Linear trends are shown for the energetic and exergetic efficiencies of the integrated system and the SOFC-GT and SRC subsystems. However, it has almost no effect on the NH₃-ORC as this cycle is not directly connected to the SOFC-GT subsystem. The energetic and exergetic efficiencies of NH₃-ORC remain constant at values of 10.52% and 63.56%, respectively. Increasing the amount of air entering the integrated system affects the overall performance negatively and reduces the energetic and exergetic efficiencies down to 66.12% and 63.97%, respectively at an excess air factor of 2.8. Similarly, the SOFC-GT energetic and exergetic efficiencies are reduced to 56.41% and 56.44%, respectively. On the other hand, as more mass flow rate leaves the SOFC-GT subsystem and provides more heat to the boiler, the higher efficiency values are achieved at the SRC. At an excess air factor of 2.8, the energetic efficiency is 22.33% and the exergetic efficiency is 60.46% for SRC.

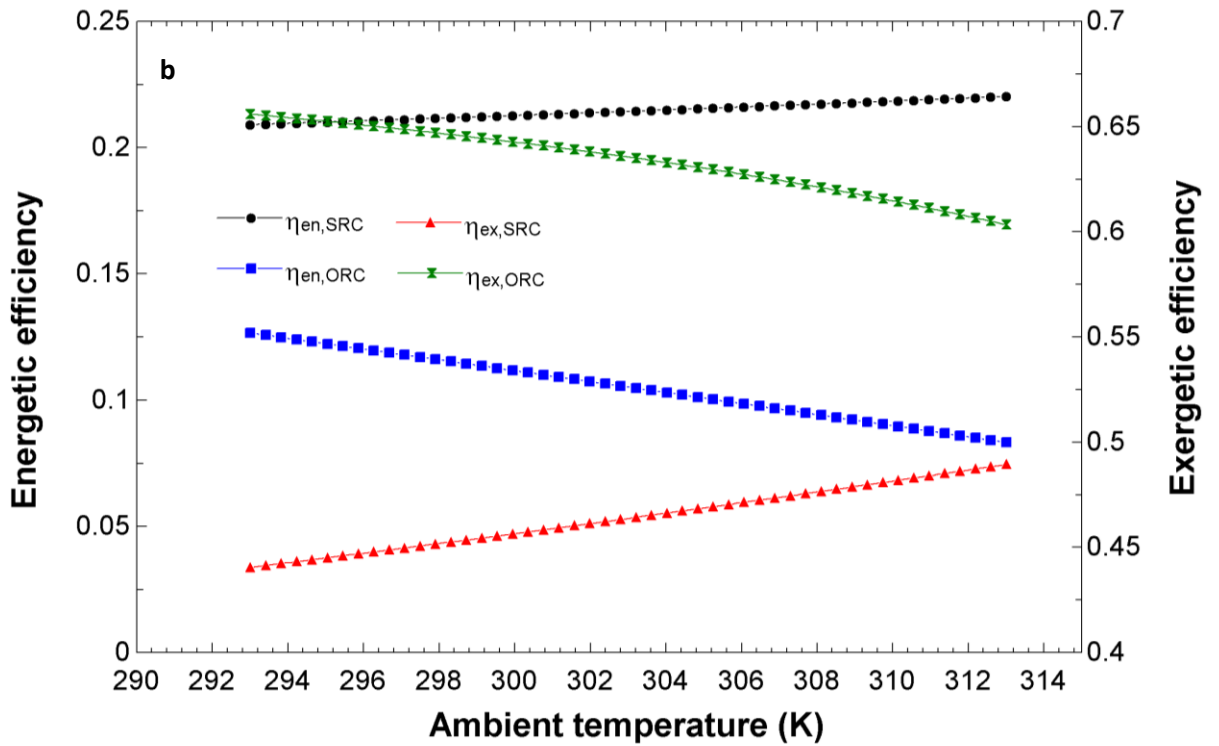
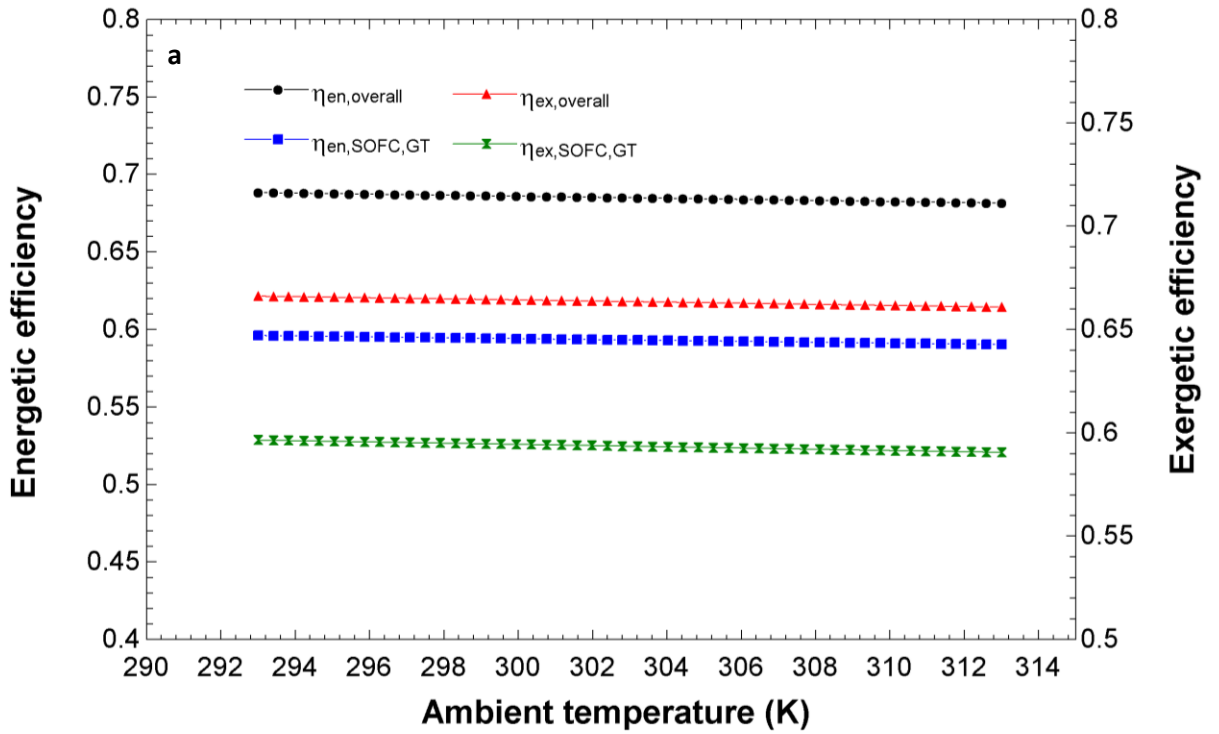


Figure 5.5: Energetic and exergetic efficiencies are plotted against ambient temperature. a) For overall integrated system and SOFC-GT subsystem. b) For SRC and NH₃-ORC subsystems.

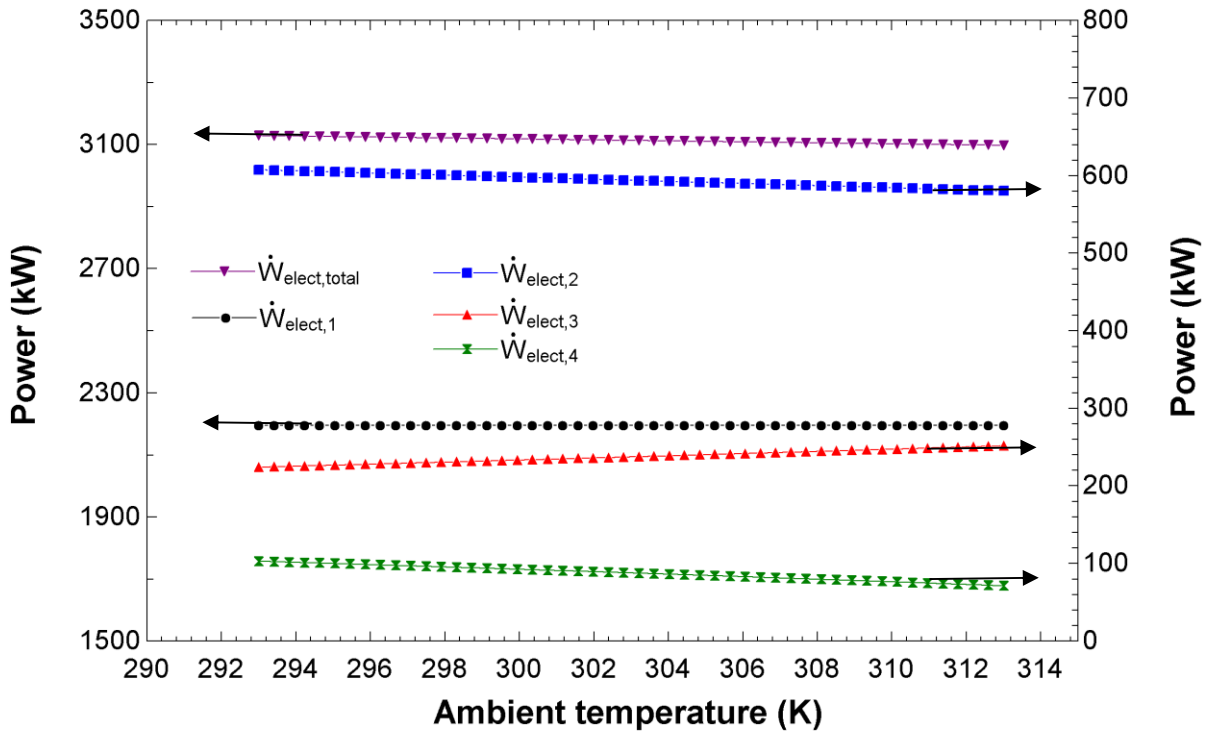


Figure 5.6: Electric power output values of the integrated system and its subsystems are plotted against ambient temperature. Arrows indicate the corresponding axis of the parameter.

In Figure 5.8, the electric power outputs of the integrated system and its subsystems only supports the discussion of the energetic and exergetic efficiencies behaviors mentioned earlier. The total power production reaches a minimum value of 3001 kW at an excess air factor of 2.8. Also, at the same variable value, the SOFC and GT power outputs are 1908 kW and 743.6 kW. We notice that the gas turbine increases its power output as more mass flow rate of air is added, unlike the fuel cell. The drop in power output in the fuel cell is more dramatic than the increase in the gas turbine. For this reason, the SOFC-GT energetic efficiency decreases as mentioned above. For the SRC and NH₃-ORC, the power outputs increase and reach maximum values of 259.1 kW and 91.03 kW, respectively at 2.8 excess air factor.

In Figure 5.9, the effects of redirecting part of the fuel stream to the combustor instead of the fuel cell are studied. This redirection is represented by the α -parameter which was defined in the previous chapter under thermodynamic analysis. The higher the value of this

parameter, the more fuel is injected directly to the combustor as shown by stream 4 in Figure 3.1. The energetic and exergetic efficiencies of the integrated system and the SOFC-GT and SRC subsystems improve significantly as α increases from zero (no redirection) to higher values of redirection. This is mostly due to the increase in inlet temperature of the gas turbine as more fresh charge of fuel comes to the combustor. More discussion on this will be provided later. At $\alpha = 0.6$, the overall energetic efficiency is 96.57% and the overall exergetic is 94.24%. The SOFC-GT and SRC subsystems achieve their best performance at $\alpha = 0.6$. Their energetic efficiencies are 73.95% and 35.10%, respectively. Also, their exergetic efficiencies are 73.84% and 67.64%, respectively. It is interesting to look at the NH₃-ORC efficiency behaviors. The energetic efficiency stays constant until $\alpha = 0.2571$ where it starts increasing. This is because heat at HX 3 is added to the Organic cycle at higher temperatures which causes the turbine to produce more power. Thus, it increases the energetic efficiency of the cycle up to 14.60%. In addition, the exergetic efficiency of NH₃-ORC increases until it reaches a maximum value of 71.46% at $\alpha = 0.3306$ then drops rapidly from there. The reason behind this is the increase in temperature of the heat source at HX 3. The increase in temperature increases the added exergy to the cycle but the cycle is not using it as efficiently as possible. Maybe at these higher temperatures, a different working fluid is suggested other than ammonia.

In Figure 5.10, the output electric power of the integrated system and its subsystems are displayed as a function of the α -parameter. In general, the higher the value of this parameter, the more power is produced by all the subsystems, namely SOFC-GT, SRC, and NH₃-ORC. This agrees well with the energetic efficiency behaviors discussed previously. Notice that the fuel cell is not much affected by this parameter while the gas turbine is heavily affected. Gas turbine net power production goes from 444.7 kW to 1376 kW. As exhaust gases leave the gas turbine at high temperature, they provide the SRC cycle with a significant amount of energy which causes the power production of both turbine 2 and turbine 3 to increase as well. They reach maximum values of 757.5 kW and 199.3 kW, respectively.

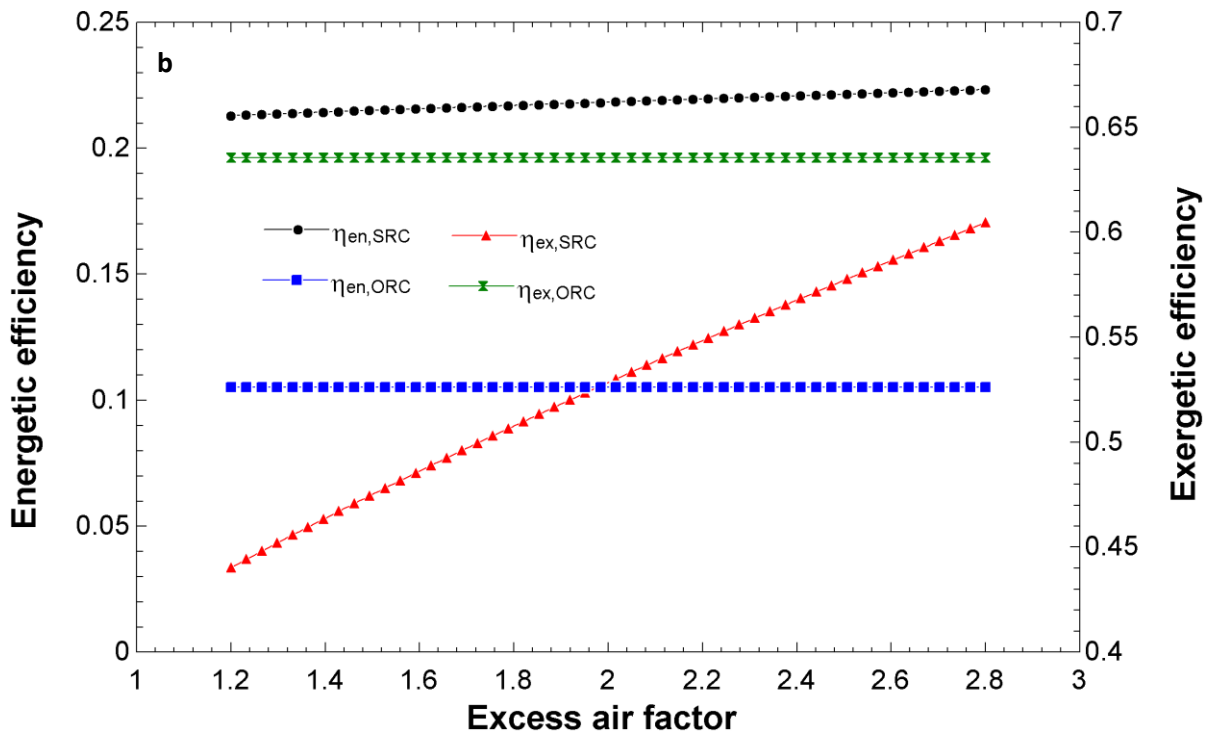
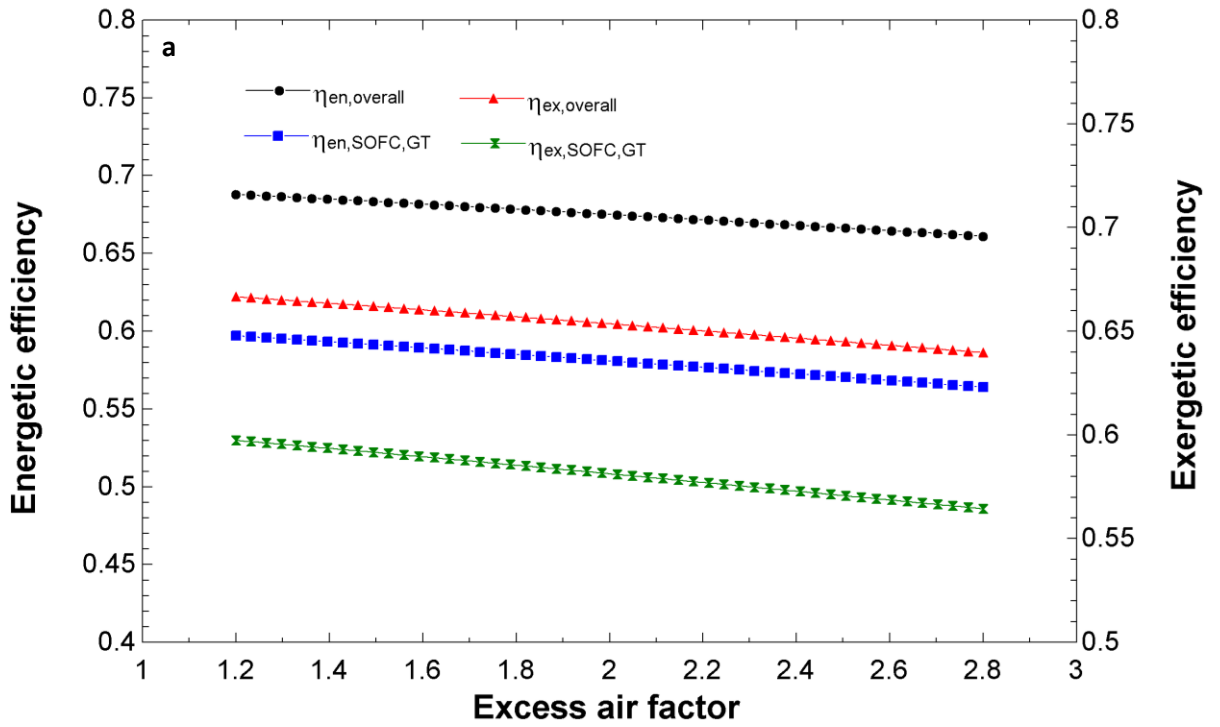


Figure 5.7: Energetic and exergetic efficiencies are plotted against excess air factor (λ). a) For overall integrated system and SOFC-GT subsystem. b) For SRC and NH₃-ORC subsystems.

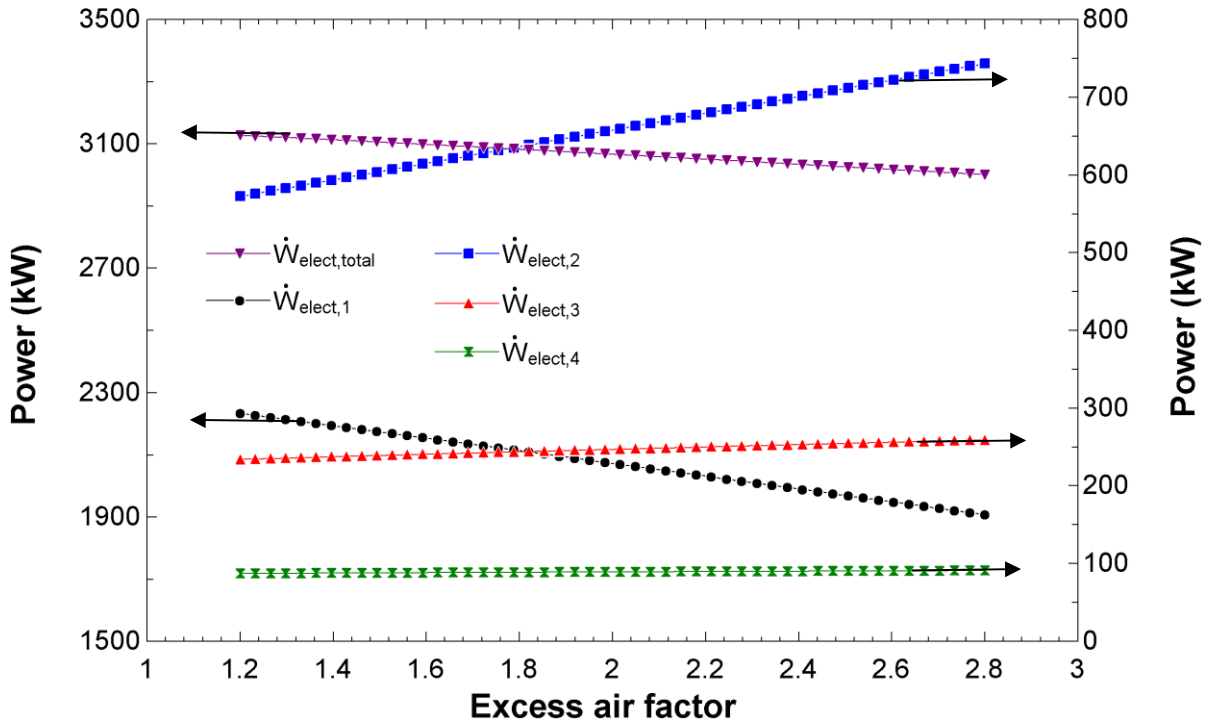


Figure 5.8: Electric power output values of the integrated system and its subsystems are plotted against excess air factor (λ). Arrows indicate the corresponding axis of the parameter.

In Figure 5.11, the temperature at state 5 of the exhaust gases studied under the effect of the α -parameter. As predicted in the previous subsection, increasing the amount of redirected fuel to the combustor, increases the inlet temperature to the gas turbine which enhances its power production as seen earlier. The inlet temperature increases linearly from 1121 K to 1728 K. It seems that using the combustor and gas turbine subsystem is the best choice to go for more power production. However, this is only true because we assumed an adiabatic combustor and an adiabatic gas turbine. As this temperature increases, heat losses from both the combustor and the gas turbine will be more significant. Another advantage for redirecting the fuel to the combustor is controlling the power split between the fuel cell and the gas turbine. This power split is a major factor in determining the space requirements of the integrated system. Also, this redirection of fuel makes the turbine operate at its design operating point and eliminate the need to overdesign the gas turbine to compensate for the low inlet temperature.

At the end, Table 5.7 summarizes the effects of the different chosen parameters on the overall performance of the integrated system.

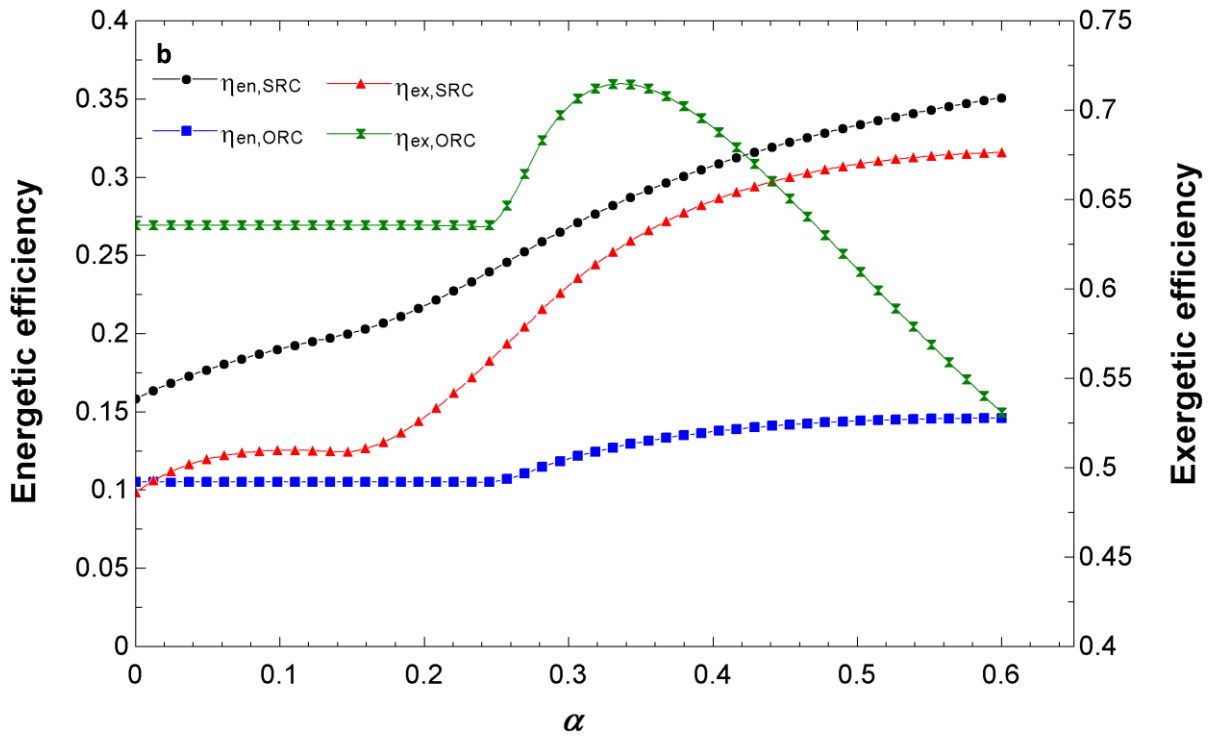
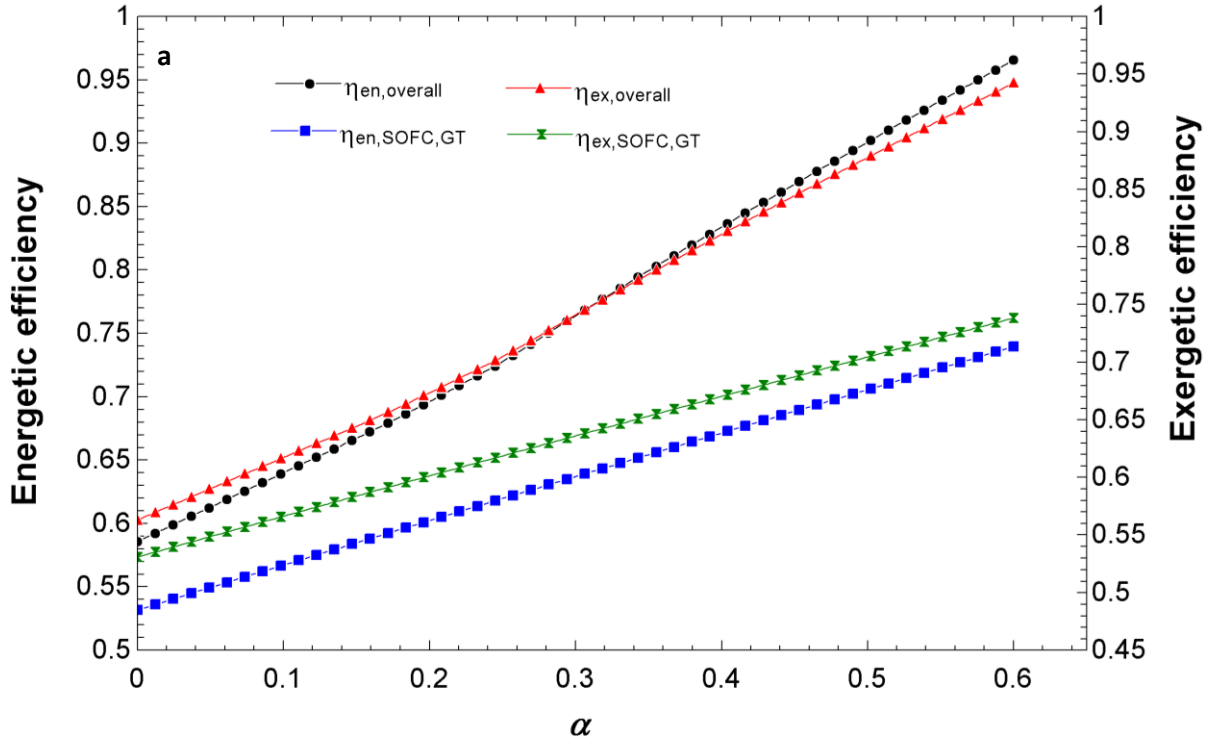


Figure 5.9: Energetic and exergetic efficiencies are plotted against α -parameter. a) For overall integrated system and SOFC-GT subsystem. b) For SRC and NH₃-ORC subsystems. $\lambda = 2$ to ensure complete combustion ($\lambda = 1 + \alpha$) and $r_p = 8$ to have reasonable exit turbine temperature.

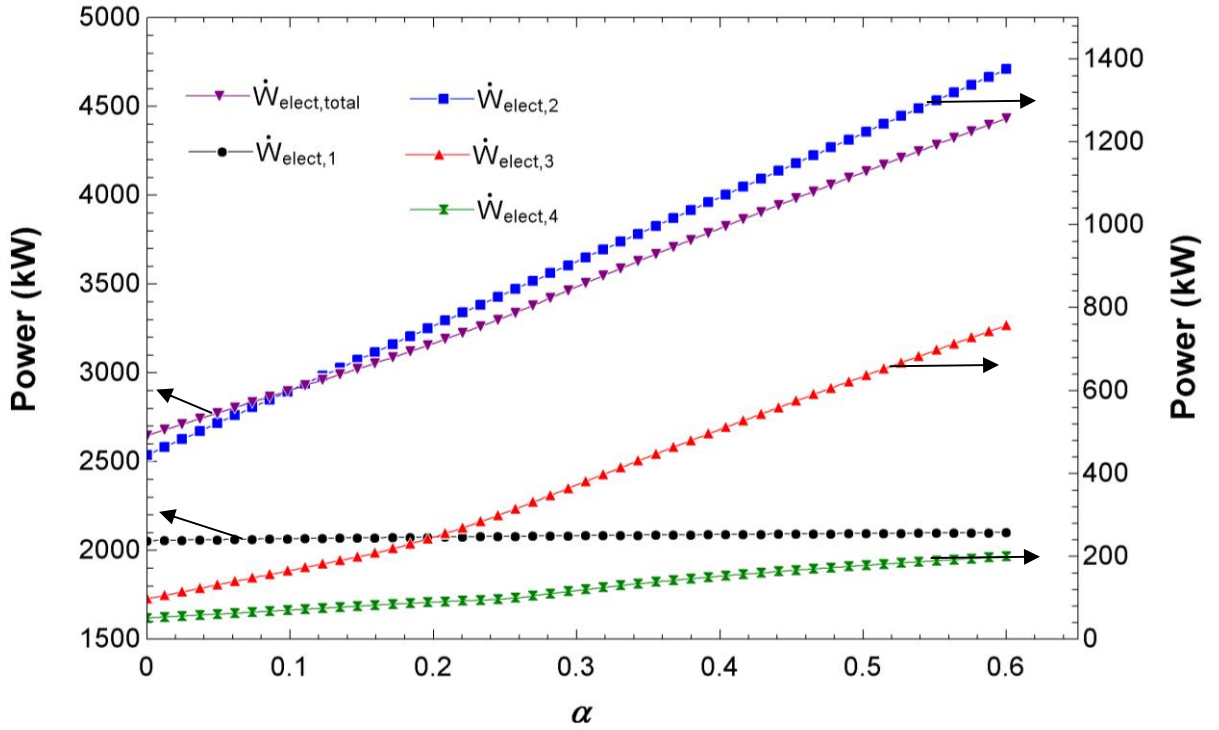


Figure 5.10: Electric power output values of the integrated system and its subsystems are plotted against α -parameter. Arrows indicate the corresponding axis of the parameter. $\lambda = 2$ to ensure complete combustion ($\lambda = 1 + \alpha$) and $r_p = 8$ to have reasonable exit turbine temperature.

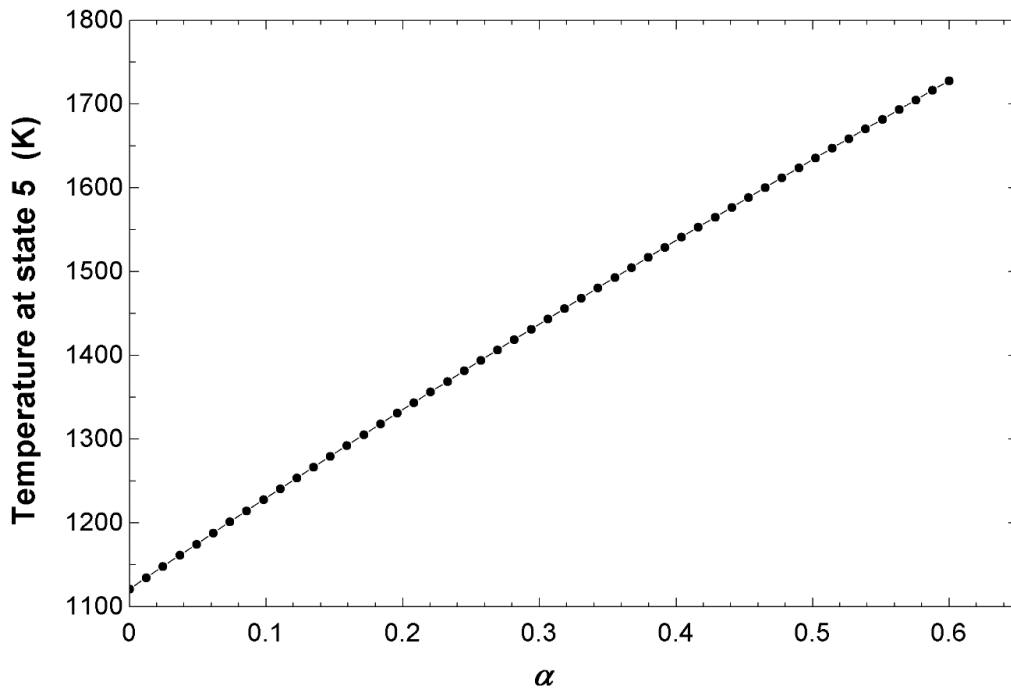


Figure 5.11: Temperature at Gas Turbine (GT) inlet (state 5) is plotted against α -parameter. $\lambda = 2$ to ensure complete combustion ($\lambda = 1 + \alpha$) and $r_p = 8$ to have reasonable exit turbine temperature.

Table 5.7: Summary of the effects of chosen parameters on the performance of the integrated system.

Parameter	Integrated system performance
Compression ratio of air (r_p)	<ol style="list-style-type: none"> 1) Increasing it, enhances the overall energetic and exergetic efficiencies, dramatically. 2) Range of $\eta_{en,overall} = 64.56\% - 69.68\%$ 3) Range of $\eta_{ex,overall} = 62.64\% - 67.37\%$
Ambient temperature (T_o)	<ol style="list-style-type: none"> 1) Minimal negative effects on the performance of the integrated system as this variable increases. 2) Range of $\eta_{en,overall} = 68.15\% - 68.83\%$ 3) Range of $\eta_{ex,overall} = 66.08\% - 66.61\%$
Excess air factor (λ)	<ol style="list-style-type: none"> 1) Its influence on the performance of the integrated system is inversely proportional, especially the fuel cell power output. 2) Range of $\eta_{en,overall} = 66.12\% - 68.80\%$ 3) Range of $\eta_{ex,overall} = 63.97\% - 66.65\%$
α -parameter	<ol style="list-style-type: none"> 1) This is the most significant factor. In general, it improves the overall energetic and exergetic efficiencies but limited by heat losses from the combustor and gas turbine (GT). 2) Range of $\eta_{en,overall} = 58.58\% - 96.57\%$ 3) Range of $\eta_{ex,overall} = 56.31\% - 94.24\%$

5.2 System 1b Results

In this section, a discussion and comparison of the arrangement of air and fuel regenerators in series and in parallel are given. Referring to Figure 3.2, it is seen that the air and fuel regenerators are placed in series and the mixing chamber is removed because there is only one stream of exhaust gases leaving the SOFC-GT cycle. The limitation in this arrangement is that the fuel temperature entering the fuel cell is lower than the parallel arrangement shown in system 1a. A parametric study on the effects of this temperature on the fuel cell power production and overall system performance will be mentioned later. Two points of this system are discussed. Firstly, a reference case is presented for this system to deliver all the demands of a locomotive, like electric power, space cooling, and domestic hot water. Secondly, the performance of this system is looked at through parametric studies.

5.2.1 Reference Case Results

In Table 5.8, the power outputs of the subsystems and their energetic and exergetic efficiencies are listed. The output power of SOFC in this arrangement has decreased from 2194 kW to 2077 kW compared to system 1a. However, the gas turbine electric power increased from 593.8 kW to 671.8 kW. This increase is due to the fact that all of the mass flow rate leaving the combustor goes to the gas turbine, unlike in system 1a where a portion of this stream goes to the fuel regenerator. Electric power outputs from turbines 2 and 3 are the same. This system has a calculated energetic and exergetic efficiency values of 70.81% and 68.56%, respectively. This integrated system is a sustainable system because the *SI* value is higher than unity which is 2.18.

In Figure 5.12, a comparison of the energetic and exergetic efficiencies of the three subsystems, also named cycles in this thesis, is displayed. Similar behavior to system 1a, the exergetic efficiencies of the Rankine cycles are higher than their energetic efficiencies. This shows that these cycles are operating with reasonable efficiencies compared to their ideal cycle counterparts as for the SRC and ORC, they are 47.41% and 63.56%, respectively.

In Table 5.9, the assumed and calculated thermodynamic properties of the state points of this system are listed. The first thing to notice is the decrease of the fuel inlet temperature to the fuel cell at state 2. The value in system 1a is 900 K, while it is 800 K in this integrated system. The decrease in the output power of the SOFC from 2194 kW to 2077 kW can be attributed by this decrease in inlet fuel temperature. A more detailed parametric study on this will be conducted later. Secondly, the exit temperature of the exhaust gases leaving the integrated system is lowered from 408.9 K to 357.5 K. This indicates that the in series arrangement uses more energy of the fuel than system 1a. This also explains the increase in energetic efficiency from 68.50% to 70.81%.

Table 5.8: Calculated parameters for the thermodynamic analysis of system 1b.

Parameter	Value
SOFC electric power	2077 kW
Gas Turbine (GT) electric power	671.8 kW
Turbine 2 electric power	237.2 kW
Turbine 3 electric power	87.74 kW
Total electric power of the integrated system	3074 kW
Total power required by the train at maximum load	3100 kW
HX 1 heat transfer rate (cooling mode)	105 kW
SOFC-GT energetic efficiency	61.21%
SOFC-GT exergetic efficiency	61.24%
SRC energetic efficiency	21.43%
SRC exergetic efficiency	47.41%
ORC energetic efficiency	10.52%
ORC exergetic efficiency	63.56%
Overall energetic efficiency	70.81%
Overall exergetic efficiency	68.56%
Environmental Impact (<i>EI</i>)	0.4586
Sustainability Index (<i>SI</i>)	2.180

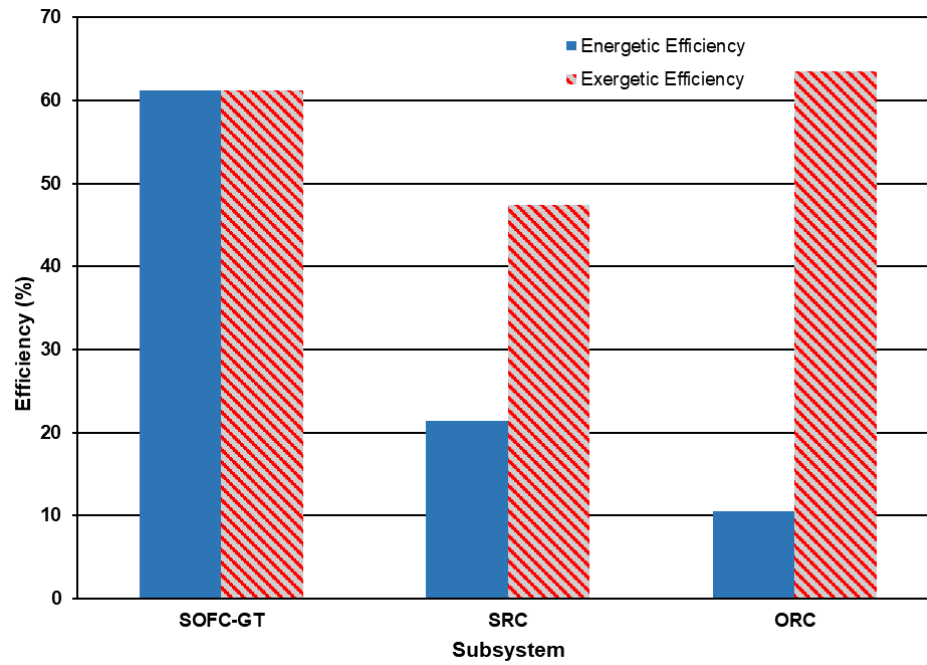


Figure 5.12: Comparison of the energetic and exergetic efficiencies between the subsystems of system 1b.

Table 5.9: State points and their thermodynamic values of system 1b.

State #	Fluid	Temperature (K)	Pressure (kPa)	Specific Enthalpy (kJ kg ⁻¹)	Specific Entropy (kJ kg ⁻¹ K ⁻¹)	Specific Exergy (kJ kg ⁻¹)	Mass Flow Rate (kg s ⁻¹)
1	Air	765.8	400	486.4	6.276	311.8	2.066
2	Methane	800	400	-3097	13.81	52868	0.0731
3	Exhaust+methane+air	950	400	-1130	7.841	481.1	2.139
4	Methane	303	400	-4639	10.93	52198	0.086
5	Exhaust gases	1434	400	-1142	8.435	966.9	2.152
6	Exhaust gases	1070	100	-1632	8.455	469.9	2.152
7	Air	303	100	5.024	5.716	0	2.066
8	Air	486.6	400	191.1	5.797	161.4	2.066
9	Exhaust gases	848.1	100	-1916	8.159	276.3	2.152
10	Exhaust gases	798.4	100	-1978	8.084	237.4	2.152
11	Water	363.3	3500	380.3	1.192	25.61	0.4
12	Water	640.7	3500	3147	6.727	1115	0.4
13	Water	363.1	70	2462	6.936	367.2	0.4
14	Water	363.1	70	376.8	1.192	22.06	0.4
15	Exhaust gases	358	100	-2492	7.154	4.931	2.152
16	Exhaust gases	357.5	100	-2493	7.152	4.838	2.152
17	Water	303	120	125.2	0.4347	0.02009	0.00625
18	Water	353	120	334.4	1.074	15.6	0.00625
19	R134a	268	242.1	247.4	0.9344	23.07	0.8251
20	R134a	334.5	1249	290.1	0.9603	57.97	0.8251
21	R134a	321	1249	120.2	0.4317	48.13	0.8251
22	R134a	268	242.1	120.2	0.4596	39.68	0.8251
23	Methane	800	400	-3097	13.81	52868	0.086
24	Methane	800	400	-3097	13.81	52868	0.0129
25	Ammonia	306.8	4000	360.2	1.533	351.4	0.7454
26	Ammonia	352.2	4000	1479	4.761	492.5	0.7454
27	Ammonia	306	1271	1357	4.806	356.7	0.7454
28	Ammonia	306	1271	355.6	1.533	346.8	0.7454

From Table 5.10, major components of system 1b exergy destruction rates and their exergetic efficiencies are listed. As previously mentioned, all the adiabatic devices have exergetic efficiencies higher than 80%, like the turbines and compressors. The only exception is the combustor which has an exergetic efficiency of 78.72%. This is mainly because of the high exergy destruction rate value of 364.1 kW. This shows a lot of irreversibility in this device even though it is assumed to be adiabatic. In Figure 5.13, the

exergy destruction rate values of the major components of this integrated system are visually compared. The highest exergy destruction value is in the SOFC with a value of 1252 kW, followed by the combustor and boiler with values of 364.1 kW and 64.36 kW, respectively. The exergy destruction rate of the boiler is decreased from 75.63 kW in system 1a to 64.36 kW. Although the mass flow rate of exhaust gases is higher, the temperature difference between the working fluid of SRC (water) and the exhaust gases leaving the SOFC-GT subsystem is lower. This causes the decrease in the exergy destruction rate of the boiler. The inlet exhaust gases temperature in the boiler in system 1a is 824.2 K, while it is 798.4 K in system 1b. This is due to the arrangement of the fuel and air regenerators from parallel to in series.

Table 5.10: Exergy destruction rates and exergetic efficiencies of major components of system 1b.

Component	Exergy Destruction Rate (kW)	Exergetic Efficiency
Air Compressor	50.98	86.74%
SOFC	1252	84.97%
Combustor	364.1	78.72%
Gas Turbine (GT)	13.28	98.76%
Boiler	64.36	87.13%
Turbine 2	25.39	91.51%
HX 3	32.88	76.19%
Turbine 3	10.03	90.09%
Heater	0.1028	48.66%
Compressor 2	6.461	81.67%
HX 1	0.2536	96.88%

5.2.2 Parametric Study Results

Here, we present some parametric studies to observe this proposed system with the in-series arrangement of regenerators in terms of energetic and exergetic efficiencies as well as output power values from the fuel cell and turbines. Two factors are varied to see their effects on the integrated system, namely fuel cell temperature at state 2, and excess air factor. Since systems 1a and 1b are very similar, previous factors, like the ambient temperature and compression ratio, will have the same effects on system 1b and all the other systems mentioned later as these are operating parameters of the SOFC-GT subsystem. Only new parameters and devices will be analyzed thoroughly.

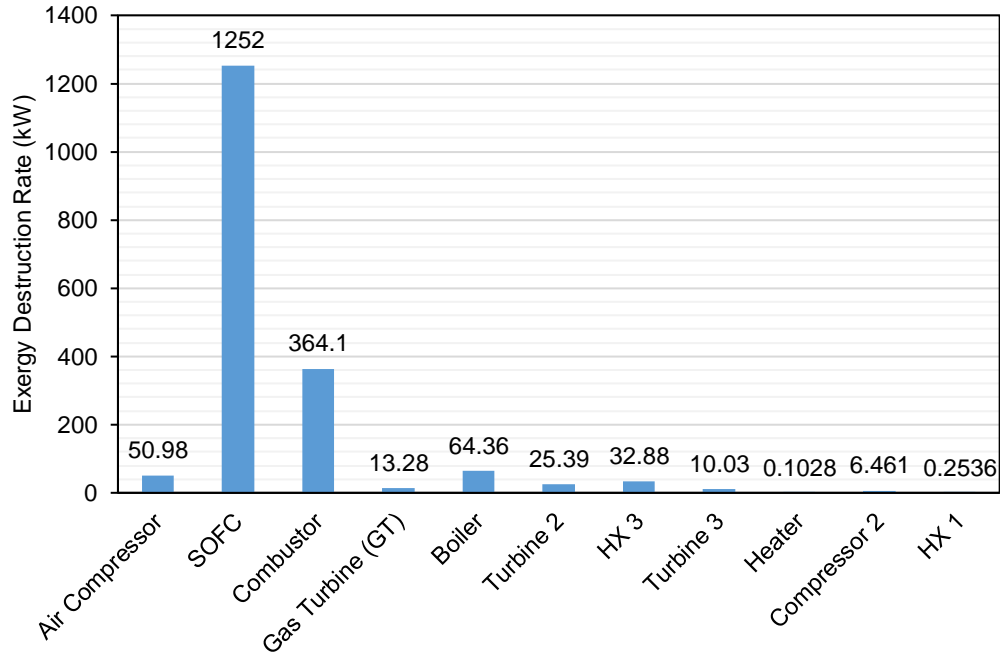


Figure 5.13: Comparison of exergy destruction rates of major components of system 1b.

In Figure 5.14, the effects of fuel inlet temperature to the SOFC on the energetic and exergetic efficiencies for the overall integrated system and the considered subsystems are presented. The fuel cell is a reduced temperature Solid Oxide Fuel Cell that uses nanostructured anode materials for reduced electric resistance values. This kind of fuel cell has been experimentally demonstrated by Zhan et al. [87]. The range of operating temperature of the reduced temperature SOFC is 500°C to 650°C, or 773 K to 923 K. Typical SOFC operating temperatures are from 700-800°C. The overall energetic and exergetic efficiency values are not much affected by the increase in the temperature at state 2. They increase from 70.77% to 70.88%, and from 68.52% to 68.63%, respectively as the temperature goes from 773 K to 848 K. Similar behavior is observed for the energetic and exergetic efficiencies of the SOFC-GT subsystem. In contrast, increasing this temperature affects the energetic and exergetic efficiencies of the SRC negatively. These values slightly drop from 21.56% to 21.20% and from 47.57% to 47.14%, respectively. For the ORC, the energetic and exergetic efficiencies remain constant over the range of temperature at state with values of 10.52% and 63.56%, respectively.

In Figure 5.15, the output power values of the integrated system, as well as its subsystems, are presented against the increase in state 2 temperature. The behavior of the energetic and exergetic efficiencies is reflected here. A marginal increase in the power production of the SOFC and GT components. SOFC electric power output increases from 2072 kW at 773 K to 2086 kW at 848 K. Gas turbine electric power output increases from 671.4 kW at 773 K to 672.4 kW at 848 K. The decrease in SRC power production is observed here. It goes down from 240.4 kW to 231.5 kW. Although the energetic and exergetic efficiencies of the NH₃-ORC remain constant, its power output decreases with the decrease in heat supplied from the condenser of SRC. ORC power output reduces from 88.25 kW to 86.78 kW as the temperature at state 2 increases.

In Figure 5.16, another parameter that affects the performance of the integrated system and the subsystems is the excess air factor. As this factor increases from 1.2 to 1.75, the overall energetic and exergetic efficiencies decrease from 70.78% and 68.53% down to 70.73% and 68.48%, respectively. This is a difference of more than 2% which is significant. A similar behavior is followed by the SOFC-GT subsystem. However, the SRC performance increases with increasing value of excess air factor. This is because more mass flow rate of the exhaust gases enters the boiler, which carries more thermal energy with it. SRC energetic and exergetic efficiencies increase from 21.26% and 44.95% to 22.10% and 51.99%, respectively. ORC is unaffected by this factor. Although there is a noticeable increase in the energetic and exergetic efficiencies of the SRC, it seems that the overall performance of the integrated system is dominated by SOFC-GT subsystem.

In Figure 5.17, we can see that the power outputs from the fuel cell and turbines are representative indicators of the performance of the integrated system and the involved subsystems. There is a minimal decrease in the total power production from 3073 kW to 3070 kW, which is 3 kW less. A sharp decrease in the SOFC output is noticed from 2110 kW to 2005 kW, but this is mostly compensated by the gas turbine increase in power output

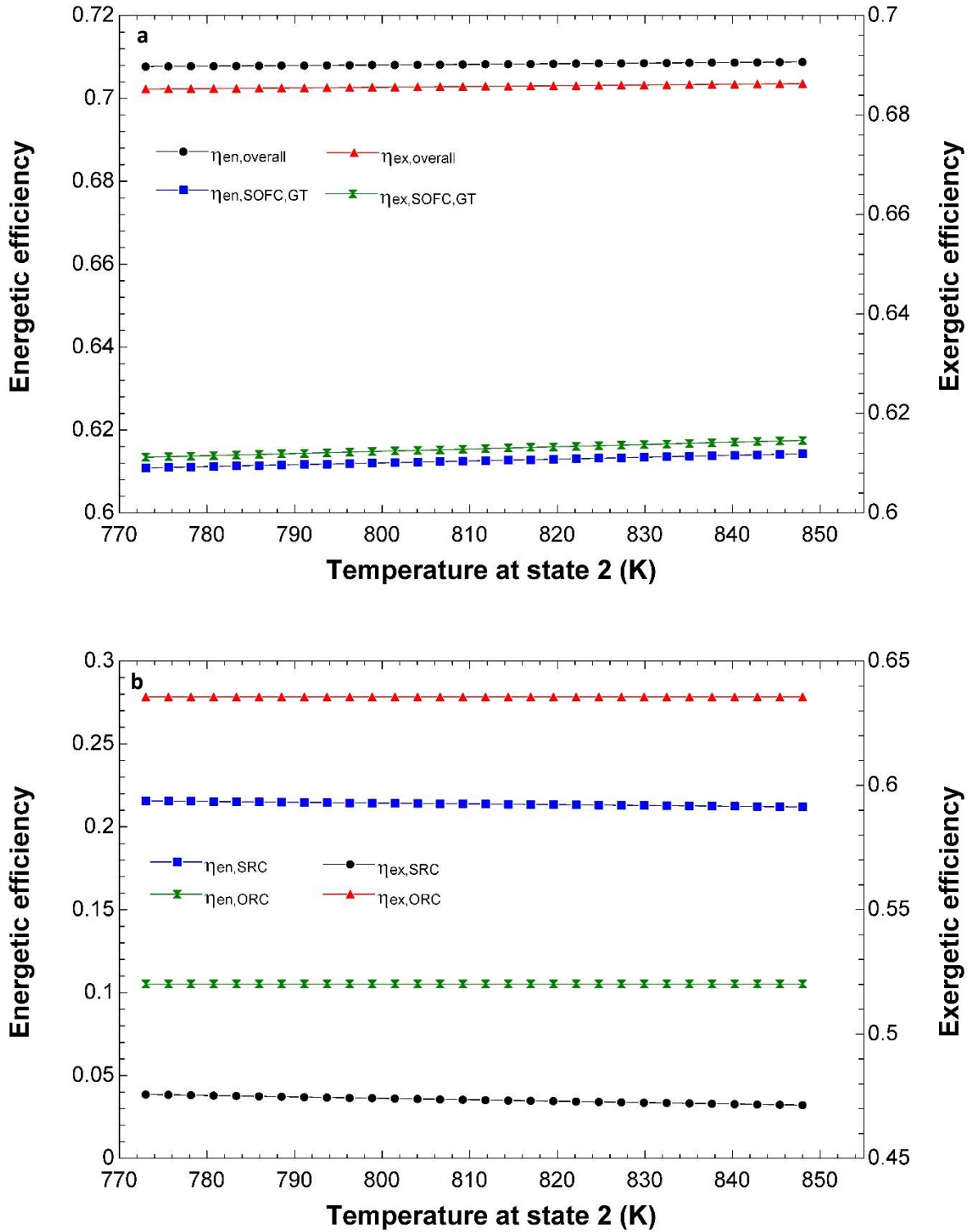


Figure 5.14: Energetic and exergetic efficiencies are plotted against temperature at state 2. a) For overall integrated system and SOFC-GT subsystem. b) For SRC and NH₃-ORC subsystems.

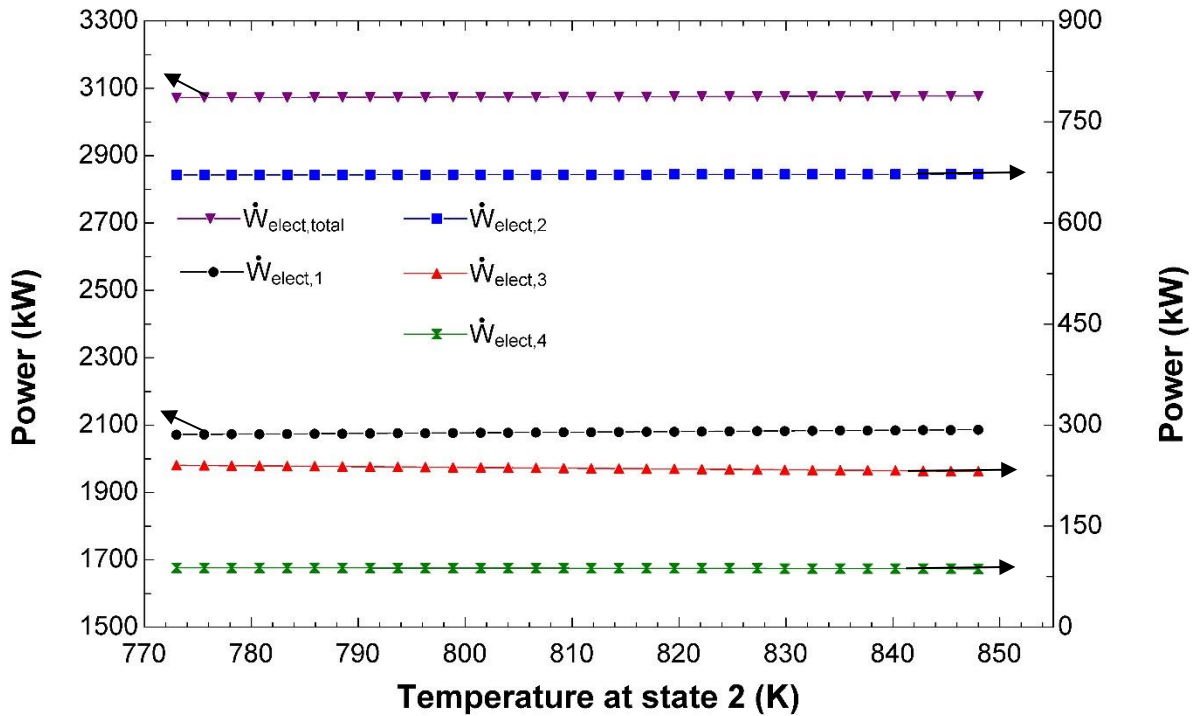


Figure 5.15: Electric power output values of the integrated system and its subsystems are plotted against temperature at state 2. Arrows indicate the corresponding axis of the parameter.

from 642.7 kW to 721.8 kW. The decrease of the SOFC power is more than the increase in GT power which is the reason behind the overall decrease in energetic and exergetic efficiency of the SOFC-GT subsystem. As the excess air factor increases, the SRC power production increases from 232.9 kW to 253.5 kW. For this reason, higher performance of the SRC is observed energetically and exergetically as mentioned earlier. The ORC increases its electric power output with increasing excess air factor although the energetic and exergetic efficiencies remain constant. This increase is proportional to the increase in supplied heat from the Steam Rankine Cycle.

In Figure 5.18, this excess air factor affects the temperature of exhaust gases going to the fuel regenerator as more energy is consumed by the air regenerator that comes before it. The more air mass flow rate is put into the integrated system, the lower the temperature at state 9 is. This is due to the higher consumption of energy by the air regenerator compared to the fuel regenerator as the excess air factor increases. State 9 temperature decreases from 904.5 K to 774.5 K, while we keep state 2 fixed at 773 K. This decrease limits the highest possible temperature for state 2 and limits the performance of the SOFC.

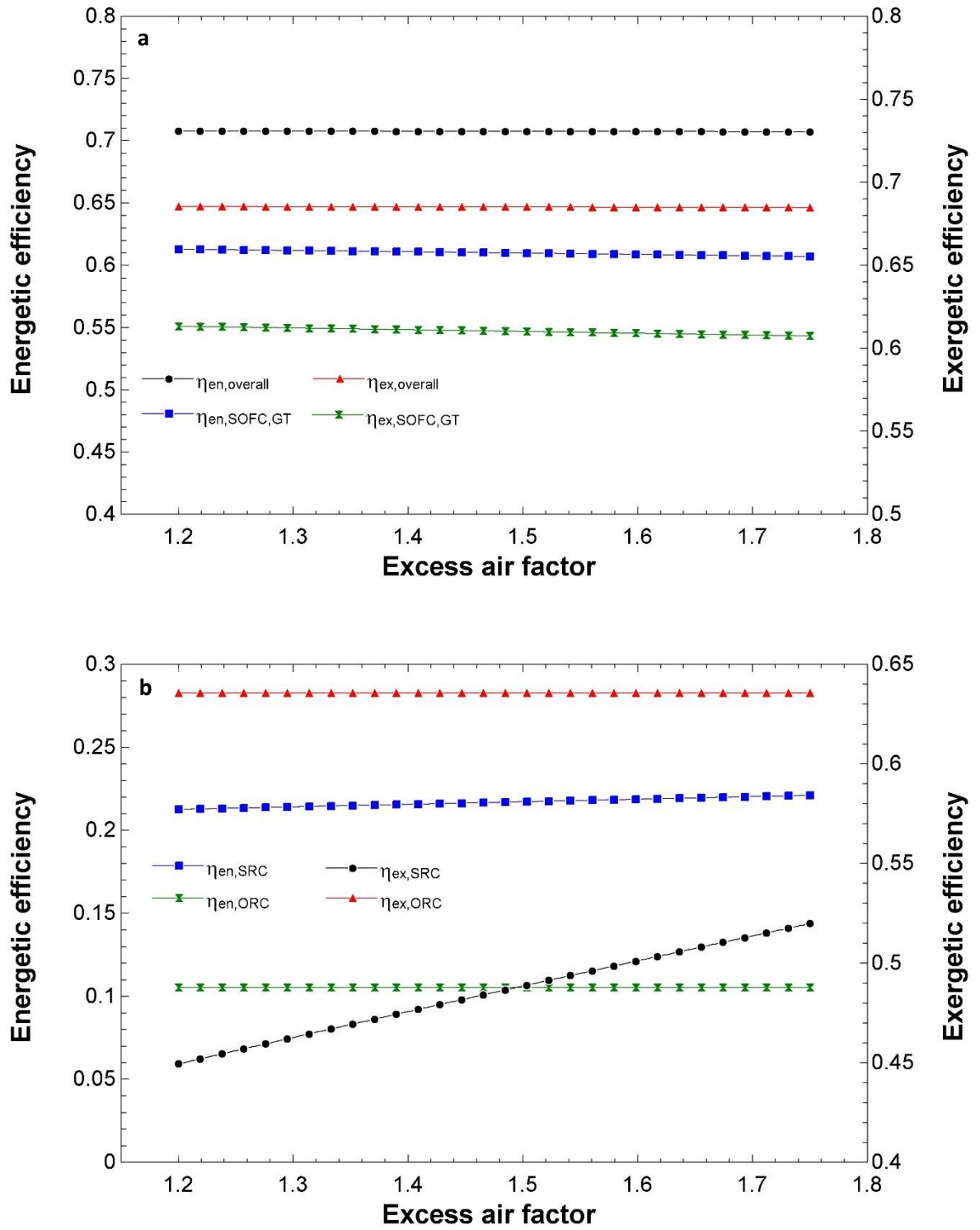


Figure 5.16: Energetic and exergetic efficiencies are plotted against excess air factor (λ). a) For overall integrated system and SOFC-GT subsystem. b) For SRC and NH₃-ORC subsystems.

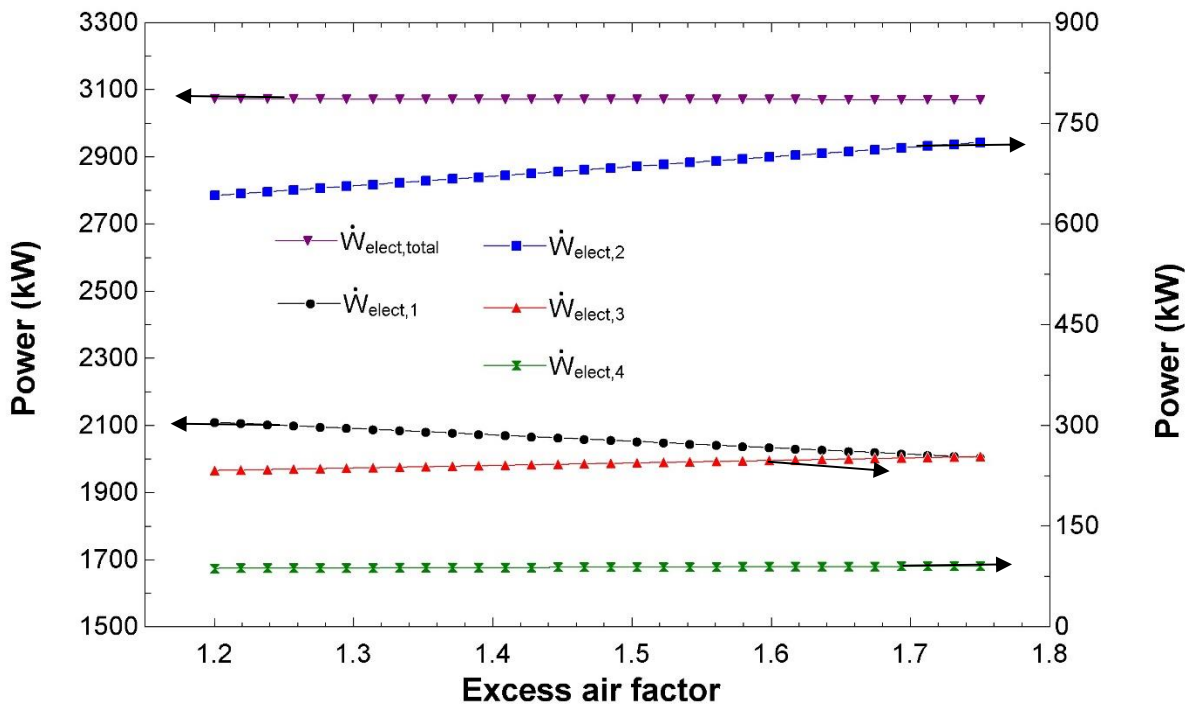


Figure 5.17: Electric power output values of the integrated system and its subsystems are plotted against excess air factor (λ). Arrows indicate the corresponding axis of the parameter.

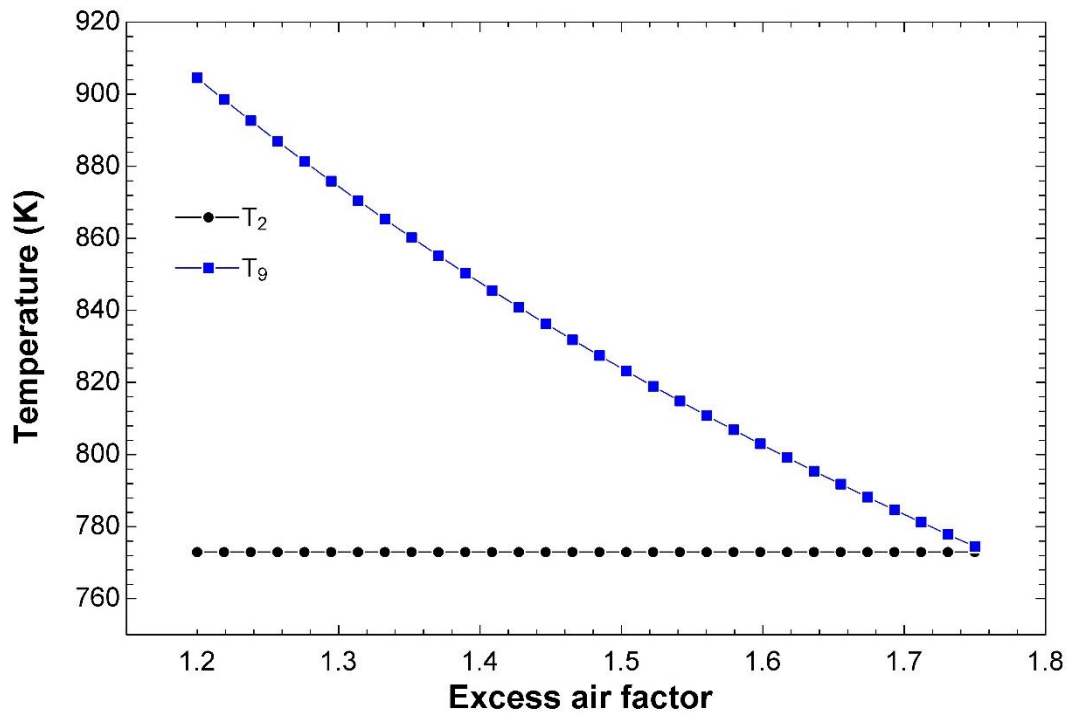


Figure 5.18: Temperatures at states 2 and 9 are plotted against excess air factor (λ).

5.3 System 2 Results

Referring to Figure 3.3, the thermodynamic modelling results of system 2 are discussed now. As the previous integrated system, we start with a reference case, then a parametric analysis of the integrated system is presented.

5.3.1 Reference Case Results

In Table 5.11, the output power values and energetic and exergetic efficiencies of the overall system and the subsystems are itemized. As seen previously, the power output of SOFC is the highest at a value of 2194 kW, followed by GT, Turbine 2, and Turbine 3. The SOFC provides 70.12% of the total power driving the locomotive. The other 29.88% is recovered by the three turbines. In this integrated system, an absorption chiller with a heat exchanger subsystem is used instead of a reversible heat pump. Although we have shown a good case for the advantages of using reversible heat pump cycles, it is interesting to see the effect of this choice on the overall energetic and exergetic efficiencies. From this table, the overall energetic and exergetic efficiencies are 68.83% and 67.24%, respectively. These are around 1% higher than system 1a which means that using an absorption chiller with a heat exchanger subsystem is not much worth it when compared to space and weight advantages of reversible heat pumps mentioned earlier.

In Figure 5.19, the energetic and exergetic efficiencies of all the subsystems of this integrated system are compared. Similar values and differences are observed here. SRC and ORC exergetic efficiencies are much higher than their corresponding energetic efficiencies.

In Table 5.12, state points and their thermodynamic property values are listed. The working fluid in the absorption chiller is chosen to be water/LiBr mixture for providing space cooling. It is providing a cooling effect at a temperature of 280 K, or 7°C.

In Table 5.13, a list of the exergy destruction rates and exergetic efficiencies of the major components of system 2 is presented. The lowest exergetic efficiency value is seen at the absorber where a significant amount of heat is lost at high temperature. The utilization of this heat could increase this efficiency. Also, the exergetic efficiency of the generator is low because the exhaust gases temperature is much higher than the needed temperature to

evaporate the refrigerant in the generator. The exhaust gases temperature entering the generator is 901.5 K, while the vapor refrigerant temperature leaving the generator is 353 K. These results are reflected in the exergy destruction rates of the absorber and generator, which are 44.19 kW and 43.02 kW, respectively. From Figure 5.20, we see that the three top highest exergy destruction rates are at the same devices observed in previous systems. These are the SOFC, combustor, and boiler with values of 1286 kW, 380.2 kW, and 75.54 kW, respectively. Furthermore, if the main components of the absorption chiller are looked at, the highest exergy destruction rate is at absorber, followed by the generator. The evaporator has a relatively lower exergy destruction rate for two reasons. Firstly, the mass flow rate going through the evaporator is much less than the other two components. It is $0.04459 \text{ kg s}^{-1}$, but the generator has a mass flow rate of 4.459 kg s^{-1} . Secondly, the heat transfer absorbed by the evaporator is at significantly low temperature, 280 K. From the entropy balance equation, lower temperature, produces lower entropy generation rate and lower exergy destruction rate as observed in the calculated value of 8.081 kW.

Table 5.11: Calculated parameters for the thermodynamic analysis of system 2.

Parameter	Value
SOFC electric power	2194 kW
Gas Turbine (GT) electric power	582.7 kW
Turbine 2 electric power	265.2 kW
Turbine 3 electric power	86.50 kW
Total electric power of the integrated system	3129 kW
Total power required by the train at maximum load	3100 kW
Evaporator heat transfer rate (cooling mode)	105 kW
SOFC-GT energetic efficiency	59.08%
SOFC-GT exergetic efficiency	59.11%
SRC energetic efficiency	24.38%
SRC exergetic efficiency	52.87%
ORC energetic efficiency	10.52%
ORC exergetic efficiency	63.56%
Overall energetic efficiency	68.83%
Overall exergetic efficiency	67.24%
Environmental Impact (<i>EI</i>)	0.4872
Sustainability Index (<i>SI</i>)	2.052

Table 5.12: State points and their thermodynamic values of system 2.

State #	Fluid	Temperature (K)	Pressure (kPa)	Specific Enthalpy (kJ kg ⁻¹)	Specific Entropy (kJ kg ⁻¹ K ⁻¹)	Specific Exergy (kJ kg ⁻¹)	Mass Flow Rate (kg s ⁻¹)
1	Air	765.8	400	486.4	6.276	311.8	2.162
2	Methane	900	400	-2685	14.3	53133	0.0765
3	Exhaust+methane+air	950	400	-1130	7.841	481.1	2.239
4	Methane	900	400	-2685	14.3	53133	0.0135
5	Exhaust gases	1436	400	-1139	8.437	968.9	2.004
6	Exhaust gases	1071	100	-1631	8.457	471.2	2.004
7	Air	303	100	5.024	5.716	0	2.162
8	Air	486.6	400	191.1	5.797	161.4	2.162
9	Exhaust gases	821.4	100	-1949	8.119	255.2	2.004
10	Exhaust gases	1436	400	-1139	8.437	968.9	0.2477
11	Methane	303	400	-4639	10.93	52198	0.09
12	Exhaust gases	901.5	400	-1849	7.821	445.7	0.2477
13	Methane	900	400	-2685	14.3	53133	0.09
14	Water	363.3	3500	380.3	1.192	25.61	0.4
15	Water	621	3500	3100	6.652	1091	0.4
16	Water	363.1	70	2433	6.856	362.3	0.4
17	Water	363.1	70	376.8	1.192	22.06	0.4
18	Exhaust gases	358	100	-2492	7.154	4.931	2.004
19	Exhaust gases	445.7	100	-2394	7.398	28.76	0.2477
20	Exhaust gases	367.7	100	-2481	7.183	6.709	2.252
21	Exhaust gases	367.2	100	-2482	7.182	6.605	2.252
22	Water	303	120	125.2	0.4347	0.02009	0.00625
23	Water	353	120	334.4	1.074	15.6	0.00625
24	Water+LiBr	353	8	322.8	1.053	15.17	0.04459
25	Water+LiBr	353	8	186.3	0.4655	7.267	4.414
26	Water+LiBr	313	8	159.3	0.561	0.7065	0.04459
27	Water+LiBr	280	0.7	159.3	0.1057	138.7	0.04459
28	Water+LiBr	280	0.7	2514	6.255	630.3	0.04459
29	Water+LiBr	313	0.7	104.7	0.2308	0.2778	4.459
30	Water+LiBr	313	8	104.7	0.2308	0.2778	4.459
31	Water+LiBr	325	8	130.8	0.3017	1.398	4.414
32	Water+LiBr	325	0.7	130.8	0.3017	1.398	4.414
33	Water+LiBr	340	8	158.1	0.3946	4.017	4.459
34	Exhaust gases	445.7	400	-2394	6.984	154.3	0.2477
35	Exhaust gases	367.2	100	-2482	7.182	6.605	2.252
36	Ammonia	306.8	4000	360.2	1.533	351.4	0.7349
37	Ammonia	352.2	4000	1479	4.761	492.5	0.7349
38	Ammonia	306	1271	1357	4.806	356.7	0.7349
39	Ammonia	306	1271	355.6	1.533	346.8	0.7349

Table 5.13: Exergy destruction rates and exergetic efficiencies of major components of system 2.

Component	Exergy Destruction Rate (kW)	Exergetic Efficiency
Air Compressor	53.35	86.74%
SOFC	1286	85.27%
Combustor	380.2	78.81%
Gas Turbine (GT)	12.35	98.76%
Boiler	75.54	84.94%
Turbine 2	24.72	91.51%
HX 2	32.41	76.19%
Turbine 3	9.890	90.09%
Heater	0.1356	41.80%
Generator	43.02	39.58%
Evaporator	8.081	63.14%
Absorber	44.19	3.614%

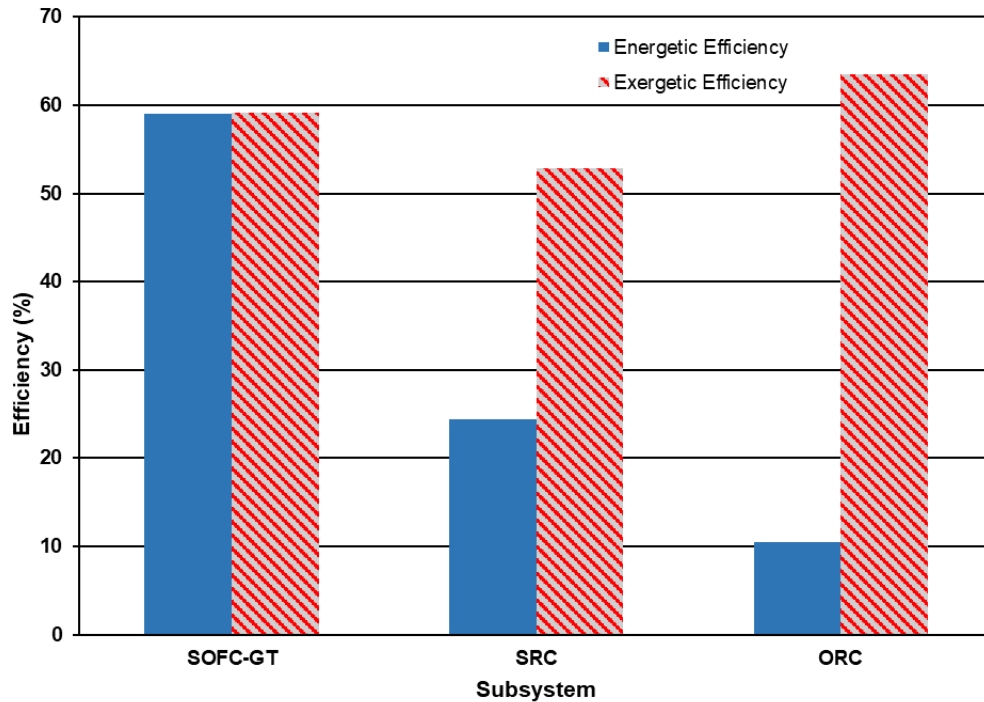


Figure 5.19: Comparison of the energetic and exergetic efficiencies between the subsystems of system 2.

5.3.2 Parametric Study Results

Now, we present a parametric analysis to compare the effects of cooling load met by the reversible heat pump in system 1a, or the absorption chiller in system 2 on the overall performance of the integrated systems and the Steam Rankine Cycle. Also, cooling load effects on state 34 temperature, in system 2, are studied.

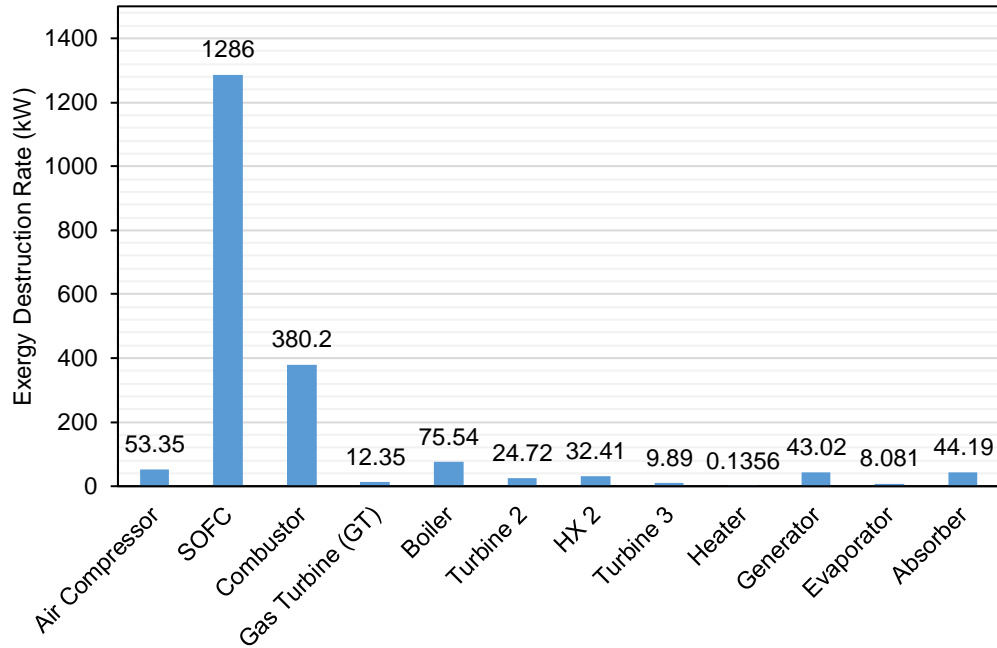


Figure 5.20: Comparison of exergy destruction rates of major components of system 2.

In Figure 5.21, the cooling load effects on the overall energetic and exergetic efficiencies of systems 1a and 2 are shown. As the cooling load increases from zero to 120 kW, the overall energetic and exergetic efficiency values of system 2 increase from 66.59% and 66.60% to 69.14% and 67.33%, respectively. On the other hand, for system 1a, as the cooling load increases, only the overall energetic efficiency increase from 67.01% to 68.71%, while the overall exergetic efficiency decrease from 67.02% to 66.25%. This is due to the increase in heat output and the decrease in total power produced, especially from turbine 3 of SRC. This will be shown later. For SRC, in system 2, the energetic and exergetic efficiencies remain unaffected by the increase in cooling load as there is no connection between the absorption chiller and the power cycles in the integrated system. However, there is a power consumption by the reversible heat pump in system 1a from the SRC. The increase in cooling load increases the power consumption and therefore decreases the energetic and exergetic SRC efficiency values as shown in the figure below. These energetic and exergetic efficiencies have significant reductions from 24.62% and 53.27% down to 20.98% and 45.40%, respectively.

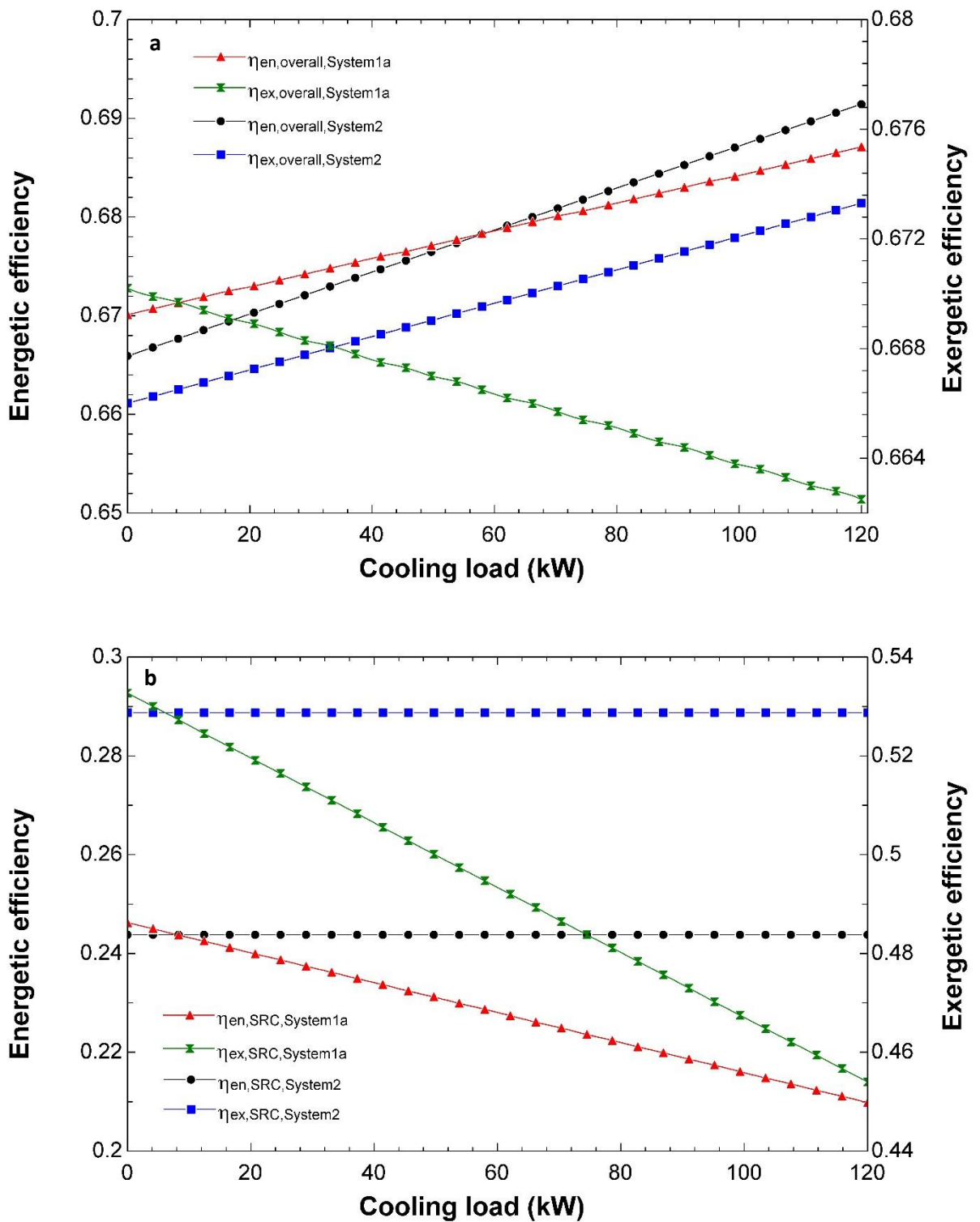


Figure 5.21: Energetic and exergetic efficiencies comparison of systems 1a and 2 are plotted against the cooling load. a) For overall integrated systems. b) For SRC subsystems.

In Figure 5.22, the total power production of the two considered integrated systems are compared. In system 2, the total power produced by this system is constant at a value of 3129 kW. In contrast, for system 1a, the total power produced decreases with increasing cooling load, from 3148 kW to 3108 kW. The difference is 40 kW less which is only 1.271% of the total power produced. This drop is completely attributed to the increase in power consumption by the reversible heat pump and it is delivered by turbine 3. The decrease in net electric power produced by turbine 3 is 40.3 kW from the figure. To explain the reduction in overall exergetic efficiency of system 1a, we see that a portion of the total power produced is converted to heat for producing the cooling effect. This conversion from high-grade type of power to a lower grade reduces the exergetic efficiency of the integrated system.

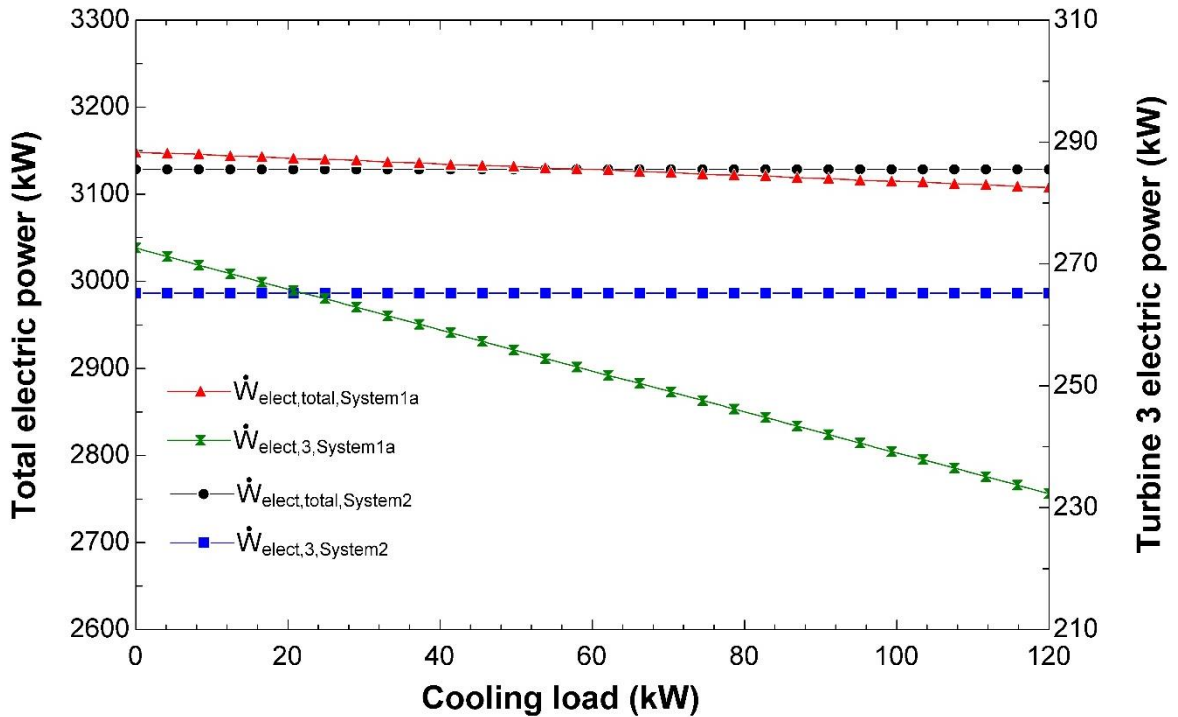


Figure 5.22: Total and turbine 3 electric power values comparison of systems 1a and 2 are plotted against the cooling load.

In Figure 5.23, state 34 temperature of system 2 which is the temperature of exhaust gases leaving the generator is plotted against the cooling load. As expected from the energy balance equation of the generator, as the cooling load increases, this temperature decreases linearly. The decrease is from 901.5 K down to 388.6 K at a cooling load of 120 kW. This

temperature is limited by the needs in the heater to deliver hot domestic water at a temperature of 353 K, or 80°C. If the cooling load gets higher, then the mass flow rate of stream 34 needs to increase accordingly.

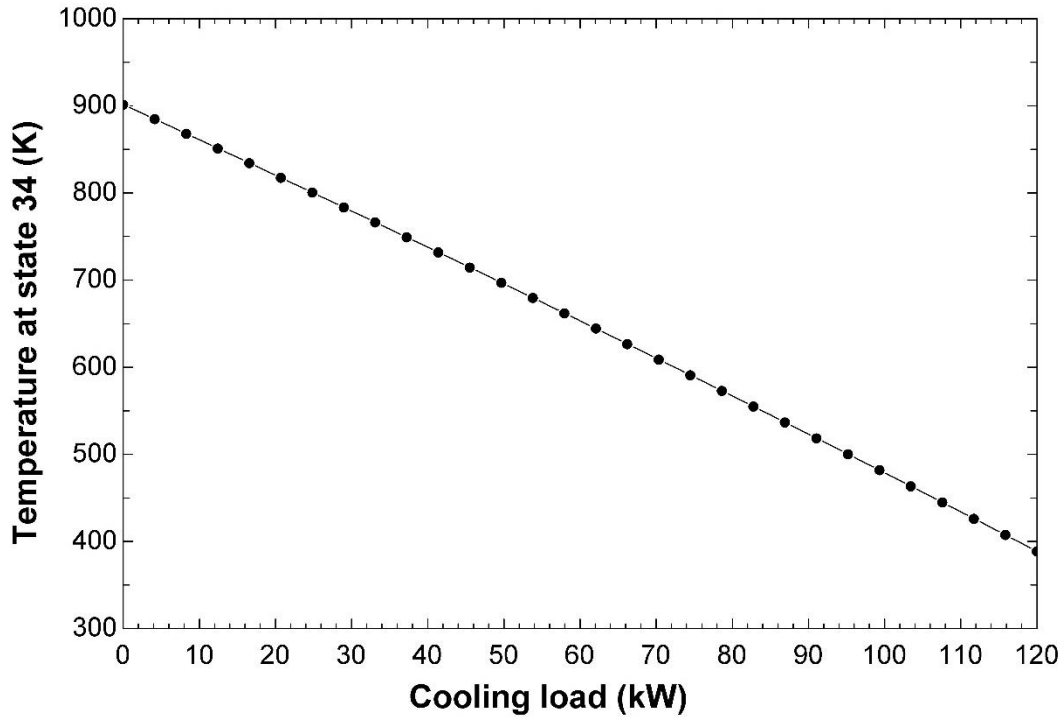


Figure 5.23: Temperature at state 34 of system 2 is plotted against absorption chiller cooling load.

5.4 System 3 Results

In Figure 3.4, the integrated SOFC-PPCI-GT-ORC system with a reversible type heat pump is presented and thermodynamically studied in this section. As before, we start with a reference case to operate a locomotive at maximum load. After that, parametric plots are generated to understand the behavior of this system under several operating.

5.4.1 Reference Case Results

In Table 5.14, the power outputs of different components and the energetic and exergetic efficiencies of subsystems in system 3 are listed. In this integrated system, SOFC power output is 59.73% which is less than the previous systems where it is 70.12% of the total power driving the locomotive. This reduction is compensated by the PPCI engine that produces 906.2 kW. Also, the gas turbine output power has dropped from 593.8 kW (system 1a) to 336.4 kW. The replacement of the combustor by the PPCI engine has

increased the energetic and exergetic efficiencies of the primary cycle to 77.15% and 77.19%, respectively. As a result, the overall energetic and exergetic reach high values of 80.07% and 77.56%, respectively. The electric power from the ORC is only 11.23 kW after consuming part of the turbine work by compressor 2. So, the ORC is capable of running the reversible heat pump but it does not contribute to driving the locomotive. Note that the compression ratio of PPCI engine at this reference case is 14.

In Figure 5.24, a comparison between the involved subsystems is displayed. The PPCI engine has high energetic and exergetic efficiency values. Most of the energy of the fuel is spent in the primary cycle of SOFC-PPCI-GT, therefore not much energy and exergy are left to operate the Organic Rankine Cycle (ORC). For this reason, the energetic and exergetic efficiencies are low which are 3.757% and 12.69%, respectively.

In Table 5.15, the thermodynamic properties of the integrated system are listed. The working fluid of ORC used here is Isobutane instead of ammonia because the temperature level of exhaust gases entering the boiler is 511.1 K which is too high for ammonia.

Table 5.14: Calculated parameters for the thermodynamic analysis of system 3.

Parameter	Value
SOFC electric power	1860 kW
PPCI engine electric power	906.2 kW
Gas Turbine (GT) electric power	336.4 kW
Turbine 2 electric power	11.23 kW
Total electric power of the integrated system	3114 kW
Total power required by the train at maximum load	3100 kW
HX 1 heat transfer rate (cooling mode)	105 kW
SOFC-PPCI-GT energetic efficiency	77.15%
SOFC-PPCI-GT exergetic efficiency	77.19%
PPCI engine energetic efficiency	65.19%
PPCI engine exergetic efficiency	74.86%
ORC energetic efficiency	3.757%
ORC exergetic efficiency	12.69%
Overall energetic efficiency	80.07%
Overall exergetic efficiency	77.56%
Environmental Impact (<i>EI</i>)	0.2893
Sustainability Index (<i>SI</i>)	3.456

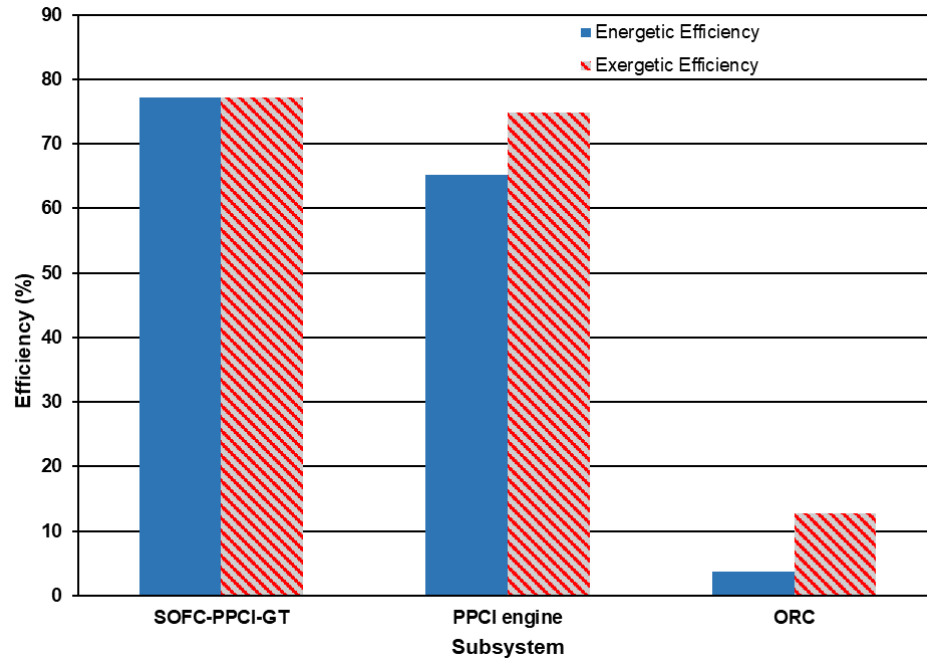


Figure 5.24: Comparison of the energetic and exergetic efficiencies between the subsystems of system 3.

In Table 5.16, the major components of system 3, including PPCI engine are listed to show their exergy destruction rates and their corresponding exergetic efficiencies. We can notice a significant reduction of exergy destruction rate from 380.2 kW, in the combustor in system 1a, down to 83.73 kW. Also, the SOFC exergy destruction rate has decreased since less mass flow rate is needed and less electric power is produced in this device due to the compensation by the PPCI engine.

From Figure 5.25, a comparison of these major components of the integrated system is presented in regards to their exergy destruction rate. The highest destruction rate is 1121 kW at the fuel cell and followed by the PPCI engine at 83.73 kW. Unlike previous integrated systems, the air compressor is the third highest exergy destruction rate instead of the boiler.

5.4.2 Parametric Study Results

Secondly, parametric studies are performed on this integrated system to observe how this system behaves under selected parameters related to the Partially-Premixed Compression Ignition (PPCI) engine. These parameters are engine compression ratio r_v , air compressor compression ratio, and the α -parameter.

Table 5.15: State points and their thermodynamic values of system 3

State #	Fluid	Temperature (K)	Pressure (kPa)	Specific Enthalpy (kJ kg ⁻¹)	Specific Entropy (kJ kg ⁻¹ K ⁻¹)	Specific Exergy (kJ kg ⁻¹)	Mass Flow Rate (kg s ⁻¹)
1	Air	765.8	400	486.4	6.276	311.8	1.85
2	Methane	800	400	-3097	13.81	52868	0.06545
3	Exhaust+methane+air	950	400	-1130	7.841	481.1	1.915
4	Methane	303	400	-4639	10.93	52198	0.077
5	Exhaust gases	1086	457.1	-1612	8.02	622.4	1.927
6	Exhaust gases	776.5	100	-2004	8.05	220.9	1.734
7	Air	303	100	5.024	5.716	0	1.85
8	Air	486.6	400	191.1	5.797	161.4	1.85
9	Exhaust gases	511.1	100	-2319	7.554	55.96	1.734
10	Exhaust gases	589.8	457.1	-2228	7.266	234.5	0.1927
11	Isobutane	306.2	3500	280.8	1.259	62.7	0.4228
12	Isobutane	500.9	3500	988	3.031	232.7	0.4228
13	Isobutane	437.1	420	872.3	3.061	108.1	0.4228
14	Isobutane	304.5	420	275.2	1.259	57.04	0.4228
15	Exhaust gases	358	100	-2492	7.154	4.931	1.734
16	Exhaust gases	357.3	100	-2493	7.152	4.815	1.734
17	Water	303	120	125.2	0.4347	0.02009	0.00625
18	Water	353	120	334.4	1.074	15.6	0.00625
19	R134a	268	242.1	247.4	0.9344	23.07	0.8251
20	R134a	334.5	1249	290.1	0.9603	57.97	0.8251
21	R134a	321	1249	120.2	0.4317	48.13	0.8251
22	R134a	268	242.1	120.2	0.4596	39.68	0.8251
23	Methane	800	400	-3097	13.81	52868	0.077
24	Methane	800	400	-3097	13.81	52868	0.01155
25	Exhaust gases	1086	457.1	-1612	8.02	622.4	0.1927
26	Exhaust gases	1086	457.1	-1612	8.02	622.4	1.734

Table 5.16: Exergy destruction rates and exergetic efficiencies of major components of system 3.

Component	Exergy Destruction Rate (kW)	Exergetic Efficiency
Air Compressor	45.64	86.74%
SOFC	1121	84.97%
PPCI engine	83.73	74.86%
Gas Turbine (GT)	15.61	97.76%
Boiler	16.59	81.25%
Turbine 2	3.79	92.81%
Heater	0.1026	48.71%
Compressor 2	6.461	81.67%
HX 1	0.2536	96.88%

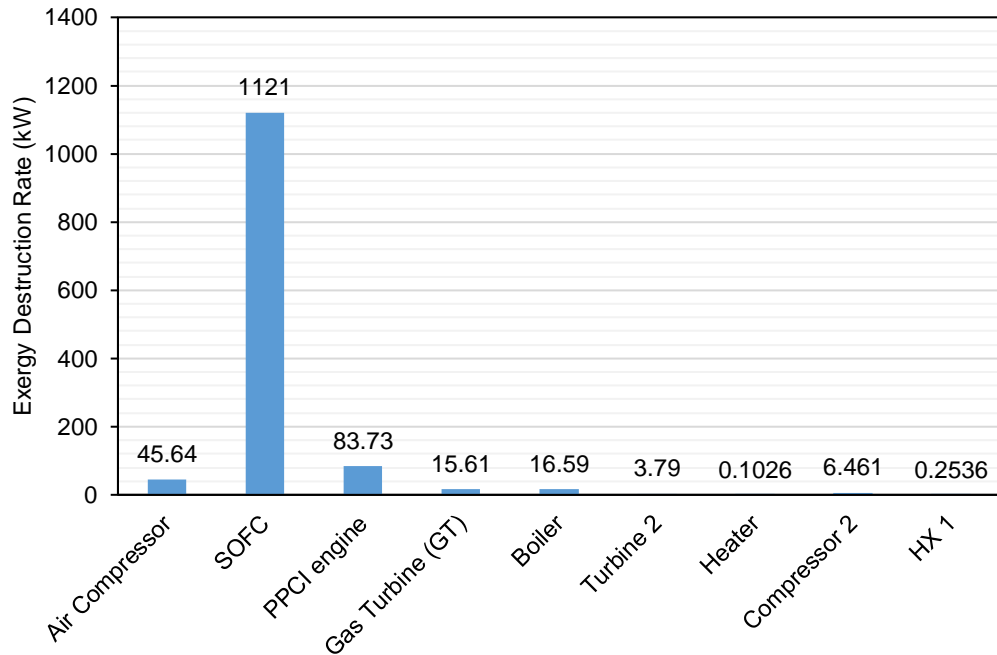


Figure 5.25: Comparison of exergy destruction rates of major components of system 3.

In Figure 5.26, increasing the engine compression ratio increases the energetic and exergetic efficiencies of the overall system and the SOFC-PPCI-GT subsystem. As this compression ratio goes from 12 to 20, the overall energetic and exergetic efficiencies increase nonlinearly from 79.71% and 77.20% to 80.82% and 78.31%, respectively. On the other hand, increasing this compression has negative effects on the energetic and exergetic efficiencies of ORC. This behavior is mainly due to the lower temperature delivered at the boiler as most of the energy and exergy of the exhaust gases stream have been consumed by the PPCI engine.

In Figure 5.27, the power outputs of the different devices, like the SOFC and the PPCI engine are plotted as the engine compression ratio is varied. SOFC power output is not affected by this variation and it remains constant at a value of 1860 kW. Increasing this ratio increases the efficiency of the PPCI engine as it follows the Otto cycle. Thus, the power output increases from 879.3 kW up to 962.5 kW, as shown in the figure. The more energy is consumed by this device, the less energy is left for the gas turbine and ORC. Their power outputs decrease as this ratio increases. The decrease in ORC power output is reflected also in its energetic and exergetic efficiencies as discussed above.

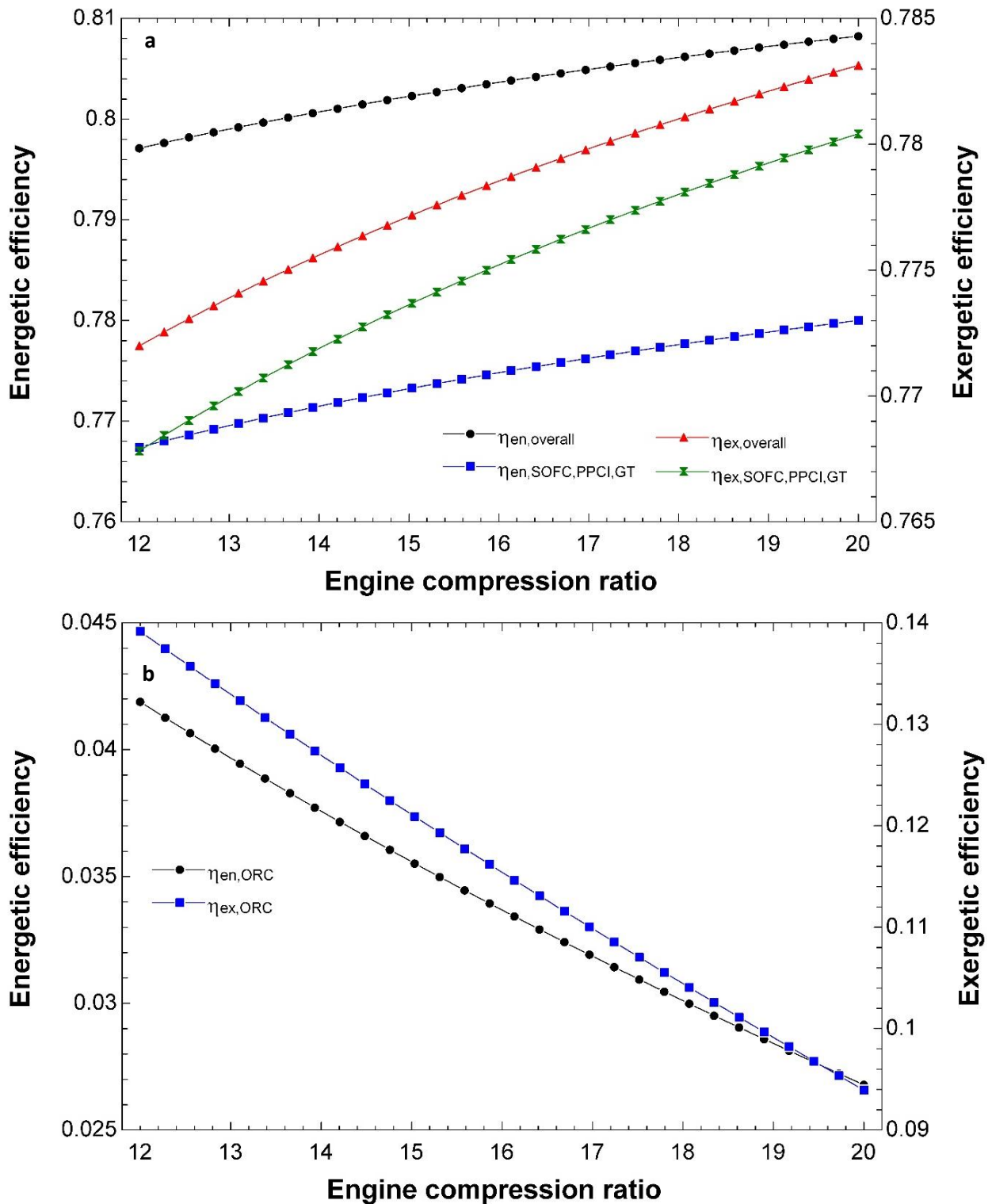


Figure 5.26: Energetic and exergetic efficiencies are plotted against engine compression ratio r_v . a) For overall integrated system and SOFC-PPCI-GT subsystem. b) For ORC subsystem.

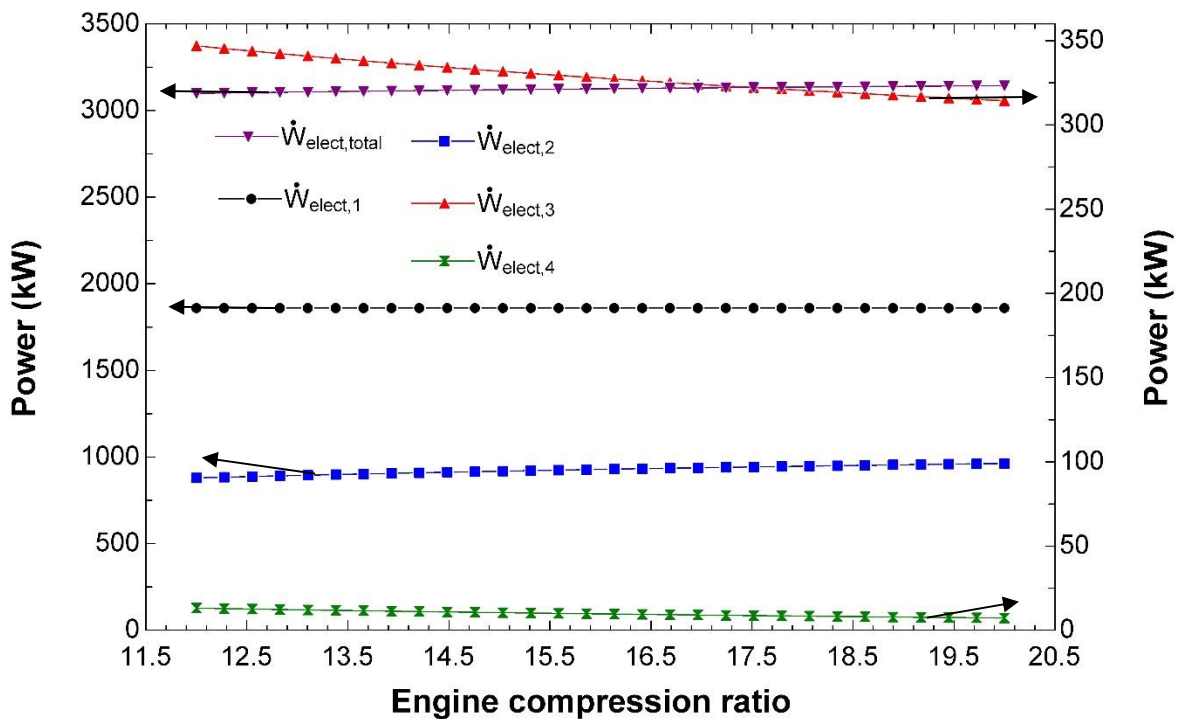


Figure 5.27: Electric power output values of the integrated system and its subsystems are plotted against engine compression ratio r_c . Arrows indicate the corresponding axis of the parameter.

In Figure 5.28, a different compression ratio of the air compressor is changed to see its effects on the performance of the integrated system. The overall energetic and exergetic efficiencies have interesting concave-down parabolic curves. They are maximized when the compression ratio is 4.917, with values of 80.20% and 77.64%, respectively. This compression ratio is lower than the one found from system 1a which is 9. Also, it can be noticed that the overall performance is dominated by the SOFC-PPCI-GT subsystem which is expected as it is the primary cycle. Looking at the ORC energetic and exergetic efficiency values, they are minimized when the primary cycle is maximized as there is a tradeoff of energy distribution between these two subsystems. At 4.917 compression ratio, the ORC energetic and exergetic efficiencies are 3.548% and 12.08%.

In Figure 5.29, we can see more insights into which power producing component is the main cause of the behaviors observed earlier of the efficiencies. The power outputs of the SOFC and the PPCI engine are not affected by the changes in the air compressor ratio. However, the gas turbine net electric power follows a parabolic curve and it is maximized at 4.917 with a value of 342.5 kW. The ORC is minimized with a value of 10.39 kW. These

results show that the compression ratio at the air compressor affect mainly the gas turbine and it is the dominant component in the integrated system.

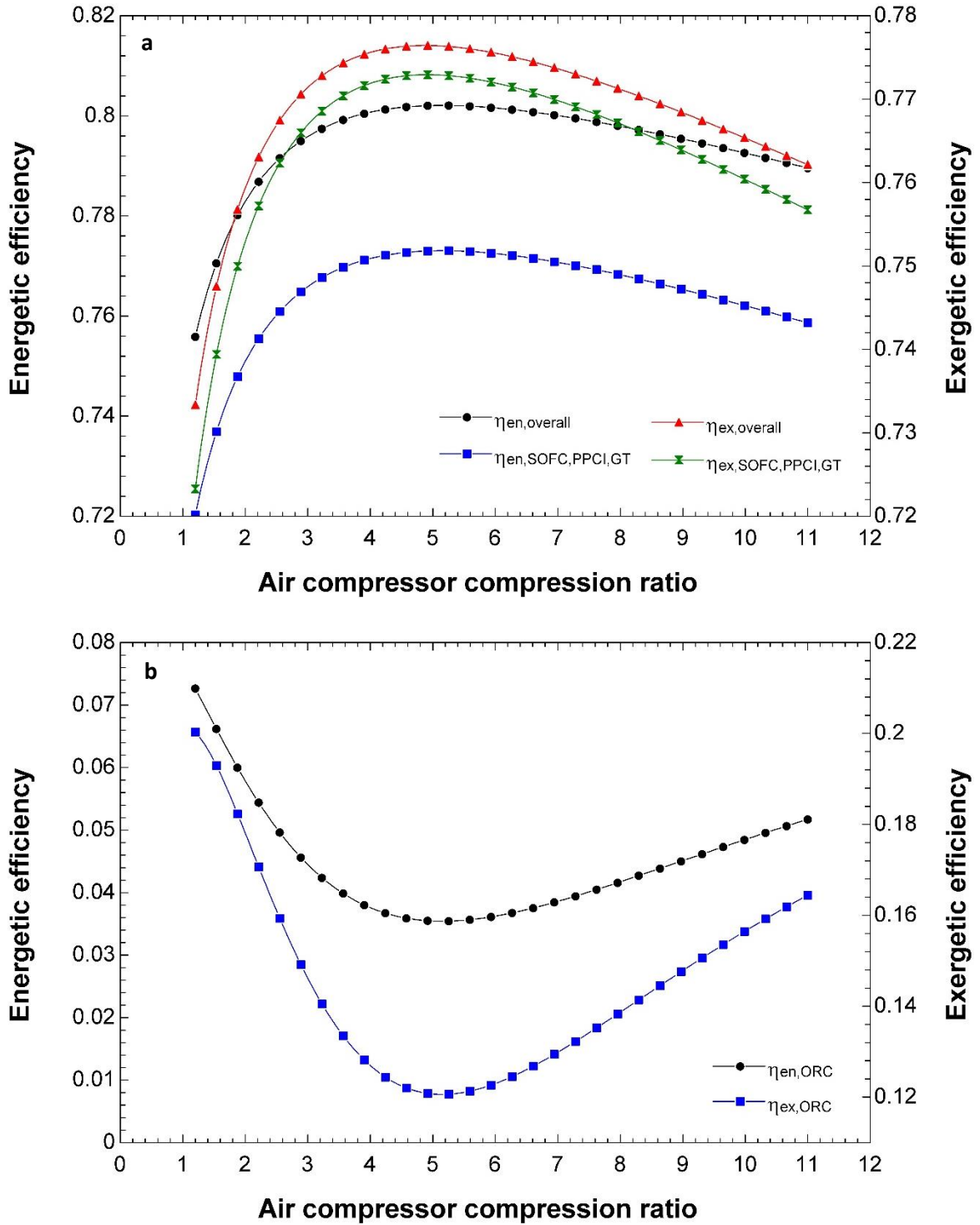


Figure 5.28: Energetic and exergetic efficiencies are plotted against air compressor compression ratio. a) For overall integrated system and SOFC-PPCI-GT subsystem. b) For ORC subsystem.

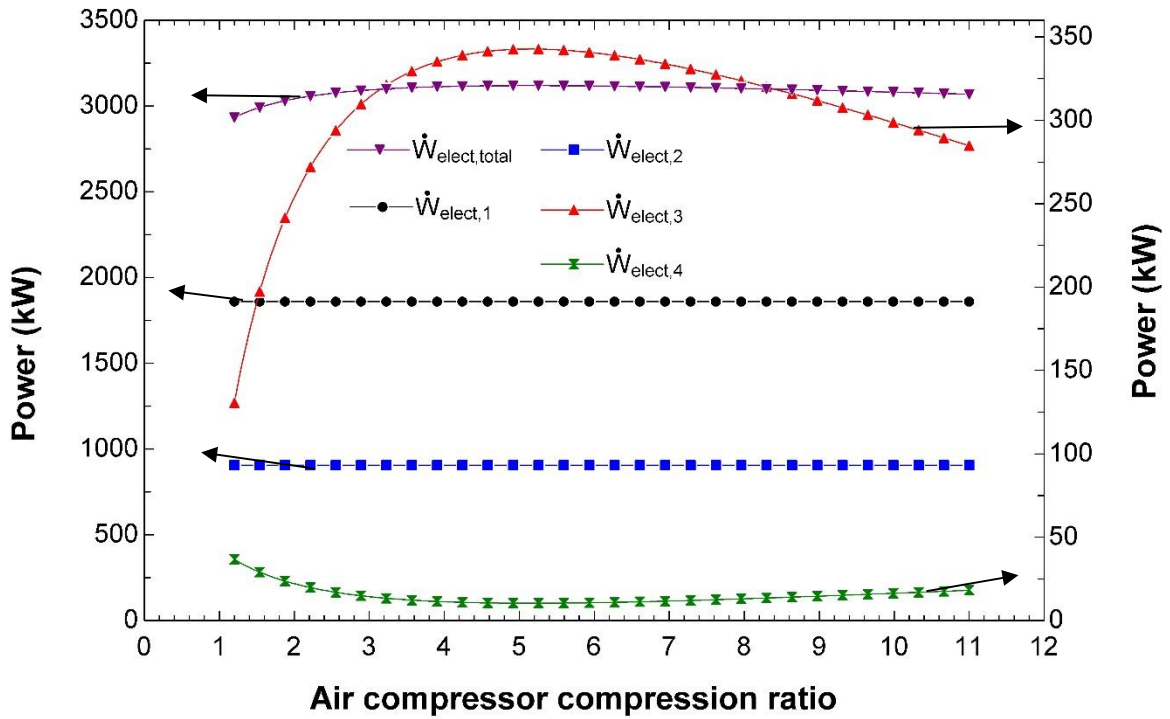


Figure 5.29: Electric power output values of the integrated system and its subsystems are plotted against air compressor compression ratio. Arrows indicate the corresponding axis of the parameter.

In Figure 5.30, the last parameter studied in this subsection is α -parameter and it is varied within a reasonable range of 0.1 to 0.35. As it has been shown in system 1a, increasing this mass flow rate ratio, enhances the values of the overall energetic and exergetic efficiencies. Unlike system 1a, the overall energetic and exergetic efficiencies reach significantly high values when $\alpha = 0.35$. This is because system 3 is much more efficient in producing power than system 1a. For the primary cycle of SOFC-PPCI-GT, it increases linearly with increasing α -parameter. In the ORC, the boiler receives higher temperature exhaust gases with increasing this parameter. As a result, the ORC energetic and exergetic efficiencies increase as shown in the figure. They increase from 2.183% and 7.756% to 5.935% and 18.23, respectively. This increase is more than double.

In Figure 5.31, the power outputs of the PPCI engine and the gas turbine are heavily affected by increasing the value of the α -parameter. They increase from 687.9 kW and 305.2 kW to 1398 kW and 407.8 kW, respectively. Similarly, the ORC power output increases from 5.661 kW to 23.05 kW. However, the SOFC electric power output is almost

constant over the range of α -parameter. These behaviors discussed here are the reasons behind the trends of the energetic and exergetic efficiencies mentioned above.

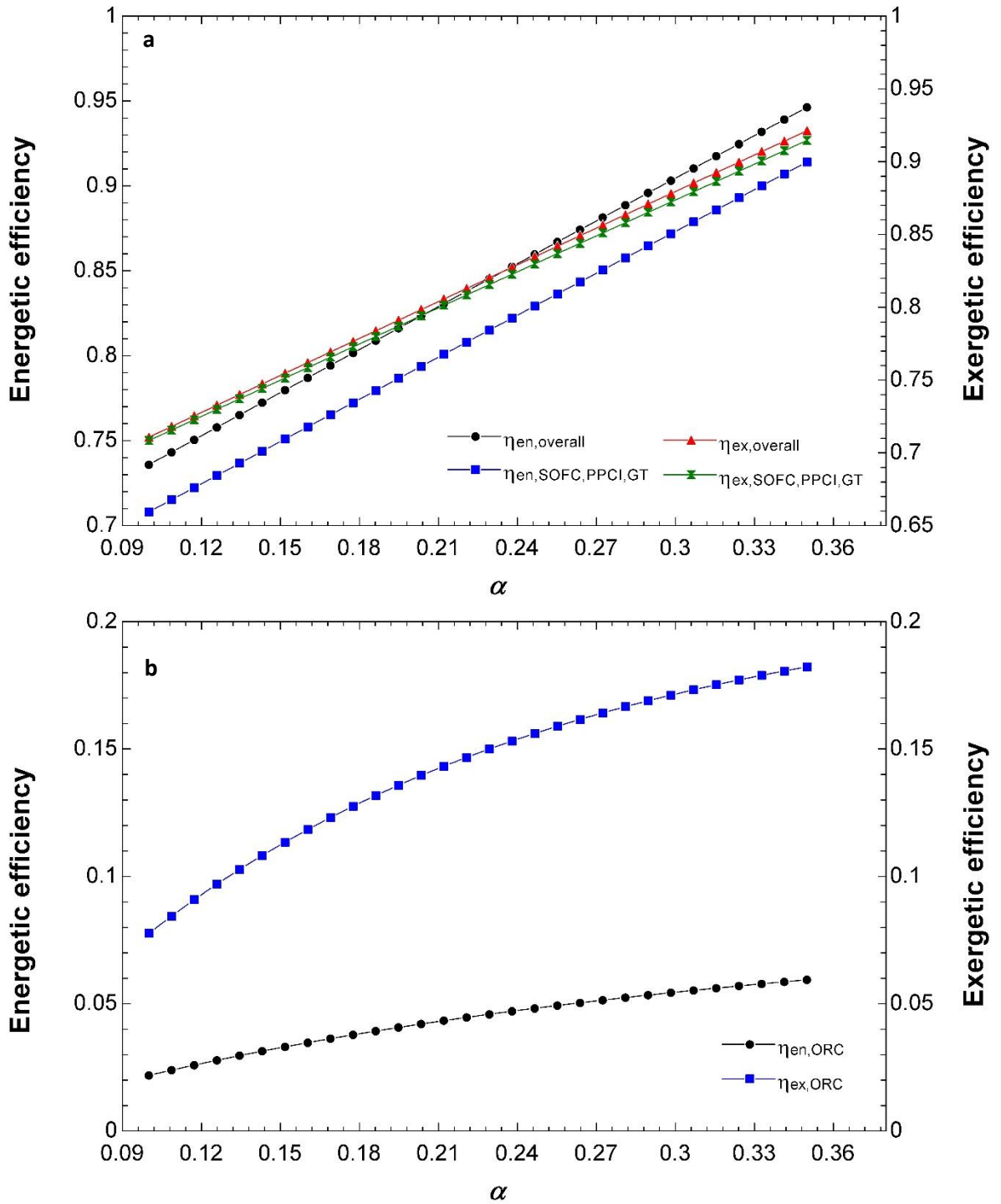


Figure 5.30: Energetic and exergetic efficiencies are plotted against α -parameter. a) For overall integrated system and SOFC-PPCI-GT subsystem. b) For ORC subsystem.

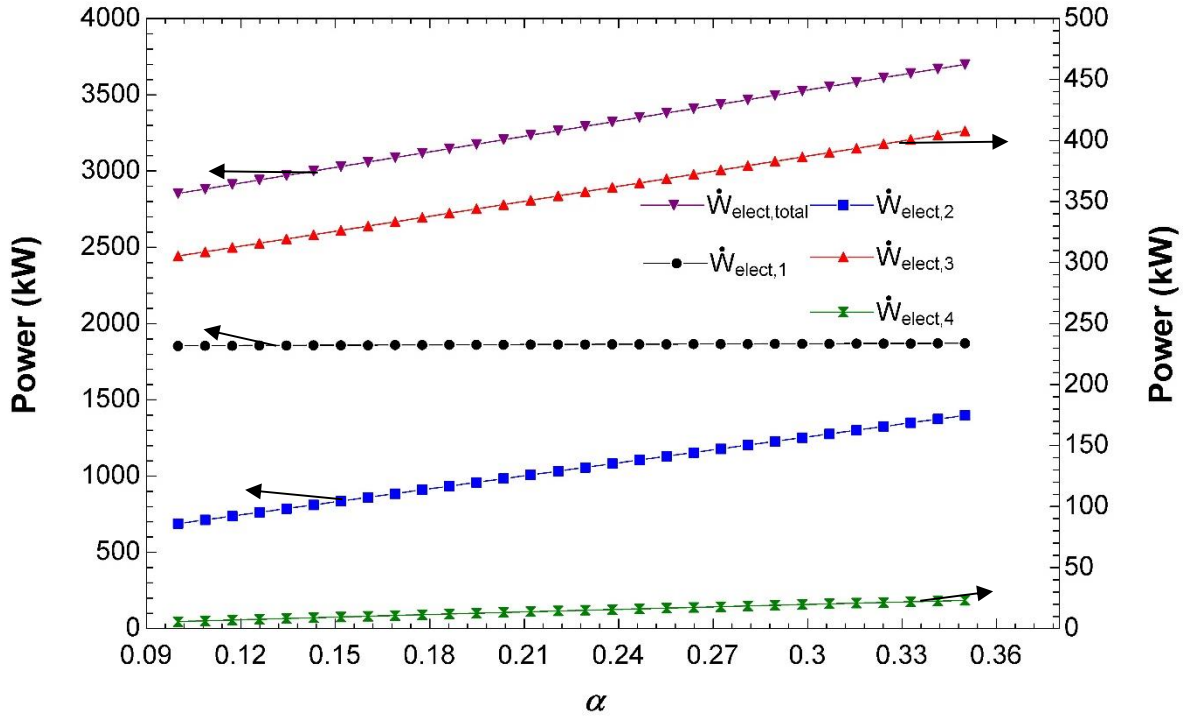


Figure 5.31: Electric power output values of the integrated system and its subsystems are plotted against α -parameter. Arrows indicate the corresponding axis of the parameter.

5.5 System 4 Results

Next, in Figure 3.6, the integrated system is similar to system 1b with an additional feature of recovering the heat loss at the fuel cell which leaves at high temperature. This means it has high exergy (high potential of producing power). One possible way to recover this heat is to absorb it by a stream of water until it evaporates and dropping this heat into a preheated-Organic Rankine Cycle. The effects of this new feature will be studied and compared thermodynamically here.

5.5.1 Reference Case Results

In Table 5.17, the calculated outputs are evaluated from the thermodynamic analysis of the integrated system at the chosen reference case. Adding the preheater has increased the energetic and exergetic efficiencies of the ORC to 13.18% and 63.71%, respectively when compared to system 1b. Also, the power output of the Preheated-ORC is 174.9 kW which is double the value of a regular ammonia-ORC of system 1b. It is interesting to notice that the energetic and exergetic efficiencies of the SOFC-GT subsystem are not changed. However, efficiencies of the SRC have changed slightly. In Figure 5.32, a clear

improvement of the ORC is noticed here. The energetic and exergetic efficiencies have improved by 2.66% and 0.15%, respectively.

Table 5.17: Calculated parameters for the thermodynamic analysis of system 4.

Parameter	Value
SOFC electric power	2053 kW
Gas Turbine (GT) electric power	664 kW
Turbine 2 electric power	232.2 kW
Turbine 3 electric power	174.9 kW
Total electric power of the integrated system	3124 kW
Total power required by the train at maximum load	3100 kW
HX 1 heat transfer rate (cooling mode)	105 kW
SOFC-GT energetic efficiency	61.21%
SOFC-GT exergetic efficiency	61.24%
SRC energetic efficiency	21.23%
SRC exergetic efficiency	46.97%
Preheated-ORC energetic efficiency	13.18%
Preheated-ORC exergetic efficiency	63.71%
Overall energetic efficiency	72.77%
Overall exergetic efficiency	70.50%
Environmental Impact (<i>EI</i>)	0.4185
Sustainability Index (<i>SI</i>)	2.389

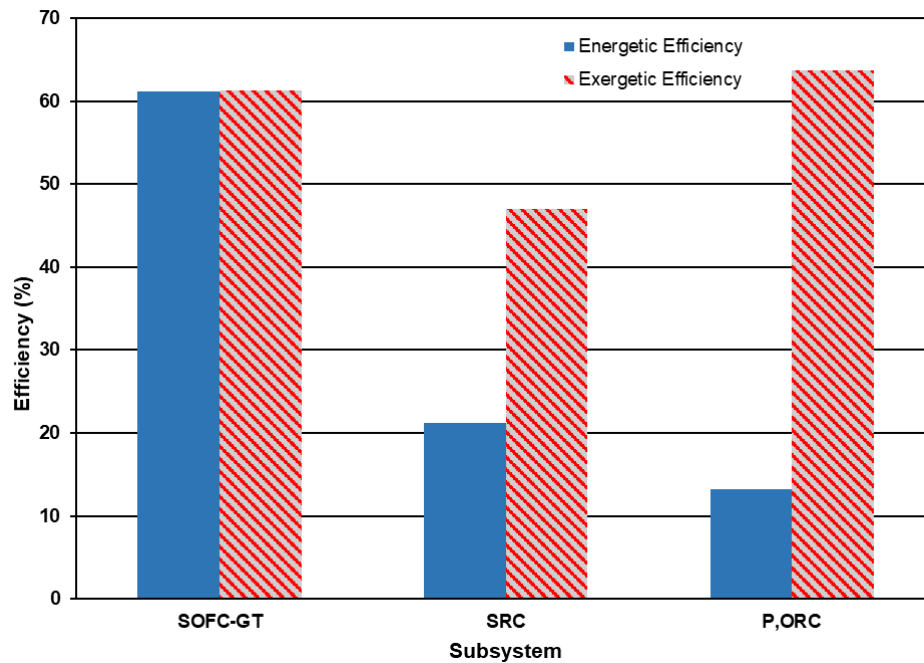


Figure 5.32: Comparison of the energetic and exergetic efficiencies between the subsystems of system 4.

In Table 5.18, a comprehensive list of thermodynamic properties of the state points of system 4 is given. The introduced states of the water feed to absorb the heat loss from the fuel cell are 25, 26, and 27. The temperature of the water leaving the SOFC is at 650 K which is high enough to drive an ORC. The water leaves the integrated system at a temperature close to the environment which is 377.9 K.

Table 5.18: State points and their thermodynamic values of system 4.

State #	Fluid	Temperature (K)	Pressure (kPa)	Specific Enthalpy (kJ kg ⁻¹)	Specific Entropy (kJ kg ⁻¹ K ⁻¹)	Specific Exergy (kJ kg ⁻¹)	Mass Flow Rate (kg s ⁻¹)
1	Air	765.8	400	486.4	6.276	311.8	2.042
2	Methane	800	400	-3097	13.81	52868	0.07225
3	Exhaust+methane+air	950	400	-1130	7.841	481.1	2.114
4	Methane	303	400	-4639	10.93	52198	0.085
5	Exhaust gases	1434	400	-1142	8.435	966.9	2.127
6	Exhaust gases	1070	100	-1632	8.455	469.9	2.127
7	Air	303	100	5.024	5.716	0	2.042
8	Air	486.6	400	191.1	5.797	161.4	2.042
9	Exhaust gases	848.1	100	-1916	8.159	276.3	2.127
10	Exhaust gases	798.4	100	-1978	8.084	237.4	2.127
11	Water	363.3	3500	380.3	1.192	25.61	0.4
12	Water	627.3	3500	3115	6.676	1099	0.4
13	Water	363.1	70	2443	6.882	363.9	0.4
14	Water	363.1	70	376.8	1.192	22.06	0.4
15	Exhaust gases	358	100	-2492	7.154	4.931	2.127
16	Exhaust gases	357.5	100	-2493	7.152	4.839	2.127
17	Water	303	120	125.2	0.4347	0.0201	0.00625
18	Water	353	120	334.4	1.074	15.6	0.00625
19	R134a	268	242.1	247.4	0.9344	23.07	0.8251
20	R134a	334.5	1249	290.1	0.9603	57.97	0.8251
21	R134a	321	1249	120.2	0.4317	48.13	0.8251
22	R134a	268	242.1	120.2	0.4596	39.68	0.8251
23	Methane	800	400	-3097	13.81	52868	0.085
24	Methane	800	400	-3097	13.81	52868	0.01275
25	Water	303	120	125.2	0.4347	0.0201	0.356
26	Water	650	120	3230	8.388	695.3	0.356
27	Water	377.9	120	1826	5.029	308.4	0.356
28	Ammonia	306.8	4000	360.2	1.533	351.4	0.8042
29	Ammonia	351.6	4000	1388	4.5	479.9	0.8042
30	Ammonia	520	4000	2010	6.013	643.4	0.8042
31	Ammonia	418.2	1271	1788	6.072	403.3	0.8042
32	Ammonia	306	1271	355.6	1.533	346.8	0.8042

In Table 5.19, the major components of system 4 are analyzed closely in terms of exergy destruction rates and exergetic efficiencies. First to discuss is the increase in exergy destruction rate from 1252 kW, in system 1b, to 1696 kW. This increase is due to the relatively low temperature of the cooling water leaving the SOFC. It is much lower than the operating temperature of the SOFC which is 950 K. A more detailed study on this will be discussed later. Two added components, namely boiler 2 and preheater have small exergy destruction rates of 6.190 kW and 33.45 kW, respectively. However, the exergetic efficiency of the preheater could improve from the current value of 75.53% by increasing the pressure of ORC working fluid in this heat exchanger. From Figure 5.33, the highest exergy destruction rate is in the fuel cell, reducing this improves the overall performance of the integrated system. It is followed by the combustor and boiler 1 as in system 1b.

5.5.2 Parametric Study Results

Specific parametric studies are performed on the parts of this integrated system related to the preheated-ORC and the cooling water of SOFC. A discussion of these studies is given on the level of enhancement in overall energetic and exergetic efficiencies. Also, the exergy destruction rate of SOFC variation is provided. Two parameters are studied in this subsection, namely state 26 temperature of the cooling water leaving the SOFC, and the mass flow rate of the preheated-ORC.

In Figure 5.34, the overall energetic and exergetic efficiencies are shown to increase as the cooling water temperature leaving the SOFC increases. This increase is linear and they go from 71.96% and 69.68% at 550 K to 73.00% and 70.73% at 680 K, respectively. For the preheated-ORC, the energetic efficiency is enhanced with increasing the temperature. The exergetic efficiency of Preheated-ORC has a concave-down parabolic curve, with a maximum value of 63.91% at 603.8 K. This behavior is because the temperature of the heat source added to the ORC is increasing faster than the increase in the power production of the cycle.

Table 5.19: Exergy destruction rates and exergetic efficiencies of major components of system 4.

Component	Exergy Destruction Rate (kW)	Exergetic Efficiency
Air Compressor	50.38	86.74%
SOFC	1696	79.39%
Combustor	359.8	78.72%
Gas Turbine (GT)	13.12	98.76%
Boiler 1	65.26	86.80%
Turbine 2	24.93	91.51%
Preheater	33.45	75.53%
Boiler 2	6.190	95.51%
Turbine 3	14.55	92.47%
Heater	0.1027	48.66%
Compressor 2	6.461	81.67%
HX 1	0.2536	96.88%

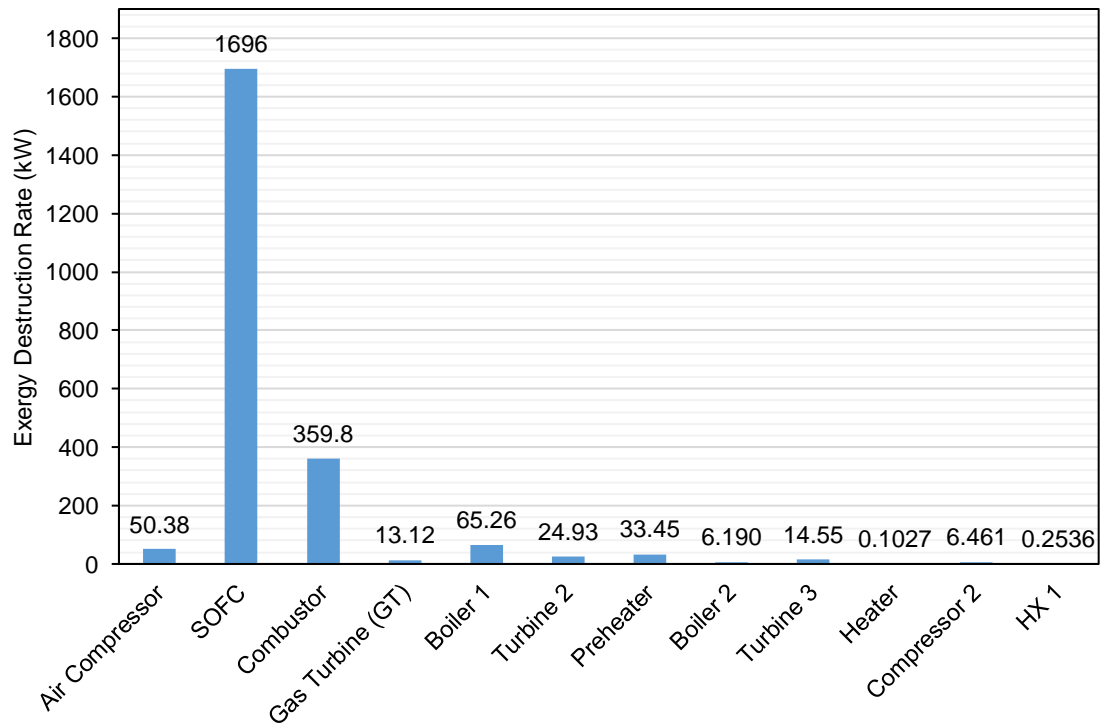


Figure 5.33: Comparison of exergy destruction rates of major components of system 4.

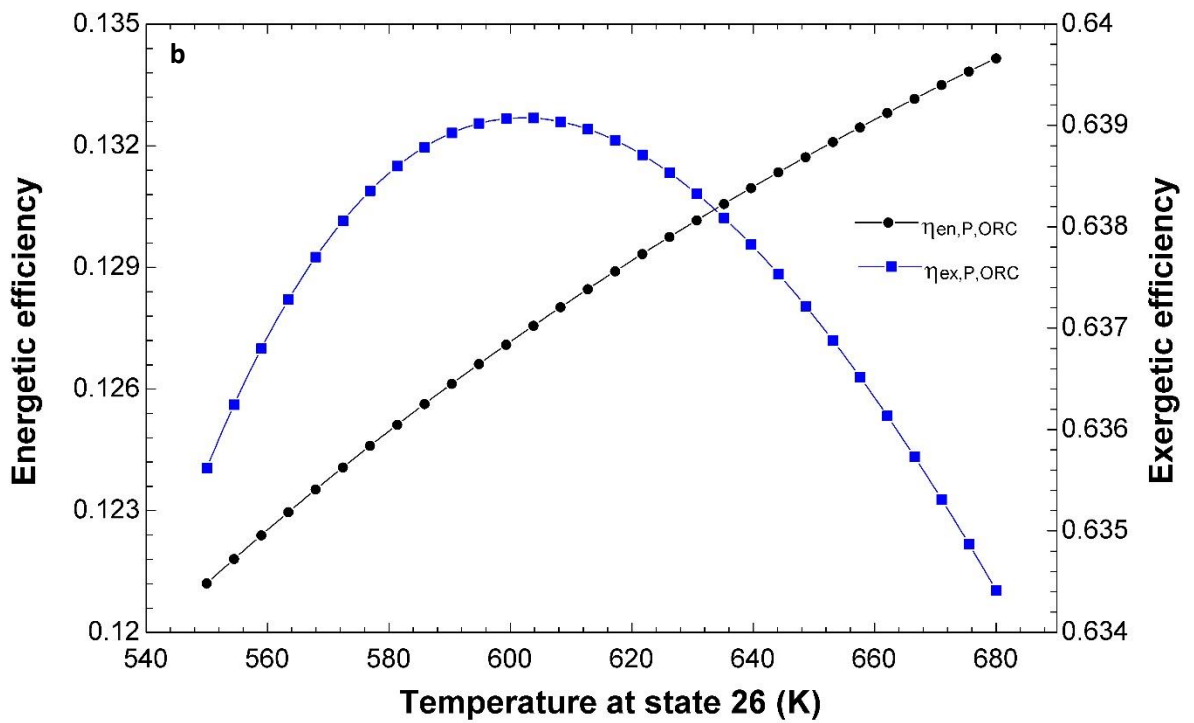
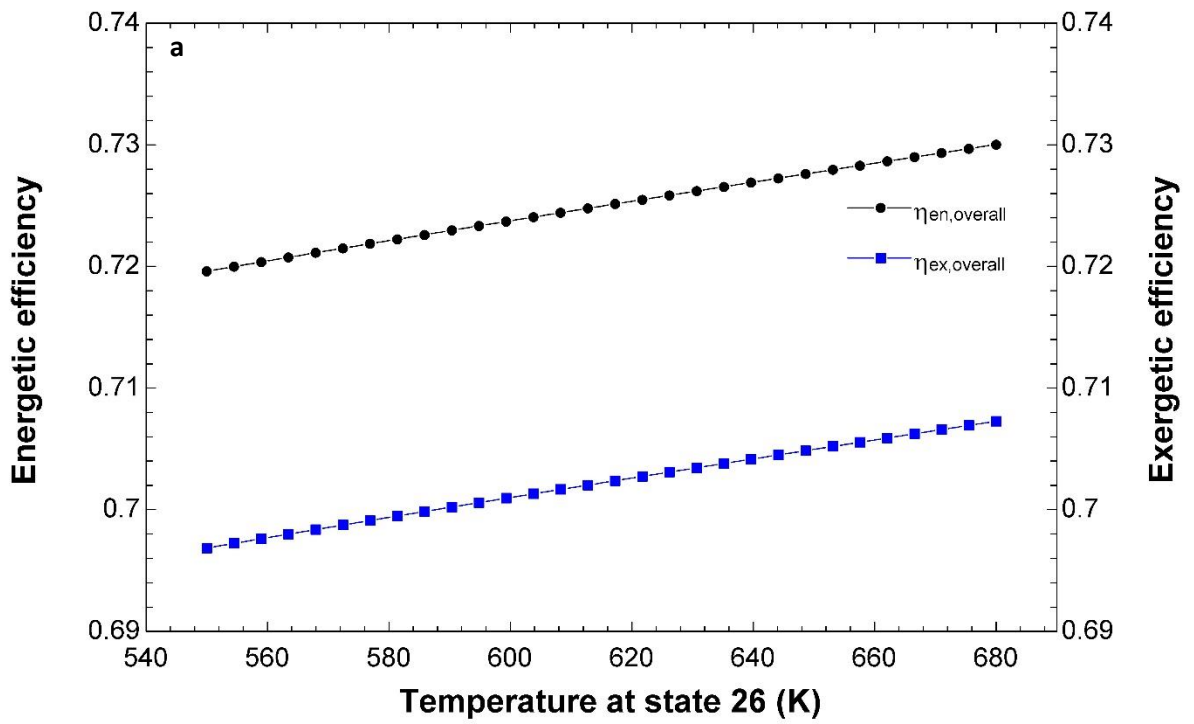


Figure 5.34: Energetic and exergetic efficiencies are plotted against temperature at state 26. a) For overall integrated system. b) For Preheated-ORC subsystem.

In Figure 5.35, two curves are presented. Firstly, the increase in turbine 3 output power with increasing the temperature at state 26. It goes from 138.9 kW to 185.2 kW. This increase explains the increase in energetic efficiency of the preheated-ORC. Secondly, the exergy destruction rate at the fuel cell drops from 1717 kW to 1689 kW. Increasing the cooling water temperature leaving the SOFC gives the fluid more potential to produce power which is exergy. Therefore, the exergy destruction rate decreases as shown in the figure. As this temperature comes closer to the operating temperature of the SOFC, the lower the exergy destruction rate. It also depends on the cooling water pressure.

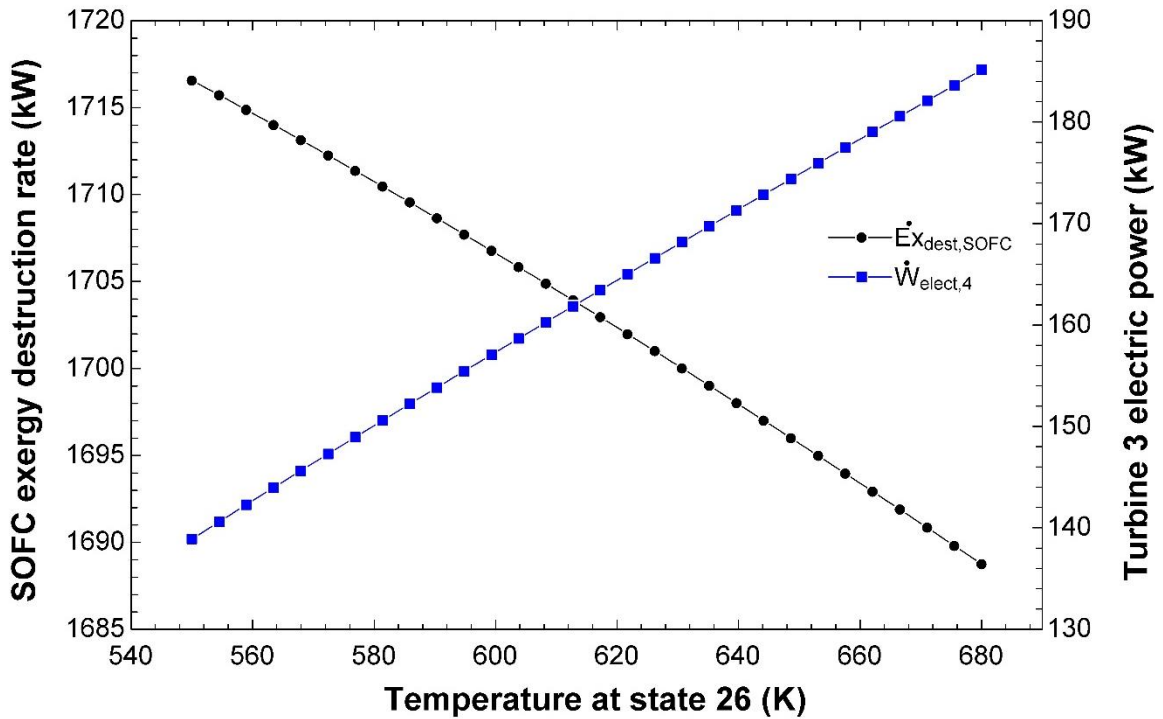


Figure 5.35: SOFC exergy destruction rate and turbine 3 electric power are plotted against temperature at state 26.

In Figure 5.36, the effects of changing the preheated-ORC mass flow rate on the energetic and exergetic efficiencies of the integrated system and ORC are shown. The overall energetic and exergetic efficiencies are linearly increasing with increasing preheated-ORC mass flow rate from 0.7100 kg s^{-1} to 1.100 kg s^{-1} . This change improves the overall energetic and exergetic efficiencies by 1.91% and 1.92%, respectively. Next, the preheated-ORC energetic efficiency remains constant at 13.18% and it is independent of the mass flow rate. This is expected as the efficiency of a Rankine cycle is usually independent of its mass flow rate and only depends on the intensive properties of the cycle.

However, for the exergetic efficiency, it increases nonlinearly with increasing mass flow rate from 63.36% to 64.44%.

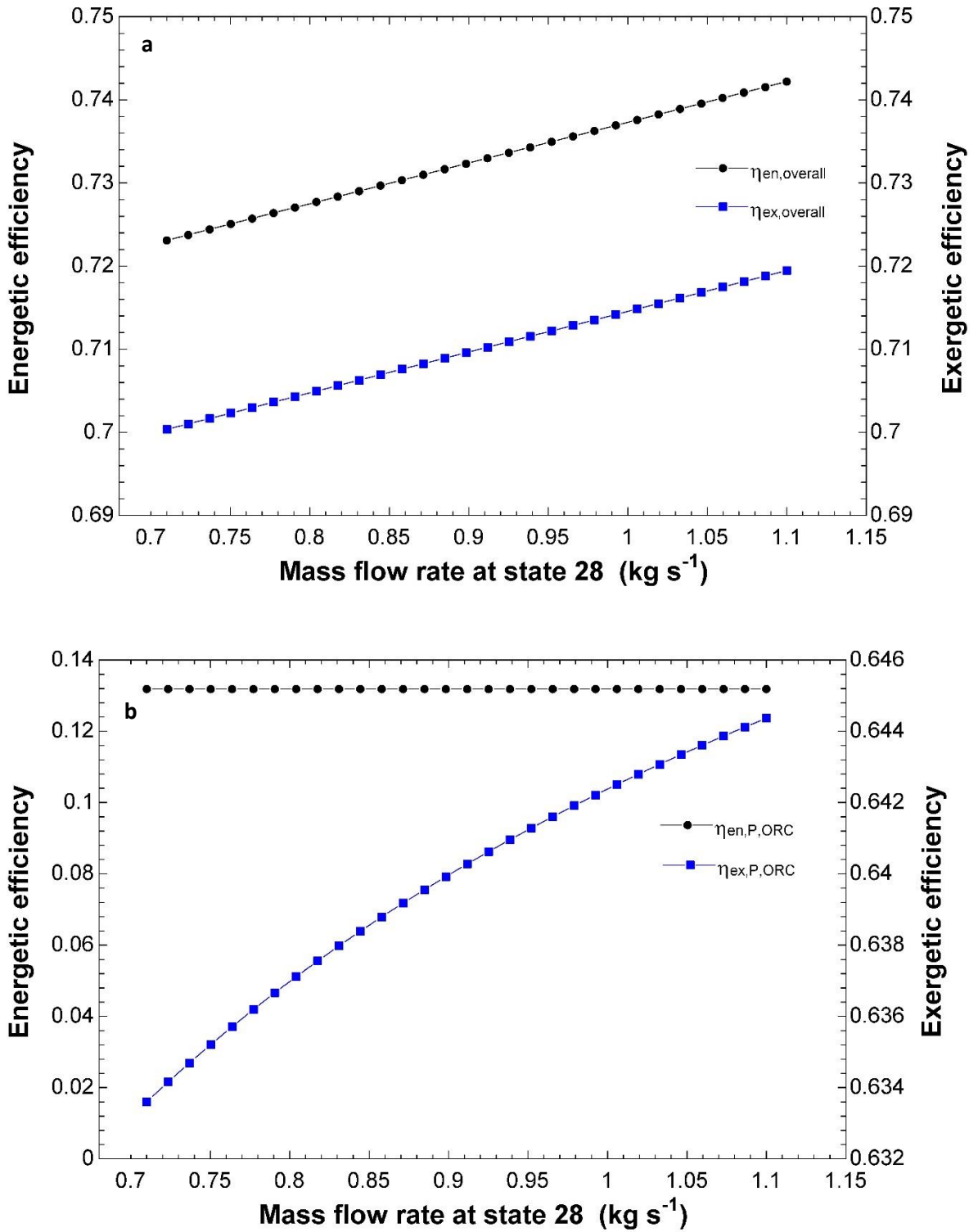


Figure 5.36: Energetic and exergetic efficiencies are plotted against Preheated-ORC mass flow rate (state 26). a) For overall integrated system. b) For Preheated-ORC subsystem.

In Figure 5.37, a normal and expected behavior is shown for the power production of turbine 3. Increasing the mass flow rate, increases the power production of the cycle linearly since the intensive properties of the cycle are fixed. The derivative of this curve is a constant value which is the energetic efficiency of the preheated-ORC as mentioned above. What is interesting, the power production of this ORC can reach a value of 239.2 kW. This is almost three times higher than the ORC cycle power production in system 1b. The above results show a clear justification for the significance of recovering SOFC heat losses to support the ORC.

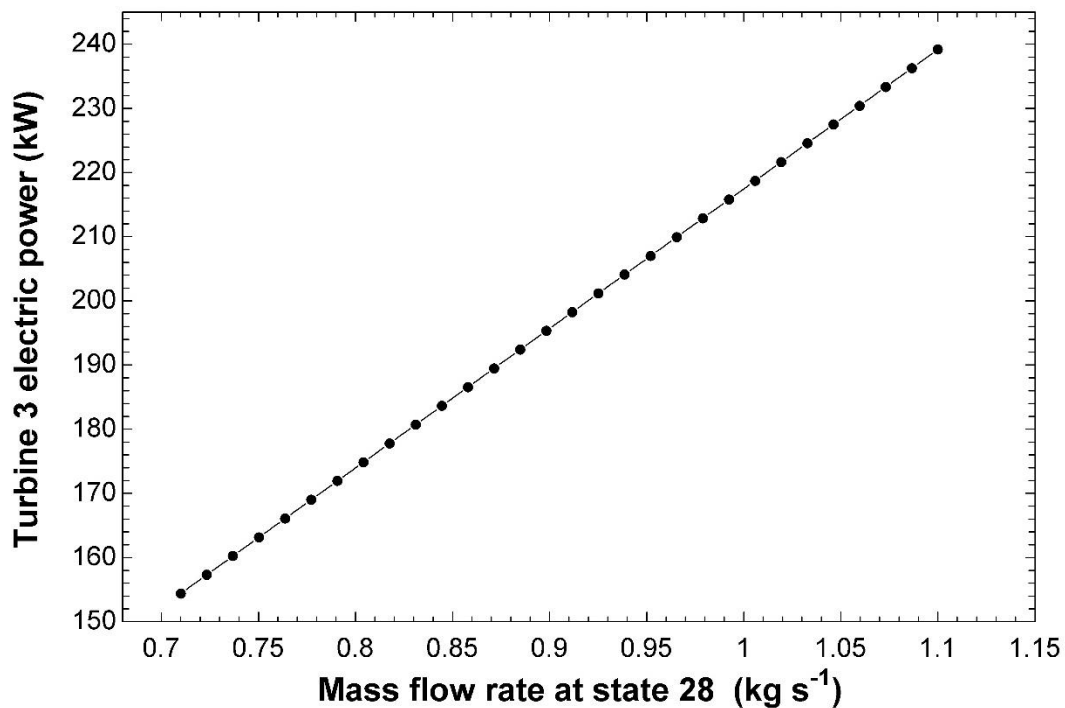


Figure 5.37: Turbine 3 electric power is plotted against Preheated-ORC mass flow rate (state 26).

5.6 System 5 Results

The fifth proposed integrated system for clean railway application is displayed in Figure 3.7. This system is studied and discussed thermodynamically below with the same details and order as previous systems.

5.6.1 Reference Case Results

In Table 5.20, the calculated outputs are evaluated from the thermodynamic modelling of this system. There are three power devices, namely SOFC, GT, and turbine 2 which are

producing output power values of 2158 kW, 782.3 kW, and 170.3 kW, respectively. Notice that the GT power output has increased from around 600 kW in previous systems to 782.3 kW in this system at the same operating pressure difference. The overall energetic and exergetic efficiencies are evaluated at 58.65% and 63.55%, respectively. These values are significantly lower than previous methane-based systems. This system and the next two systems are using ammonia as fuel. Ammonia has much less high heating value than methane as reported in the thermodynamic modelling chapter above. Although this system is exergetically less efficient, its *SI* is still higher than unity which means using ammonia as a fuel can operate a sustainable system without any CO₂ emissions.

In Figure 5.38, looking at the energetic and exergetic efficiencies of SOFC-GT and ORC subsystems, we find that the exergetic efficiencies are higher than their energetic counterparts. The energetic efficiency of the ammonia-ORC is 18.30% which is higher than previous cycles mentioned above which have an average value of 10%. This increase is due to the fact that the heat source is coming directly from the SOFC-GT subsystem not the condenser of a Steam Rankine Cycle.

Table 5.20: Calculated parameters for the thermodynamic analysis of system 5.

Parameter	Value
SOFC electric power	2158 kW
Gas Turbine (GT) electric power	782.3 kW
Turbine 2 electric power	170.3 kW
Total electric power of the integrated system	3110 kW
Total power required by the train at maximum load	3100 kW
Evaporator heat transfer rate (cooling mode)	105 kW
SOFC-GT energetic efficiency	53.61%
SOFC-GT exergetic efficiency	60.00%
ORC energetic efficiency	18.30%
ORC exergetic efficiency	42.96%
Overall energetic efficiency	58.65%
Overall exergetic efficiency	63.55%
Environmental Impact (<i>EI</i>)	0.5735
Sustainability Index (<i>SI</i>)	1.744

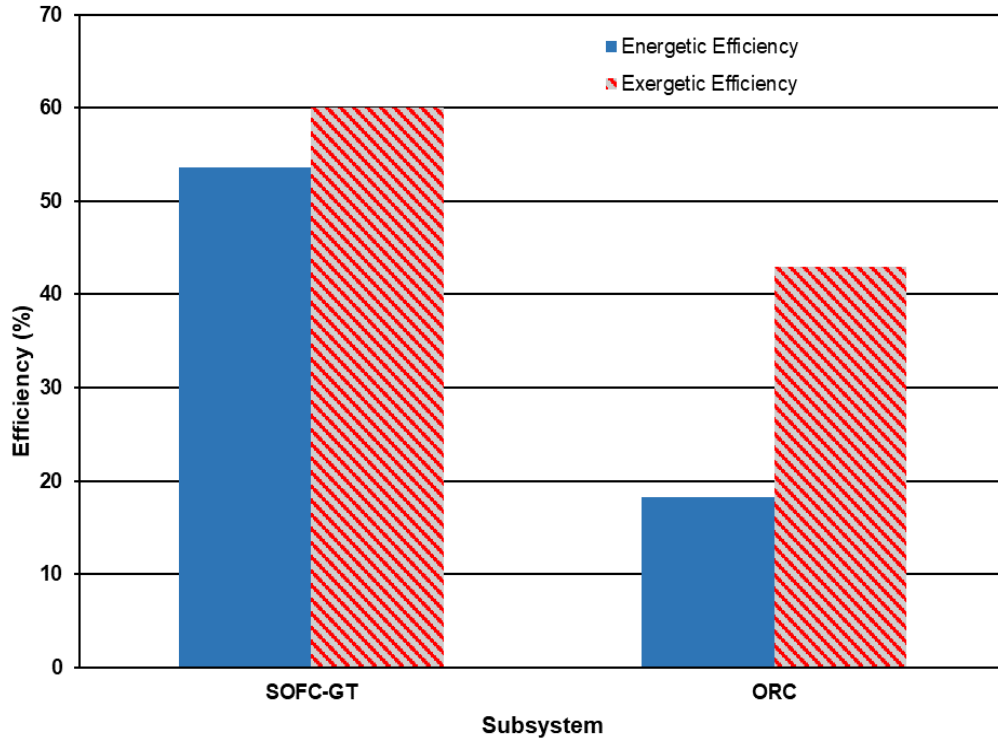


Figure 5.38: Comparison of the energetic and exergetic efficiencies between the subsystems of system 5.

In Table 5.21, the thermodynamic properties of each state point of system 5 are listed. Since the fuel used here is ammonia, the exhaust gases composition is different and it has water vapor, nitrogen, and oxygen. No carbon emissions leave this clean integrated system. Also, most of the working fluid in all the cycles is ammonia or an ammonia mixture.

In Table 5.22, the exergetic efficiencies and exergy destruction rates of major components of the proposed system are reported. The lowest exergetic efficiency is found at the generator and this is because the exhaust gases supporting this device is entering at a high temperature of 738.5 K while the separated ammonia mixture in vapor and liquid forms leave at a lower temperature of only 354.5 K. In Figure 5.39, the three highest exergy destruction rate devices are SOFC, combustor and the boiler. Their calculated values are 1435 kW, 434.7 kW, and 185.6 kW, respectively. The generator exergy destruction rate is found to be significantly high at 46.96 kW, when compared to the evaporator and absorber values of 4.084 kW and 3.072 kW, respectively.

Table 5.21: State points and their thermodynamic values of system 5.

State #	Fluid	Temperature (K)	Pressure (kPa)	Specific Enthalpy (kJ kg ⁻¹)	Specific Entropy (kJ kg ⁻¹ K ⁻¹)	Specific Exergy (kJ kg ⁻¹)	Mass Flow Rate (kg s ⁻¹)
1	Air	765.8	400	486.4	6.276	311.8	2.069
2	Ammonia	800	400	-1416	13.09	20621	0.2074
3	Exhaust+ammonia+air	950	400	-1145	8.368	513.7	2.276
4	Ammonia	303	400	-2687	10.68	20081	0.244
5	Exhaust gases	1385	400	-1150	9.063	983.3	2.313
6	Exhaust gases	1034	100	-1654	9.098	468.1	2.313
7	Air	303	100	5.024	5.716	0	2.069
8	Air	486.6	400	191.1	5.797	161.4	2.069
9	Exhaust gases	840.4	100	-1918	8.816	289.5	2.313
10	Exhaust gases	738.5	100	-2053	8.646	207	2.313
11	Ammonia	299	5000	323.6	1.406	353.1	0.48
12	Ammonia	612.7	5000	2262	6.354	792.1	0.48
13	Ammonia	461.5	1000	1900	6.443	403.9	0.48
14	Ammonia	298	1000	317	1.406	346.5	0.48
15	Exhaust gases	358	100	-2526	7.749	5.353	1.966
16	Exhaust gases	357.4	100	-2526	7.747	5.251	1.966
17	Water	303	120	125.2	0.4347	0.02009	0.00625
18	Water	353	120	334.4	1.074	15.6	0.00625
19	Exhaust gases	738.5	100	-2053	8.646	207	0.3469
20	Exhaust gases	398.9	100	-2477	7.879	15.12	0.3469
21	Ammonia+water	354.5	1500	1435	4.607	387.8	0.09148
22	Ammonia+water	354.5	1500	128.9	1.003	47.76	0.4599
23	Ammonia	800	400	-1416	13.09	20621	0.244
24	Ammonia	800	400	-1416	13.09	20621	0.03661
25	Ammonia+water	310.1	516	1324	4.753	233.4	0.09148
26	Ammonia+water	303.2	516	-97.35	0.2944	57.16	0.5514
27	Ammonia+water	303.2	1500	-96.11	0.2944	58.4	0.5514
28	Ammonia+water	308.5	1500	-80.69	0.3696	29.95	0.4599
29	Ammonia+water	308.7	516	-80.69	0.3735	28.77	0.4599
30	Ammonia+water	341.2	1500	78.74	0.8375	68.7	0.5514
31	Exhaust gases	738.5	100	-2053	8.646	207	1.966
32	Exhaust gases	357.4	100	-2526	7.747	5.251	1.966
33	Ammonia+water	312.4	1500	176.6	0.6882	317.3	0.09148
34	Ammonia+water	278.6	516	176.6	0.6885	317.2	0.09148

5.6.2 Parametric Study Results

Moreover, the performance of this integrated system is looked at more thoroughly in terms of its energetic and exergetic efficiencies. Two parameters are studied here, namely the air

compressor compression ratio and the ORC boiler pressure (state 12). The latter will be varied from subcritical to supercritical to see its effects on power production and overall performance of the integrated system.

Table 5.22: Exergy destruction rates and exergetic efficiencies of major components of system 5.

Component	Exergy Destruction Rate (kW)	Exergetic Efficiency
Air Compressor	51.04	86.74%
SOFC	1435	85.03%
Combustor	434.7	77.41%
Gas Turbine (GT)	24.29	97.96%
Boiler	185.6	60.19%
Turbine 2	12.88	93.09%
Heater	0.1027	48.66%
Generator	46.96	29.45%
Evaporator	4.084	46.74%
Absorber	3.072	91.12%

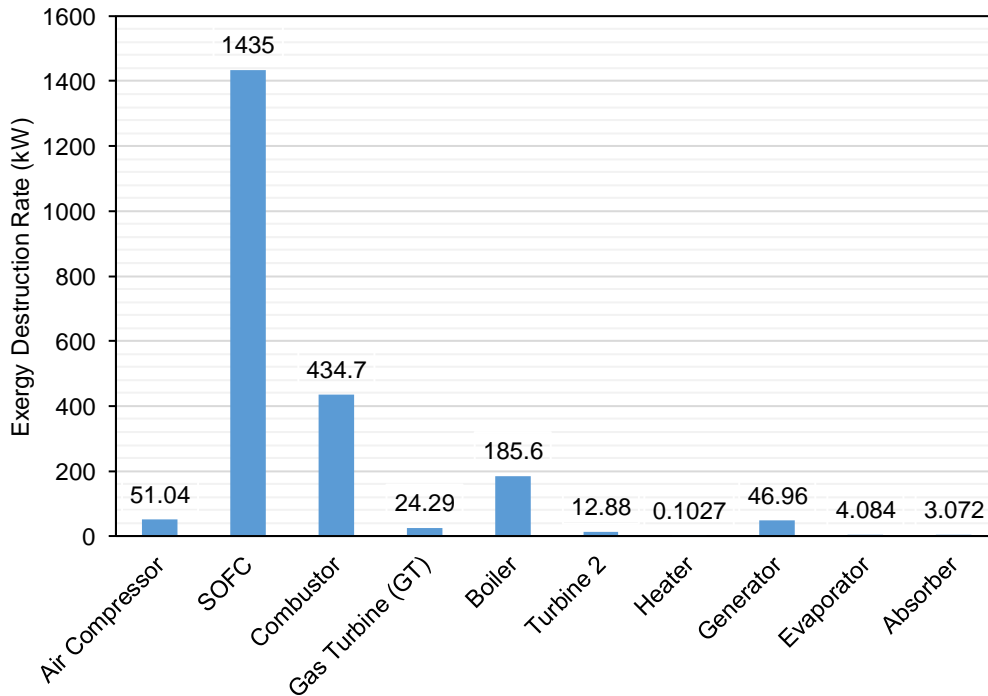


Figure 5.39: Comparison of exergy destruction rates of major components of system 5.

In Figure 5.40, the compression ratio effects on the energetic and exergetic efficiencies are plotted. As seen in previous systems, increasing the compression ratio causes nonlinear and parabolic trends of the overall energetic and exergetic efficiencies of the integrated

systems. This is mainly because of the Brayton cycle which is the air compressor and gas turbine combination. The overall system is maximized at a higher compression ratio than system 1a. It is optimized at a compression ratio of 11.67 and the energetic and exergetic efficiencies are 61.46% and 66.18%, respectively. At the same ratio, the ORC energetic and exergetic efficiencies are locally minimized with values of 16.66% and 42.25%, respectively. This decrease is because less energy and exergy are supplied to the cycle. Another point to be addressed is the exergetic efficiency of the ORC is extremely low at low compression ratios. This is because the heat is supplied at high temperatures and the power production is low comparatively. However, with an initial increase of compression ratio, the temperature at state 31 decreases and becomes within the same level as the power production of the ORC. This is the reason for the existence of a maximum point of 42.99% at a compression ratio of 4.531. After this point, the exergetic efficiency decreases as less energy is supplied to the cycle.

In Figure 5.41, a more detailed visual representation of the effects of compression ratio on the power production devices is offered. Firstly, the SOFC is unaffected by this variation of compression ratio. Secondly, the total power production trend is dominated by the gas turbine and not by the ORC power output. At a compression ratio of 11.67, the GT power production and turbine 2 output power are 979.7 kW and 127 kW, respectively.

In Figure 5.42, the second parameter of this study is considered, that is the ORC pressure at the boiler. As this pressure increases, the overall and ORC performances are enhanced energetically and exergetically. The improvement in ORC is clearly noticed, and it causes the overall energetic and exergetic efficiencies to improve by 2.46% and 2.75%, respectively. Here, the pressure of the ORC working fluid (ammonia) is increased beyond its critical value, which is 11333 kPa. So, taking this ORC to supercritical operation is recommended. Some safety issues might arise with this as this cycle is to be operated on a passenger train [88].

In Figure 5.43, the power output of the ORC is increasing nonlinearly from as low as 104.2 kW to 238.7 kW. At the same time, the exergy destruction rate at the boiler decreases. This means that the higher the working fluid pressure of the ORC, the more power potential is supplied to the cycle.

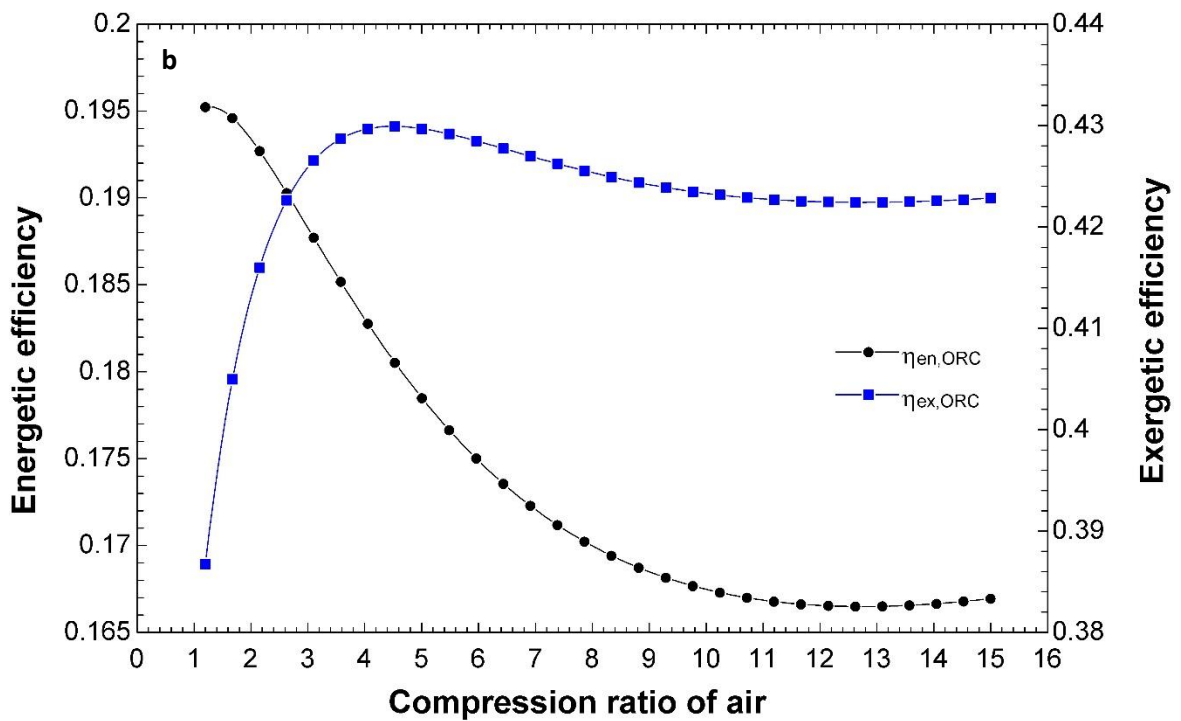
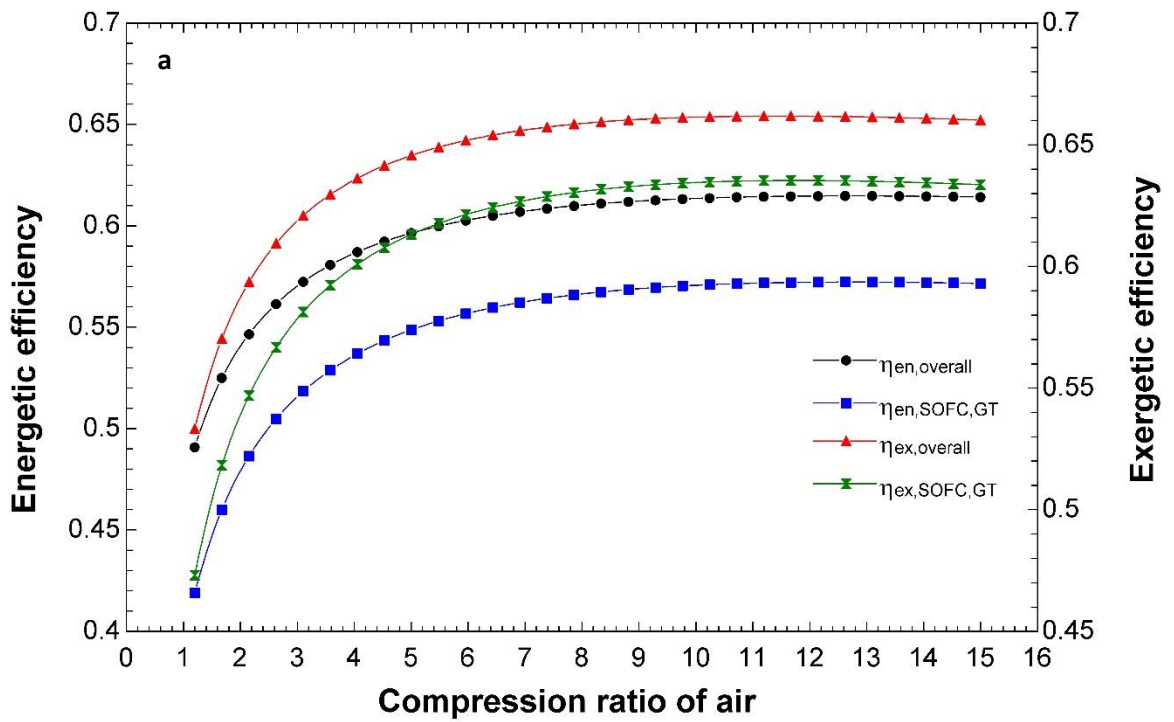


Figure 5.40: Energetic and exergetic efficiencies are plotted against compression ratio across the air compressor. a) For overall integrated system and SOFC-GT subsystem. b) For NH₃-ORC subsystem.

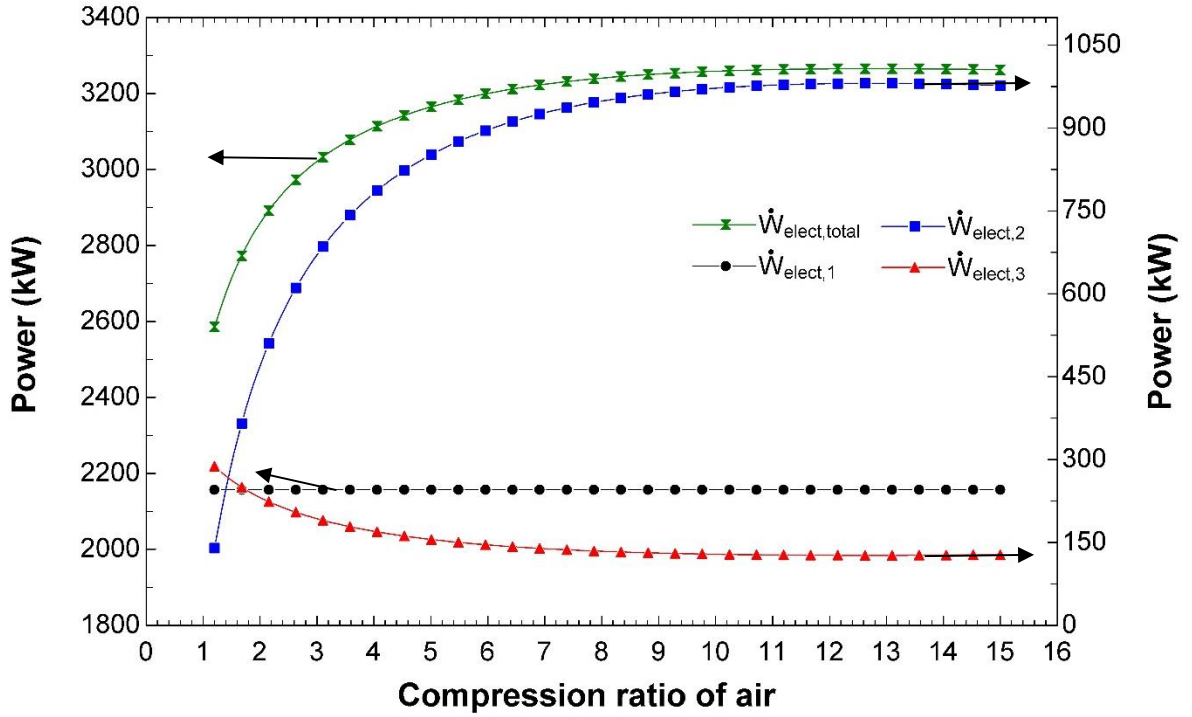


Figure 5.41: Electric power output values of the integrated system and its subsystems are plotted against compression ratio across the air compressor. Arrows indicate the corresponding axis of the parameter.

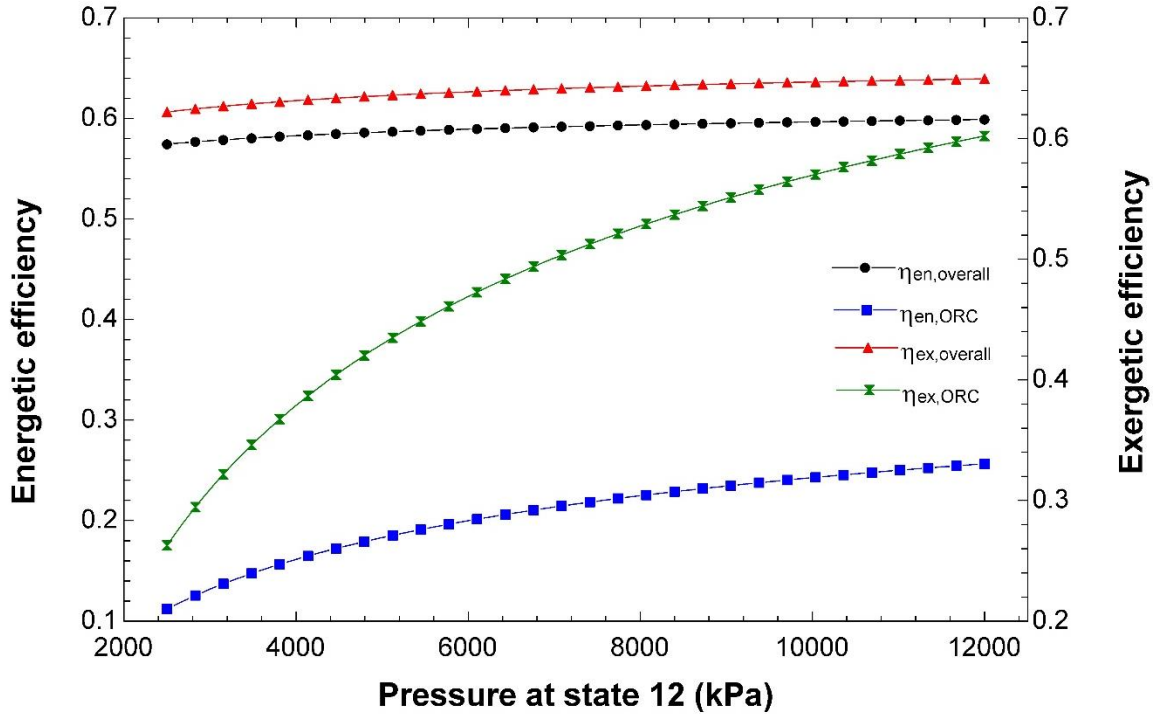


Figure 5.42: Energetic and exergetic efficiencies are plotted against ORC boiler pressure (state 12), for overall integrated system and NH_3 -ORC subsystem.

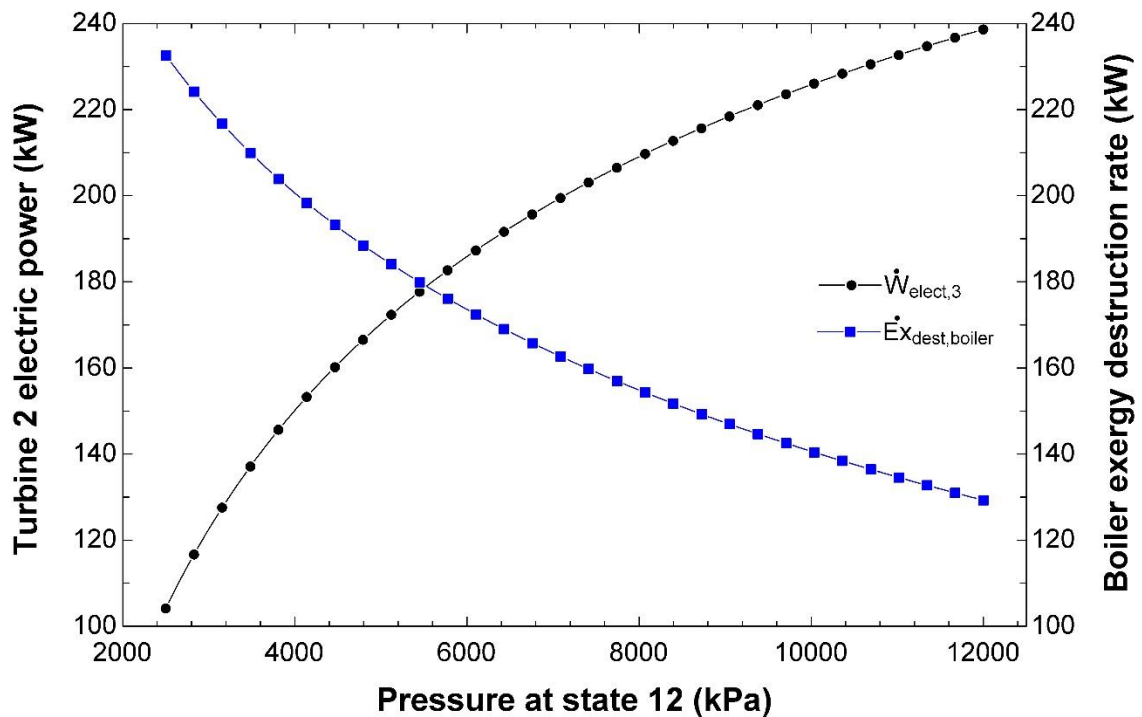


Figure 5.43: Turbine 2 electric power and boiler exergy destruction rate are plotted against ORC boiler pressure which is at state 12.

5.7 System 6 Results

The integrated SOFC-GT-SRC-ORC system with ammonia-DSU and PEMFC is shown in Figure 3.8. This system features onboard hydrogen production and uses a cascaded SRC-ORC subsystem in parallel. Here, we present some thermodynamic and parametric analyses for this system.

5.7.1 Reference Case Results

The ratios related to ammonia redirecting to ADSU (β) and the other related to hydrogen storage (ϵ) are set to 1% and 10%, respectively. Furthermore, for the PEM fuel cell, the energetic efficiency is set to 46% and the PEMFC excess air factor is 1.

In Table 5.23, the total output power of the integrated system is 3107 kW, which is sufficient to drive a passenger locomotive as mentioned before. It is coming from six different power devices, two fuel cells, and 4 turbines. 89.99% of the total power production is coming from the SOFC-GT subsystem which means that this subsystem controls the performance of the integrated system as expected. Also, the rate of stored

hydrogen in the tank is reported to be $0.0000348 \text{ kg s}^{-1}$. This is only 10% of the hydrogen stream leaving the ADSU. The rest goes to the PEM fuel cell and produce 17.99 kW. The ADSU-PEMFC subsystem contributes a marginal fraction of 0.5906% of the total power produced. This can be increased by changing the β and ε parameters. Looking at the entire system, the overall energetic and exergetic efficiencies are 61.20% and 66.30%, respectively. Also, the proposed system is a sustainable system with an SI value of 1.967.

In Figure 5.44, a clear comparison between the subsystems is presented. It is interesting to see that the ADSU-PEMFC subsystem is more efficient energetically than both SRC and ORC. It has a value of 46.50%. Exergetically, it falls between SRC and ORC values with a value of 51.31%.

Table 5.23: Calculated parameters for the thermodynamic analysis of system 6.

Parameter	Value
SOFC electric power	2052 kW
Gas Turbine (GT) electric power	743.9 kW
Turbine 2 electric power	210.7 kW
Turbine 3 electric power	82.73 kW
PEMFC electric power	17.99 kW
Turbine 4 electric power	0.3613 kW
Total electric power of the integrated system	3107 kW
Total power required by the train at maximum load	3100 kW
HX 1 heat transfer rate (cooling mode)	105 kW
Hydrogen storage rate (state 30)	$0.0000348 \text{ kg s}^{-1}$
SOFC-GT energetic efficiency	53.15%
SOFC-GT exergetic efficiency	59.50%
SRC energetic efficiency	20.40%
SRC exergetic efficiency	48.04%
ORC energetic efficiency	10.52%
ORC exergetic efficiency	63.56%
ADSU-PEMFC energetic efficiency	46.50%
ADSU-PEMFC exergetic efficiency	51.31%
Overall energetic efficiency	61.20%
Overall exergetic efficiency	66.30%
Environmental Impact (EI)	0.5083
Sustainability Index (SI)	1.967

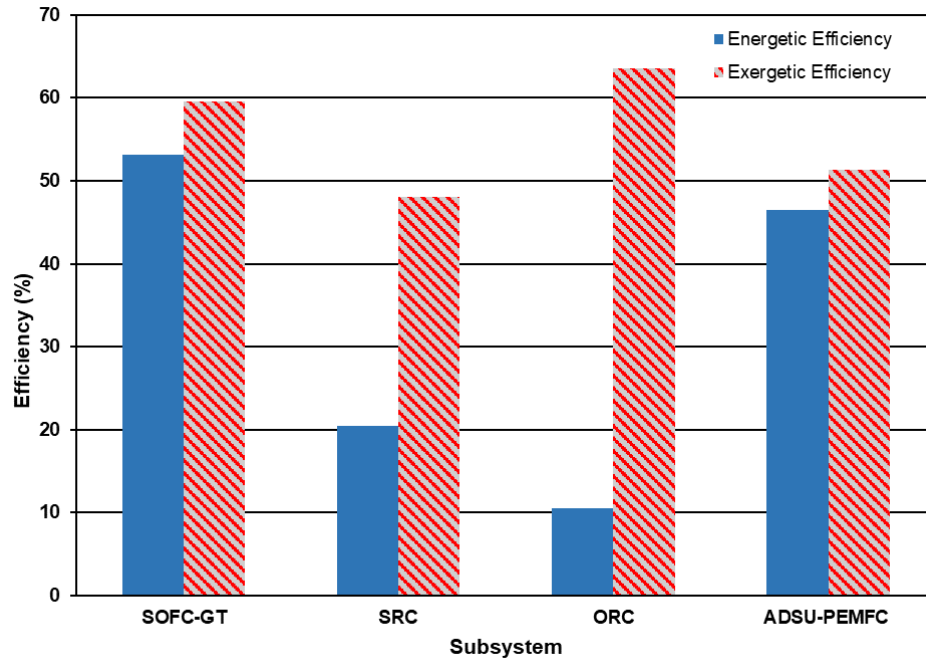


Figure 5.44: Comparison of the energetic and exergetic efficiencies between the subsystems of system 6.

In Table 5.24, a comprehensive list of thermodynamic properties of system 6 is provided. The first thing to notice is the separation of ammonia to hydrogen and nitrogen. They leave the unit at a temperature of 735.6 K. The nitrogen gas gets expanded in turbine 4 and leaves the integrated system at a temperature of 530.5 K and atmospheric pressure. More energy can be recovered from this stream. Like the previous system, all the exhaust gases are carbon-free since ammonia and hydrogen are used as fuels.

In Table 5.25, major components of the integrated system are examined in terms of their exergy destruction rates and exergetic efficiencies. The ADSU and turbine 4 are performing very well as they have exergetic efficiencies of 97.61% and 92.78%, respectively at this reference case. However, the PEM fuel cell has a lower exergetic efficiency of 49.98%. This is because we assumed an energetic efficiency of 46%. Increasing this, enhances this device exergetic efficiency and power production. In Figure 5.45, these major components are compared to see the highest exergy destruction rates. As found in previous systems except system 3, the highest two exergy destruction rates are in SOFC and combustor with values of 1364 kW and 413.4 kW. The third one is the air compressor and not the boiler as in the previous integrated systems. The boiler exergy destruction rate has decreased down to 39.52 kW because less temperature of exhaust gases

are supplied to the boiler. This is expected since some of the energy is used at the ADSU before reaching the boiler. Furthermore, the PEM fuel cell has a relatively high exergy destruction rate of 18.87 kW compared to the ADSU and turbine 4 which have rates of 1.053 kW and 0.02811, respectively.

Table 5.24: State points and their thermodynamic values of system 6.

State #	Fluid	Temperature (K)	Pressure (kPa)	Specific Enthalpy (kJ kg ⁻¹)	Specific Entropy (kJ kg ⁻¹ K ⁻¹)	Specific Exergy (kJ kg ⁻¹)	Mass Flow Rate (kg s ⁻¹)
1	Air	765.8	400	486.4	6.276	311.73	1.967
2	Ammonia	800	400	-1416	13.09	20621	0.1972
3	Exhaust+ammonia+air	950	400	-1145	8.368	513.7	2.164
4	Ammonia	303	400	-2687	10.68	20081	0.234
5	Exhaust gases	1385	400	-1150	9.063	983.3	2.199
6	Exhaust gases	1034	100	-1654	9.098	468.1	2.199
7	Air	303	100	5.024	5.716	0	1.967
8	Air	486.6	400	191.1	5.797	161.4	1.967
9	Exhaust gases	840.4	100	-1918	8.816	289.5	2.199
10	Exhaust gases	737.6	100	-2054	8.644	206.3	2.199
11	Water	363.3	3500	380.3	1.192	25.61	0.4
12	Water	567	3500	2962	6.419	1023	0.4
13	Water	363.1	70	2343	6.608	347.5	0.4
14	Water	363.1	70	376.8	1.192	22.06	0.4
15	Exhaust gases	358	100	-2526	7.749	5.353	2.199
16	Exhaust gases	357.5	100	-2526	7.747	5.263	2.199
17	Water	303	120	125.2	0.4347	0.02009	0.00625
18	Water	353	120	334.4	1.074	15.6	0.00625
19	R134a	268	242.1	247.4	0.9344	23.07	0.8251
20	R134a	334.5	1249	290.1	0.9603	57.97	0.8251
21	R134a	321	1249	120.2	0.4317	48.13	0.8251
22	R134a	268	242.1	120.2	0.4596	39.68	0.8251
23	Ammonia	800	400	-1416	13.09	20621	0.234
24	Ammonia	800	400	-1416	13.09	20621	0.03481
25	Ammonia	800	400	-1416	13.09	20621	0.001972
26	Exhaust gases	735.6	100	-2056	8.64	204.8	2.199
27	Nitrogen	735.6	400	465.8	7.385	300.5	0.001624
28	Nitrogen	530.5	100	243.4	7.442	60.74	0.001624
29	Hydrogen	735.6	400	6335	72.17	122159	0.000348
30	Hydrogen	735.6	400	6335	72.17	122159	0.0000348
31	Hydrogen	735.6	400	6335	72.17	122159	0.0003132
32	Hydrogen	735.6	100	6335	77.88	120426	0.0003132
33	Air	303	100	5.024	5.716	0	0.01075
34	Exhaust gases	353	100	-3351	7.979	4.671	0.01106
35	Ammonia	306.8	4000	360.2	1.533	351.4	0.7028
36	Ammonia	352.2	4000	1479	4.761	492.5	0.7028
37	Ammonia	306	1271	1357	4.806	356.7	0.7028
38	Ammonia	306	1271	355.6	1.533	346.8	0.7028

Table 5.25: Exergy destruction rates and exergetic efficiencies of major components of system 6.

Component	Exergy Destruction Rate (kW)	Exergetic Efficiency
Air Compressor	48.54	86.74%
SOFC	1364	85.03%
Combustor	413.4	77.41%
Gas Turbine (GT)	23.10	97.96%
Boiler	39.52	90.99%
Turbine 2	22.94	91.51%
HX3	31.00	76.19%
Turbine 3	9.458	90.09%
Heater	0.1029	48.63%
Compressor 2	6.461	81.67%
HX 1	0.2536	96.88%
ADSU	1.053	97.61%
PEMFC	18.87	49.98%
Turbine 4	0.02811	92.78%

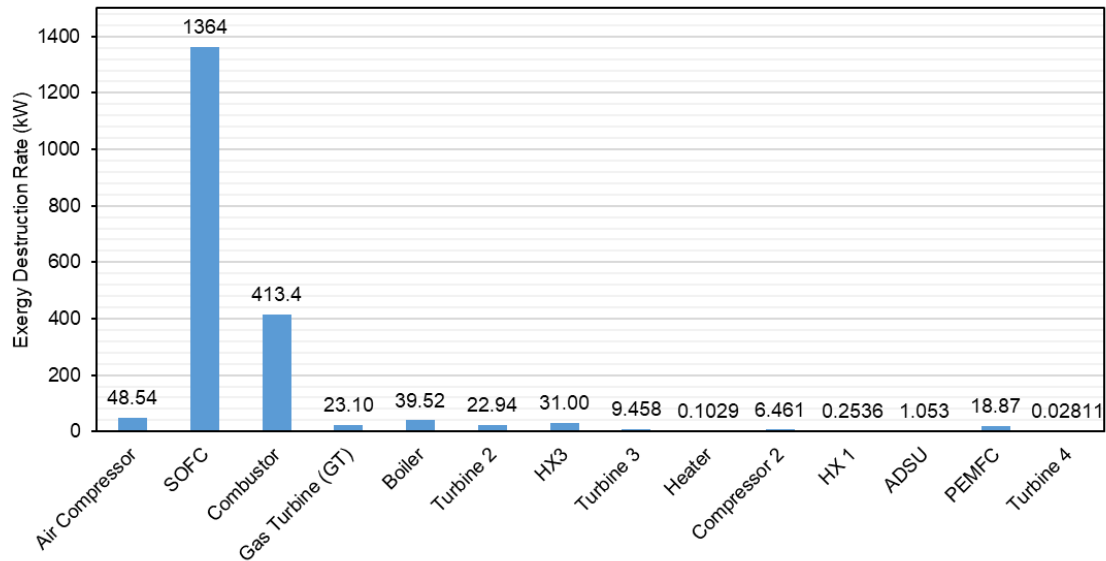


Figure 5.45: Comparison of exergy destruction rates of major components of system 6.

5.7.2 Parametric Study Results

Now, parametric investigations of the performance of the integrated system are given. Three parameters are varied, namely β , ε , and PEM fuel cell energetic efficiency. In Figure 5.46, the plots of the energetic and exergetic efficiencies of the integrated system and its four subsystems are shown. The first parameter to be studied is the β -parameter which determines the ratio of ammonia fuel that goes to the Ammonia

Dissociation and Separation Unit (ADSU). As this ratio increases from zero to 0.5, the overall energetic and exergetic efficiencies decrease from 61.32% and 66.45% to 56.99% and 61.07%, respectively. This decrease is not as dramatic as the efficiency reduction in the SOFC-GT subsystem because the energetic and exergetic efficiencies of the ADSU-PEMFC subsystem increases with increasing value of β -parameter. For SRC, the energetic and exergetic efficiencies decrease nonlinearly, but the ORC is not affected by this parameter.

In Figure 5.47, the power output of the six power devices is plotted against the β -parameter to see the effects of this parameter on them. The power output of SOFC, GT, SRC, ORC all decrease as more ammonia stream goes through the ADSU instead of being directly injected to the SOFC. Although the power output of the PEM fuel cell and turbine 4 increase, the total power production decreases as the other power devices have more significant reductions in power outputs. It is interesting to see that the PEMFC increases its power production from zero up to 627.2 kW at $\beta = 0.5$.

In Figure 5.48, the second parameter, namely ε , is changed over a range of 0 to 0.5 to see its effects on the overall energetic and exergetic efficiencies as well as the ADSU-PEMFC efficiencies. The more hydrogen stored in the tank, the higher the energetic and exergetic efficiencies of the ADSU-PEMFC which go from 40.64% and 46.20% to 69.95% and 71.76%, respectively. Although this increase in performance is tremendous, it does not affect the overall performance of the integrated system by much. The overall energetic and exergetic efficiencies improve only by 0.28% and 0.24%, respectively.

In Figure 5.49, as expected, the more hydrogen fuel is stored, the less of it is supplied to the PEM fuel cell which decreases both the power production and the exergy destruction rate linearly at the power device. They reduce from 19.99 kW and 20.96 kW down to 9.996 kW and 10.48 kW, respectively. A reduction of almost 10 kW of power produced in the PEM fuel cell which is not significant but it can be more dramatic if the β -parameter has a higher value as discussed previously.

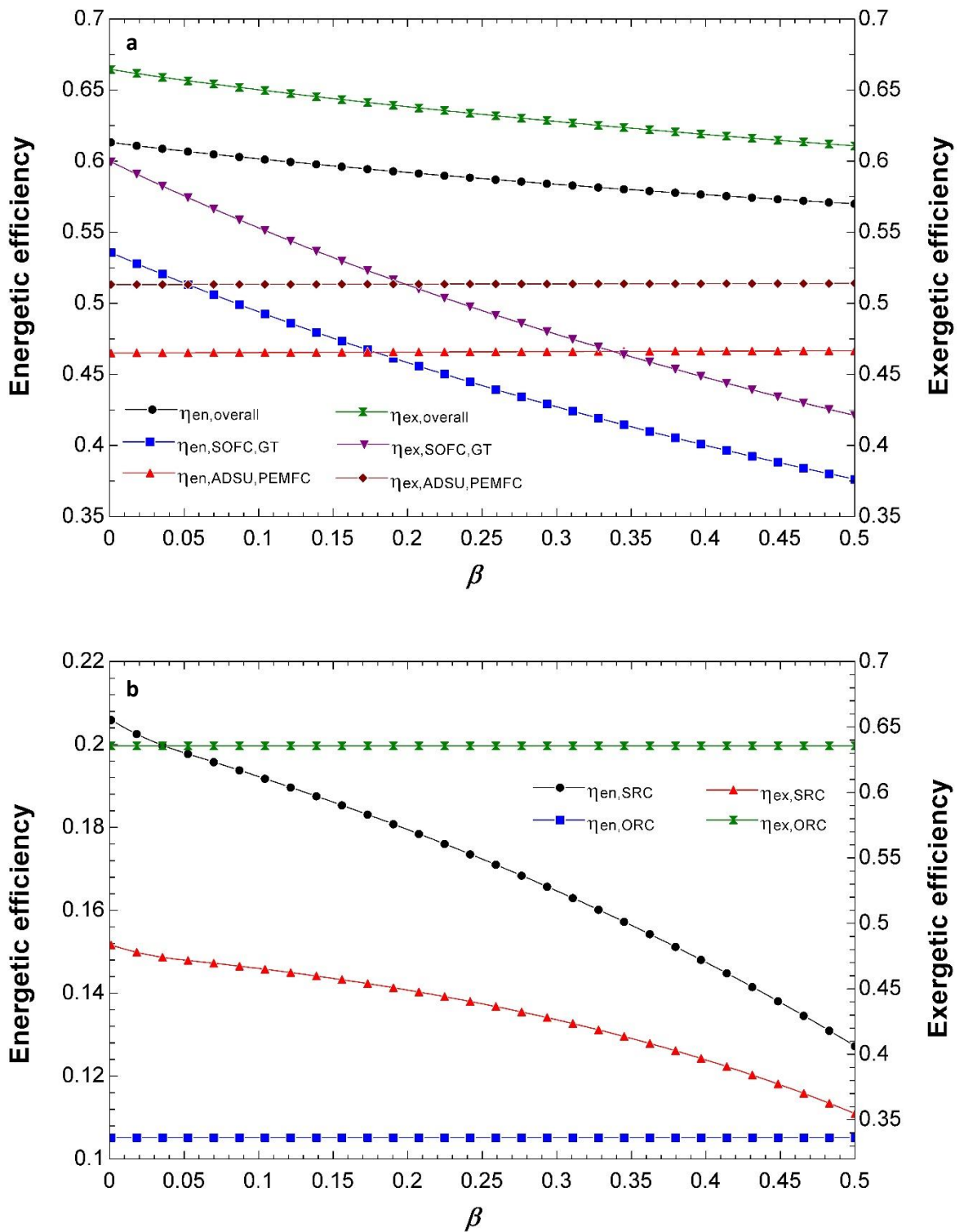


Figure 5.46: Energetic and exergetic efficiencies are plotted against β -parameter. a) For overall integrated system, SOFC-GT and ADSU-PEM subsystems. b) For SRC and NH₃-ORC subsystems.

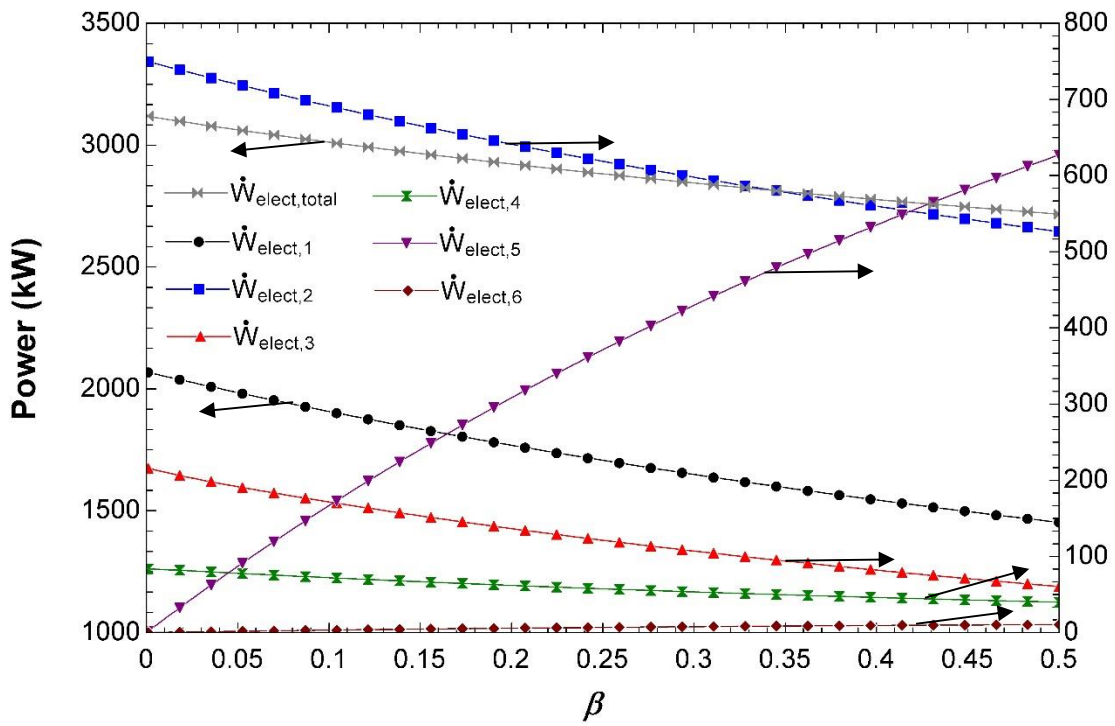


Figure 5.47: Electric power output values of the integrated system and its subsystems are plotted against β -parameter. Arrows indicate the corresponding axis of the parameter.

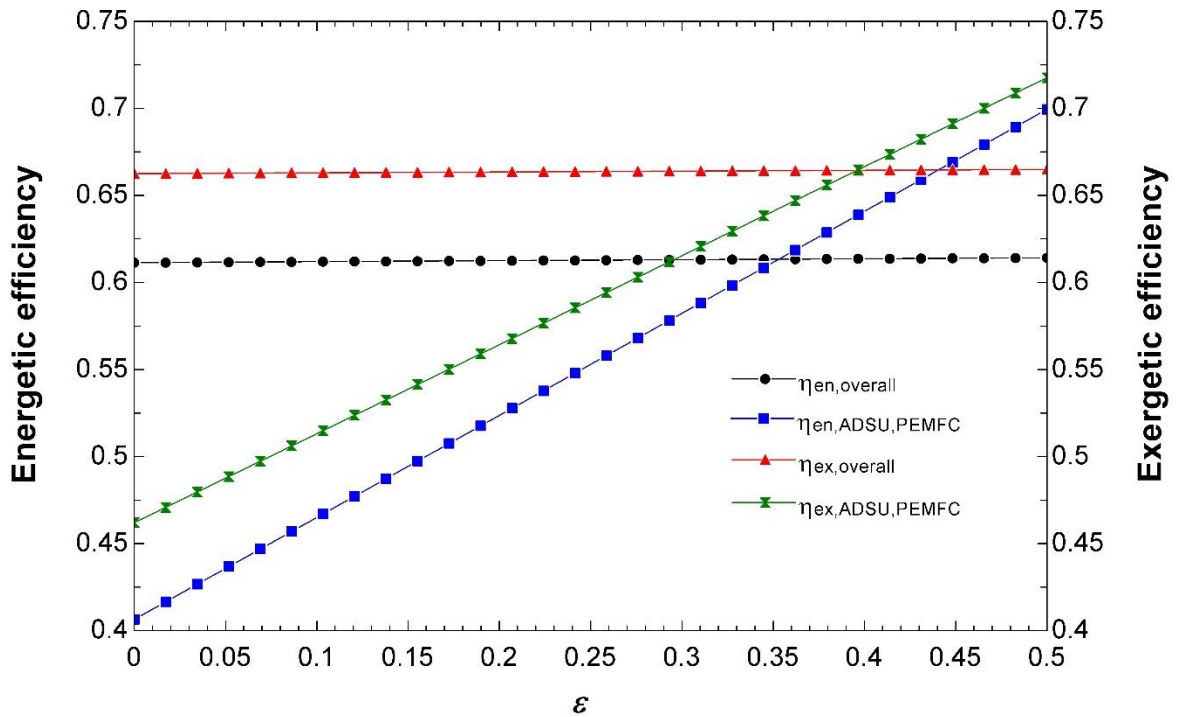


Figure 5.48: Energetic and exergetic efficiencies are plotted against ϵ -parameter. For overall integrated system and ADSU-PEM subsystem.

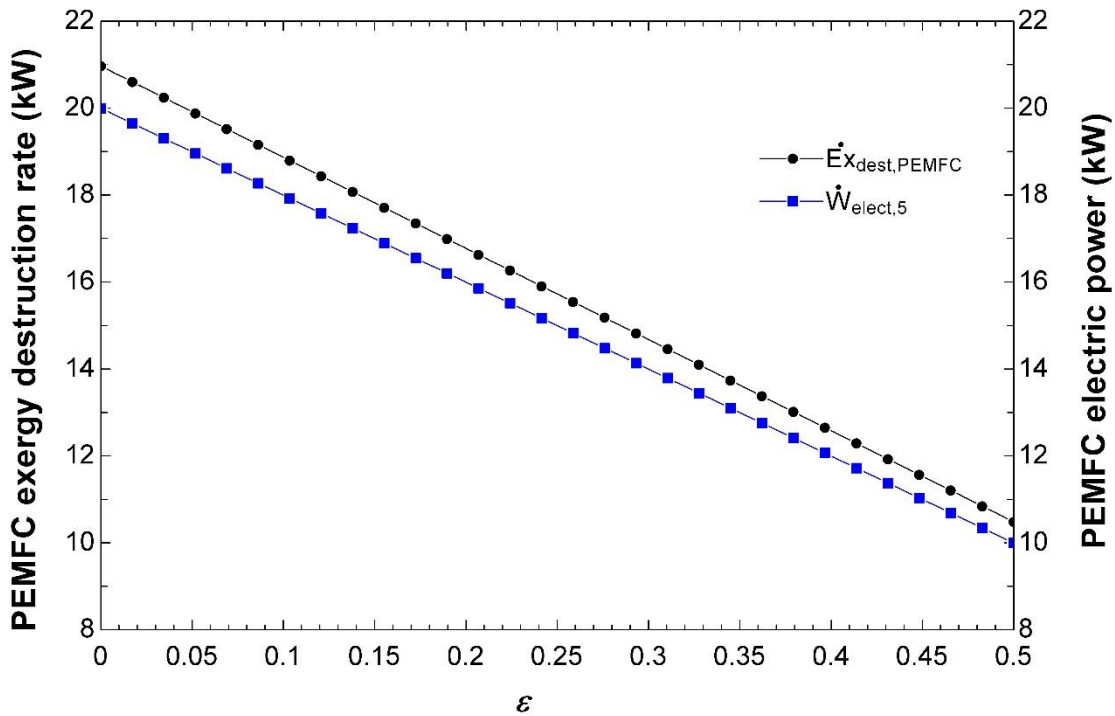


Figure 5.49: PEM fuel cell exergy destruction rate and electric power are plotted against ε -parameter.

In Figure 5.50, the effects of changing the PEMFC energetic efficiency from 40% to 60% on the overall performance of the integrated system is observed. As the efficiency of the PEM fuel cell increases, a small enhancement is noticed for the overall energetic and exergetic efficiencies from 61.15% and 66.25% to 61.30% and 66.42%, respectively. On the other hand, the increase in energetic and exergetic efficiencies of the ADSU-PEMFC subsystem is more dramatic. The improvement is as high as 15.62% energetically and 17.75% exergetically.

In Figure 5.51, positive linear behavior is observed for the power production of the PEM fuel cell with increasing its energetic efficiency. This means more exergy rate is recovered and therefore the lower the exergy destruction rate which is observed in the figure. The exergy destruction rate decreases linearly from 20.88 kW to 14.17 kW.

5.8 System 7 Results

In Figure 3.9, the last studied system uses a Molten Alkaline Hydroxide Electrolyte Fuel Cell (MAHEFC) instead of the Solid Oxide Fuel Cell (SOFC). This kind of fuel cell operates at an intermediate temperature range. In this section, we present a reference case

for this integrated system at an operating point of a passenger locomotive at its maximum power load. As has been done above, parametric studies are described below.

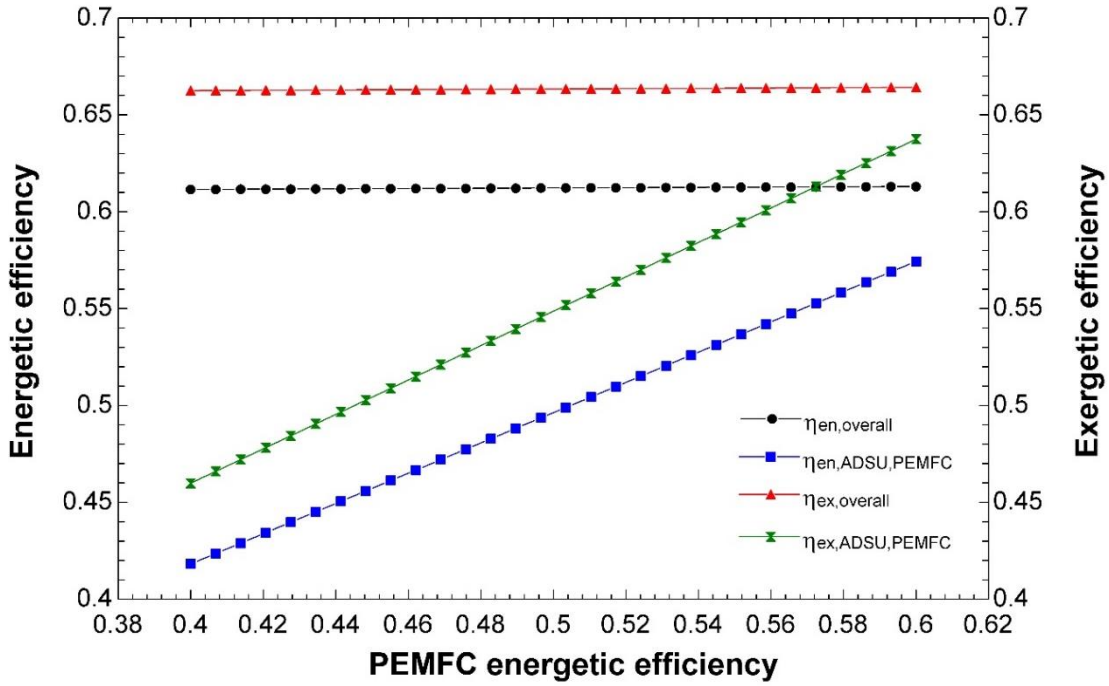


Figure 5.50: Energetic and exergetic efficiencies are plotted against PEM fuel cell energetic efficiency. For overall integrated system and ADSU-PEM subsystem.

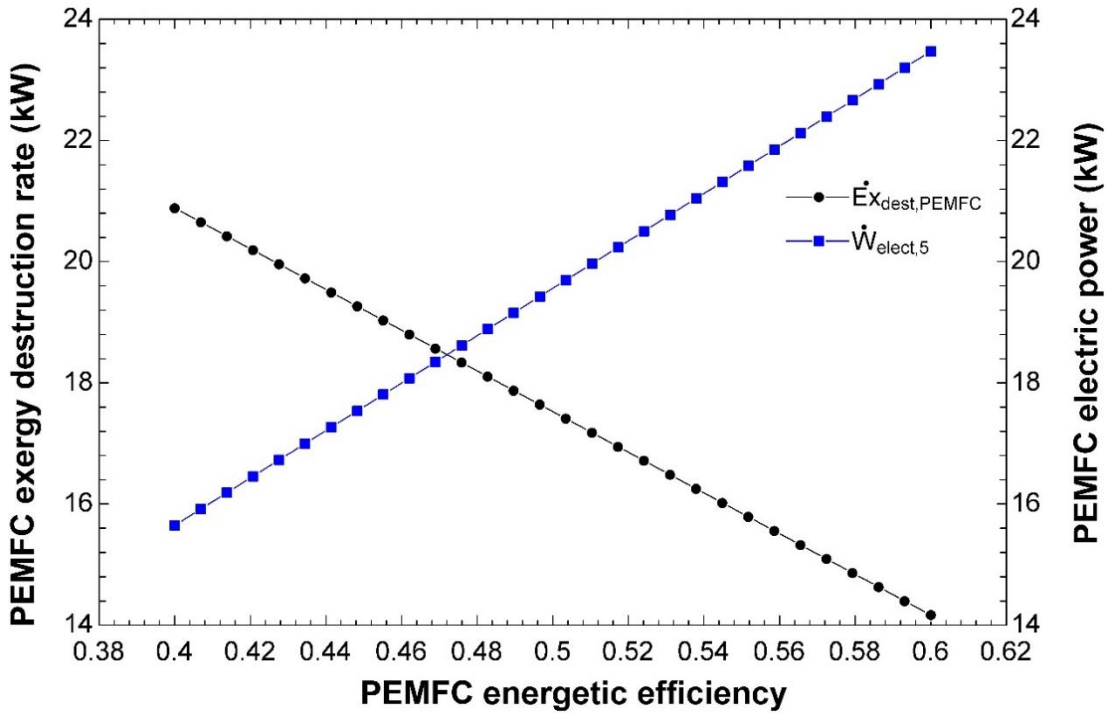


Figure 5.51: PEM fuel cell exergy destruction rate and electric power are plotted against PEM fuel cell energetic efficiency.

5.8.1 Reference Case Results

For this reference case. The energetic efficiency of the fuel cell is selected to be 35%, which can go up to 40% as it has been demonstrated experimentally by Siddiqui and Dincer [26,89]. They used ammonia fuel with direct injection.

In Table 5.26, the values of the electric power of the fuel cell and three turbines are given. The fuel cell produces most of the total output power with a value of 2193 kW. The turbines supply the rest which accounts for 29.38% of the total power production. At the reference case, overall energetic and exergetic efficiencies are 43.57% and 47.70%, respectively. The exergetic efficiency is lower than 50% and the SI is lower than unity. This means that this system is not considered a sustainable system according to Figure 4.1. This is mainly due to the low efficiency of the fuel cell which is 35%. The waste heat recovery system increased this value by 13.57%. However, it is not as efficient as the previous ammonia systems.

In Figure 5.52, all three Rankine cycles are compared, energetically and exergetically. SRC seems to perform the best in terms of energetic efficiency with a value of 30.76%. Also, the highest exergetic efficiency is observed to be 72.42% in the ammonia-ORC 2 subsystem. This is because the temperature of the heat source supplied to this cycle is relatively low.

In Table 5.27, the thermodynamic properties of all the state points in the integrated system are listed. The exhaust gases leaving the integrated system, which is state point 16, has a high temperature of 522.2 K and a flow exergy rate of 205.1 kW. This indicates that we could recover this thermal energy to be used for more power production by using an Organic Rankine Cycle. However, having four Rankine cycles in a single integrated system will take a lot of space and will be costly. Furthermore, the temperature at state 5 of the exhaust gases leaving the combustor is 1046 K, which is not high enough to run a gas turbine. For this reason, a Steam Rankine Cycle is implemented.

Table 5.26: Calculated parameters for the thermodynamic analysis of system 7.

Parameter	Value
MAHEFC electric power	2193 kW
Turbine 1 electric power	323.9 kW
Turbine 2 electric power	87.39 kW
Turbine 3 electric power	501.4 kW
Total electric power of the integrated system	3106 kW
Total power required by the train at maximum load	3100 kW
HX 1 heat transfer rate (cooling mode)	105 kW
SRC energetic efficiency	30.76%
SRC exergetic efficiency	46.19%
ORC 1 energetic efficiency	10.72%
ORC 1 exergetic efficiency	72.42%
ORC 2 energetic efficiency	16.74%
ORC 2 exergetic efficiency	15.02%
Overall energetic efficiency	43.57%
Overall exergetic efficiency	47.70%
Environmental Impact (<i>EI</i>)	1.097
Sustainability Index (<i>SI</i>)	0.9119

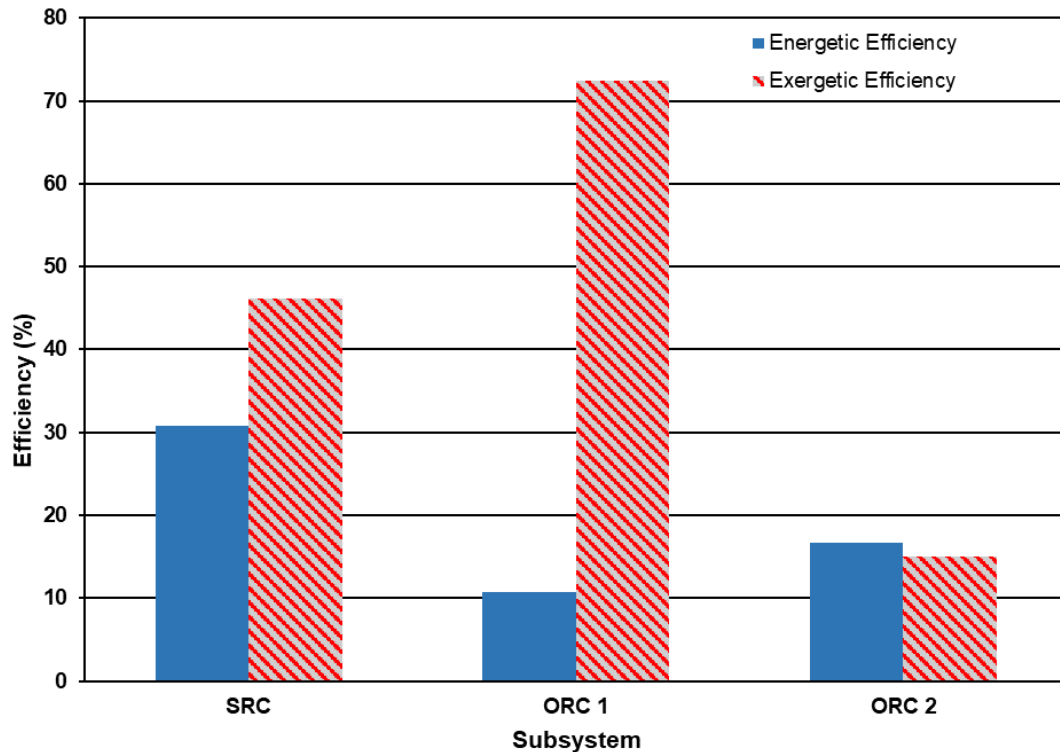


Figure 5.52: Comparison of the energetic and exergetic efficiencies between the subsystems of system 7.

Table 5.27: State points and their thermodynamic values of system 7.

State #	Fluid	Temperature (K)	Pressure (kPa)	Specific Enthalpy (kJ kg ⁻¹)	Specific Entropy (kJ kg ⁻¹ K ⁻¹)	Specific Exergy (kJ kg ⁻¹)	Mass Flow Rate (kg s ⁻¹)
1	Air	570	101	277.5	6.356	78.51	2.781
2	Ammonia	570	101	-2061	12.82	20060	0.2788
3	Exhaust+ammonia+air	570	101	-1632	8.158	91.2	3.06
4	Ammonia	303	101	-2687	11.35	19877	0.328
5	Exhaust gases	1046	101	-1638	9.11	480.4	3.109
6	Exhaust gases	765.6	100	-2017	8.693	228.1	3.109
7	Air	303	100	5.024	5.716	0	2.781
8	Air	304.1	101	6.107	5.716	0.8654	2.781
9	Exhaust gases	575.7	100	-2260	8.329	95.69	3.109
10	Exhaust gases	522.5	100	-2326	8.208	66.14	3.109
11	Water	354.7	3800	344.4	1.091	20.27	0.3375
12	Water	941.3	3800	3833	7.569	1547	0.3375
13	Water	410.8	50	2756	7.884	374	0.3375
14	Water	354.5	50	340.5	1.091	16.42	0.3375
15	Ammonia	570	101	-2061	12.82	20060	0.04921
16	Exhaust gases	522.2	100	-2326	8.207	65.96	3.109
17	Water	303	120	125.2	0.4347	0.02009	0.00625
18	Water	353	120	334.4	1.074	15.6	0.00625
19	R134a	268	242.1	247.4	0.9344	23.07	0.8251
20	R134a	334.5	1249	290.1	0.9603	57.97	0.8251
21	R134a	321	1249	120.2	0.4317	48.13	0.8251
22	R134a	268	242.1	120.2	0.4596	39.68	0.8251
23	Ammonia	570	101	-2061	12.82	20060	0.328
24	Ammonia	306.8	4000	360.2	1.533	351.4	0.6808
25	Ammonia	369.8	4000	1558	4.978	505	0.6808
26	Ammonia	306	1271	1425	5.027	357.4	0.6808
27	Ammonia	306	1271	355.6	1.533	356.8	0.6808
28	Ammonia	307.4	6000	363.6	1.533	354.8	1.874
29	Ammonia	513	6000	1962	5.736	679.7	1.874
30	Ammonia	377.8	1271	1687	5.819	379.2	1.874
31	Ammonia	306	1271	355.6	1.533	346.8	1.874

In Table 5.28, a list of the major components of the integrated system with their exergy destruction rates and exergetic efficiencies is presented. Although the three turbines have exergetic efficiencies higher than 90% and they are performing as efficiently as possible,

the exergetic efficiency of both the fuel cell and the combustor are very low, they are 39.56% and 34.64%, respectively. From Figure 5.53, the highest three exergy destruction rates are found in the fuel cell, combustor, and boiler with values of 3512 kW, 827.5 kW, and 269.1 kW, respectively. These high values of exergy destruction rates explain and justify the low exergetic efficiencies observed in the fuel cell and the combustor.

Table 5.28: Exergy destruction rates and exergetic efficiencies of major components of system 7.

Component	Exergy Destruction Rate (kW)	Exergetic Efficiency
Air Compressor	0.6059	79.89%
MAHEFC	3512	39.56%
Combustor	827.5	34.64%
Boiler	269.1	65.69%
Turbine 1	32.23	91.86%
HX 3	16.10	86.65%
Turbine 2	9.959	90.09%
Turbine 3	46.76	91.70%
Heater	0.4515	17.74%
Compressor 2	6.461	81.67%
HX 1	0.2536	96.88%

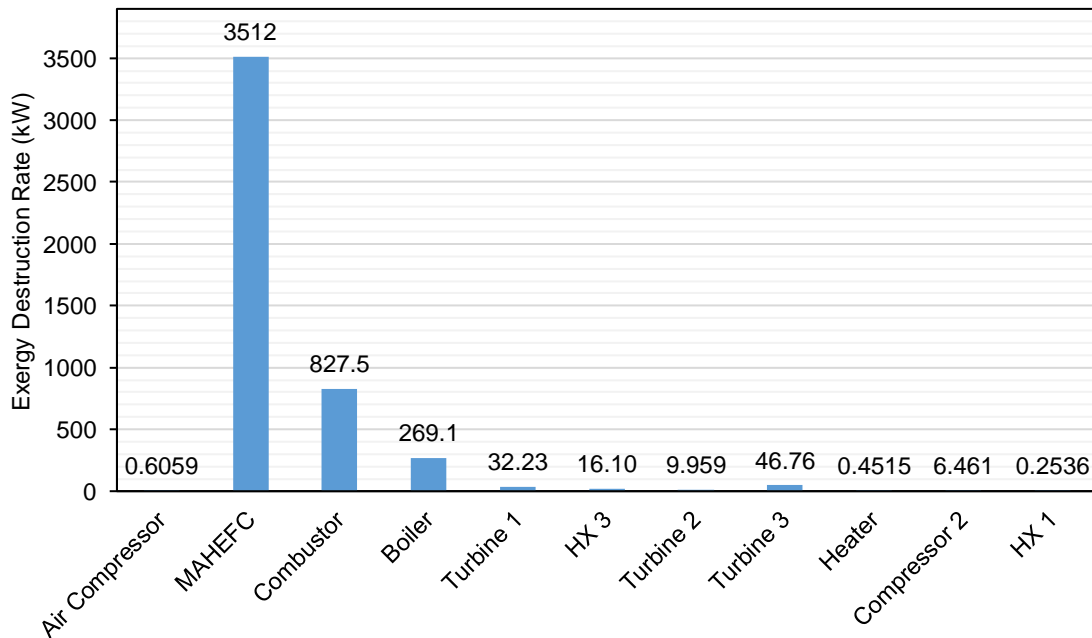


Figure 5.53: Comparison of exergy destruction rates of major components of system 7.

5.8.2 Parametric Study Results

Next, parametric studies of this system are presented and discussed. Two specific parameters are considered, namely the fuel cell operating temperature and the SRC boiler pressure (pressure at state 12).

In Figure 5.54, increasing the operating temperature of the fuel cell reduces the overall energetic and exergetic efficiencies from 43.85% and 48.01% down to 42.04% and 45.96%, respectively. For the SRC, the energetic efficiency increases, but the exergetic efficiency decreases. These behaviors are seen mainly because higher temperature requirements are needed at the air and fuel regenerators which limit the amount of thermal energy absorbed by the SRC. Also, the ORC 1 subsystem performance is enhanced with increasing temperature. A more noticeable improvement is in the ORC 2 subsystem which has an increase of 2.370% energetically and 2.070% exergetically. This because the temperature of the heat supplied to the cycle is higher.

In Figure 5.55, the electric power productions of the fuel cell and the three turbines are plotted as the operating temperature of the fuel cell increases from 523 K to 723 K, or 250°C to 450°C. The power output of the fuel cell is not affected by this temperature increase as long as the current density is adjusted to keep the same energetic efficiency of the fuel cell. For turbine 1 of the SRC, the power output decreases linearly from 358.3 kW to 196.4 kW. This seems contrary to the increase in energetic efficiency, but it is actually not since the amount of supplied heat decreases faster than the decrease in produced electric power. From the energetic efficiency definition, the ratio should increase which was observed earlier. The ORC 1 output power follows that of its upper cycle. It decreases linearly. On the other hand, ORC 2 power production rises in a slow nonlinear manner and it is not enough to compensate for the other reductions of power production. Therefore, the total power produced becomes less with the increasing operating temperature of the fuel cell.

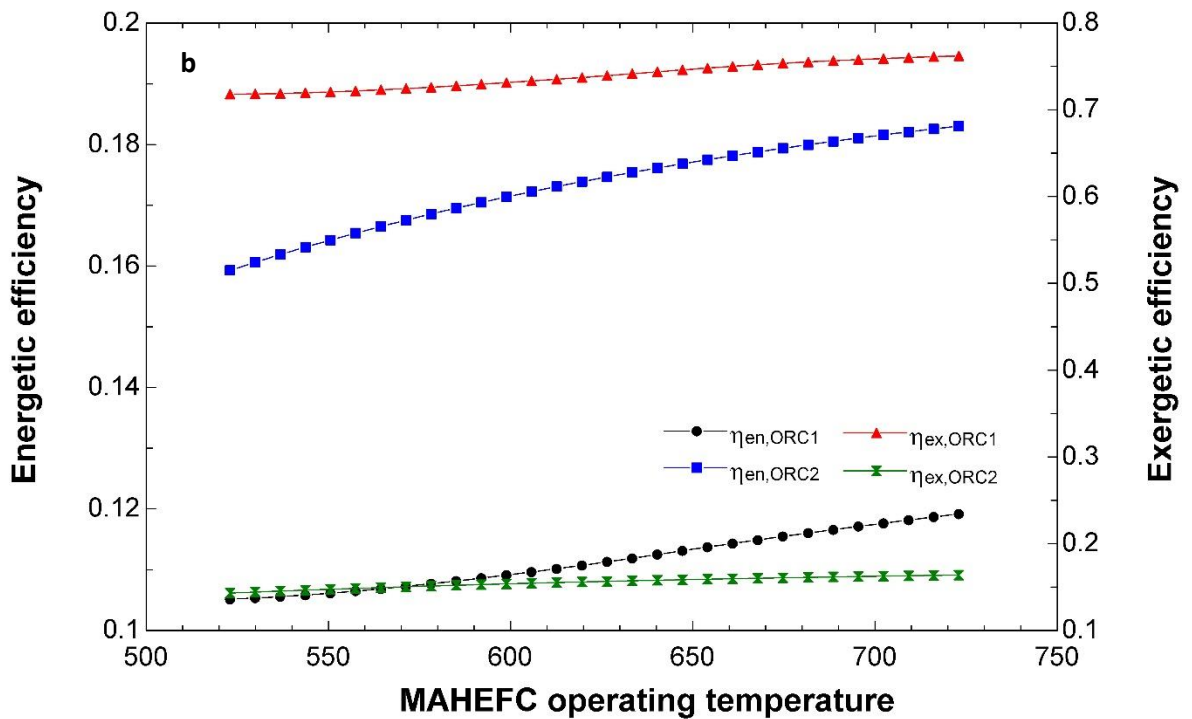
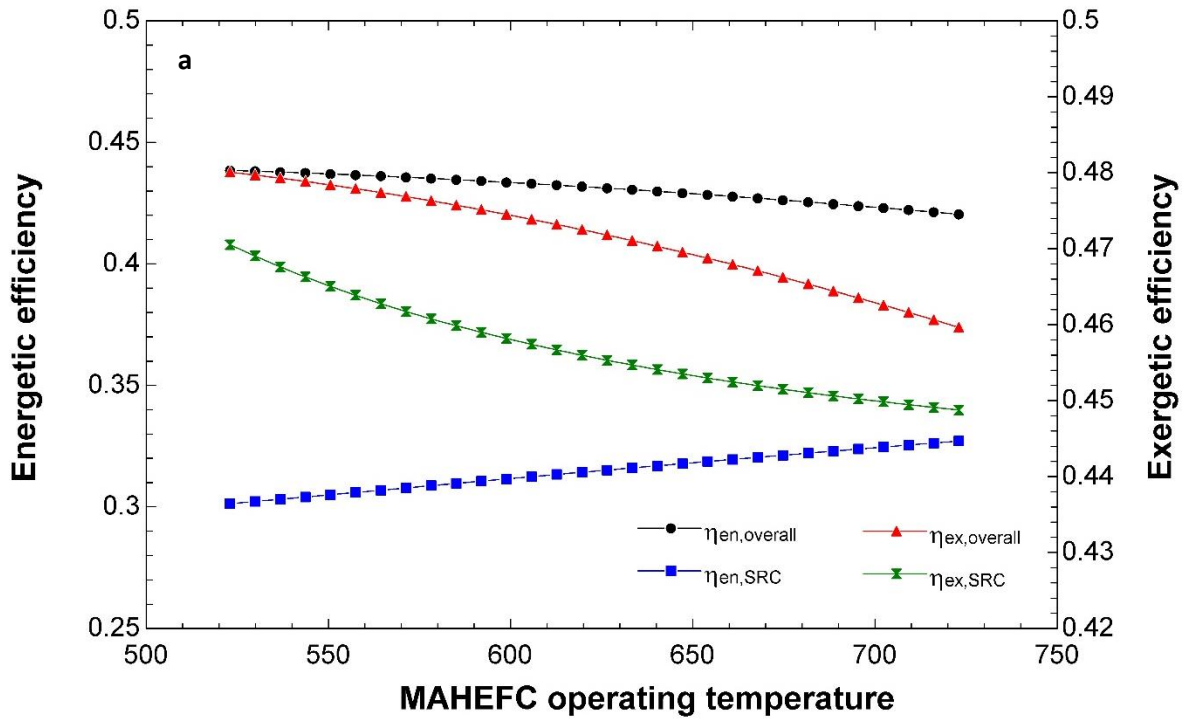


Figure 5.54: Energetic and exergetic efficiencies are plotted against fuel cell operating temperature. a) For overall integrated system and SRC subsystem. b) For NH₃-ORC 1 and 2 subsystems.

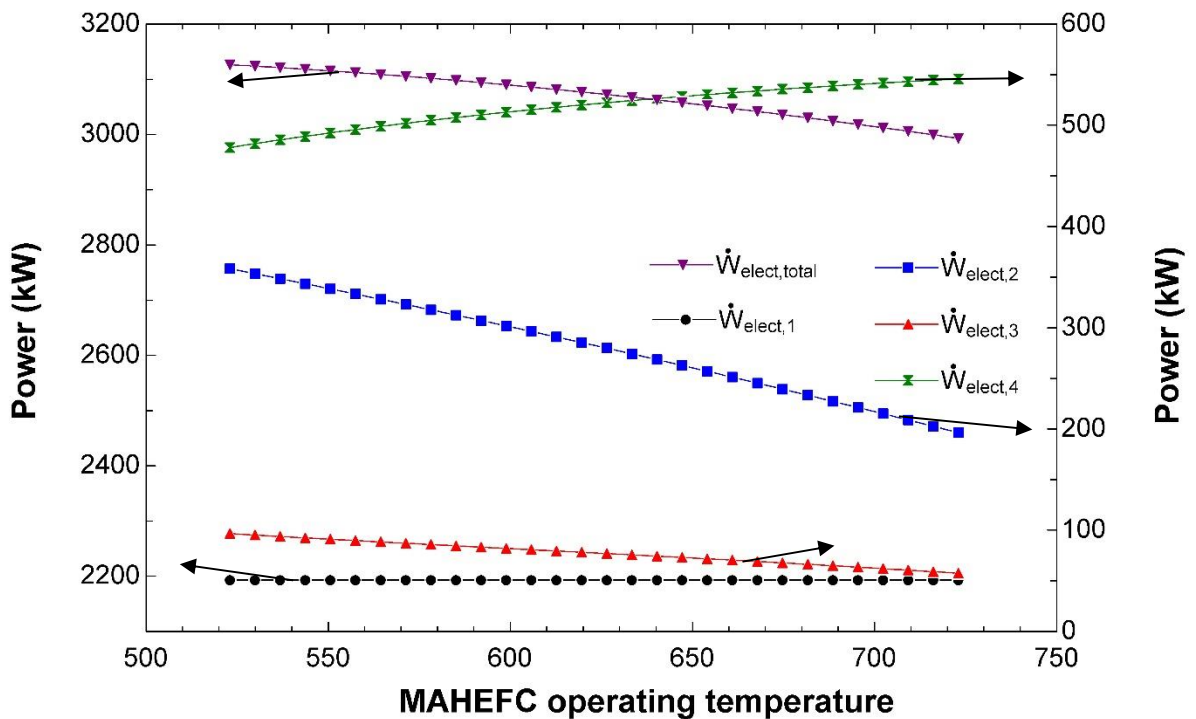


Figure 5.55: Electric power output values of the integrated system and its subsystems are plotted against fuel cell operating temperature. Arrows indicate the corresponding axis of the parameter.

In Figure 5.56, the effects of the SRC boiler pressure (pressure at state 12) or turbine 1 inlet pressure are seen on the energetic and exergetic efficiencies of the integrated system as well as its subsystems. Increasing the pressure level at turbine 1 inlet enhances both the overall and SRC energetic and exergetic efficiencies. The overall performance is slightly increased compared to SRC improvement. For the SRC, the energetic and exergetic efficiencies increase from 28.02% and 42.07% to 31.42% and 47.18%, respectively. On the contrary, the energetic and exergetic efficiencies of the ORC 1 reduces with increasing pressure. They go down from 12.30% and 79.53% to 11.01% and 74.93%, respectively, as the pressure goes from 2000 kPa to 4500 kPa. The decrease behaviors are nonlinear as displayed in the figure.

In Figure 5.57, the total power production of the integrated system increases by a small value due to the tradeoff between the increase in SRC power production and reduction in ORC 1 power production. This reduction observed in ORC 1 causes the decreases in energetic and exergetic efficiencies discussed earlier. Increasing the pressure from 2000 kPa to 4500 kPa, increases the power output of the SRC nonlinearly from 291.7 kW to

331.7 kW. This nonlinear behavior is influencing the trend noticed in the total power produced by the integrated system.

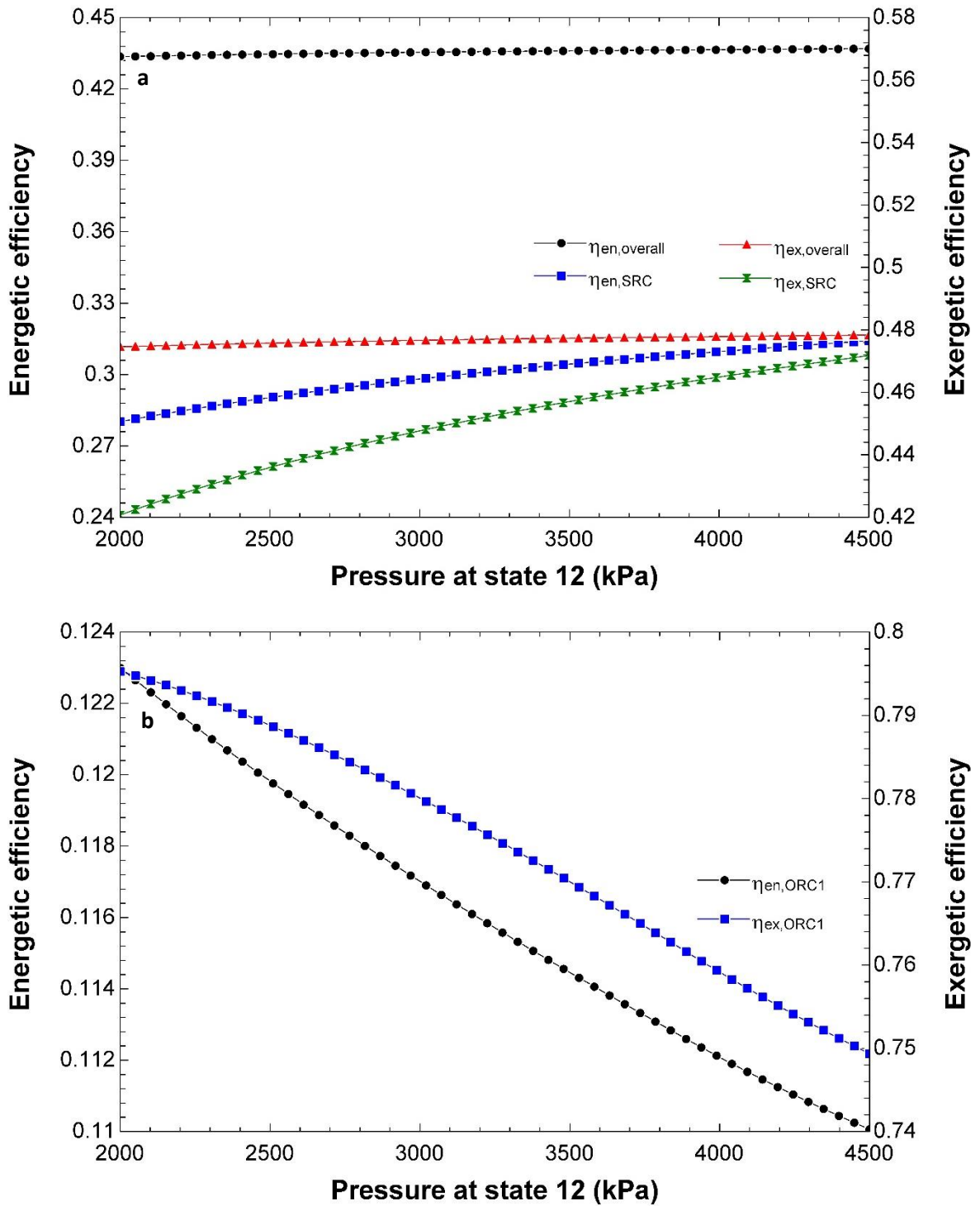


Figure 5.56: Energetic and exergetic efficiencies are plotted against SRC boiler pressure (state 12). a) For overall integrated system and SRC subsystem. b) For NH₃-ORC 1 subsystem.

In Figure 5.58, the temperature variation of the exit stream of turbine 1 (state 13) is shown against the inlet pressure. We can see that as the temperature leaving the turbine which is also the same temperature entering HX3 decreases with increasing pressure. This temperature decline is from as high as 464.9 K down to 397.2 K. This reduces the potential for power production in the ORC 1 subsystem which reduces its power output and energetic and exergetic efficiencies as mentioned above.

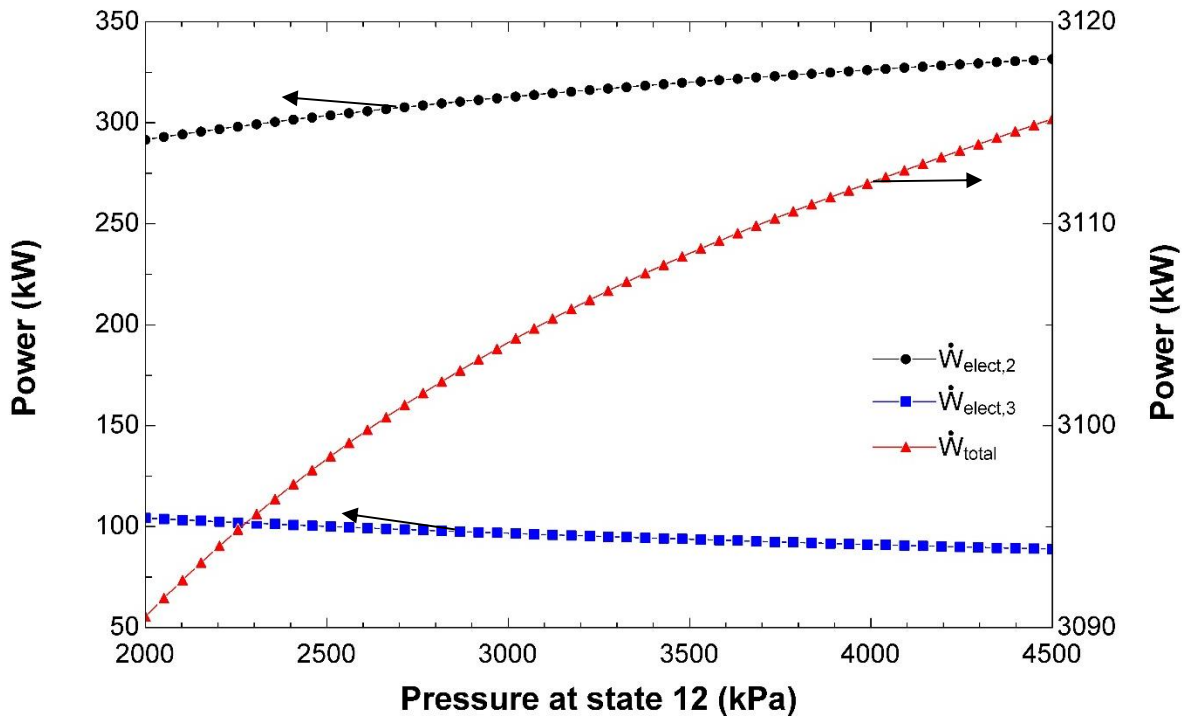


Figure 5.57: Electric power output values of the integrated system and its subsystems are plotted against SRC boiler pressure (state 12). Arrows indicate the corresponding axis of the parameter.

5.9 Systems Optimization Results

After introducing the proposed integrated systems for clean railway applications by providing a specific operation point for each system and then seeing how the efficiencies of the systems change under some parameters, it is time to optimize these integrated systems. The eight proposed systems are grouped into four optimization problems in terms of similarity of operation. Starting with the first group, namely systems 1a, 1b, 2, 4, and 5, we employ the sequence of multi-objective optimization methods with data visualization explained in the previous chapter. The objective functions are the overall exergetic

efficiency, SOFC electric power output, and GT electric power output. The optimization method tries to maximize the first two functions and minimize the last one as increasing the GT electric power output means more space is required to mount the integrated systems, since the reported volumetric power density of gas turbines is in the range of 0.048-0.05 W cm^{-3} , while SOFC volumetric power density is calculated to be 1.00 W cm^{-3} [19]. The resulted objective function models from genetic programming (GP) are listed in Table 5.29. These models help us understand the relationships between the objective functions and the parameters affecting the system in a more explicit way. For example, the α -parameter has more dramatic effects on the overall exergetic efficiency than the excess air factor (λ). This is true because the coefficient of α -parameter is 0.44752, while the excess air factor coefficient is less with a magnitude of 0.010367. The genetic programming method gives a range of possible models for each objective function, but only a single model is chosen according to two factors, namely the correlation coefficient (R^2) and the complexity level. These models are chosen based on a compromise between higher accuracy and lower complexity of the solution.

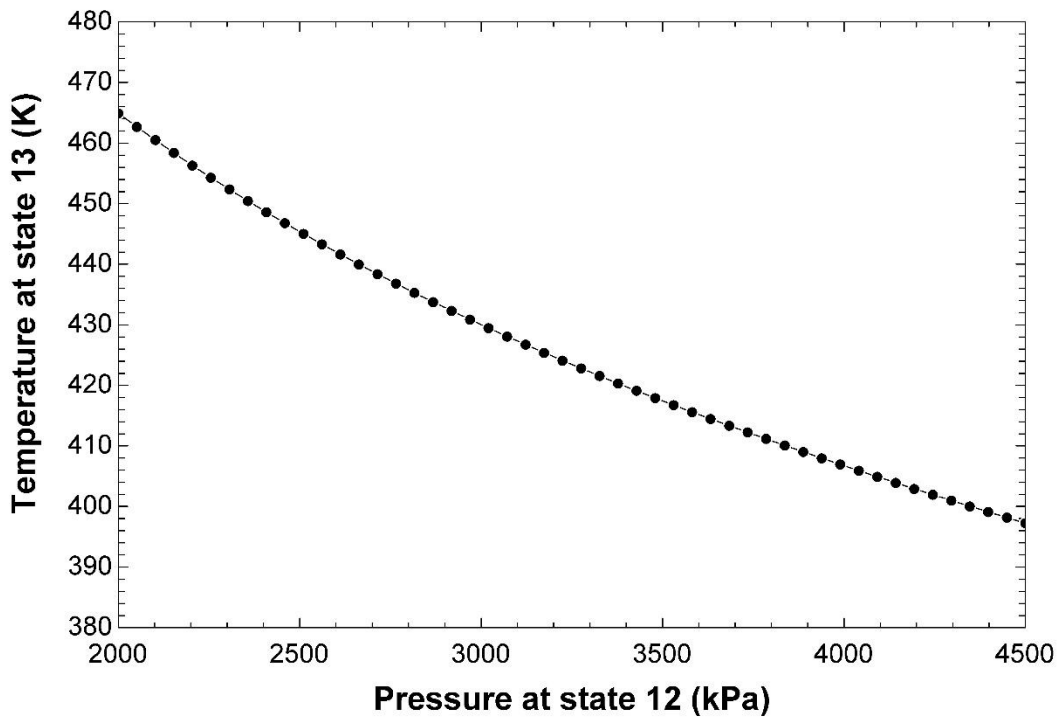


Figure 5.58: Temperature of the stream leaving turbine 1 (state 13) is plotted against SRC boiler pressure (state 12).

Next, the Multi-Objective Genetic Algorithm (MOGA) produced a Pareto front of possible optimized solutions for system 1a and these are presented visually in a parallel-coordinates plot as shown in Figure 5.59. The plot indicates a clear tradeoff between maximizing the exergetic efficiency of the system and maximizing the SOFC electric power output. Also, increasing the exergetic efficiency should be a result of increasing the gas turbine electric power output which is not desired as it requires more installation space on the locomotive. This Pareto front has two extreme solutions in which the overall exergetic efficiency and GT power are maximized, while the SOFC power is minimized as presented in the 18th solution. The second extreme solution is the 3rd solution which is completely opposite to the first one. Note that there are overlapping solutions which are 1st with 6th, and 2nd with 4th. As a result, we can only visually see 16 possible solutions out of the total 18.

Table 5.29: A list of the chosen objective functions models with their corresponding correlation coefficient and level of complexity resulting from genetic programming (GP) of system 1a.

Objective Function	Genetic Programming (GP) Chosen Model	Correlation Coefficient (R^2)	Complexity Level
Overall exergetic efficiency	$\eta_{ex,overall} = 0.589 + 0.448\alpha + 0.00514r_p$ $+ 0.131\alpha^2 + 0.00413r_p\lambda\alpha$ $- 0.0104\lambda - 0.00210r_p\lambda$ $- 0.000176r_p^2$	0.999	39
SOFC power output	$\dot{W}_{elect,SOFC} = 2605 + \frac{427}{r_p} + 119\lambda\alpha + 7.77r_p\lambda$ $+ 1097\alpha^2 - 193\lambda - 2013\alpha$ $- 18.4r_p\lambda\alpha$	0.999	40
GT power output	$\dot{W}_{elect,Gas,turb} = 194 + 1953\alpha + 196\lambda + 26.4r_p$ $- \frac{4449\alpha}{r_p} - 14.8r_p\lambda - 0.772r_p^2$ $- 1120\alpha^2$	0.997	38

The final step in the sequence of any multi-objective optimization method is making a decision. In this optimization problem, the 7th solution which is distinctly plotted in Figure 5.59 is the decided optimum solution because it offers reasonable values for all the objective functions. This solution corresponds to operational parameter values of 14.659, 1.5129, and 0.061099 for r_p , λ , and α , respectively. When these parametric values are inputted into systems 1a, 1b, 2, 4, and 5, the resulting overall energetic and exergetic efficiencies, SOFC power outputs, and GT power outputs are calculated in Table 5.30. The extension of these parametric values to other systems beyond system 1a can be done since

all the other systems share the similar design of the SOFC-GT subsystem and only the bottoming cycles are different which are out-of-scope for this optimization problem. Also, these values will be implemented in system 6. Comparing systems 1a and 1b, we see that the GT power output is higher for the second system with values of 480.8 kW and 633.8 kW, respectively, since more mass flow rate goes to the gas turbine and there is no split of streams after the combustor. However, the energetic and exergetic efficiencies are enhanced for system 1b by differences of 2.67% and 2.58%, respectively. System 5 has the lowest performance and the gas turbine operation is at higher operating load as the fuel used is ammonia that has lower high heating value compared to methane and the bottoming cycle in this integrated system is only an Organic Rankine Cycle (ORC), unlike other integrated systems that utilize cascaded SRC-ORC subsystems.

Here, we discuss an approximate volumetric sizing of system 1a and how it compares to current diesel-electric engines and the simple SOFC-GT hybrid system suggested by Martinez et al. [19]. Assuming volumetric power density values of the different components as tabulated in Table 5.31, the total volumes of a diesel-electric engine, simple SOFC-GT with overrated gas turbine and fuel processing, and proposed system 1a at its

Table 5.30: Overall energetic and exergetic efficiencies of integrated systems and SOFC and GT power outputs at the decided optimum operational point. At this point, these parameters are $r_p = 14.659$, $\lambda = 1.5129$, and $\alpha = 0.061099$.

System	$\eta_{en,overall}$	$\eta_{ex,overall}$	$\dot{W}_{elect,SOFC}$ (kW)	$\dot{W}_{elect,Gas,turb}$ (kW)
1a	62.04%	59.85%	2378	480.8
1b	64.71%	62.43%	2249	633.8
2	61.87%	60.19%	2384	445.7
4	67.15%	64.78%	2174	611.0
5	55.62%	59.69%	2241	777.6

Table 5.31: Volumetric power density of several power components.

Power Components	Volumetric Power Density ($W\ cm^{-3}$)
Diesel-electric engines [19]	0.063
SOFCs [19]	1.0
Gas turbines [19]	0.05
Steam-Organic Cycles [77].	0.2018

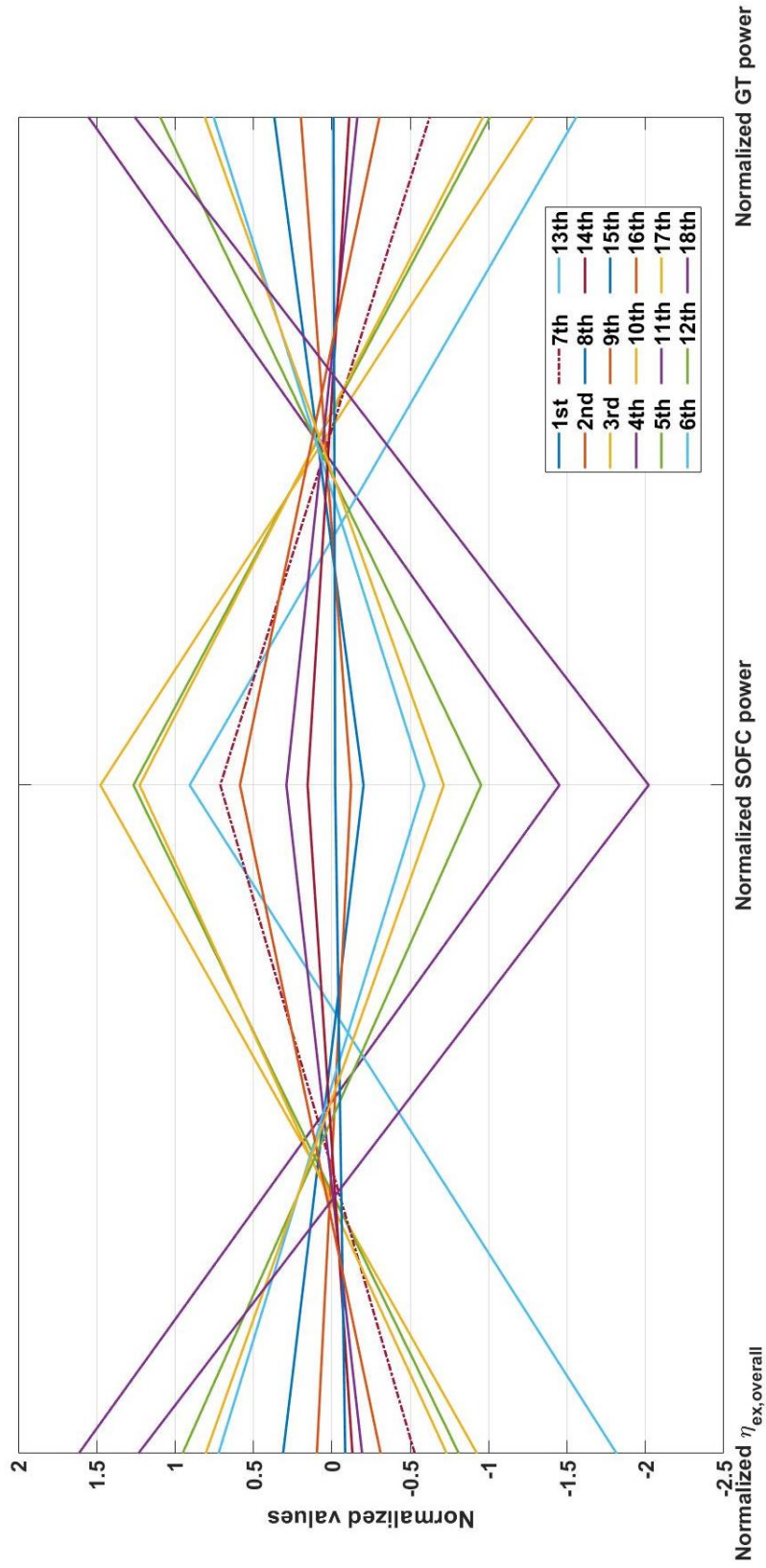


Figure 5.59: Normalized values of the optimized possible solutions of MOGA (Pareto front) of system 1a are plotted in parallel coordinates. The mean values for the overall exergetic efficiency, SOFC power, and GT power are 0.63379, 2245.7 kW, and 570.06 kW, respectively. Also, the standard deviation values are 0.069459, 192.40 kW, and 146.35 kW, respectively. The 7th solution is chosen to be the optimum point of operation which is plotted in bold dot-dash line.

reference case and optimized operating point are computed. The results are presented in Table 5.32. These volumes are computed for a total power load of 3100 kW and the SOFC with its auxiliary devices are accounted for by a size factor of 4.75 as adopted from Martinez et al. [19]. The heat pump volume has already been calculated in an earlier section of system 1a. It is noticed that system 1a space requirements are considerably less than both diesel-electric engines and simple SOFC-GT with fuel processing. Looking at the volume of GT, it is noticed that for system 1a, it has a value of 11.88 m³, while for simple SOFC-GT, it is 21.74 m³. This is because the gas turbine in system 1a is expected to operate at its rated operation point, unlike in simple SOFC-GT hybrid system because of the effects of the α -parameter as shown previously in the parametric studies of system 1a. This parameter which redirects fuel into the combustor makes the inlet turbine temperature high enough for proper operation of the gas turbine. This feature is nonexistent in a simple hybrid system. Moreover, since the SOFC in system 1a is a direct injection, there is no need for fuel processing equipment which saves a volume of up to 7.74 m³.

Next, comparing the reference case of system 1a with its optimized operation found earlier. At the optimized case, the total volume required is 23.68 m³, but at the reference case, it is higher at a value of 25.48 m³. This shows the importance of the multi-objective optimization of the power split between the SOFC and the gas turbine and how it affects the packaging feasibility of the proposed powering system in a locomotive.

Table 5.32: Space required by power components and total systems of diesel-electric engine, simple hybrid SOFC-GT system, and system 1a.

System	SOFC Space (m³)	Fuel Processing Space (m³)	GT Space (m³)	SRC-ORC Space (m³)	Heat Pump Space (m³)	Total System Space (m³)	% Difference with Diesel-Electric Engine
Diesel-electric engine	**	**	**	**	**	48.97	0.00
Simple SOFC-GT by Martinez et al. [19]	12.15	7.74	21.74	0	0	41.63	-14.99
System 1a at Reference case	10.42	0	11.88	1.609	1.574	25.48	-47.96
System 1a at Optimized case	11.3	0	9.616	1.194	1.574	23.68	-51.64

Additionally, system 3 is optimized in terms of the same objective functions plus the PPCI engine power output. This compression engine has an estimated volumetric power density of 0.063 W cm^{-3} [19]. For this reason, it is desired to minimize the power output of the engine and maximize the SOFC power output. The parameters (also called variables) are the compression ratio of air compressor (r_p), engine compression ratio (r_v), and the α -parameter. In Table 5.33, the GP objective function models are listed and several points can be noticed. To begin with, the overall exergetic efficiency explicit expression is highly accurate with a correlation coefficient value of 0.999 and low complexity level of only 24. Furthermore, the engine compression ratio has significant effects on both the power output of PPCI and GT. Its presence is dominant in both of these models and occurrences is high.

After implementing MOGA to these objective functions, the Pareto front is presented in a convenient way using parallel coordinates plotting technique as displayed in Figure 5.60. The first thing to notice is that there are 50 possible optimum solutions compared to 18 in the previous case. This is because there is one more objective function which increases the number of possibilities that can occur for optimum operation of system 3. Another point to be mentioned is that the overall exergetic efficiency increases with increasing PPCI engine power output and inversely proportional to SOFC power output. For the GT power output, there is a scatter and no clear relationship between it and the efficiency can be identified. This is because the gas turbine depends on the energy level and pressure of exhaust gases leaving the PPCI engine. Lastly, the 8th solution has been selected to be the optimum point of operation for system 3 because it has low GT power output, but higher than average overall exergetic efficiency. The values of parameters for this solution are 1.7054, 17.304, and 0.23260 for r_p , r_v , and α , respectively. After setting these values to system 3 thermodynamic model, the overall energetic and exergetic efficiencies are found to be 82.86%, and 80.46%, respectively. These are higher than the values presented for the reference case. Also, the SOFC, PPCI engine, GT power output values are 1793 kW, 1064 kW, and 217.2 kW, respectively. The gas turbine power load has decreased compared to the reference case which has a value of 336.4 kW. This means less space is required with an increase in performance has been achieved due to this optimization.

Table 5.33: A list of the chosen objective functions models with their corresponding correlation coefficient and level of complexity resulting from genetic programming (GP) of system 3.

Objective Function	Genetic Programming (GP) Chosen Model	Correlation Coefficient (R^2)	Complexity Level
Overall exergetic efficiency	$\eta_{ex,overall} = 0.663 + 0.762\alpha + 0.00650r_v\alpha$ $+ \frac{-0.0746 - 0.0864\alpha}{r_p}$ $- 0.00391r_p$	0.999	24
SOFC power output	$\dot{W}_{elect,SOFC} = 2182 + 12.8r_p + 1912\alpha^2$ $+ \frac{289 - 289\alpha}{r_p} - 3.29r_v$ $- 2484\alpha - 19.4r_p\alpha$	0.999	34
PPCI engine power output	$\dot{W}_{net,engine} = 269 + 2334\alpha + 19.8r_v + 4.52r_p$ $+ \frac{123}{r_p} + 13.8r_v\alpha - 0.425r_v^2$ $- 1837\alpha^2$	0.999	36
GT power output	$\dot{W}_{elect,Gas,turb} = 440 + \frac{850}{r_v} - \frac{410}{r_p} + 32.1r_p\alpha$ $- r_v\alpha - 18.6r_p - 1.08r_p r_v\alpha$	0.997	33

Thirdly, the system that features hydrogen production (system 6) needs to be optimized for this purpose. In this problem, the optimized parameters $r_p = 14.659$, $\lambda = 1.5129$, and $\alpha = 0.061099$ are added to the model before optimizing the additional objective functions for this system. This is because there is no need to repeat the optimization of these parameters as they only affect the SOFC-GT subsystem which is similar to system 1a. Here, we are concerned with the Ammonia-Dissociation and Separation Unit (ADSU) for hydrogen production and the PEM fuel cell output power. As for the previous optimization problems presented above, we start by listing the chosen objective function models. In Table 5.34, it is seen that the hydrogen production rate model is very accurate with a correlation coefficient value of 0.999 and it has a reasonable level of complexity. It is a function of both β and ε as expected. Looking at the overall exergetic efficiency model, there is a strong correlation between this efficiency and the parameters of redirecting ammonia fuel to the ADSU which are β and ε . The sensitivity coefficient is 0.750. Comparing the complexity levels of these expressions to the previous models found for systems 1a and system 3, it is seen that, for system 6, the complexity levels are 10 points more complex than system 1a and system 3 GP models.

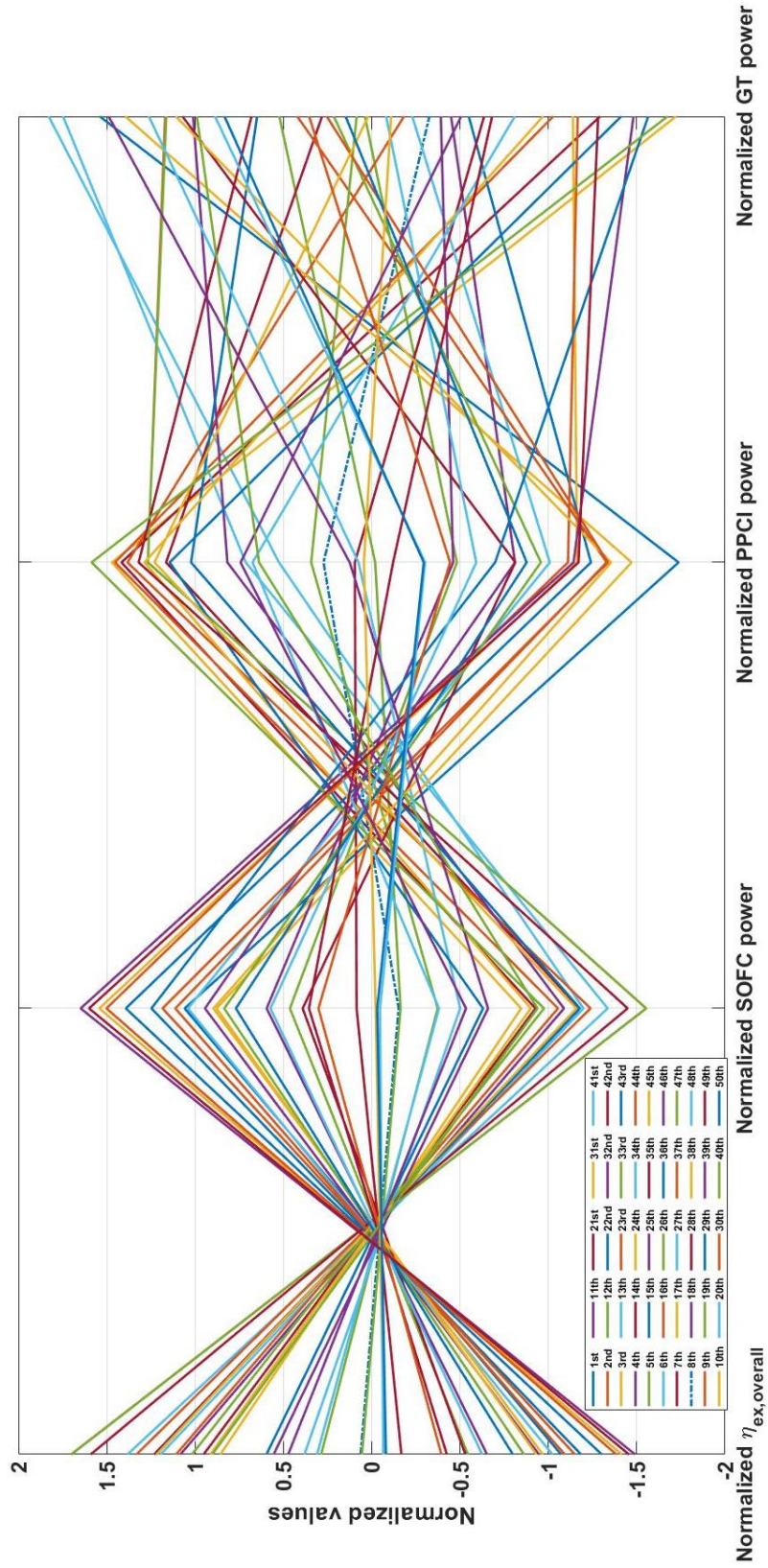


Figure 5.60: Normalized values of the optimized possible solutions of MOGA (Pareto front) of system 3 are plotted in parallel coordinates. The mean values for the overall exergetic efficiency, SOFC power, PPCI power, and GT power are 0.79902, 1820.7 kW, 1020.2 kW, and 240.36 kW, respectively. Also, the standard deviation values are 0.076635, 170.86 kW, 160.22 kW, and 67.524 kW, respectively. The 8th solution is chosen to be the optimum point of operation which is plotted in bold dot-dash line.

Table 5.34: A list of the chosen objective functions models with their corresponding correlation coefficient and level of complexity resulting from genetic programming (GP) of system 6.

Objective Function	Genetic Programming (GP) Chosen Model	Correlation Coefficient (R^2)	Complexity Level
Overall exergetic efficiency	$\eta_{ex,overall} = 0.602 + 0.0179\eta_{en,PEMFC} + 0.00835\varepsilon + 0.750\beta\varepsilon + 0.669\beta\eta_{en,PEMFC} - 0.424\beta - 0.721\beta\varepsilon\eta_{en,PEMFC} - 0.0932\varepsilon\beta^2$	0.998	41
Hydrogen production rate	$\dot{m}_{30} = 0.0416\beta\varepsilon + 0.0114\eta_{en,PEMFC}\varepsilon\beta^3 + 0.0468\eta_{en,PEMFC}\beta^2\varepsilon^2 - 0.0527\eta_{en,PEMFC}\varepsilon\beta^2$	0.999	39
PEMFC power output	$\dot{W}_{elect,PEMFC} = 8.62 + 4755\beta\eta_{en,PEMFC} + 5643\varepsilon\beta^2\eta_{en,PEMFC}^2 - 180\varepsilon - 4365\varepsilon\beta\eta_{en,PEMFC} - 4365\beta^2\eta_{en,PEMFC}^2$	0.999	45

In Figure 5.61, there is a clear indication from the behavior of the Pareto front that as the power production of the PEM fuel cell increases, less hydrogen is produced and stored in the tank. This is predictable since the supply of hydrogen leaving the ADSU gets shared between the tank and the PEM fuel cell. The overall exergetic efficiency seems to be strongly correlated with the amount of hydrogen stored and it reduces as the PEM power increases. All of these three quantities are wanted to be maximized, but definitely, this is not possible. In this case, we choose the 10th solution to be the optimum configuration for system 6. It has both high overall exergetic efficiency and high hydrogen production rate while the PEM fuel cell power output is not decreased dramatically. For this solution, β , ε , and $\eta_{en,PEMFC}$ have values of 0.48780, 0.47813, and 0.58761, respectively. When these values are substituted into the thermodynamic model of system 6, we find the overall energetic and exergetic efficiencies to be 63.93% and 66.59%, respectively. Moreover, the mass flow rate of hydrogen going to the tank is 0.008037 kg s⁻¹ and the PEM fuel cell power output is 622.8 kW. This power production is almost 20.09% of the total power production which is a significant increase than the reference case discussed earlier. As a result of this and the fact that PEM fuel cells typically have high volumetric power densities, like 3.1 W cm⁻³ [16], the total space required for installing this integrated system is reduced.

For system 7, a simpler type of optimization is applied to it. Single-objective genetic algorithm method of optimization is used to look for the optimum point of operation. No power distribution concerns for this system as it does not utilize low volumetric power density devices, like compression engines and gas turbines. Both the Molten Alkaline fuel cell and the SRC have appropriate volumetric power densities which make them feasible for clean operation of a locomotive. The objective function for this optimization problem is the overall exergetic efficiency. The parameters are MAHEFC operating temperature and SRC boiler pressure (pressure at state 12). The optimum configuration has been found to be 523 K for the fuel cell operating temperature and a pressure of 4500 kPa at state 12. This results in energetic and exergetic efficiencies of 43.98% and 48.14%, respectively. The Sustainability Index (*SI*) is close but less than unity at a value of 0.9284. This indicates that this system can become a sustainable system if either the pressure is increased at state 12, as concluded from the parametric studies and these optimization results, or the energetic efficiency of the fuel cell is only slightly improved.

5.10 Comparative Evaluation of the Integrated Systems

The last section of the modelling results and discussion chapter compares the above-mentioned systems. There are two main things compared here. Firstly, the overall energetic and exergetic efficiencies of all the eight systems. Secondly, the fuel costs of a case study of an intercity passenger train will be provided to show some justification for the use of such integrated systems in railway applications.

5.10.1 Comparison of Proposed Integrated Systems at their Reference Cases and Optimum Operation Points

The systems are evaluated in regards to their overall energetic and exergetic efficiencies at both the chosen reference cases and optimized operation configurations.

In Figure 5.62, a comparison between the integrated systems is shown. It is clear that methane-based systems (1 through 4) are performing better than the ammonia-based systems (5 through 7). This is mainly because methane has a higher heating value of 52225 kJ kg⁻¹, compared to 22477 kJ kg⁻¹. Another point to be noticed is that the exergetic

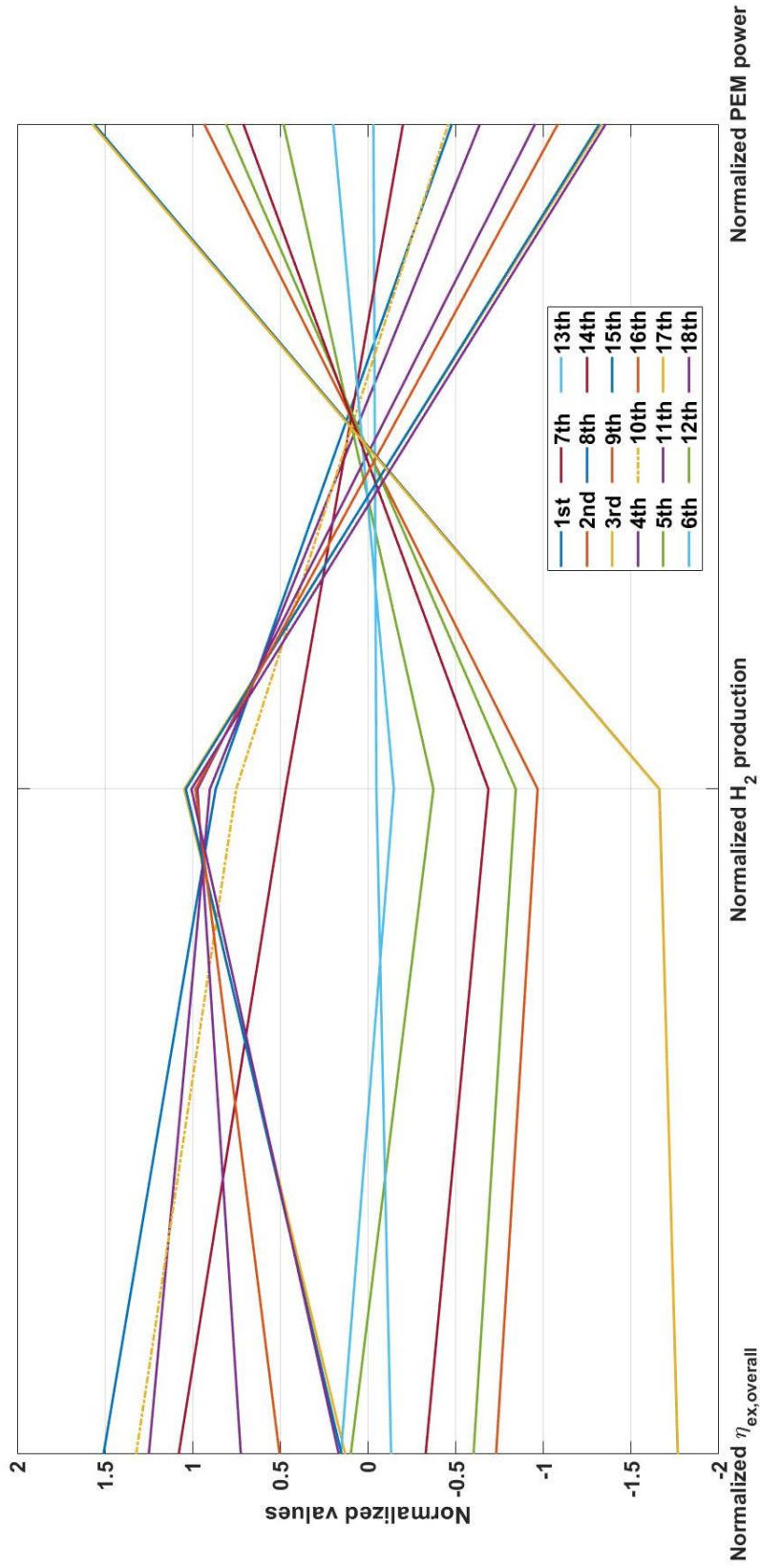


Figure 5.61: Normalized values of the optimized possible solutions of MOGA (Pareto front) of system 6 are plotted in parallel coordinates. The mean values for the overall exergetic efficiency, Hydrogen production, and PEM power are 0.63759, 0.005572 kg s⁻¹, and 710.19 kW, respectively. Also, the standard deviation values are 0.022075, 0.003296 kg s⁻¹, and 187.64 kW, respectively. The 10th solution is chosen to be the optimum point of operation which is plotted in bold dot-dash line.

efficiencies of the ammonia-based systems are always higher than their corresponding energetic efficiencies. This is the opposite in methane-based systems. Although the ammonia-based systems are not performing as well as methane-based systems, they have zero CO₂ emissions, unlike the other systems. This will be discussed further in the next subsection. The lowest energetic and exergetic efficiency values are found in system 7 as this system uses an intermediate-temperature fuel cell with low efficiencies of around 35%, compared to SOFC efficiency of almost 65%. This temperature level does not enable the system to run a Bryton cycle for power production, unlike the other systems. In contrast, the integrated SOFC-PPCI-GT-ORC system (system 3) has the highest energetic and exergetic efficiencies at values of 80.06% and 77.55%, respectively. This is due to the fact that the PPCI engine has a low exergy destruction rate of 83.73 kW, while the combustor in system 1b has it at 364.1 kW. This is a significant reduction of 77.00%. System 6 has the highest energetic and exergetic efficiencies out of the ammonia-based systems since it utilizes the ADSU for power and hydrogen production.

In Figure 5.63, the energetic and exergetic efficiencies of the integrated systems at their optimum operation points are compared. Comparing systems 1a, 1b, 2, 4, and 5 between when they are at the reference cases and when they are at their optimum points, we see that they have the same patterns. This is a strong indication that the optimized values of parameters are applicable in all of them, even though these values resulted from the optimization of only system 1a. Furthermore, these systems have reduced overall energetic and exergetic performances since they have been sacrificed for a better power split between the SOFC and GT. In contrast, system 3, 6, and 7 are enhanced energetically and exergetically. For system 6, the energetic and exergetic efficiencies are closer in the optimized operation since more hydrogen is produced than at the reference case.

5.10.2 Fuel Costs and CO₂ Emissions Comparison: A Case Study

In Table 5.35, the duty cycle of an intercity passenger locomotive is taken as a case study for fuel costs and CO₂ emissions comparisons. From this set of data and choosing the rated power to be 3100 kW, the total energy consumed is found to be 16979.57 kWh which is used to compute the fuel costs and CO₂ emissions for a diesel-electric engine and all the proposed systems. In this case study, fuel costs of diesel, methane, and ammonia are \$1.153 CAD kg⁻¹, \$1.284 CAD kg⁻¹, and \$0.900 CAD kg⁻¹, respectively, which are adopted from these 2016 reports [9,10].

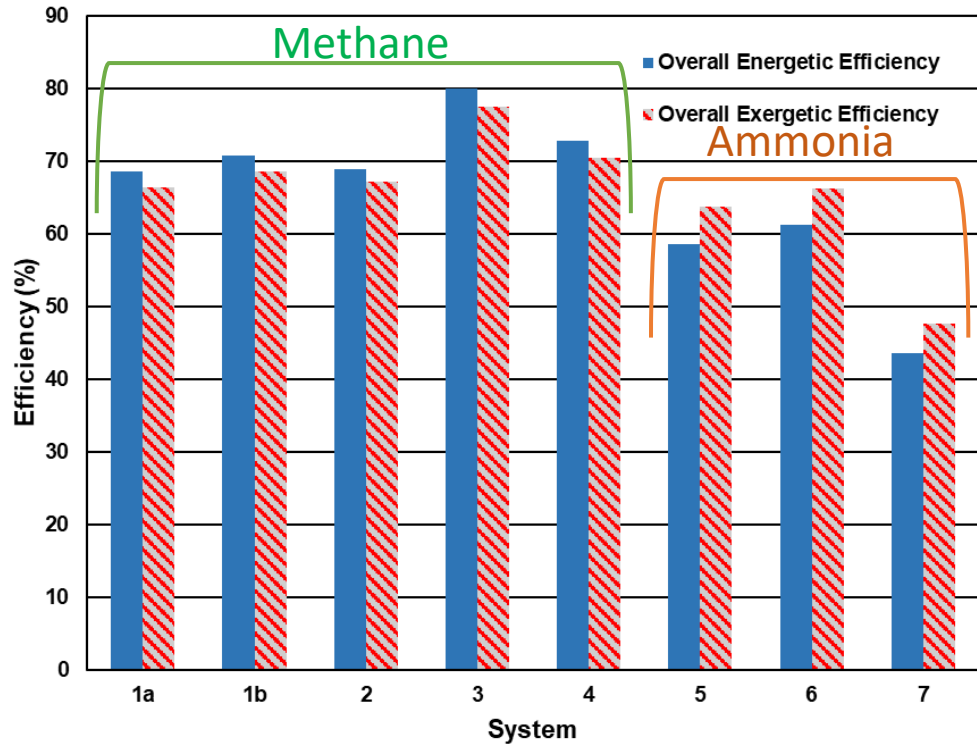


Figure 5.62: Overall energetic and exergetic efficiencies are plotted for all the proposed integrated systems at their chosen reference cases.

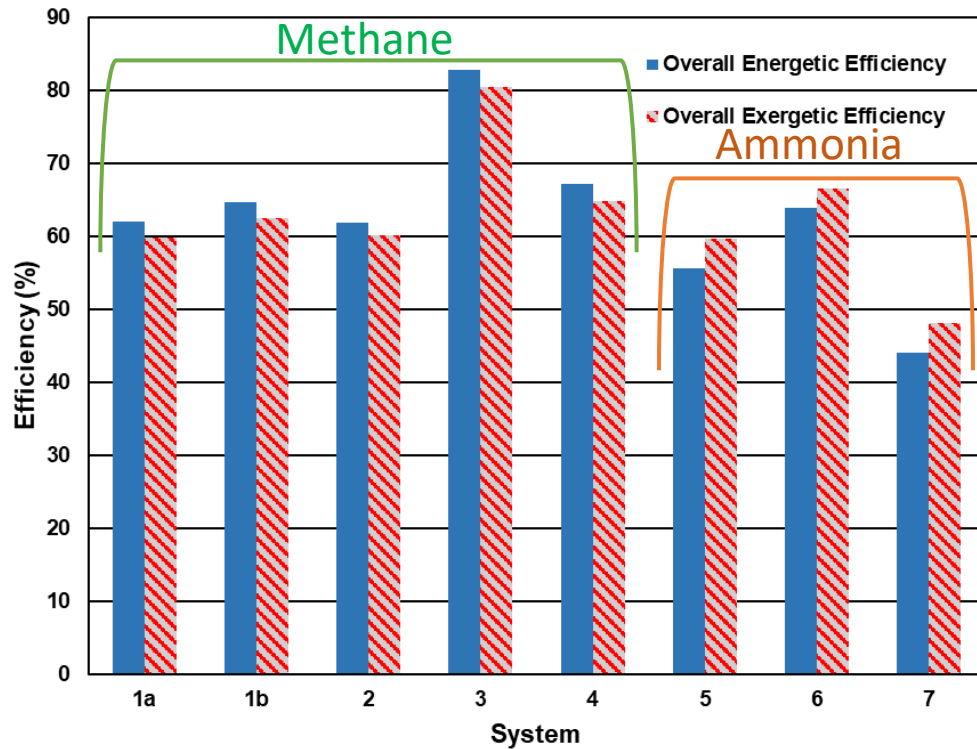


Figure 5.63: Overall energetic and exergetic efficiencies are plotted for all the proposed integrated systems at their optimum operation points.

Table 5.35: Intercity passenger locomotive duty cycle [90].

	Idle	N1	N2	N3	N4	N5	N6	N7	N8	DB
Operation in daily time (%)	49.7	16.5	4.9	3.4	2.2	1.3	1.2	0.3	18.3	2.2
Rated Power Percentage (%)	0.0	4.5	11.5	23.5	35	48	64	85	100	0

In Table 5.36, a list of brake specific fuel consumption of a diesel-electric engine and all the proposed systems is given. It is seen that the highest fuel consumption per a kilowatt-hour of energy is found in system 7 at a value of 0.3802 kg kWh⁻¹ due to its low efficiency as discussed earlier. Methane-based systems are performing much better than the diesel-electric engine. On the other hand, ammonia-based systems have higher fuel consumption values compared to the diesel-electric engine.

Table 5.36: Brake specific fuel consumption for a diesel-electric engine and the proposed systems at their reference cases.

System	Brake Specific Fuel Consumption (kg kWh ⁻¹)
Diesel-electric [91]	0.2318
1a	0.1041
1b	0.1007
2	0.1035
3	0.08902
4	0.09795
5	0.2824
6	0.2711
7	0.3802

In Figure 5.64, fuel costs for the case study of an intercity passenger locomotive are compared for a diesel-electric engine and the integrated systems. We notice that systems 1 through 6 have lower costs than the diesel-electric engine which means this is an economic justification for the adaptation of these proposed systems in railway applications. The lowest fuel cost for the case study is calculated for system 3 at a value of \$1940 CAD. The highest fuel cost per duty cycle of \$5810 CAD is in system 7. This is a result of the low energetic and exergetic efficiencies of this system and it is not considered a sustainable system as mentioned above. When comparing system 3 and the diesel-electric engine fuel

costs for this case study, system 3 offers lower fuel costs by a great difference of 57.22% when the diesel-electric engine is taken as a reference.

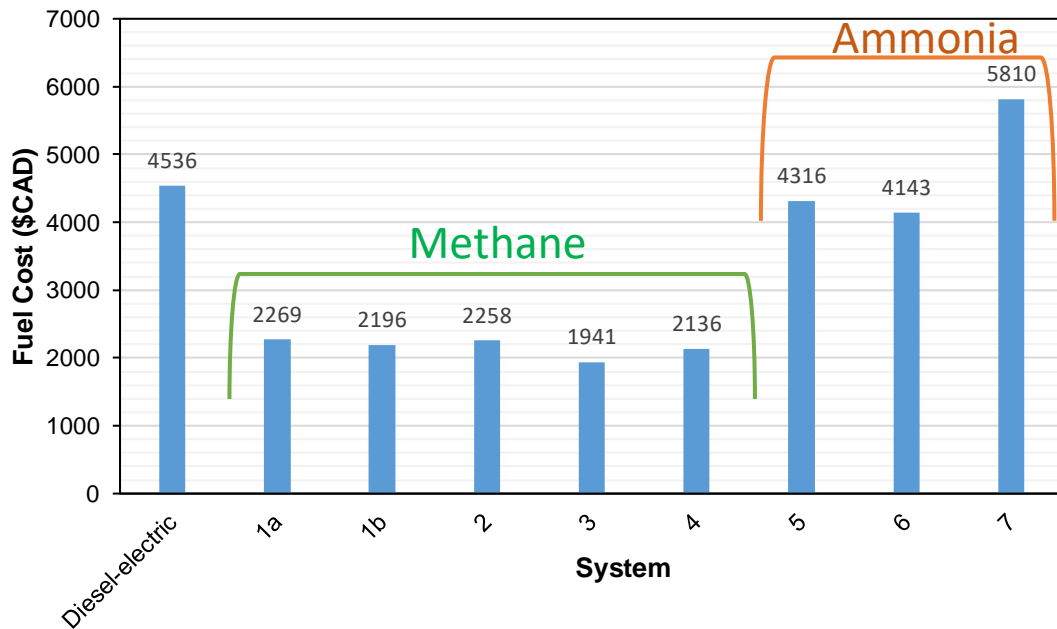


Figure 5.64: Fuel costs of a diesel-electric engine and all the proposed systems evaluated at their reference cases for the chosen case study.

In Figure 5.65, another factor is considered for the case study of a duty cycle of an intercity passenger train. CO₂ emissions of the methane-based systems are lower than the diesel-electric engine as expected since less carbon exists in methane molecule than diesel fuel. Implementing system 3 which has the lowest emissions of carbon dioxide of the methane-based systems reduces the emissions by almost 60.98% compared to using diesel fuel. Although, ammonia-based systems have shown lower energetic and exergetic efficiencies and higher fuel costs per duty cycle, they produce zero CO₂ emissions. This is under the assumption that the ammonia fuel has been produced using clean energy sources. If one wants to eliminate these harmful emissions, he needs to adopt an ammonia-based system while sacrificing some efficiency. Nevertheless, these ammonia-based systems, except system 7, provide lower fuel costs than current diesel-electric engines that are being used today. A better option could be operating system 3 with ammonia fuel or even better pure

hydrogen fuel which has much higher heating value. However, hydrogen storage technologies for transportation and specifically railway applications must be improved in terms of safety, space requirements and storage conditions [15]. These issues are not present when using ammonia as a transportation fuel as discussed in [12,13].

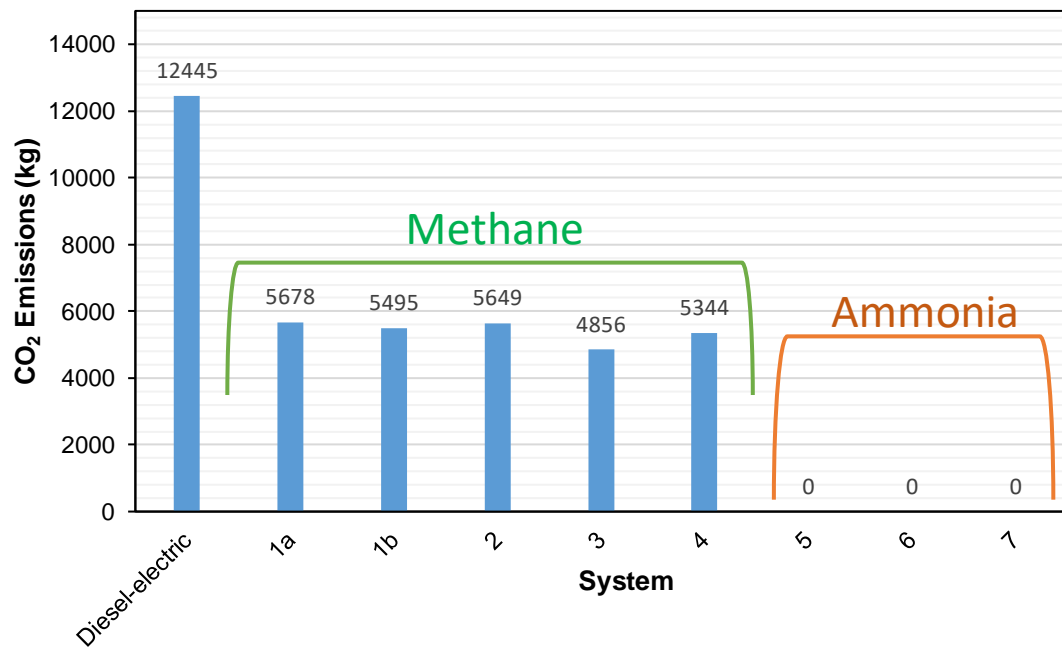


Figure 5.65: CO₂ emissions of a diesel-electric engine and all the proposed systems evaluated at their reference cases for the chosen case study.

Chapter 6: Conclusions and Recommendations

This thesis has presented and discussed the proposal of eight integrated systems for cleaner railway applications. Each system has been studied in the following order. A reference case for a locomotive operation, parametric studies, optimization, and then a case study of an intercity passenger train is given for fuel costs and CO₂ emissions comparison. The main focus of these studies are the overall energetic and exergetic efficiencies, and the optimization of power split between devices for feasible packaging of these integrated systems. The final chapter of this thesis summarizes the main findings and suggests future research directions.

6.1 Conclusions

Several remarks of the thermodynamic studies conducted above are listed below:

- Using air-source reversible heat pumps has shown advantages over other possible options. It causes a reduction in annual operating costs from \$1854 CAD down to \$873 CAD when compared to a furnace with air conditioning option. Furthermore, it requires 4 times less space than an absorption chiller unit and the weight requirements are less from 2993.7 kg to 1354.5 kg, for the same cooling capacity.
- From system 1a analysis at the reference case, the system is evaluated by its overall energetic and exergetic efficiency values which are 68.50% and 66.35%, respectively. Also, the system has a Sustainability Index (*SI*) of 1.971. From this, it is considered a sustainable system. The system can operate a passenger locomotive at a maximum load of 3100 kW.
- The thermodynamic model of system 1a is validated by using the SOFC-GT energetic efficiency for comparison with previously published simulation and experimental results. The accuracy of the present model is found to be acceptable by a difference of 12.2% from an experimental result.
- The optimization results of system 1a show that when the parameters are set to their selected optimum values, the system has overall energetic and exergetic efficiencies of 62.04% and 59.85%, respectively. The power split is better as the gas turbine has

a reduced power load of 480.8 kW compared to its reference case. This proper power split makes this system more feasible with regards to packaging.

- Onboard hydrogen production in system 6 is optimized at a value of 0.008037 kg s⁻¹ and the increasing in this production is directly proportional to the increase in overall exergetic efficiency. So, adding this feature is recommended.
- Comparing all the integrated systems in terms of their energetic and exergetic efficiencies, methane-based integrated systems (1 through 4) are more efficient than ammonia-based systems (5 through 7) because methane has a higher heating value and can provide thermal energy at higher temperature levels. System 7 is not a sustainable one as it has an *SI* value of 0.9119. So, the use of Solid Oxide Fuel Cells (SOFC) is the better option.
- The presented case study of the duty cycle of an intercity passenger locomotive in Canada justifies the adaptation of such integrated systems that utilize cleaner fuels as it has much less CO₂ emissions. They provide either a reduction of emissions, during operation, by 60.98% compared to using diesel fuel or even eliminate the emissions by using a clean fuel (i.e. ammonia).
- Also, from the case study, the reduction in fuel costs is clearly presented. For example, system 3 has a lower fuel cost per duty cycle by a difference of 57.22% when compared to using diesel.

6.2 Recommendations

In addition, future research directions are suggested below in order to learn more about these integrated systems and how they can be implemented for cleaner railway applications:

- Prototyping of these integrated systems is required before implementing them to locomotives. This is because actual performance data are needed to further validate the presented thermodynamic modelling of the systems.
- Scaling up these proposed powering systems for locomotives needs further investigation, both theoretically and experimentally.
- More precise sizing of such integrated systems is necessary to show the feasibility of replacing current diesel-electric engines with these proposed systems without

any major design modifications. Such modifications can be costly and not attractive in the eyes of railway companies.

- Equipment compatibility analysis is required to make sure these systems can operate properly without any failures.
- Multi-objective optimization studies of these systems with the inclusion of exergoeconomic analysis and greenhouse gas emissions are desired to compare these systems in a more detailed manner.
- Dynamic analyses of these systems must be conducted to provide more operational information. Also, other electric components need to be considered, like supercapacitors and electric motors.
- A complete life cycle assessment is essential to see the total costs and harmful emissions associated with the production and use of these alternative fuels for railway applications.
- More development in hydrogen storage technologies is needed in order to use hydrogen as a transportation fuel, since it has higher heating value than ammonia and zero carbon dioxide emissions.

References

- [1] Environment and Climate Change Canada. Canadian Environmental Sustainability Indicators: Progress Towards Canada's Greenhouse Gas Emissions Reduction Target. 2019.
- [2] Railway Association of Canada. Locomotive Emissions Monitoring Program. 2015. <https://www.railcan.ca/wp-content/uploads/2017/12/2015-LEM-Report.pdf> (accessed June 9, 2019).
- [3] B. Boundy, S. W. Diegel L. Wright and S. C. Davis. Biomass Energy Data Book. U.S. Department of Energy. 2011.
- [4] Götz M, Lefebvre J, Mörs F, McDaniel Koch A, Graf F, Bajohr S, et al. Renewable Power-to-Gas: A technological and economic review. *Renew Energy* 2016;85:1371–90. doi:10.1016/j.renene.2015.07.066.
- [5] Stempien JP, Ni M, Sun Q, Chan SH. Production of sustainable methane from renewable energy and captured carbon dioxide with the use of Solid Oxide Electrolyzer: Athermodynamic assessment. *Energy* 2015;82:714–21. doi:10.1016/j.energy.2015.01.081.
- [6] Burkhardt M, Jordan I, Heinrich S, Behrens J, Ziesche A, Busch G. Long term and demand-oriented biocatalytic synthesis of highly concentrated methane in a trickle bed reactor. *Appl Energy* 2019;240:818–26. doi:10.1016/j.apenergy.2019.02.076.
- [7] Environment and Climate Change Canada. Canadian Environmental Sustainability Indicators: Greenhouse Gas Emissions. Gatineau, Quebec, Canada. 2019. <https://www.canada.ca/content/dam/eccc/documents/pdf/cesindicators/ghg-emissions/2019/national-GHG-emissions-en.pdf> (accessed June 14, 2019).
- [8] Hogerwaard J. Comparative study of ammonia-based clean rail transportation systems for Greater Toronto area. MASc thesis, Automotive, Mechanical and Manufacturing Engineering Department, University of Ontario Institute of Technology, 2014.
- [9] Agriculture and Agri-Food Canada. Canadian Farm Fuel and Fertilizer: Prices and Expenses. 2017. http://www.agr.gc.ca/resources/prod/doc/misb/mag-gam/mor-rmar/pdf/rmar_05_01_2013_eng.pdf (accessed June 15, 2019).
- [10] Natural Resources Canada. Fuel Focus. Minister of Natural Resources 2016;11. <https://www.nrcan.gc.ca/sites/www.nrcan.gc.ca/files/energy/files/pdf/2016/Issue16.pdf> (accessed June 14, 2019).
- [11] Giddey S, Badwal SPS, Munnings C, Dolan M. Ammonia as a Renewable Energy Transportation Media. *ACS Sustain Chem Eng* 2017;5:10231–9. doi:10.1021/acssuschemeng.7b02219.
- [12] Zamfirescu C, Dincer I. Ammonia as a green fuel and hydrogen source for vehicular applications. *Fuel Process Technol* 2009;90:729–37. doi:10.1016/j.fuproc.2009.02.004.

- [13] Klerke A, Christensen CH, Nørskov JK, Vegge T. Ammonia for hydrogen storage: Challenges and opportunities. *J Mater Chem* 2008;18:2304–10. doi:10.1039/b720020j.
- [14] International Energy Agency (IEA). *The Future of Hydrogen: Seizing today's opportunities*. IEA Publications, France 2019. https://webstore.iea.org/download/direct/2803?fileName=The_Future_of_Hydrogen.pdf (accessed June 15, 2019).
- [15] Sharma S, Ghoshal SK. Hydrogen the future transportation fuel: From production to applications. *Renew Sustain Energy Rev* 2015;43:1151–8. doi:10.1016/j.rser.2014.11.093.
- [16] Toyota Mirai – The Turning Point. Toyota 2019. <https://ssl.toyota.com/mirai/fullspecs.html> (accessed June 9, 2019).
- [17] U.S. Department of Energy | Fuel Cell Technologies Office. *Fuel Cells 2015*. https://www.energy.gov/sites/prod/files/2015/11/f27/fcto_fuel_cells_fact_sheet.pdf (accessed June 15, 2019).
- [18] Martinez AS, Brouwer J, Samuelsen GS. Feasibility study for SOFC-GT hybrid locomotive power: Part I. Development of a dynamic 3.5 MW SOFC-GT FORTRAN model. *J Power Sources* 2012;213:203–17. doi:10.1016/j.jpowsour.2012.04.023.
- [19] Martinez AS, Brouwer J, Samuelsen GS. Feasibility study for SOFC-GT hybrid locomotive power part II. System packaging and operating route simulation. *J Power Sources* 2012;213:358–74. doi:10.1016/j.jpowsour.2012.04.023.
- [20] Afif A, Radenahmad N, Cheok Q, Shams S, Kim JH, Azad AK. Ammonia-fed fuel cells: A comprehensive review. *Renew Sustain Energy Rev* 2016;60:822–35. doi:10.1016/j.rser.2016.01.120.
- [21] Bogolowski N, Iwanschitz B, Drillet JF. Development of a coking-resistant NiSn anode for the direct methane SOFC. *Fuel Cells* 2015;15:711–7. doi:10.1002/fuce.201400187.
- [22] Lo Faro M, Antonucci V, Antonucci PL, Aricó AS. Fuel flexibility: A key challenge for SOFC technology. *Fuel* 2012;102:554–9. doi:10.1016/j.fuel.2012.07.031.
- [23] Ma Q, Peng R, Tian L, Meng G. Direct utilization of ammonia in intermediate-temperature solid oxide fuel cells 2006;8:1791–5. doi:10.1016/j.elecom.2006.08.012.
- [24] Wachsman ED, Lee KT. Lowering the Temperature of Solid Oxide Fuel Cells. *Science* (80-) 2011;334:935–9.
- [25] Shao Z, Haile SM, Ahn J, Ronney PD, Zhan Z, Barnett SA. A thermally self-sustained micro solid-oxide fuel-cell stack with high power density. *Nature* 2005;435:795–8. doi:10.1038/nature03673.

- [26] Siddiqui O, Dincer I. Experimental investigation and assessment of direct ammonia fuel cells utilizing alkaline molten and solid electrolytes. *Energy* 2019;169:914–23. doi:10.1016/j.energy.2018.12.096.
- [27] Safari F, Dincer I. Assessment and optimization of an integrated wind power system for hydrogen and methane production. *Energy Convers Manag* 2018;177:693–703. doi:10.1016/j.enconman.2018.09.071.
- [28] Michalsky R, Parman BJ, Amanor-Boadu V, Pfromm PH. Solar thermochemical production of ammonia from water, air and sunlight: Thermodynamic and economic analyses. *Energy* 2012;42:251–60. doi:10.1016/j.energy.2012.03.062.
- [29] Veselovskaya J V, Parunin PD, Okunev AG. Catalytic process for methane production from atmospheric carbon dioxide utilizing renewable energy. *Catal Today* 2017;298:117–23. doi:10.1016/j.cattod.2017.05.044.
- [30] Bailera M, Lisbona P, Romeo LM, Espatolero S. Power to Gas projects review: Lab, pilot and demo plants for storing renewable energy and CO₂. *Renew Sustain Energy Rev* 2017;69:292–312. doi:10.1016/j.rser.2016.11.130.
- [31] Parra D, Zhang X, Bauer C, Patel MK. An integrated techno-economic and life cycle environmental assessment of power-to-gas systems. *Appl Energy* 2017;193:440–54. doi:10.1016/j.apenergy.2017.02.063.
- [32] Sternberg A, Bardow A. Life Cycle Assessment of Power-to-Gas: Syngas vs Methane. *ACS Sustain Chem Eng* 2016;4:4156–65. doi:10.1021/acssuschemeng.6b00644.
- [33] Hoppe W, Thonemann N, Bringezu S. Life Cycle Assessment of Carbon Dioxide–Based Production of Methane and Methanol and Derived Polymers. *J Ind Ecol* 2018;22:327–40. doi:10.1111/jiec.12583.
- [34] Bicer Y, Dincer I, Zamfirescu C, Vezina G, Raso F. Comparative life cycle assessment of various ammonia production methods. *J Clean Prod* 2016;135:1379–95. doi:10.1016/j.jclepro.2016.07.023.
- [35] Bicer Y, Dincer I. Life cycle assessment of ammonia utilization in city transportation and power generation. *J Clean Prod* 2018;170:1594–601. doi:10.1016/j.jclepro.2017.09.243.
- [36] Makhoulouf A, Serradj T, Cheniti H. Life cycle impact assessment of ammonia production in Algeria: A comparison with previous studies. *Environ Impact Assess Rev* 2015;50:35–41. doi:10.1016/j.eiar.2014.08.003.
- [37] Average Retail Prices in Canada | Energy Sources | Natural Resources Canada. *Nat Resour Canada* 2019. http://www2.nrcan.gc.ca/eneene/sources/pripri/prices_byyear_e.cfm?ProductID=5#pricesTable (accessed August 10, 2019).
- [38] Park S, Vohs JM, Gorte RJ. Direct oxidation of hydrocarbons in a solid-oxide fuel cell. *Nature* 2000;404:265–7. doi:10.1038/35005040.

- [39] Schroeder DJ, Majumdar P. Feasibility analysis for solid oxide fuel cells as a power source for railroad road locomotives. *Int J Hydrogen Energy* 2010;35:11308–14. doi:10.1016/j.ijhydene.2010.07.067.
- [40] Damo UM, Ferrari ML, Turan A, Massardo AF. Solid oxide fuel cell hybrid system : A detailed review of an environmentally clean and efficient source of energy. *Energy* 2019;168:235–46. doi:10.1016/j.energy.2018.11.091.
- [41] Hyundai Nexo Fuel Cell SUV | Hyundai USA. HyundaiUSA 2019. <https://www.hyundaiusa.com/nexo/index.aspx> (accessed June 17, 2019).
- [42] Statistics of the Week: Comparing Vehicle Ranges for Gas, BEV and PHEV Models – EVAdoption. EVAdoption 2018. <https://evadoption.com/statistics-of-the-week-comparing-vehicle-ranges-for-gas-bevs-and-phevs/> (accessed June 17, 2019).
- [43] Ikäheimo J, Kiviluoma J, Weiss R, Holttinen H. Power-to-ammonia in future North European 100 % renewable power and heat system. *Int J Hydrogen Energy* 2018;43:17295–308. doi:10.1016/j.ijhydene.2018.06.121.
- [44] Acar C. A comprehensive evaluation of energy storage options for better sustainability. *Int J Energy Res* 2018;42:3732–46. doi:10.1002/er.4102.
- [45] Germany launches world’s first hydrogen-powered train | Environment | The Guardian. Guardian 2018. <https://www.theguardian.com/environment/2018/sep/17/germany-launches-worlds-first-hydrogen-powered-train> (accessed June 16, 2019).
- [46] Regional Express Rail Program Hydrail Feasibility Study Report. 2018.
- [47] Yang J, Muroyama H, Matsui T, Eguchi K. Development of a direct ammonia-fueled molten hydroxide fuel cell. *J Power Sources* 2014;245:277–82. doi:10.1016/j.jpowsour.2013.06.143.
- [48] Ganley JC. An intermediate-temperature direct ammonia fuel cell with a molten alkaline hydroxide electrolyte. *J Power Sources* 2008;178:44–7. doi:10.1016/j.jpowsour.2007.11.093.
- [49] Wang A, Gyenge EL. Borohydride electro-oxidation in a molten alkali hydroxide eutectic mixture and a novel borohydride-periodate battery. *J Power Sources* 2015;282:169–73. doi:10.1016/j.jpowsour.2015.02.007.
- [50] Dincer I, Rosen MA. Exergy Analysis of Integrated Trigeneration and Multigeneration Systems. *Exergy*, 2013, p. 303–17. doi:10.1016/B978-0-08-097089-9.00014-0.
- [51] Siddiqui O, Dincer I. Analysis and performance assessment of a new solar-based multigeneration system integrated with ammonia fuel cell and solid oxide fuel cell-gas turbine combined cycle. *J Power Sources* 2017;370:138–54. doi:10.1016/j.jpowsour.2017.10.008.
- [52] Sadeghi M, Chitsaz A, Mahmoudi SMS, Rosen MA. Exergoeconomic analysis of

- a trigeneration system driven by a solid oxide fuel cell. *Energy Convers Manag* 2015;106:921–31. doi:10.1016/j.enconman.2015.10.009.
- [53] Meratizaman M, Monadizadeh S, Amidpour M. Introduction of an efficient small-scale freshwater-power generation cycle (SOFC-GT-MED), simulation, parametric study and economic assessment. *Desalination* 2014;351:43–58. doi:10.1016/j.desal.2014.07.023.
- [54] Najafi B, Shirazi A, Aminyavari M, Rinaldi F, Taylor RA. Exergetic, economic and environmental analyses and multi-objective optimization of an SOFC-gas turbine hybrid cycle coupled with an MSF desalination system. *Desalination* 2014;334:46–59. doi:10.1016/j.desal.2013.11.039.
- [55] Jing R, Wang M, Brandon N, Zhao Y. Multi-criteria evaluation of solid oxide fuel cell based combined cooling heating and power (SOFC-CCHP) applications for public buildings in China. *Energy* 2017;141:273–89. doi:10.1016/j.energy.2017.08.111.
- [56] Buonomano A, Calise F, d'Accadia MD, Palombo A, Vicidomini M. Hybrid solid oxide fuel cells-gas turbine systems for combined heat and power: A review. *Appl Energy* 2015;156:32–85. doi:10.1016/j.apenergy.2015.06.027.
- [57] Eveloy V, Karunkeyoon W, Rodgers P, Al Alili A. Energy, exergy and economic analysis of an integrated solid oxide fuel cell – gas turbine – organic Rankine power generation system. *Int J Hydrogen Energy* 2016;41:13843–58. doi:10.1016/j.ijhydene.2016.01.146.
- [58] Singh R, Singh O. Comparative study of combined solid oxide fuel cell-gas turbine-Organic Rankine cycle for different working fluid in bottoming cycle. *Energy Convers Manag* 2018;171:659–70. doi:10.1016/j.enconman.2018.06.009.
- [59] Yan Z, Zhao P, Wang J, Dai Y. Thermodynamic analysis of an SOFC-GT-ORC integrated power system with liquefied natural gas as heat sink. *Int J Hydrogen Energy* 2013;38:3352–63. doi:10.1016/j.ijhydene.2012.12.101.
- [60] Zhang S, Liu H, Liu M, Sakaue E, Li N, Zhao Y. An efficient integration strategy for a SOFC-GT-SORC combined system with performance simulation and parametric optimization. *Appl Therm Eng* 2017;121:314–24. doi:10.1016/j.applthermaleng.2017.04.066.
- [61] Gholamian E, Zare V. A comparative thermodynamic investigation with environmental analysis of SOFC waste heat to power conversion employing Kalina and Organic Rankine Cycles. *Energy Convers Manag* 2016;117:150–61. doi:10.1016/j.enconman.2016.03.011.
- [62] Bertsch SS, Groll EA. Two-stage air-source heat pump for residential heating and cooling applications in northern U.S. climates. *Int J Refrig* 2008;31:1282–92. doi:10.1016/j.ijrefrig.2008.01.006.
- [63] Lazzarin R, Noro M. District heating and gas engine heat pump: Economic analysis based on a case study. *Appl Therm Eng* 2006;26:193–9.

doi:10.1016/j.applthermaleng.2005.05.013.

- [64] Cui Y, Geng Z, Zhu Q, Han Y. Review: Multi-objective optimization methods and application in energy saving. *Energy* 2017;125:681–704. doi:10.1016/j.energy.2017.02.174.
- [65] Sinha S, Chandel SS. Review of recent trends in optimization techniques for solar photovoltaic-wind based hybrid energy systems. *Renew Sustain Energy Rev* 2015;50:755–69. doi:10.1016/j.rser.2015.05.040.
- [66] Ramadhani F, Hussain MA, Mokhlis H, Hajimolana S. Optimization strategies for Solid Oxide Fuel Cell (SOFC) application: A literature survey. *Renew Sustain Energy Rev* 2017;76:460–84. doi:10.1016/j.rser.2017.03.052.
- [67] Syafaruddin S. Review on Multi-Objectives Optimization Methods in Hybrid Power Generation. *J Eng Sci Technol Rev* 2019;12:143–52. doi:10.25103/jestr.121.17.
- [68] Sharifzadeh M, Meghdari M, Rashtchian D. Multi-objective design and operation of Solid Oxide Fuel Cell (SOFC) Triple Combined-cycle Power Generation systems: Integrating energy efficiency and operational safety. *Appl Energy* 2017;185:345–61. doi:10.1016/j.apenergy.2016.11.010.
- [69] Gholamian E, Hanafizadeh P, Habibollahzade A, Ahmadi P. Evolutionary based multi-criteria optimization of an integrated energy system with SOFC, gas turbine, and hydrogen production via electrolysis. *Int J Hydrogen Energy* 2018;43:16201–14. doi:10.1016/j.ijhydene.2018.06.130.
- [70] Khani L, Mahmoudi SMS, Chitsaz A, Rosen MA. Energy and exergoeconomic evaluation of a new power/cooling cogeneration system based on a solid oxide fuel cell. *Energy* 2016;94:64–77. doi:10.1016/j.energy.2015.11.001.
- [71] Salehi Z, Gholaminezhad I. Multi-objective modeling, uncertainty analysis, and optimization of reversible solid oxide cells. *Int J Energy Environ Eng* 2018;9:295–304. doi:10.1007/s40095-018-0269-5.
- [72] Woolf D, Lehmann J, Lee DR. Optimal bioenergy power generation for climate change mitigation with or without carbon sequestration. *Nat Commun* 2016;7. doi:10.1038/ncomms13160.
- [73] Seyam S, Al-Hamed KHM, Qureshy AMMI, Dincer I, Agelin-Chaab M, Rahnamayan S. Multi-objective Optimization of Hydrogen Production in Hybrid Renewable Energy Systems. 2019 IEEE Congr. Evol. Comput., IEEE Congress on Evolutionary Algorithms; 2019.
- [74] Szargut J. Exergy. Calculation and application guide. 2007. doi:https://doi.org/10.1017/CBO9780511976049.
- [75] Rosen MA, Dincer I, Kanoglu M. Role of exergy in increasing efficiency and sustainability and reducing environmental impact. *Energy Policy* 2008;36:128–37. doi:10.1016/j.enpol.2007.09.006.

- [76] Deb K, Pratap A, Agarwal S, Meyarivan T. A fast and elitist multiobjective genetic algorithm: NSGA-II. *IEEE Trans Evol Comput* 2002;6:182–97. doi:10.1109/4235.996017.
- [77] 100 Kw Steam Turbine 3344 Intelligent Steam Generator 2019. https://www.alibaba.com/product-detail/100-kw-steam-turbine-3344-intelligent_60726034594.html?spm=a2700.7724857.normalList.22.57256b1dcHazoP (accessed June 8, 2019).
- [78] EES: Engineering Equation Solver | F-Chart Software : Engineering Software. F-Chart Softw 2019;2012. <http://fchart.com/ees/> (accessed June 17, 2019).
- [79] Heating and Cooling With a Heat Pump. Natural Resources Canada; 2004. <https://www.nrcan.gc.ca/sites/oe.nrcan.gc.ca/files/pdf/publications/infosource/pub/home/heating-heat-pump/booklet.pdf> (accessed April 18, 2019).
- [80] 24000 BTU Concealed Duct Air Conditioner - Heat Pump - SENA/24HF/ID - SoGoodToBuy.ca n.d. <https://www.sogoodtobuy.ca/24000-btu-concealed-duct-air-conditioner-heat-pump-sena-24hf-id/> (accessed April 18, 2019).
- [81] Hot Water Driven Vapor Absorption Machine. Thermax; 2019. <http://www.thermax-usa.com/pdf/Hot-Water-driven-absorption-Chillers/Hot-Water-driven-absorption-Chillers.pdf> (accessed April 18, 2019).
- [82] Leeper J. 220 kW Solid Oxide Fuel Cell/Microturbine Generator Hybrid proof of Concept Demonstration Report. 2001.
- [83] Shirazi A, Aminyavari M, Najafi B, Rinaldi F, Razaghi M. Thermal-economic-environmental analysis and multi-objective optimization of an internal-reforming solid oxide fuel cell-gas turbine hybrid system. *Int J Hydrogen Energy* 2012;37:19111–24. doi:10.1016/j.ijhydene.2012.09.143.
- [84] Chan SH, Ho HK, Tian Y. Modelling of simple hybrid solid oxide fuel cell and gas turbine power plant. *J Power Sources* 2002;109:111–20. doi:10.1016/S0378-7753(02)00051-4.
- [85] Saisirirat P. The Solid Oxide Fuel Cell (SOFC) and Gas Turbine (GT) Hybrid System Numerical Model. *Energy Procedia* 2015;79:845–50. doi:10.1016/j.egypro.2015.11.576.
- [86] Hosseini M, Dincer I, Ahmadi P, Avval HB, Ziaasharhagh M. Thermodynamic modelling of an integrated solid oxide fuel cell and micro gas turbine system for desalination purposes. *Int J Energy Res* 2013:426–34.
- [87] Zhan Z, Bierschenk DM, Cronin JS, Barnett SA. A reduced temperature solid oxide fuel cell with nanostructured anodes. *Energy Environ Sci* 2011;4:3951–4. doi:10.1039/c1ee01982a.
- [88] Clavier JY, Perrut M. Safety in supercritical operations. *Process Technology Proceedings* 1996 Jan 1 (Vol. 12, pp. 627-631). Elsevier.
- [89] Siddiqui O. Development and Investigation of Alkaline Electrolyte Based Direct

Ammonia Fuel Cells. MASc thesis, Automotive, Mechanical and Manufacturing Engineering Department, University of Ontario Institute of Technology, 2018.

- [90] Marin P, Chairperson TC, Pellerin N, Roberge K, Chairperson CP. Locomotive Emissions Monitoring Program 2010.
- [91] Ali M. Al. Development of Novel Energy Systems for LNG Locomotives. MASc thesis, Automotive, Mechanical and Manufacturing Engineering Department, University of Ontario Institute of Technology, 2015.